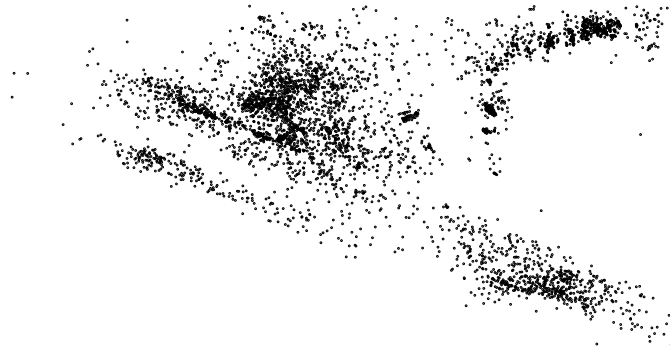


**In-situ Properties of the Subducting Nazca Slab:  
Constraints on the Deep Water Cycle  
and the Dynamics of Subduction  
from Seismological Observations**



**Dissertation**

zur Erlangung des Doktorgrades der Naturwissenschaften (Dr. rer. nat.)  
am Fachbereich Geowissenschaften  
Institut für Geologische Wissenschaften  
Fachrichtung Geophysik  
der Freien Universität Berlin

vorgelegt von

Wasja Bloch, M.Sc.

Berlin  
2017

Erstgutachter: Prof. Dr. Serge A. Shapiro  
Zweitgutachter: Prof. Dr. Onno Oncken

Tag der Disputation: 26. Juni 2017

Your methods turn out to be ideal.  
Go ahead.

---

Fortune Cookie



# Summary

In this thesis I use local earthquake data to investigate physical rock properties near the nucleation point of small earthquakes in the Central Andean subduction system at 21° S. The subduction of the oceanic crust below the continental lithosphere causes complex processes in both plates. The subducting Nazca plate is pushed below the continental South American plate by the elevated newly forming oceanic crust from the mid-ocean ridge and is pulled into the mantle by the dense subducted slab. At the plate interface, compressional stress is transferred to the overriding plate, causing uplift of the continent.

Small earthquakes may nucleate due to different processes within this system. Brittle failure along the major crustal fault-zones, the plate interface, or subduction-induced bend-faults can occur at shallow depth. At intermediate depth, the breakdown of hydrous mineral phases has been hypothesized to be involved in the nucleation process.

I observe abundant seismicity in the overriding plate as well as at shallow and intermediate depth within the subducting plate. I localize the seismic events with high precision. The oceanic lithosphere clearly exhibits a Wadati-Benioff-zone that is structured in three slab-parallel bands. One is located at the plate interface at shallow depth, one near the oceanic Moho, and a third one 20 km below the oceanic Moho within the lithospheric mantle. The comparison with results from the ANCORP'96 active source seismic experiment yields a tight correlation between seismicity and reflectivity. Seismicity of the continental crust is pervasive to lower crustal levels onshore towards the trench. It is constrained to the upper crust towards the magmatic arc. The sharp lower limit of seismicity delineates the brittle-ductile boundary.

In order to investigate the acting forces and to identify pre-defined structures within the subducting slab, I compute focal mechanisms for 180 weak earthquake using first motion polarities and P/S-amplitude ratios. For 10 of the events I further perform a full waveform inversion for the whole moment tensor at relatively short periods. The results show that shallow seismicity is dominated by compressive ridge-push and collisional forces, and intermediate depth seismicity by dilatational slab-pull. An overall steepening of the tension-direction of the focal mechanisms pleads for a successive intensification of the downward-pulling force component, possibly attributed to a densification of the rock matrix.

To test the mineral dehydration hypothesis for the nucleation of intermediate depth earthquakes, I construct a petrophysical model that allows me to predict the mineral assemblage of the subducting oceanic crust and mantle, considering metamorphic mineral reactions. I compute elastic rock properties and investigate for selected mineralogies

---

the influences of fluid-filled pore-space and elastic anisotropy. The results show that high seismic P- to S-wave velocity ratios ( $V_P/V_S$ -ratios) are indicative for the presence of fluids in pressurized compliant pores. Low  $V_P/V_S$ -values can be attributed to certain orientations of anisotropic rock fabrics.

I critically review a method to estimate  $V_P/V_S$ -ratios in the direct vicinity of a set of seismic events from arrival time measurements of elastic body waves. I demonstrate that the method yields a biased estimator if the subsurface  $V_P/V_S$ -ratio is heterogeneous, but that it cannot produce artificial anomalies. I apply a revised version of this method to the entire seismic event cloud. The near-source  $V_P/V_S$ -ratio in the continental crust is in accordance with mafic lithologies in the onshore trench-ward side of the forearc region and with more intermediary lithologies in the arc-ward region.

In the subducting slab at shallow depth, I find  $V_P/V_S$ -values that are in agreement with the presence of a blueschist. At intermediate depth I find anomalous values. At shallow intermediate depth, a high  $V_P/V_S$ -value probably indicates the presence of a compliant network of interconnected pressurized veins. This network may facilitate effective slab devolatilization. The petrophysical model indicates the dehydration of antigorite in the presence of brucite at this point in the slab. At deeper intermediate depth two clusters of high and low  $V_P/V_S$ -ratios also indicate the presence of a free fluid-phase within the medium and additionally require the presence of a strongly anisotropic medium. The petrophysical model suggests that at this point the final dehydration of antigorite takes place.

Altogether, the results deliver a coherent picture from the perspective of observational seismology of the driving forces of subduction, the transfer of stress to the overriding plate, the transport of seawater below the continent, its release there and the attributed successive densification of the descending lithosphere.

# Resumen

En esta tesis se utilizan datos locales para investigar las propiedades cerca del punto de nucleación de pequeños terremotos en el sistema de subducción de los Andes Centrales a 21 ° S. La subducción del océano por debajo de la litósfera continental provoca procesos complejos en ambas placas. Es así que la placa de Nazca es empujada por debajo de la placa continental de Sudamérica debido a la formación de corteza oceánica en la dorsal mesoceánica y al mismo tiempo es atraída hacia el manto por propia densidad. En la interfaz de las placas (Nazca-Sudamérica), el estrés de compresión se transfiere a la placa cabalgante, causando la elevación del continente.

Pequeños terremotos pueden nuclearse por diferentes procesos dentro de este sistema. Dominio reológico frágil a lo largo de las principales zonas de falla de la corteza, la fricción ocurrida en la interfase de la placa o la curvatura en fallas inducidas por subducción pueden ser fenómenos que ocurrirían a profundidad somera. A profundidad intermedia, se ha planteado la hipótesis de que la desintegración de las fases minerales hidratadas estaría involucrada en la nucleación de los terremotos.

Es así que se observa una abundante sismicidad en la placa cabalgante, como también a profundidad somera e intermedia dentro de la placa subductada. Los eventos sísmicos fueron localizados con alta precisión. La litósfera oceánica muestra claramente una zona de Wadati-Benioff que está estructurada en tres bandas paralelas. La primera está situada en la interfaz de la placa a poca profundidad, la otra banda se ubica cerca del Moho oceánico, y la tercera a 20 km debajo del Moho oceánico (dentro del manto litosférico). En comparación con los resultados del experimento sísmico de fuente activa ANCORP'96 se puede establecer una estrecha correlación entre la sismicidad y la reflectividad. La sismicidad de la corteza continental es intensa en los niveles corticales inferiores de la Cordillera de la Costa hasta la fosa. Por otro lado, esta se restringe a la corteza superior, hacia el arco magmático. El nítido límite inferior de la sismicidad marca el límite reológico frágil-dúctil.

Con el fin de investigar las fuerzas que actúan e identificar estructuras predefinidas dentro de la placa subductante, se calcularon los mecanismos focales para 180 terremotos pequeños de magnitudes entre 2,0 y 4,0 utilizando las primeras polaridades de movimiento y las relaciones de amplitud P / S. Para 10 de los eventos se realizó además una inversión completa de la forma de onda para todo el tensor de momento en periodos relativamente cortos. Los resultados muestran que la sismicidad superficial está dominada por las fuerzas compresivas de empuje de la dorsal y las fuerzas colisionales entre las placas; en la sismicidad de profundidad intermedia domina la dilatación producida por la tracción de la placa subductada. Una predominancia general de la dirección de

---

tensión de los mecanismos focales aboga por una intensificación sucesiva de la componente de fuerza de tracción hacia abajo, posiblemente atribuida a una densificación de la matriz de roca.

Para probar la hipótesis de deshidratación mineral para la nucleación de terremotos de profundidad intermedia, se construyó -considerando las reacciones minerales metamórficas- un modelo petrofísico que permite predecir el arreglo mineral de la corteza oceánica y manto subductado. Además se calcularon las propiedades elásticas de las rocas y se evaluó, para las mineralogías seleccionadas, las influencias del espacio poroso lleno de líquido y la anisotropía elástica. Esto dió como resultado que las altas relaciones de velocidades sísmicas de P v/s S ( $V_P/V_S$ ) son indicativas de la presencia de fluidos en los poros presurizados compatibles. Los valores bajos de  $V_P/V_S$  se pueden atribuir a ciertas orientaciones de los tejidos rocosos anisotrópicos.

Se realizó una revisión crítica de un método para estimar, mediante las mediciones del tiempo de arribo de las ondas elásticas de cuerpo, la relación  $V_P/V_S$  en la directa vecindad de un conjunto de eventos sísmicos. Se aplicó una versión revisada de este método a toda la nube de eventos sísmicos. La relación  $V_P/V_S$ , cercana a la fuente, de la corteza continental está de acuerdo con las litologías máficas en las zonas de la Cordillera de la Costa hacia la fosa de la región del antearco y a litologías más intermedias hacia la región del arco.

En la placa subductada a poca profundidad, se encontró valores de  $V_P/V_S$  que están de acuerdo con la presencia de la facies esquistos azules. A profundidad intermedia se encontró valores anómalos. En una profundidad intermedia poco profunda, un alto valor  $V_P/V_S$  indica probablemente la presencia de una red de venas presurizadas interconectadas. Esta red puede facilitar la desvolatilización eficaz de la placa subductada. El modelo petrofísico indica la deshidratación de la antigorita en presencia de brucita en este punto de la placa. A una profundidad intermedia más profunda, dos 'clusters' de alta y baja relaciones de  $V_P/V_S$  también indican la presencia de una fase fluida libre dentro del medio que además requiere la presencia de un medio fuertemente anisotrópico. El modelo petrofísico sugiere que en este punto tiene lugar la deshidratación final de la antigorita.

En conjunto, los resultados proporcionan una imagen coherente desde la perspectiva de la sismología observacional de las fuerzas motrices de la subducción, la transferencia del estrés a la placa cabalgante, el transporte del agua de mar por debajo del continente, su posterior liberación y la atribuida densificación sucesiva de la Litosfera descendente.



# Zusammenfassung

In dieser Arbeit verwende ich lokale Erdbebendaten, um die Eigenschaften in der Umgebung von kleinen Erdbeben in der Subduktionszone der Zentralen Anden bei 21° S zu untersuchen. Bei der Subduktion der ozeanischen unter die kontinentale Lithosphäre treten komplexe Prozesse in beiden Platten auf. Die abtauchende Nazca Platte wird von nachrückender ozeanischer Lithosphäre, die am mittelozeanischen Rücken neu entsteht, unter die kontinentale Südamerikanische Platte geschoben. Sie wird außerdem durch den dichten, subduzierten Slab in den Mantel gezogen. An der Plattengrenze übertragen sich Spannungen auf die hangende Platte und verursacht eine Hebung des Kontinents.

Kleine Erdbeben entstehen in diesem System aufgrund von verschiedenen Prozessen. In geringen Tiefen kann es zum spröden Bruch entlang von großen krustalen Störungszonen, an der Plattengrenze oder an Biegefalten innerhalb der subduzierenden Platte kommen. Für mitteltiefe Erdbeben wird vermutet, dass die Entwässerung von wasserhaltigen Mineralphasen an der Erdbebenentstehung beteiligt ist.

Ich beobachte Seismizität in der kontinentalen Kruste und möglicherweise im kontinentalen Mantel, sowie in flachen und mittleren Tiefen innerhalb des subduzierenden Slabs. Ich führe eine genaue Erdbebenlokalisierung durch. In der ozeanischen Lithosphäre tritt Seismizität in drei platten-parallelen Bändern auf. Das obere Band befindet sich in flacher Tiefe an der Plattengrenze, ein weiteres Band nahe der ozeanischen Moho und ein drittes Band 20 km unterhalb der ozeanischen Moho im lithosphärenischen Mantel. Der Vergleich mit den Ergebnissen des reflexionsseismischen Experiments AN-CORP'96 zeigt eine enge Korrelation zwischen Seismizität und Reflektivität. Krustale Seismizität tritt nahe der Küste bis in tiefe Krustenstockwerke auf. In Richtung des vulkanischen Bogens ist sie auf die Oberkruste beschränkt. Die scharfe untere Grenze der Seismizität markiert hier die spröd-duktil Grenze.

Um die Kräfte zu untersuchen, die bei der Subduktion wirken, und um vordefinierte Störungszonen innerhalb der subduzierenden Platte zu identifizieren, berechne ich Herdmechanismen für 180 schwache Erdbeben. Dazu verwende ich Ersteinsatzpolaritäten und P/S-Amplitudenverhältnisse. Für 10 der Ereignisse führe ich eine vollständige Wellenforminversion bei kurzen Perioden durch, um den vollständigen Momententensor zu erhalten. Die Ergebnisse zeigen, dass flache Seismizität in der subduzierenden Platte von kompressiven 'ridge push'- und Kollisions-Kräften dominiert wird, während mitteltiefe Seismizität hauptsächlich durch 'slab pull'-Zugkräfte hervorgerufen wird. Insgesamt deuten die Herdmechanismen entlang des Subduktionsweges auf eine Versteilung der Zug-Achse hin. Dies spricht für eine sukzessive Verstärkung der in die Tiefe weisenden Kraftkomponente, was möglicherweise ein Hinweis darauf ist, dass die Dichte der

---

Gesteinsmatrix während der Subduktion bereits in mittleren Tiefen zunimmt.

Um die Mineralentwässerungshypothese für mitteltiefe Seismizität zu testen, stelle ich ein petrophysikalisches Modell auf, das es mir erlaubt, Vorhersagen über die Mineralzusammensetzung der subduzierenden Platte zu treffen und elastische Gesteinseigenschaften zu berechnen. Für einige Mineralogien werte ich außerdem den Einfluss von Fluid gefülltem Porenraum und elastischer Anisotropie auf die elastischen Gesteinseigenschaften aus. Es zeigt sich, dass ein hohes seismisches P- zu S-Wellen Geschwindigkeitsverhältnis ( $V_P/V_S$ -Verhältnis) auf das Vorhandensein von Fluid gefülltem Porenraum schließen lässt. Niedrige  $V_P/V_S$ -Werte deuten auf bestimmte Ausrichtungen einer anisotropen Gesteinstextur hin.

Ich entwickle eine Methode weiter, die es erlaubt direkt aus den Ankunftszeiten von P- und S-Wellen das  $V_P/V_S$ -Verhältnis in der Umgebung eines Clusters von seismischen Ereignissen zu berechnen. Ich zeige, dass die Methode einen fehlerhaften Schätzer produziert, wenn das  $V_P/V_S$ -Verhältnis im Untergrund heterogen verteilt ist. Sie erzeugt jedoch keine unechten Anomalien. Ich wende die weiter entwickelte Methode auf die gesamte Wolke von seismischen Ereignissen an. Die quellnahen  $V_P/V_S$ -Verhältnisse stimmen in der kontinentalen Kruste nahe der Küste mit den Werten von mafischen Lithologien überein. In Richtung des vulkanischen Bogens deuten sie auf intermediäre Lithologien hin.

In der subduzierten Platte schätze ich  $V_P/V_S$ -Verhältnisse ab, die auf das Vorhandensein von Blauschiefer schließen lassen. In mittleren Tiefen werden die  $V_P/V_S$ -Werte anomal. In etwa 50 km Tiefe, im unteren Seismizitätsband, weist ein hoher  $V_P/V_S$ -Wert darauf hin, dass sich dort ein verbundenes, unter Fluiddruck stehendes Adernetzwerk befindet. Dieses Netzwerk kann die effektive Entwässerung des Slabs ermöglichen. Das petrophysikalische Modell deutet darauf hin, dass an dieser Stelle die Entwässerung von Antigorit in Anwesenheit von Brucit stattfindet. Auch in tieferen mittleren Tiefen weisen zwei Bereiche von sehr hohem und sehr niedrigem  $V_P/V_S$ -Verhältnis auf die Anwesenheit einer freien Fluidphase hin, die hier jedoch in einem stark anisotropen Medium vorhanden sein muss. Das petrophysikalische Modell zeigt dort den endgültigen Zusammenbruch von Antigorit.

Insgesamt liefern die Ergebnisse ein zusammenhängendes Bild der bei der Subduktion wirkenden Kräfte, der Übertragung von Spannung in die hangende Platte, des Transportes von Meereswasser unter den Kontinent, von dessen Freisetzung dort, und des kontinuierlichen dichter werdens der abtauchenden Lithosphäre, aus der Perspektive von seismologischen Beobachtungen.

# Danksagung

Mein Dank gilt Prof. Serge Shapiro für die Bereitstellung des Themas und die Betreuung dieser Arbeit und Prof. Onno Oncken für die Übernahme des Zweitgutachtens und die aufschlussreichen Diskussionen im Gelände.

Ich danke weiterhin Dr. Jörn Kummerow, Prof. Timm John, Prof. Frederik Tilmann und Dr. Bernd Schurr für die gründliche methodische Ausbildung, die kritischen Diskussionen und die genialen Ideen.

Ein besonderer Dank gilt Antonia Oelke und Jonas Folesky für den Support in allen Angelegenheiten.

Vielen Dank auch an meine Kollegen Anton, Aurelian, Carsten, Cornelius, Jörg, Julio, Lisa, Naoyuki, Olli, Pablo, Peter, Sibylle, Slava und Stine für die wunderbare Zeit in der Arbeitsgruppe.

Ich danke den Communities von *obspy* und *Perple\_X* für den Software Support und die technischen Diskussionen und allen Open Source Projekten für die Bereitstellung von Programmen.

Einen ganz herzlichen Dank auch an die Korrekturlesenden Chris und Ayse.

Danke auch an Benni, Bashar, Chris, Henning, Jakob, Jeanine, Jonas, Judith, Kim, Nadja, Niklas, Sophie, Stephan, Suniva und Wendy.

Danke Delaja und Lua.

Danke liebe Eltern.



# Contents

<b>Summary</b>	<b>5</b>
<b>Resumen</b>	<b>7</b>
<b>Zusammenfassung</b>	<b>9</b>
<b>Danksagung</b>	<b>11</b>
<b>Contents</b>	<b>13</b>
<b>1 Introduction</b>	<b>17</b>
1.1 Subduction of seawater . . . . .	18
1.2 Seismicity at shallow and intermediate depth . . . . .	19
1.3 Failure mechanisms for intermediate depth earthquakes . . . . .	20
1.4 Driving and slowing forces of subduction . . . . .	21
1.5 Processes in the overriding plate . . . . .	21
1.6 The Central Andean Subduction System . . . . .	22
1.7 Data base . . . . .	24
<b>2 Local seismicity</b>	<b>27</b>
2.1 Previous work . . . . .	27
2.2 The dataset . . . . .	28
2.3 Localization procedure . . . . .	28
2.4 Results . . . . .	30
2.4.1 Seismicity in the continental crust . . . . .	30
2.4.2 Seismicity of the subducting slab . . . . .	32
2.5 Comparison with seismic reflectivity . . . . .	33
2.5.1 Plate Interface . . . . .	33
2.5.2 Subducting Slab . . . . .	33
2.5.3 Continental Crust . . . . .	34
2.6 Conclusion . . . . .	36
2.7 Outlook . . . . .	36
<b>3 Focal mechanisms</b>	<b>39</b>
3.1 Previous work . . . . .	39
3.2 Methodology . . . . .	40

3.2.1	Using first motion polarity and P- to S-amplitude ratio . . . . .	41
3.2.2	Using the full waveform . . . . .	41
3.2.2.1	Theory . . . . .	41
3.2.2.2	Application . . . . .	43
3.2.3	Quality measure . . . . .	44
3.2.4	Representation . . . . .	45
3.3	Results . . . . .	45
3.3.1	Upper bands (UB) . . . . .	46
3.3.2	Lower band at shallow intermediate depth (LB) . . . . .	46
3.3.3	Transitional zone (TZ) . . . . .	46
3.3.4	Deeper intermediate depth (DID) . . . . .	49
3.4	Discussion . . . . .	52
3.5	Conclusion . . . . .	55
<b>4</b>	<b>Petrophysical modeling</b>	<b>57</b>
4.1	Properties of isotropic non-porous subducting lithosphere . . . . .	57
4.1.1	Thermodynamic considerations . . . . .	58
4.1.2	Elastic properties . . . . .	58
4.1.3	Dynamic creation of pore-space . . . . .	59
4.1.4	Petrology of subducting oceanic crust . . . . .	60
4.1.5	Petrology of subducting oceanic mantle . . . . .	62
4.1.6	Petrology of the continental crust . . . . .	63
4.2	The influence of fluid-filled pore-space on elasticity . . . . .	63
4.2.1	Poroelastic modeling . . . . .	63
4.2.2	Results . . . . .	65
4.2.3	Sensitivity on pore pressure . . . . .	66
4.3	Effects of anisotropic elastic properties . . . . .	67
4.3.1	Nomenclature . . . . .	67
4.3.2	Parameterization . . . . .	67
4.3.3	Crystallographic anisotropy . . . . .	69
4.3.4	Structural anisotropy . . . . .	71
4.3.5	The $V_P/V_S$ -ratio of anisotropic mantle rocks . . . . .	71
4.4	Conclusion . . . . .	72
<b>5</b>	<b>Estimation of the <math>V_P/V_S</math>-ratio using arrival time differences of closely spaced seismic events</b>	<b>73</b>
5.1	Seismic tomography studies of other subduction zones . . . . .	73
5.2	Method . . . . .	75
5.2.1	Assumptions and theory . . . . .	75
5.2.1.1	Original problem statement . . . . .	75
5.2.1.2	Revision of assumptions . . . . .	77
5.2.1.3	Relation between the $\gamma$ -slope and the $V_P/V_S$ -ratio . . . . .	78
5.2.1.4	Inversion scheme . . . . .	80
5.2.2	Application to the microseismic event cloud in the Central Andes . . . . .	82
5.2.2.1	Search for constant $\gamma$ . . . . .	82

## CONTENTS

---

5.2.2.2	Lookup tables . . . . .	86
5.2.3	Verification of results using event repicking . . . . .	86
5.3	Regional distribution of $\gamma$ . . . . .	86
5.3.1	Coastal Cordilleran crust . . . . .	88
5.3.2	Precordilleran crust . . . . .	88
5.3.3	Upper band of seismicity . . . . .	91
5.3.4	Lower band of seismicity . . . . .	91
5.3.5	Deeper intermediate depth . . . . .	92
5.4	Validation of $V_P/V_S$ in the shallow oceanic mantle . . . . .	93
5.4.1	Result for the whole cluster . . . . .	94
5.4.2	Results for subsets of events . . . . .	94
5.4.3	Station selection . . . . .	96
5.4.4	Distribution of take-off angles . . . . .	97
5.5	Discussion . . . . .	100
5.5.1	Lithology at deeper intermediate depth . . . . .	101
5.5.2	Pore geometry in regions of high $\gamma$ . . . . .	101
5.6	Conclusion . . . . .	102
<b>6</b>	<b>Conclusion</b>	<b>105</b>
6.1	Joint interpretation . . . . .	105
6.2	Outlook . . . . .	108
	<b>Appendices</b>	<b>109</b>
<b>A</b>	<b>Fault plane solutions</b>	<b>111</b>
<b>B</b>	<b>Results of full-waveform moment tensor inversions</b>	<b>119</b>
<b>C</b>	<b>Mineral phase models</b>	<b>141</b>
<b>D</b>	<b>Quantification of a complex shortcut effect</b>	<b>145</b>
	<b>Bibliography</b>	<b>155</b>
	<b>Curriculum Vitae</b>	<b>166</b>
	<b>Publications and Conference Abstracts</b>	<b>167</b>





# Chapter 1

## Introduction

The Earth would be uninhabitable without subduction zones. They couple the cycling of water through the atmosphere and hydrosphere with the deep water cycle through the lithosphere. In this way they provide the basis for a broad range of planetary processes that are unique within the solar system: The withdrawal of water and carbon dioxide from the atmosphere through the oceans at oceanic trenches prevents extreme greenhouse conditions. Their release within the lithosphere induces melting, allowing for the process of magmatic differentiation that leads to the creation of juvenile crust and the rise of continents. Magmatic differentiation enriches the chemical elements in the Earth's crust that are vital to living beings. The ascent of magma culminates in volcanic eruptions that disperse water and inorganic nutrients in the atmosphere and the oceans, allowing life to flourish. A small portion of water subducts further into the Earth, where it lowers the viscosity of the mantle, facilitating plate convection and hot-spot volcanism.

Water that is released from the deep water cycle evaporates from lavas, hydrothermal ponds, and vents. While the journey of this water through the atmosphere and hydrosphere is readily available for observation, its origin is not. The mechanisms by which water is extracted from the hydrosphere, transported through the lithosphere, and liberated back to the atmosphere take place tens of kilometers below the surface of the planet. But the presence of water there is by no means of lesser importance. On the contrary, volatiles in subduction zones participate in the most violent natural phenomena that the inanimate Earth can cause, namely volcanic eruptions and megathrust earthquakes.

Subduction zones provide a fascinating phenomenon that can be used to overcome the observational difficulties of the deep lithosphere. They produce frequent and typically imperceptible background seismicity. Seismological methods allow the use of the elastic energy that is radiated by these seismic events to extract information about the stresses and the elastic properties of their close surroundings. Moreover, it has been hypothesized that some of the weak earthquakes that occur in subduction zones are attributed to the breakdown of mineral phases that contain hydrogen within their lattice. Seismic background activity at subduction zones therefore provides a convenient source of information to study the deep water cycle.

In this thesis I use ground velocity recordings of small but abundant earthquakes that occur within the Central Andean subduction zone to estimate the direction of the prin-

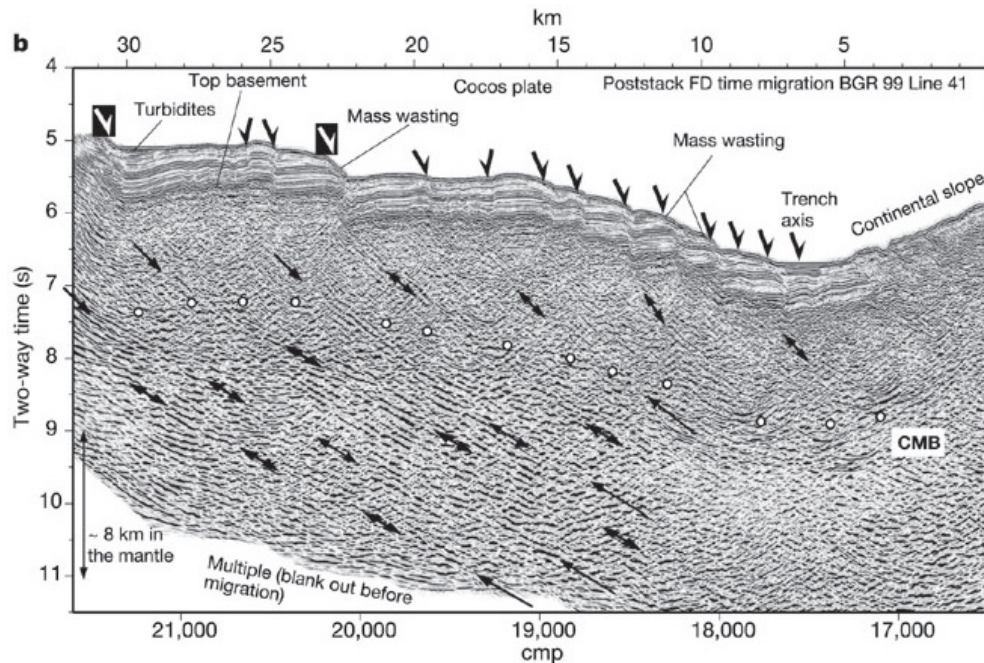


**Figure 1.1:** Seismic image of bend-faults in the oceanic Cocos plate off the coast of South Costa Rica. CMB: Crust mantle boundary (Moho). Arrows: Surface traces and subsurface continuations of bend-faults. From Ranero et al. (2003).

cipal stresses as well as the seismic P- to S-wave velocity ratio in the close vicinity of these earthquakes. I construct a petrophysical model that facilitates the interpretation of the results in the framework of the deep water cycle.

## 1.1 Subduction of seawater

Oceanic lithosphere is produced at mid-ocean ridges. At fast spreading ridges it typically has a layered structure. On top is the mafic oceanic crust, which consists of a basaltic upper crust and a gabbroic lower crust. It has a typical thickness of 6 to 8 kilometers. Slower spreading oceanic ridges generally develop a thinner and less differentiated crust. Below the crust lies the ultra-mafic mantle, which is usually of harzburgitic composition.

With progressing time at the Earth's surface, the oceanic lithosphere cools down, accumulates a sediment layer, and moves towards the subduction zone. When it reaches the convergent plate boundary, it collides the other tectonic plate, bends down, and sinks into the mantle. Upon bending, fault scarps develop at the slab surface that have been imaged to penetrate the oceanic crust and the uppermost oceanic mantle (Fig. 1.1, Ranero et al. (2003)). It has been suggested that sea water may enter the oceanic lithosphere to a depth of several tens of kilometers below the Moho. As a consequence, a number of hydrous mineral phases would form within the oceanic crust and mantle (e.g. Rüpke et al. (2004)).

Upon entering the subduction zone, the oceanic lithosphere is subject to increasing pres-

sure and temperature. Mineral phases that are stable at the relatively low-temperature conditions of the near surface break down and evolve into others. In laboratory experiments it has been shown that some of the hydrous mineral phases that may exist within the subduction system are stable to pressures of a few Gigapascals and temperatures of many hundreds of degrees Celsius. They facilitate the transport of sea-water into the subduction zone (Ulmer and Trommsdorff, 1995)

## 1.2 Seismicity at shallow and intermediate depth

Shallow earthquakes far away from convergent plate boundaries are typically restricted to the uppermost 15 to 20 kilometers of the crust, where they occur in response to crustal deformation in a regime of large differential stresses. They are generally related to active fault zones or regions of geothermal activity.

In subduction zones, shallow seismicity can be observed to greater depth. In the forearc region of the overriding plate, seismicity occurs in deeper crustal levels, because the plate is cooled from below by the subducting plate. Megathrust earthquake can rupture the plate interface from the trench to a maximal depth of 50 to 60 kilometers. The deepest extent of these earthquakes and their related aftershocks defines the lower limit of shallow seismicity.

Intermediate depth earthquakes are classically defined as earthquakes that occur within the interval between 60 and 300 kilometers depth. They are observed almost exclusively within subduction zones. In fact, subduction related intermediate depth earthquakes are among the first pieces of evidence of the active subduction of cold oceanic lithosphere deep into the Earth's mantle. As a first order observation they globally constitute a dipping band of seismic activity on the landward side of deep-ocean trenches that is common to all subduction zones and that is known as Wadati-Benioff-zone (s.f. Frohlich (2006), Chap. 3.3).

Over time it has been recognized that Wadati-Benioff-zones are not always single bands of seismic activity, but may consist of two (Brudzinski et al., 2007) or possibly three (Igarashi et al., 2001; Bloch et al., 2014) parallel bands of seismicity. It is a current topic of research to find out where these bands are located in relation to the slab itself and what causes them.

The deformation of a medium at seismic slip rates requires brittle failure of the fault-plane. The term brittle here indicates that the accumulated stress is released catastrophically. At shallow depth, the normal stress on the fault-plane is low enough for shear stresses to open microscopic cracks (Griffith cracks) in the direction of the lowest principal stress. When the crack density is large enough, the cracks unite, the rock loses its integrity, and ruptures (e.g. Green and Houston (1995)).

Intermediate depth earthquakes must have a different failure mechanism compared to shallow earthquakes. First, the high confining pressure inhibits the opening of tensile cracks. Some other mechanism must exist that allows for the disintegration of the rock matrix prior to brittle failure. Second, with increasing temperature at depth, the probability that lattice dislocations within the mineral grains of the rock will begin to creep increases. Deformation as relatively slow ductile flow becomes more important at

higher temperatures. The occurrence of intermediate depth seismicity therefore requires the presence of special circumstances that allow for seismic rupture despite confinement and high temperatures (s.f. Frohlich (2006), Chap. 7.1).

### **1.3 Failure mechanisms for intermediate depth earthquakes**

The obvious occurrence of earthquakes at intermediate depth has motivated a broad range of rock deformation experiments, field studies, and numerical simulations of seismic rupture. Three main processes are currently discussed as failure mechanisms for intermediate depth earthquakes: transformational faulting, dehydration embrittlement, and shear-heating thermal runaway. These mechanisms are end-members of certain internal responses of the rock to external forcing.

Transformational faulting and dehydration embrittlement address the phenomenon that rocks fail in a brittle manner when certain minerals begin to break down near the limit of their thermodynamic stability fields.

Transformational faulting ascribes this phenomenon to the emergence of nanocrystalline reaction products along the evolving fault plane that disintegrate the medium locally and so facilitate seismic rupture. The process has been observed in anhydrous (Kirby, 1987) as well as hydrous mineral assemblages (Proctor and Hirth, 2015; Plümper et al., 2017; Incel et al., 2017).

Dehydration embrittlement attributes the failure of the fault plane to an increase in pore pressure and the reduction of effective normal stress during the breakdown of a hydrous mineral phase. This mechanism is based on the observation of microstructures within the deformed rock sample that indicate a near-lithostatic fluid-pressure along the fault plane (Dobson et al., 2002; Jung et al., 2004, 2009).

These two mechanisms are scientifically especially appealing, because the thermodynamic stability fields of a number of mineral phases correlate remarkably well with the distribution of intermediate depth seismicity, when projected from pressure-temperature space to depth in the Earth (Hacker et al., 2003a). Especially the breakdown of hydrous mineral phases has attracted wide spread attention, because their mostly pressure-invariant stability fields can explain first order patterns in intermediate depth seismicity (Yamasaki and Seno, 2003). The occurrence of intermediate depth earthquakes may therefore be linked to the deep water cycle through the nucleation processes that involve the breakdown of a hydrous mineral phase.

The third nucleation mechanism for intermediate depth earthquakes is spontaneous shear-heating thermal runaway. This mechanism occurs as a consequence of the positive feedback between heat dissipation during viscous flow and viscosity reduction upon heating. The ductile deformation of the rock under great stresses may generate enough heat to induce melting along a localized plane, allowing for catastrophic failure of the rock at intermediate depth (Braeck and Podladchikov, 2007; Kelemen and Hirth, 2007; John et al., 2009).

## 1.4 Driving and slowing forces of subduction

A number of forces have been named that contribute to the dynamics of plate tectonics. The two main driving forces are ridge push and slab pull. While being subducted, the slab is further subject to bending and unbending as well as to collisional forces.

Ridge push originates from a topographic slope in sea floor topography. The mid-ocean ridge is elevated by a few kilometers relative to the oceanic trench, thousands of kilometers away. The slope is a result of the thermal densification of the ageing oceanic lithosphere and its subsequent gravitational sagging in the Earth's mantle. Ridge push exerts horizontally compressional stresses on the slab (e.g. Turcotte and Schubert (2014)).

Slab pull similarly describes a gravitational force that the subducted slab experiences. In this case, the slab is even denser than the surrounding mantle. The additional gravitational force component is thought to result in the far-field of the subduction zone from an earlier densification of the cold slab compared to the warmer surrounding mantle (e.g. Spence (1987)). The densification is due to high-pressure olivine polymorphs that emerge earlier at shallower depth above the 410 km discontinuity when the temperature is lower (Green and Houston, 1995). The stress is transferred elastically to shallower portions of the slab. Slab pull is thought to be the main component of the driving force of plate tectonics. It exerts dilatational stresses within the slab.

At the convergent plate boundary, where the oceanic plate subducts beneath the other plate, collisional forces occur at the interface and stress is partially transferred to the overriding plate. This process is evident from accumulating slip deficit along the coupled zone of the plate interface that manifests itself in shortening and uplift of the overriding plate (Chlieh et al., 2011; Métois et al., 2013), the cyclical accumulation and release of elastic deformation in megathrust earthquakes (e.g. Schurr et al. (2014)), and the longterm rise of orogens (Lamb, 2006). Collisional forces impede subduction.

The incoming lithosphere needs to bend prior to subduction when its direction of movement starts to deviate from purely horizontal to an inclined one near the outer-rise. It needs to unbend when the slab realigns with the straight but inclined orientation that is evident in the receiver function images of subducting slabs and from the distribution of local seismicity. Bending of the lithosphere induces dilatational stresses at the top of the slab and compressional stresses at its bottom. Unbending induces compression at the top and dilatation at the bottom (e.g. Faccenda et al. (2012)). The forces involved act in the slab plane and are therefore probably indistinguishable from ridge-push and slab-pull forces.

## 1.5 Processes in the overriding plate

On top of the overriding plate, the single most prominent expression of subduction is certainly the development of a chain of volcanoes that is located at a place where Wadati-Benioff zone seismicity arrives at a depth below  $\sim 100$  km. The volcanic arc is thought to be the surface expression of fluid release from the subducting slab that induces melting and magma ascent. The rise of magma also causes heat to be transferred to shallower crustal levels, leading to a more ductile deformation regime and seismic

events being constrained to the uppermost crustal levels. In contrast to that, the forearc crust is cooled from beneath by the underthrusting subducting slab. This leads to seismicity that reaches to deeper crustal levels than elsewhere. A major change in deformation regime should therefore exist within the continental forearc crust.

At the coupled plate interface, stress is transferred from the subducting to the overriding plate. This leads to compressional forces in the overriding plate and to orogenesis. The stress may partly be accommodated by movement along major crustal fault zones.

## 1.6 The Central Andean Subduction System

In this thesis, I aim to study the subduction and release of seawater and the components of the driving force of subduction by the study of background seismicity in the Central Andean arc and forearc region of Chile between 20° and 22° S. The tectonic situation is summarized in Figure 1.2.

The Nazca plate subducts beneath the South American Plate with a velocity of 67 mm/yr and in a direction of N77° E (e.g. Angermann et al. (1999)). At the surface, both plates are separated by the Peru-Chile-Trench, which is oriented almost perfectly in North–South-direction. At depth, the upper and lower plate are known to be mechanically strongly coupled to a depth of about 20 to 30 km. The degree of coupling varies along-strike, dividing the plate boundary into strongly coupled segments and weakly coupled inter-segments (Métois et al., 2013).

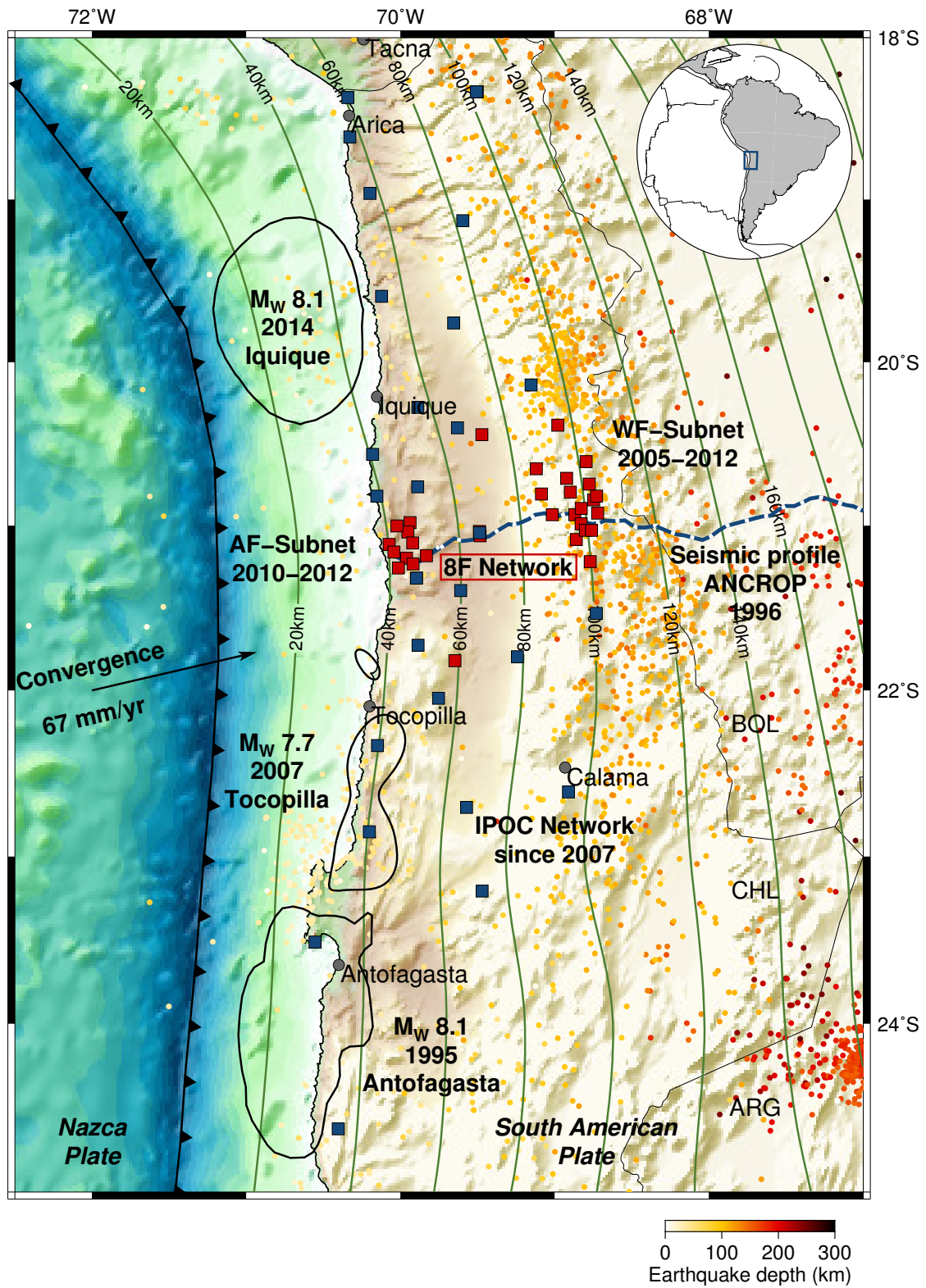
A number of segments of the megathrust have ruptured, at least partly, in recent years, namely in the  $M_W = 8.1$ , 1995 Antofagasta earthquake (Ruegg et al., 1996; Chlieh et al., 2004), the  $M_W = 8.4$ , 2001 Arequipa earthquake (Pritchard et al., 2007), the  $M_W = 7.7$ , 2007 Tocopilla earthquake (Delouis et al., 2009; Schurr et al., 2012), and the  $M_W = 8.1$ , 2014 Iquique earthquake (Schurr et al., 2014; Hayes et al., 2014; Ruiz et al., 2014). The segment between  $\sim 20.5^\circ$  and  $21.5^\circ$  S has not ruptured recently. Seismicity at the fully coupled plate interface is typically low during the interseismic phase of the earthquake cycle and governed by aftershocks in the postseismic phase.

Coupling may continue downdip to a lesser degree until where the slab intersects the mantle wedge. This transitionally coupled zone yields seismicity of low magnitudes (Schurr et al., 2012). Métois et al. (2013) suggest that 15% of the interseismically

---

**Figure 1.2:** (opposite) Overview of the neotectonic framework and used seismic networks in the Central Andean subduction system. Red squares: West–Fissure- and Atacama-Fault Seismic Network (Wigger et al., 2016). Blue squares: IPOC-Network (GFZ and IGP, 2006). Blue-white line: ANCORP profile (Oncken et al., 2003). 1 m slip contours of the Iquique, Tocopilla and Antofagasta megathrust earthquakes after Schurr et al. (2014), Schurr et al. (2012), and Chlieh et al. (2004). Convergence vector after Angermann et al. (1999). Seismicity from the real-time earthquake catalog produced by USGS, National Earthquake Information Center (NEIC, 2017), covering the operation time of the 8F-network. Green contour lines: the envelope of the Wadati-Benioff-Zone (Slab 1.0, Hayes et al. (2012)).

---



accumulated strain that is transferred to the overriding plate may be accommodated by slip on the Andean backarc fold and thrust belt of Bolivia and Argentine. Furthermore, major forearc faults may have been reactivated and accommodate deformation. Intermediate depth seismicity as listed in global catalogs is constrained to a band between 90 and 150 km depth. It is located just in front of and below the magmatic arc.

## 1.7 Data base

I use ground velocity data that was recorded in the years between 2005 and 2012 by the temporary local seismic network *West-Fissure- and Atacama-Fault Seismic Network (2005/2012)* (Wigger et al. (2016), FDSN Network code 8F, Fig. 1.3). The major aim of the network was to monitor the distribution of crustal seismicity related to the Atacama Fault Zone in the Coastal Cordillera and the West Fissure Fault Zone in the Precordillera at  $\sim 21^\circ$  S (AFZ and WFFZ, in Fig. 1.3). The average station distance was  $\sim 20$  km. The network was instrumented with Mark short period seismometers that recorded continuously with a sampling frequency of mostly 200 Hz. Only some intervals were recorded at 100 Hz. Data were digitized on Earth Data PR-24 data loggers and stored on a local hard drive that was exchanged during network maintenance, approximately twice a year. The eastern seismic sub-network at the WFFZ (station codes beginning with WF) was in operation from November 2005 until November 2009 (Salazar, 2011), and was re-installed between March 2010 and March 2012. The western sub-network at the AFZ (station codes beginning with AF) in the east was active only in the second period from 2010 until 2012.

The network was placed on the profile line of the ANCORP'96 seismic experiment (Oncken et al., 2003) and near the first deployments of the *Integrated Plate Boundary Observatory Chile* (IPOC, GFZ and IGP (2006), FDSN network code CX). In this manner, a wealth of complementary geophysical data could be incorporated in the processing and the interpretation of the data.



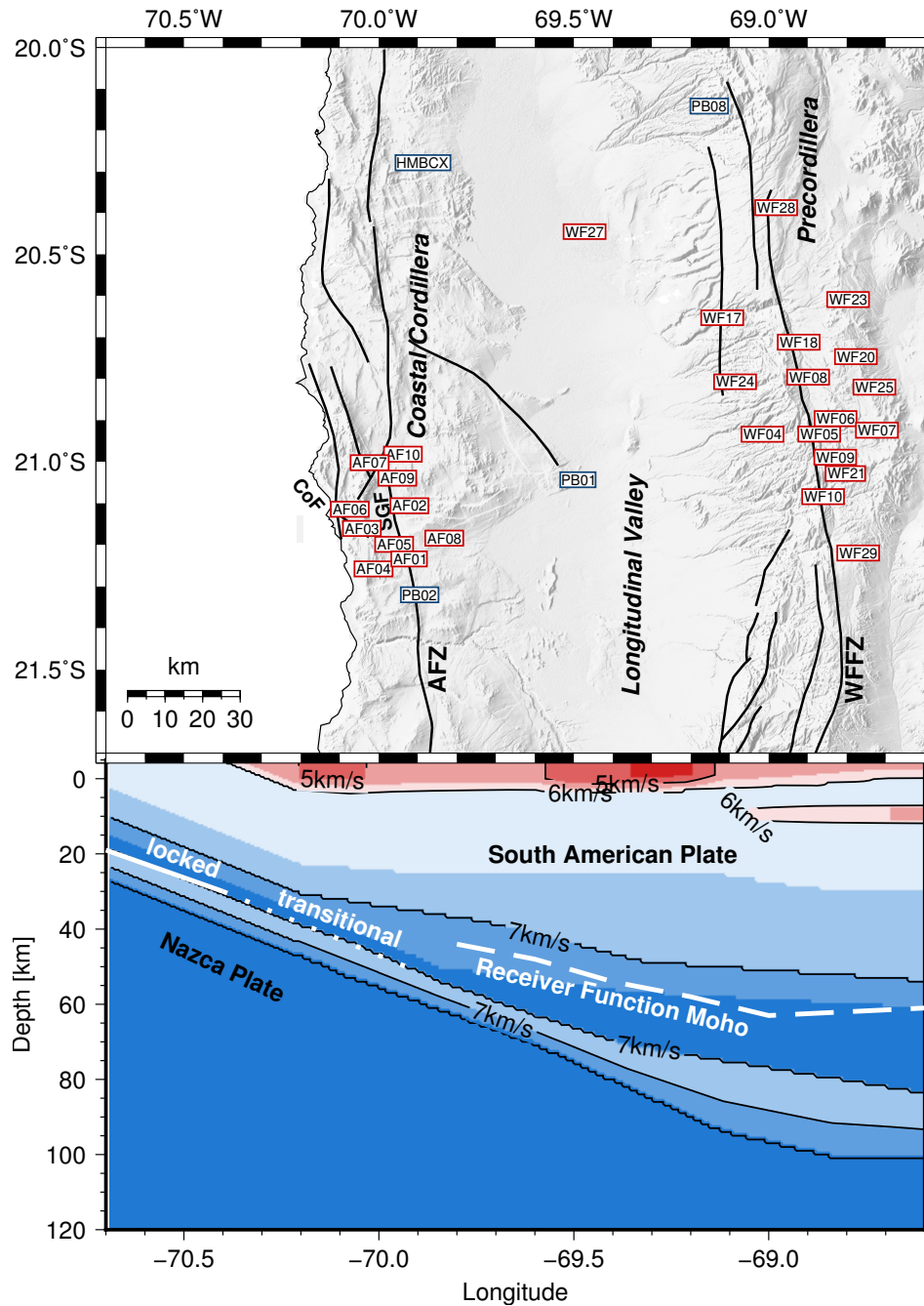


**Figure 1.3:** Experimental setup of this and previous studies. Top: Map view of the study area which is located in the Central Andean forearc. Text boxes indicate locations of seismological stations. Red Boxes are from the short period seismometers from the 8F-network. Blue boxes are broadband seismometers from the CX-network. AFZ: Atacama Fault Zone, WFFZ: West Fissure Fault Zone, SGF: Salar–Grande Fault, CoF: Chomache Fault (Gonzalez et al., 2003; Reutter et al., 1994). Also shown is the location of the seismic profile ANCORP (Oncken et al., 2003). Bottom: Cross-section. Color-coded in 0.5 km/s intervals and contoured: P- velocity model from Lüth (2000). Inter-plate coupling after Klotz et al. (2006). Receiver Function Moho after Yuan et al. (2000).



# Chapter 2

## Local seismicity

The exact location of a seismic event is the very first information that needs to be known in order to describe it. It is necessarily needed to later formulate assumptions regarding processes that lead to its occurrence. The better the location is resolved, the more detailed it can be discussed.

In this chapter I present high-resolution seismic event locations and their relation to an earlier image of seismic reflectivity along the ANCORP profile at 21° S (Oncken et al., 2003). I discuss the distribution with a focus on the internal structure of crustal and slab-related seismicity.

I find abundant seismicity within the continental crust that features a sharp limit in seismicity that likely indicates the transition from brittle failure in the cold forearc crust to ductile flow in the ductile crust towards the volcanic arc. The boundary coincides with a highly reflective volume that has earlier been interpreted as a fluid ascent path and follows the 350° C isotherm.

The slab-related seismicity discloses a sharp downdip end of interface seismicity that probably marks the terminal limit of interplate coupling. I can resolve internal structures of interface seismicity. Slab-related seismicity further exhibits a clear zonation into three bands of a triple seismic zone. The bands correlate well with discontinuities within the slab that have previously been observed as reflectors or converters of elastic waves. This chapter is an extension and update of Bloch et al. (2014).

### 2.1 Previous work

Many seismological studies of the Iquique region at 20°–22° S have a clear focus on the seismic gap that until the 2014 Iquique earthquake extended from Mejillones peninsula to the Arica bend, on the megathrust earthquakes of the recent past, and on their related aftershocks (Sec. 1.6).

Fewer studies focus on background seismicity within the subducting system (Comte and Suarez, 1994; Gräber and Asch, 1999; Comte et al., 1999; Rietbrock and Waldhauser, 2004; Comte et al., 2016). They qualitatively reproduce the long-term pattern of intermediate depth seismicity that can be seen in Figure 1.2. In detail, they find a ~20° to 25° eastward dipping band of seismicity, sparse shallow seismicity within the

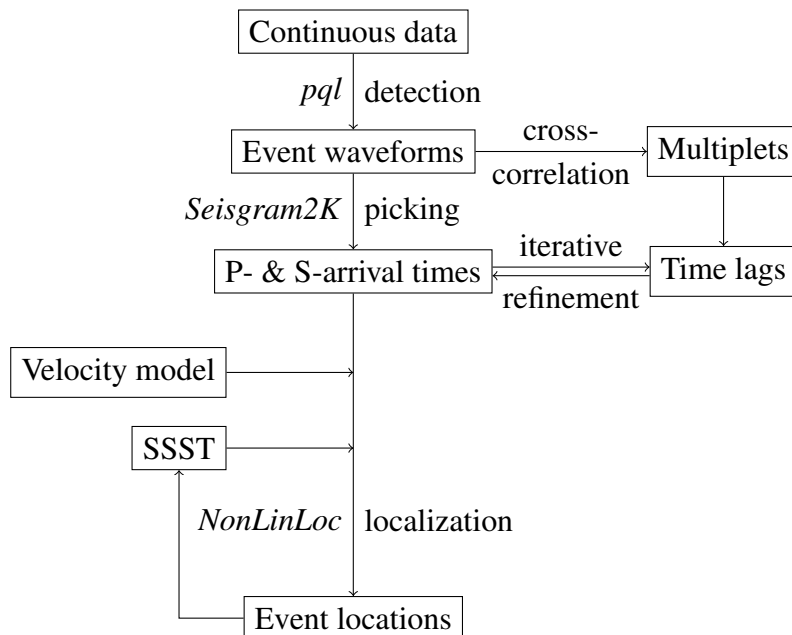


**Figure 2.1:** Flowchart that illustrates the procedure of seismic event localization.

subducting slab, and a relatively dense nest of intermediate depth seismicity between  $\sim 100$  and 150 km depth that more or less clearly has the form of a double seismic zone. Furthermore, Gräber and Asch (1999), Comte et al. (1999), and Comte et al. (2016) see seismicity within the overriding continental crust, but are not able to resolve internal structures.

## 2.2 The dataset

From the continuous ground velocity seismograms (Sec. 1.7), members of Freie Universität Berlin visually detected 7165 seismic events and manually picked P- and S-wave arrival times for 5456 events. To correct for picking uncertainties, groups of events that have a similar waveform by means of their mutual cross-correlation coefficient (multiplets) were defined. Inside each multiplet, the relative positioning of arrival time picks on similar waveforms were compared to each other using their cross-correlation function. The time lag of the maximum of the cross-correlation function was used in combination with the original picks to invert for a set of refined arrival time picks (Shearer, 1997; Kummerow et al., 2010). Seismic events that do not belong to any multiplet did not receive an arrival time update.

## 2.3 Localization procedure

The steps of the entire localization procedure are shown as a flowchart in Figure 2.1. I located the seismic events using the regional 2D velocity model that was obtained from the active source wide-angle seismic profile along the ANCORP line at  $21^\circ$  S (Lüth,

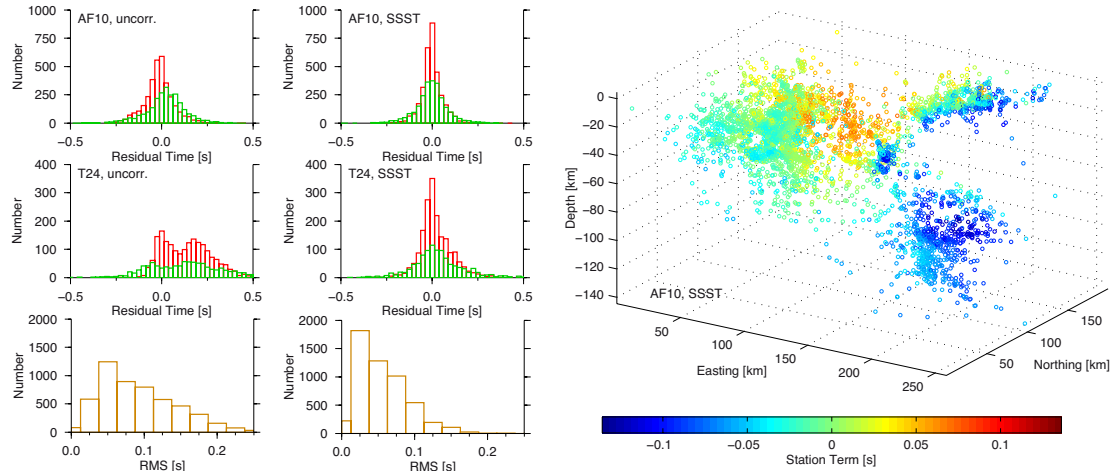


**Figure 2.2:** Left: Histogram of arrival time residuals (top and middle) of P- and S-phases (red and green) and RMS error (bottom) before (far left) and after (middle) the application of source specific station terms (SSST). Right: 3D view of the distribution of SSST for P-wave arrivals for station AF10.

2000), which I extrapolated to the north and to the south (Fig. 1.3). To obtain the S-wave velocity model, I assumed a constant ratio of  $V_P/V_S = 1.72$ .

For event localization, I used the probabilistic earthquake localization algorithm *Non-LinLoc* (Lomax et al., 2000). After a first event localization, arrival time residuals exhibited a systematic trend as a function of their respective source location. I attributed these long-wavelength variation in arrival time residuals to unmodeled variations in the subsurface velocity field. To correct for them I applied source-specific station terms (SSST, Richards-Dinger and Shearer (2000)): I performed a Delaunay triangulation on the seismic event cloud. I used the resulting graph as a distance measure to determine the natural neighbors of each event. For each event, I computed a correction term for each station as the mean of the arrival time residuals of the 300 neighboring events. I subtracted this term as a static time shift ('station term') from the arrival time. I applied station terms to all arrival time picks and iteratively re-localized the events. In each iteration I removed localizations that fell on the edge of the velocity model. Within four iterations, subsequent station terms differed by less than 1 ms. An example of the final distribution of SSST is shown in Figure 2.2. This procedure further mitigated the biasing effect of unmodeled 3D velocity heterogeneities.

I ruled out biasing effects of the inhomogeneous station distribution on the event locations by verifying that the sharply defined clusters below the eastern subnet (C1–C3 in Fig. 2.3) were localized to the same position and conserved their internal structure when using either only the eastern subnet or both subnets for localization. In total 5250 events could be successfully located.

Location uncertainties within the dataset vary depending on the number of picked P- and S- arrival times, waveform similarity, and correctness of the velocity model along the ray path. Uncertainties range from  $\sim 100$  m for strong, clustered events to few kilometers for weak, single events. The typical root-mean-square (RMS) localization misfit is 30 ms,

corresponding to location uncertainties of  $\sim 200$  m. Only events with an  $\text{RMS} < 200$  ms are shown in Figures 2.3 and 2.4.

## 2.4 Results

The resulting hypocenters are shown in Figure 2.3. Note that due to the inhomogeneous station distribution and the different operation periods of the two seismic subnets, the spatial variations of seismic energy release needs to be interpreted with caution. In particular, the seismicity rate below the western AF-subnetwork ( $\sim 4$  events per day) is significantly higher than below the eastern WF-subnetwork ( $\sim 1$  event per day). The apparent reduction in seismicity at about  $69.7^\circ \text{W}$ – $69.3^\circ \text{W}$  longitude, i.e. between the two networks, may be partly attributed to the sparse instrumental coverage (Fig. 2.3).

I observed local seismicity in the continental crust of the overriding South American Plate (Fig. 2.3, green) and in the subducting Nazca Plate (blue). The slab related seismicity occurs at shallow and intermediate depth. In contrast to the classical definition that defines the lower limit of shallow seismicity at 60 or 70 km depth (Frohlich, 2006), here, a phenomenological change seems to occur at a depth of only  $\sim 50$  km: At the plate interface, seismicity terminates abruptly ('4' in Fig. 2.3) and within the oceanic mantle a lower band of seismicity begins ('5'). In this sense, I discriminate seismicity at shallower intermediate depth (between 50 and 80 km) and at deeper intermediate depth (below 80 km, the intermediate depth seismicity that has been analyzed previously).

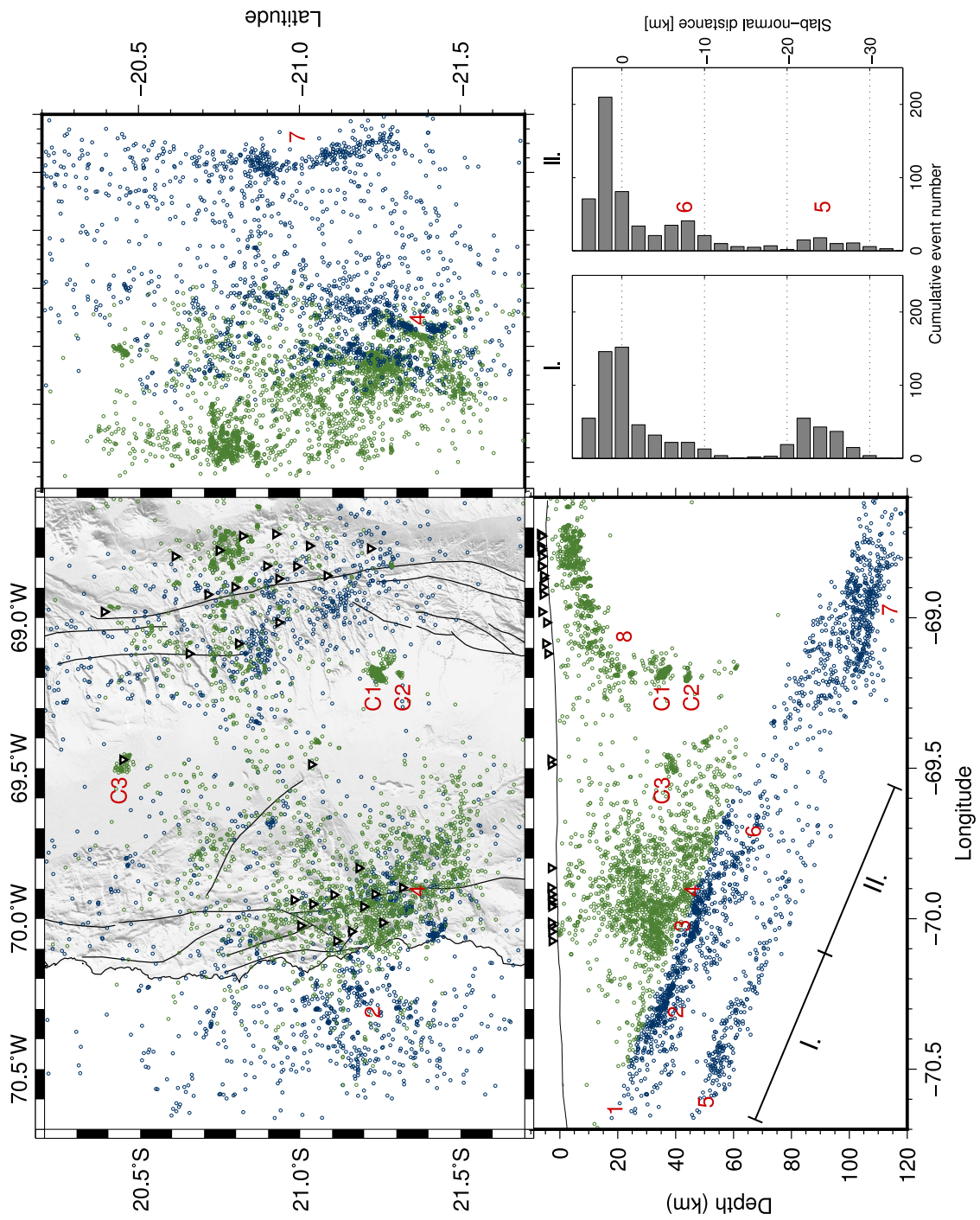
### 2.4.1 Seismicity in the continental crust

I find that crustal seismic activity is pervasive in the cold continental forearc crust below the Coastal Cordillera around the western AF-subnet and extends to depths of  $> 30$  km. Several  $M_l > 0.5$  events per day were recorded, generally of low magnitudes ( $M_l < 3.5$ ). Planar, steeply dipping features in the seismicity distribution strike SW to SSW and correlate with topography, as well as with mapped fault zones, namely the Salar–Grande Fault and the Chomache Fault (Reutter et al. (1994); Gonzalez et al. (2003), s. Fig. 2.3a). Seismic activity here likely indicates stick-slip faulting on these major crustal faults.

---

**Figure 2.3:** (opposite) Seismicity in the study area in the years between 2005 and 2012. Green: Seismicity in the continental crust; blue: slab-related seismicity. (a) Map view; (b) N-S-section; (c) E-W-section; the shaded area indicates sparse instrumental coverage; (d) slab-normal earthquake distribution for the two sections (I. and II.) indicated in the left E-W-section (zero depth at the plate interface). C1–C3: crustal clusters discussed in the text. (1) locked zone, (2) transitional zone exhibiting streak-like structures, (3) region of reduced seismicity above the slab interface, (4) seismicity cluster at and above the slab interface, (5) second band of seismicity, (6) possible third band of seismicity near the oceanic Moho, (7) deep double seismic zone with kink-like structure, (8) boundary between seismic and aseismic continental crust.

---



In the Precordilleran crust, seismicity is less frequent (about one recorded event per day) and is constrained to the uppermost 20 km of the continental crust, where it constitutes a set of steeply westward dipping structures. The most prominent feature is the west-dipping lower bound of seismicity, which represents a sharp transition to an aseismic zone at depth (labeled '8' in Fig. 2.3). This transition correlates approximately with the 400° C isotherm calculated by Springer (1999). The relation between seismicity and the West–Fissure–Fault–Zone is discussed in greater detail by Salazar et al. (2016).

In the lower continental crust, three distinct seismicity clusters occur at depths of 35–45 km (C1–C3 in Fig. 2.3). All clusters were persistently active throughout the recording period in the years of 2005–2012 and consist of 50–200 events per cluster. To the West, an abrupt decrease in seismic activity coincides with the coastline.

## 2.4.2 Seismicity of the subducting slab

A triple seismic zone in the down-going Nazca slab can be clearly identified. One band of seismicity is located at and below the plate interface, a second one 20–25 km deeper in the lithospheric oceanic mantle and a third one near the oceanic Moho (Yuan et al., 2000). The lower band of seismicity can be traced up-dip to uncommonly shallow levels of 50 km. This is significantly shallower than the usually observed intermediate hypocenter depths, which is greater than 70 km in other subduction zones (Brudzinski et al., 2007). The slab normal zonation of seismicity is most obvious at these shallow intermediate depths, west of  $\sim 69.6^\circ$  W. Here, the upper and the lower band are sub-parallel and have a constant dip of  $\sim 22^\circ$ . At deeper intermediate depths greater than 80 km, east of  $69.6^\circ$  W, two slab-parallel planes of seismicity may be distinguished as well ('7' in Fig. 2.3). They form a narrow double seismic zone that produces the highest seismicity rate in the subducting slab and that has been studied using earlier seismic networks (see Sec. 2.1). This zone defines in north–south direction a kink-like structure at  $21.0^\circ$  S that has earlier been interpreted as a tear in the slab (Rietbrock and Haberland, 2001).

Along the plate interface, seismicity is not continuous. It is essentially restricted to the partially locked zone between 30 and 50 km depth (Chlieh et al., 2004; Klotz et al., 2006; Schurr et al., 2012; Métois et al., 2013). Within this zone, seismicity is further concentrated in two patches at around 37 and 47 km depth at the western end. Both structures are streak-like and sub-parallel to the convergence vector (labeled '2' in Fig. 2.3a), presumably indicating a connection to the slab-surface topography. The deeper patch marks the region where seismicity of the plate interface decreases abruptly ('4' in Fig. 2.3). It is only here that seismicity ascends into a several kilometers thick region directly above the plate interface. The region above the plate interface is characterized by reduced seismicity updip of this point ('3' in Fig. 2.3). Seismicity is comparatively low in the fully coupled zone between the two plates above  $\sim 20$  km depth, where no relative movement of the two plates occurs.

The lower band of seismicity is separated 20–25 km from the upper two bands and has a width of about 10 km. It can be observed updip to depths as shallow as 50 km at  $70.6^\circ$  W longitude. The concentration of seismic events is highest in the shallowest part of the lower band between 50 and 60 km depth and decreases downdip.



The third band of seismicity can be identified at a slab-normal distance of about 8 km below the plate interface ('6' in Fig. 2.3), near the oceanic Moho. It is best pronounced right below the western subnet near 69.9°W.

Altogether, these three bands make up a shallow triple seismic zone. The lower band and the Moho-band continue arc-ward beyond the downdip end of interface seismicity to deeper intermediate depth where they constitute the double seismic zone at intermediate depth that has been observed previously (Comte and Suarez, 1994; Rietbrock and Waldhauser, 2004). On the contrary to Rietbrock and Waldhauser (2004) I observe both bands, also the upper, below the oceanic Moho within the oceanic mantle.

## 2.5 Comparison with seismic reflectivity

The projection of my earthquake locations on the W-E trending ANCORP section discloses several features which exhibit a clear positive correlation between seismicity and seismic reflectivity (Fig. 2.4, Yoon et al. (2008)).

### 2.5.1 Plate Interface

The seismically active zone of the slab interface coincides with a strong band of seismic reflectivity between 30 and 50 km depth. This suggests the presence of free fluids, which are expected to trigger seismic activity as well as to increase reflectivity, especially at the lower end of the coupled zone ('4' in Fig. 2.3). The seismicity cluster here is possibly related to an expulsion of fluids that escape through pre-existing fractures into the overriding plate.

Both, reflectivity and seismicity decrease abruptly downdip at ~50 km depth (69.9° W), defining the downdip end of inter-plate coupling, where the transition from frictional slip to ductile flow occurs (e.g. Lamb (2006)). This zone appears as a broader, less sharply defined reflector, comparable to the 'E-layer' found in Northern Cascadia (Nedimovic et al., 2003) that has an aseismic nature. Nedimovic et al. (2003) also describe a similarly strong and thin reflector for the coupled and partially coupled zone in northern Cascadia, but their seismicity data do not cover the area.

### 2.5.2 Subducting Slab

Beneath the plate interface, moderate reflectivity indicates the thickness of the ~8 km thick oceanic crust. Reflectivity continues on a reduced level below the oceanic Moho, whose location is constrained by receiver functions (Yuan et al. (2000), indicated by the lower dotted line in Fig. 2.4), down to the lower band of seismicity. It is interesting to note that reflectivity decreases down to noise level at about the depth of the lower band of seismicity below the Coastal Cordillera around 70.0° W. Reflective structures are oriented sub-parallel to the slab surface (Fig. 2.4).

Seismicity of this band may be related to the incipient unbending of the subducting slab in combination with mineral dehydration reactions that are driven by changing pressure-temperature conditions during the subduction process, such as the breakdown of antig-

orite (e.g. Wang (2002); Yamasaki and Seno (2003)), possibly at low temperatures in the presence of brucite. A more detailed discussion of acting forces and earthquake nucleation processes in the lower band of seismicity is given in Section 3.4 and Section 5.5.

If the lower band of seismicity represents a fluid source, these fluids are expected to migrate upward, which could explain the enhanced level of seismic reflectivity in the uppermost mantle of the Nazca slab. The observed pervasive reflectivity pattern above the lower band of seismicity would, for the case of the Northern Chilean subduction zone, be an argument against the recent proposal from geodynamic modeling that the lower plane of seismicity itself represents a layer of percolating fluids (Faccenda et al., 2012).

At depths greater than 80 km, the seismicity distribution nicely reproduces the double seismic zone found by Comte and Suarez (1994) and Rietbrock and Waldhauser (2004), who were analyzing data from earlier sub-regional seismic networks. The thickness of the double seismic zone is here about 15–20 km, which is less than the 25 km thick zone up-dip. The comparison with the depth location of the receiver function Moho indicates that most of these earthquakes also occur in the oceanic mantle and few of them in the oceanic crust. Following the mineral dehydration hypothesis for intermediate depth seismicity, these earthquakes are probably related to metamorphic mineral reactions such as the transition from basalt/gabbro to eclogite in the oceanic crust or the dehydration of antigorite or chlorite in the slab mantle (Hacker et al., 2003a).

The highly reflective zone above the slab has been interpreted by Oncken et al. (2003) and Yoon et al. (2008) as the hydrated mantle wedge. My study additionally shows that this zone is aseismic.

### 2.5.3 Continental Crust

The west-dipping lower bound of crustal seismicity in the Precordillera and the lower crustal event clusters (C1, C2 in Fig. 2.3) follow the western, at depth nearly vertical contour line of high crustal reflectivity at  $\sim 69.2^\circ$  W longitude. This contour line corresponds to the location of the rheological boundary within the crust, namely between the cold and rigid forearc crust to the west and the warmer, probably partially molten and essentially ductile Altiplano crust to the east. This rheological boundary was invoked by earlier studies to explain the lateral contrast in seismic velocities (Koulakov et al., 2006), seismic attenuation (Schurr et al., 2003), and temperature gradients (Springer, 1999).

The lower crustal seismic clusters apparently align in the westward continuation of highly reflective layers and also show a comparable eastward dip (Fig. 2.4). Following Yoon et al. (2008), who argue that the reflectivity indicates a network of ascending fluid paths, the earthquake cluster locations may be explained by migrating fluids which meet a strong lateral stress contrast at the sharp rheological boundary (Ito, 1999).

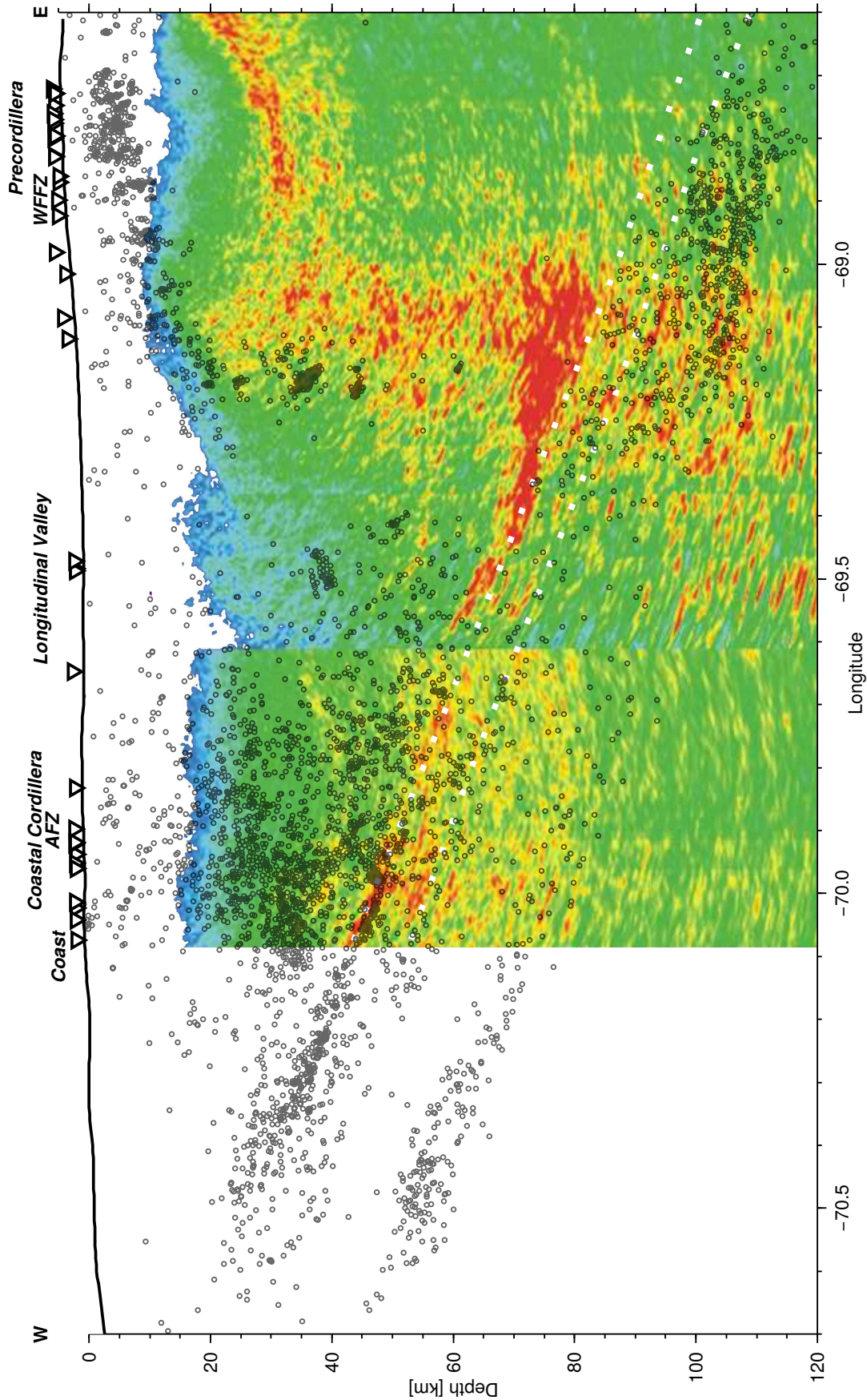


**Figure 2.4:** Superposition of seismicity from this study with the onshore reflectivity image of the ANCORP profile at 21° S (Yoon et al., 2008). Dashed lines indicate top and bottom of the oceanic crust.

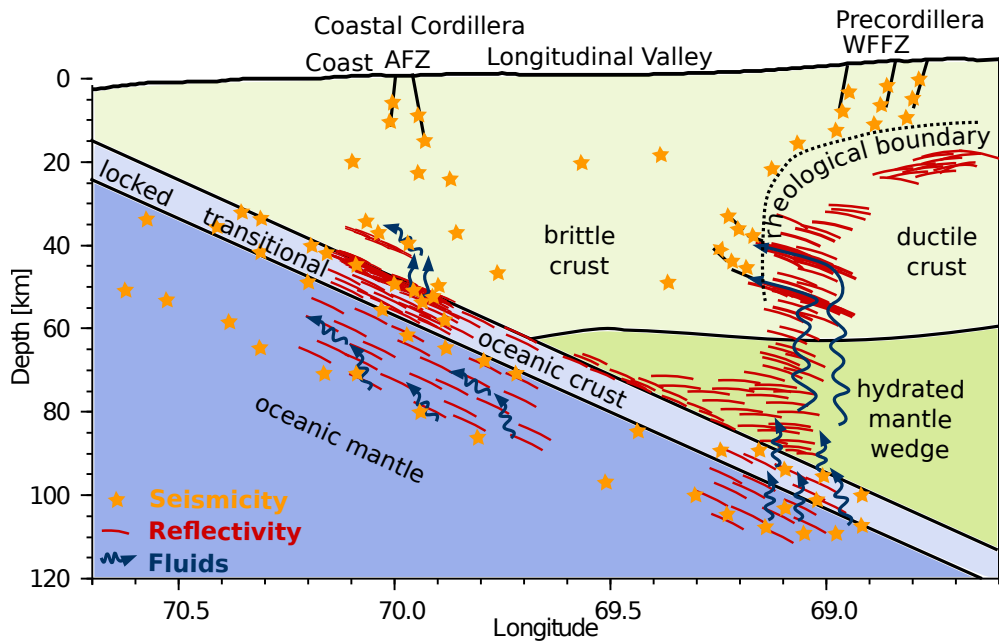


**Figure 2.5:** Summarizing interpretation of possible fluid pathways and rheology of the continental crust in the forearc of the Central Andean subduction zone, inferred from observed seismicity distribution and seismic reflectivity patterns. Support of the interpretations by earlier studies is discussed in the text.

## 2.6 Conclusion

The main observations discussed in this chapter based on both, earthquake hypocenters and seismic reflectivity are summarized as a conceptual model in Figure 2.5.

Crustal seismicity is pervasive below the Coastal Cordillera. Beneath the Precordillera, the lower bound of crustal seismicity delineates a sharp west-dipping boundary down to 20 km depth, consistent with earlier findings indicating a rheological boundary. In the subducting slab, seismicity is organized in three parallel bands. The upper band is located at the plate interface and ends at the downdip end of seismic coupling, where in terms of seismic reflectivity the 'E'-layer begins. The lower band begins at 50 km depth, ~15 km below the oceanic Moho and intensifies in terms of seismicity rate at 110 km depth, ~10 km below the oceanic Moho. A third band, or Moho-band, exists near the oceanic Moho, but has a low seismicity rate.

The combined interpretation of seismicity and reflectivity along the seismic ANCORP'96 experiment suggests the prevalence of fluid processes in the subducted oceanic crust as well as in the uppermost 20 kilometers of the mantle.

## 2.7 Outlook

I found seismological indications for fluid processes within the subducting slab. The presence of free fluids within the subduction system has also been proposed in other disciplines (Sec. 1.3).

In the following I attempt to test the mineral dehydration hypothesis for intermediate depth seismicity by establishing more properties of the seismic events and of the medium in which they occur. In the next chapter I will derive focal mechanisms. They allow me to identify large scale patterns of the stress-field and to assess the direction of fault zones. I will then construct a petrophysical model to formulate expectations on the elastic parameters of anhydrous, hydrated, and fluid-filled rocks under subduction conditions. Finally, I will estimate the  $V_P/V_S$ -ratio in the subduction system.



# Chapter 3

## Focal mechanisms

In order to understand the stress-field and the nature of faulting within the subducting slab, I computed focal mechanisms for intra-slab seismic events.

A seismic event is a deformation of the subsurface fast enough to radiate elastic waves. The deformation pattern contains information on the subsurface stress-field and the orientation of possible fault planes. The stress-field in the subducting slab is an indicator for the nature of the forces that act during subduction within different portions of the slab. Fluids have an influence on the stress-field in the sense that they exert pressure on the surrounding. The fluid pressure reduces the effective stress on a fault plane and can trigger seismic rupture.

I sample the slab homogeneously from top to bottom. The results show a clear overall pattern of compression at shallow depths within the coupling zone and tension at intermediate depth. Within this large trend, small scale variations can be recognized. Focal mechanisms become more homogeneous along the subduction pathway. T-axes that dip shallower than the slab are common at shallow intermediate depth and progressively vanish downwards. Within distinct regions, the rather regular overall pattern breaks down and focal mechanisms become oriented more randomly, indicating a disturbance of the large-scale external stress-field, possibly due to internal fluid pressure variations.

### 3.1 Previous work

Focal mechanisms are typically represented either as beach balls, which show the possible orientation of the fault plane and the slip direction, or as distribution of P- and T-axes, which indicate approximately the direction of principal compression and tension.

From a global perspective, the Harvard CMT catalog (Dziewonski et al., 1981; Ekström et al., 2012) reports normal faulting events for intermediate depth seismicity in the Central Andean forearc and arc region. The T-axes point downdip and the P-axes are oriented in a slab-normal direction. Conclusively it is stated that the slab is under tension at intermediate depth in the Central Andes (Frohlich, 2006).

The nodal planes of selected Harvard CMT focal mechanisms of intermediate depth earthquakes coincide in strike with the surface traces of outer-rise bend-faults, just updip

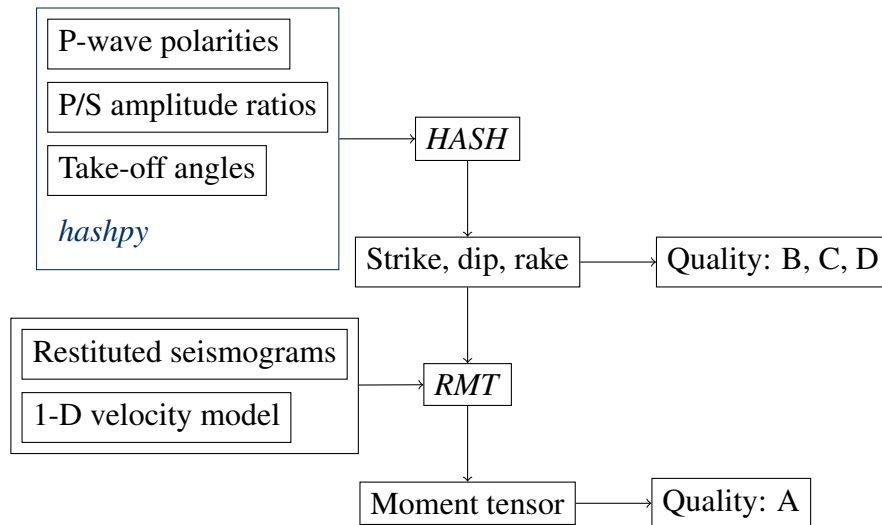


**Figure 3.1:** Flowchart that illustrates how source parameters were computed.

the subduction trajectory. Their dip approximately  $45^\circ$  to the plate interface suggests that these earthquakes represent slip along reactivated bend-faults (Ranero et al., 2005).

Data from local networks describe the narrow double seismic zone below  $\sim 90$  km in more detail. Rietbrock and Waldhauser (2004) report varying but predominantly tensional events. They see a subtle difference in the orientation of P- and T-axes. In the upper band the T-axes dip slightly shallower, are more distributed in the slab plane, and the P-axes are all slab-normal. In the lower band, the T-axes are a little steeper, plunge in convergence direction, and the P-axes are more planarly distributed. Comte and Suarez (1994) report a double seismic zone for two deployments around  $\sim 23^\circ\text{S}$  and  $\sim 21^\circ\text{S}$ . Contradictory to Rietbrock and Waldhauser (2004), they state that the upper band displays tensional and the lower band compressional focal mechanisms. A little further north, near the Arica bend, Comte et al. (1999) report a large variability in focal mechanisms, but do not attempt a more detailed characterization.

## 3.2 Methodology

I performed a two-step inversion to obtain focal mechanisms of small earthquakes. In the first step, I observed the P-wave first motion polarities and the P- to S-amplitude ratios of an earthquake and inverted for the parameters of a double couple (DC) source. In the second step, I selected a few strong and representative earthquakes for certain source regions. I used the source parameters of the first step as a starting model and performed a full waveform inversion for the complete moment tensor (Fig. 3.1). Even though I do not expect a large non-DC component, using the entire seismogram imposed much stronger constraints also on the DC-component.



### 3.2.1 Using first motion polarity and P- to S-amplitude ratio

For determination of the strike, dip, and rake of a double couple source, I used the *HASH*-algorithm (Hardebeck and Shearer, 2003, 2002). The algorithm finds the parameters that best explain the observed first motion polarities ( $\text{sign } u_P^z$ ) and the P- to S-amplitude ratios ( $|u_P|/|u_S|$ ) on the focal sphere which are sampled by the seismic stations.

To gather the observations needed to run *HASH*, I developed a helper script *hashpy* that essentially gathers and displays seismograms. For a specific earthquake, the script looks up the take-off angles to the available seismic stations in the angle-grids produced by the *NonLinLoc*-subroutine *Grid2Time*. It then presents first the unfiltered and later the 1 Hz high-pass filtered displacement trace of the vertical component and asks the user to determine the polarity. It then presents the normalized absolute amplitude trace (the Cartesian sum of the three components) and asks the user to enter the maximal amplitude of the P- and S-wave trains. It provides this information to *HASH*. In principle, a priori information about the overall data quality can be provided to *HASH*, but this functionality has not been included into *hashpy*.

*HASH* computes expectation values for  $\text{sign } u_P^z$  and  $|u_P|/|u_S|$  for arbitrary rotation angles of a double couple source and returns the one rotation in terms of strike, dip, and rake which has, in my case, the lowest composite misfit. It perturbs the take-off angles with a standard deviation of  $5^\circ$  and returns sets of resulting perturbed source parameters. They allow for a qualitative estimate of the robustness of the solution. I visually inspect and group them into three quality categories: B, C, and D (see Sec. 3.2.3).

### 3.2.2 Using the full waveform

For computing the moment tensor  $M_{ij}$ :

$$M_{ij} = \begin{bmatrix} m_{xx} & m_{xy} & m_{xz} \\ m_{xy} & m_{yy} & m_{yz} \\ m_{xz} & m_{yz} & m_{zz} \end{bmatrix}, \quad (3.1)$$

I used the algorithm *RMT* (Nábělek and Xia, 1995). The source parameterization and inversion procedure is laid out in great detail in Chapter 2 and Appendix A of Nábělek (1984). Here I summarize the formulation of the misfit function, the linearization strategy of the forward problem and the main physical simplifications.

#### 3.2.2.1 Theory

*RMT* minimizes the difference between the samples  $k$  of all components of the observed seismograms ( $s_d^k$ ) and the modeled ones ( $s_m^k$ ), which are computed in dependence of  $M_{ij}$ :

$$\chi^2 = \sum_{k=1}^K (s_d^k - s_m^k(M_{ij}))^2. \quad (3.2)$$

I had no *a priori* information on the data covariance and did not invert for the source time function so that a corresponding terms have vanished here compared to Eq. (2.3.1) in Nábělek (1984). I removed the instrument response from the observed seismograms  $s_d$  during the preprocessing so that they represent true ground displacement. I rotated the horizontal components relative to the seismic source to a radial and a transverse component and left the vertical component unchanged.

The ground displacement  $u_\gamma$  in direction  $\gamma$  (vertical, radial, or transverse) at a station site  $x$  at time  $t$  in response to the release of the seismic moment  $M_{ij}$  with the time dependence  $S(t)$  can generally be computed with the help of the appropriate elastodynamic Green's function  $g_{\gamma i}$ :

$$u_\gamma(x, t) = [g_{\gamma i, j}(x, t) * S(t)] M_{ij}, \quad (3.3)$$

where the comma denotes spacial differentiation. The linearization strategy to compute the far-field displacement from the moment tensor is based on the prerequisite that the medium is axial symmetric. In the  $(r, z)$ -components of the cylindrical coordinate system, medium response functions  $H$  can be formulated, that are independent of the station azimuth (Nábělek, 1984):

$$H_\gamma^0 = g_{\gamma z, z}, \quad (3.4)$$

$$H_\gamma^1 = g_{\gamma r, z} + g_{\gamma z, r}, \quad (3.5)$$

$$H_\gamma^2 = g_{\gamma r, r}. \quad (3.6)$$

The response functions for the P–SV- and the SH-system are independent of each other. The transverse component of the moment tensor can be factored out from Equation 3.3. The components of the modeled seismograms at a station site is characterized only by the azimuth ( $\Phi$ ) and the epicentral distance ( $r$ ) can then be computed in a linearized manner. They are the sum of the medium response functions  $H(r, z, t)$  for a source at the known depth ( $z$ ), each multiplied with the corresponding radiation weighting term  $w(\Phi, M)$ , convolved with the far field source time function  $\Omega(t) = \dot{S}(t)$ . For the P–SV-system, the equation reads (Nábělek, 1984):

$$\begin{aligned} u_\gamma^{PSV} = & (H_\gamma^{PSV2}(r, z, t)w^{PSV2}(\Phi, M) + \\ & H_\gamma^{PSV1}(r, z, t)w^{PSV1}(\Phi, M) + \\ & H_\gamma^{PSV0}(r, z, t)w^{PSV0}(\Phi, M)) * \Omega(t), \end{aligned} \quad (3.7)$$

and for the SH-system:

$$\begin{aligned} u_\gamma^{SH} = & (H_\gamma^{SH2}(r, z, t)w^{SH2}(\Phi, M) + \\ & H_\gamma^{SH1}(r, z, t)w^{SH1}(\Phi, M)) * \Omega(t), \end{aligned} \quad (3.8)$$

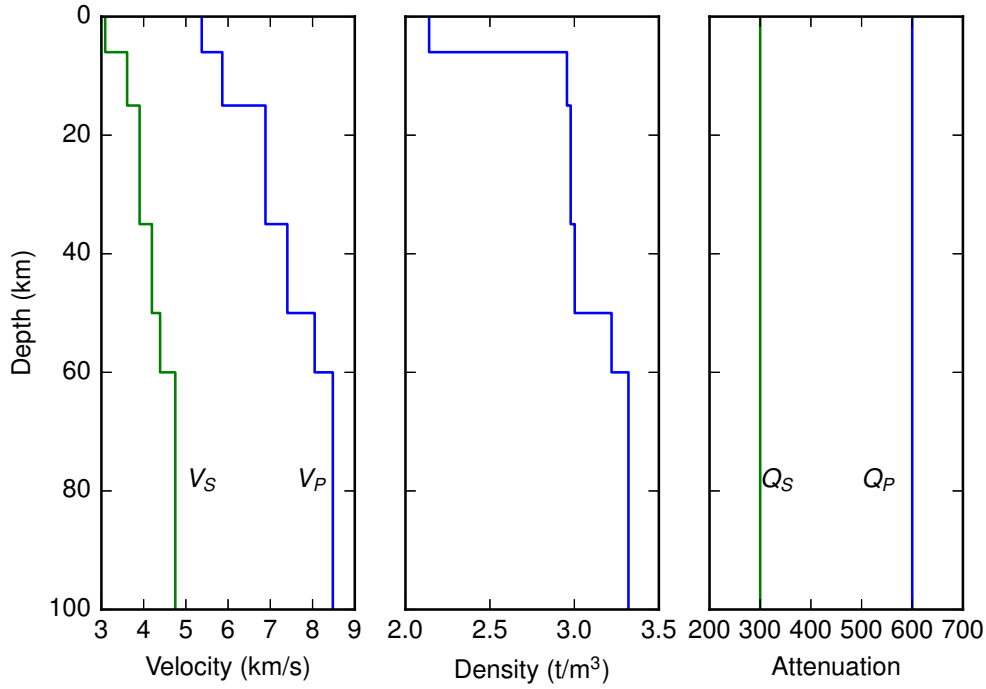


**Figure 3.2:** Seismic velocities, density, and attenuations of the Husen et al. (1999) minimum 1-D velocity model for the Central Andean forearc crust.

where the respective radiation weighting terms of the moment tensor are:

$$w^{PSV2}(\Phi, M) = (1/2(m_{yy} + m_{xx}) - 1/2(m_{yy} - m_{xx}) \cos 2\Phi + m_{xy} \sin 2\Phi) \quad (3.9)$$

$$w^{PSV1}(\Phi, M) = (m_{yz} \sin \Phi + m_{xz} \cos \Phi) \quad (3.10)$$

$$w^{PSV0}(\Phi, M) = m_{zz} \quad (3.11)$$

$$w^{SH2}(\Phi, M) = (1/2(m_{yy} + m_{xx}) \sin 2\Phi + m_{xy} \cos 2\Phi) \quad (3.12)$$

$$w^{SH1}(\Phi, M) = (m_{yz} \cos \Phi + m_{xz} \sin \Phi). \quad (3.13)$$

The Green's functions  $g_{\gamma i}$  are computed by the method of discrete wavenumber summation of Bouchon (1981).

In this representation, the moment tensor is approximated only as the moment tensor of degree zero, which implies that the seismic moment is radiated from a single point in space at a single point in time (point source approximation).

### 3.2.2.2 Application

To compute the Green's functions, I provided the minimum 1-D velocity model of Husen et al. (1999) to *RMT*. The model was derived from the aftershock sequence of the 1995,  $M_w=8.0$  Antofagasta Earthquake, approximately 250 km south of the study area with a comparable morphotectonic subsurface structure (Fig. 3.2). The model coincides best with the Lüth (2000) 2-D model at  $\sim 70^\circ$  W. From this model, I computed Green's functions for periods between 1/8 s and 20 s.

For the interactive waveform fitting process that includes alignment of seismograms and removal of overly complex observed waveforms, I applied a range of narrow band filters. For magnitudes above  $\sim 4.0$  the influence of microseisms on the seismogram was small and I could use periods as long as 20 s. For weaker events, periods above 5 s were typically affected by microseisms, below a magnitude of 3.5 the largest usable period was  $\sim 4$  s. In order to have a sufficiently broad frequency band for inversion, events with lower magnitudes therefore required the usage of shorter periods. However, periods shorter than 0.5 s are essentially unresolved by the velocity model and even at 1 s I noticed that some modeled waveforms started to produce unreasonable results. Using the short periods still tended to constrain the moment tensor towards a higher DC-component, so that I typically tried to incorporate the 0.5 to 1 s band for the inversion. For the fixed far-field source time function  $\Omega$  I always used a triangle function with half duration of 0.2 s. I constrained the moment tensor not to contain a volumetric component (to be purely deviatoric), because the volume changes of the possibly involved mineral phase changes are small (Secs. 4.1.4 and 4.1.5). The moment tensor was allowed to contain a compensated linear vector (CLVD) component. It is noteworthy that the relative CLVD-component of the moment tensor increases, the further the hypocenter is located away from  $\sim 50$  km depth and  $70^\circ$  W, the region for which the 1D velocity model (Husen et al., 1999) has been optimized. In a suite of synthetic tests, Schurr and Nábělek (1999) show that this behavior may stem from unmodeled subsurface structures or a mislocation of the earthquake source. I therefore only interpret the DC- but not the CLVD-component of the moment tensors.

### 3.2.3 Quality measure

I inspected the resulting fault plane solutions for robustness, uniqueness, and coherence with the data. Based on these criteria, I assigned four different qualities:

- A: *RMT* moment tensor which is consistent with the starting model.
- B: *HASH* focal mechanism with a well covered focal sphere and internally consistent polarities and P/S amplitude ratios.
- C: *HASH* focal mechanism where the type of faulting (normal, reverse, strike-slip) is constrained, but where either the focal sphere is only poorly covered or the observations are inconsistent.
- D: The focal mechanism cannot be resolved or is ambiguous. The result will not be considered further.

An example of each quality is shown in Figure 3.3. In total I could determine 187 focal mechanisms, 10 with quality A, 72 with quality B, 76 with quality C, and 29 with quality D. All inversion results are shown in Table A.1. The results of the full waveform inversions are presented in Appendix B.

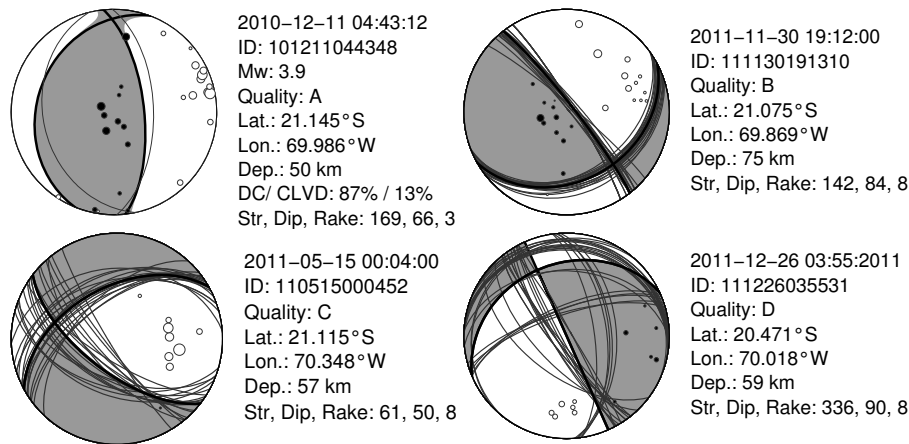


**Figure 3.3:** Examples of fault plane solutions with qualities A, B, C, and D. Circles represent positive (black) and negative (white) first motion P-wave polarities. The size of the circle is proportional to  $\sqrt{|u_P|/|u_S|}$ . Thin lines are the starting model (for quality A) or rather solutions with perturbed take-off angles (for qualities B, C, D).

### 3.2.4 Representation

I represent the focal mechanisms in two ways. On maps and profiles, I drew beach ball plots. They show the two nodal planes on the upper hemisphere of the focal sphere. One of the nodal planes is the fault plane so that the beach ball plot represents the two possible fracture directions. The quadrants of the focal sphere (in between the nodal planes) that move away from the source are conventionally filled with a color, while the quadrants that move towards the source are filled white.

The other representation is the orientation of the tension (T) and the pressure (P) axis. They are the smallest and the largest eigenvector of the moment tensor. They point within  $\sim 45^\circ$  in the minimal and maximal stress direction and in this sense give an approximate indication of the orientation of the effective stresses. I plotted them as lower hemisphere projections on the focal sphere, where again the T-axes are drawn with a color and the P-axes are drawn white.

## 3.3 Results

I observed focal mechanisms in four spatially and geodynamically distinct regions of the subducting slab. I discriminated them by their location within the slab relative to the large seismicity patterns. All focal mechanisms are shown as beach ball plots and color-coded by region in Figure 3.4. The first region (upper bands, UB) contains the upper two bands of seismicity, the one at the plate interface and the one near the oceanic Moho, at shallow levels. The second region (lower band, LB) contains the events in the oceanic mantle at shallow intermediate depth. The third region (transitional zone, TZ) contains the events that occur below the downdip end of interface seismicity but west of the nest of deeper intermediate depth seismicity. The fourth region (deeper intermediate depth, DID) contains the events that make up the nest of deeper intermediate depth seismicity.

### 3.3.1 Upper bands (UB)

In the upper bands of shallow seismicity, the overall quality of focal mechanisms is better near the plate interface and a little worse near the oceanic Moho. This may be the case because the calculation of take-off angles near the oceanic Moho can be imprecise. The focal mechanisms show mostly thrusting events (Fig. 3.5). They clearly divide into two subgroups. One subgroup consists of events that are characterized by rather shallow thrust on a  $\sim 20^\circ$ E dipping plane. The T-axes accordingly plunge  $60^\circ$  to  $75^\circ$ E and have an approximate azimuth in convergence direction (N $75^\circ$ E), and the P-axes cluster at a shallow plunge of  $15^\circ$  to  $30^\circ$ W. This group very likely represents seismic slip on the plate interface. The group of events is well constrained by two quality A events. Most events that show this focal mechanism are indeed located close to the plate interface (darker symbols on Fig.3.5), but some are located closer to the oceanic Moho, suggesting the presence of a fault plane parallel to the plate interface, deeper within the oceanic crust.

The other group consists of thrust events that have nodal planes that dip significantly steeper than the plate interface. Their T-axes plunge around  $75^\circ$  to the west or are subvertically, the P-axes dip  $15^\circ$  to  $30^\circ$ , some even  $45^\circ$  shallower than the slab. There is no clear correlation of the orientation of the axes with the convergence direction. The nodal planes have an angle to the plate interface of  $\sim 45^\circ$ . These events are slightly more concentrated at a deeper level of the oceanic crust, near the oceanic Moho, but also occur near the plate interface.

An abrupt change in focal mechanisms occurs at the downdip end of seismicity at the plate interface at  $69.85^\circ$  W,  $21.30^\circ$  S, 55 km depth. At this point, a typical interface thrust event occurs less than 5 km west of a normal faulting event with an along-strike striking T-axis. Both events are of quality A.

### 3.3.2 Lower band at shallow intermediate depth (LB)

The earthquakes that occur in the mantle of the subducting slab at shallow intermediate depth are mostly normal faulting events, but also a few thrust earthquakes occur (Fig. 3.6). The normal faulting events subdivide into two groups. One group consists of events whose T-axes plunge in slab-dip direction  $\pm 20^\circ$  and have an azimuth that is loosely directed in convergence direction. These events occur exclusively in the basal part of the lower band of seismicity (dark colored events in Fig. 3.6).

The other group has T-axes that plunge steeper and are more randomly distributed. It also contains a small number of thrust faulting events. The events of this group occur exclusively in the upper part of the band, closer to the plate interface (light colored events). Each of these groups is substantiated by a quality A event.

### 3.3.3 Transitional zone (TZ)

In the transitional zone, focal mechanisms are rather well constrained, because of a good coverage of the focal spheres by the two subnetworks. The events show almost exclusively normal faulting focal mechanisms. Most T-axes dip  $\pm 20^\circ$  in the slab plane

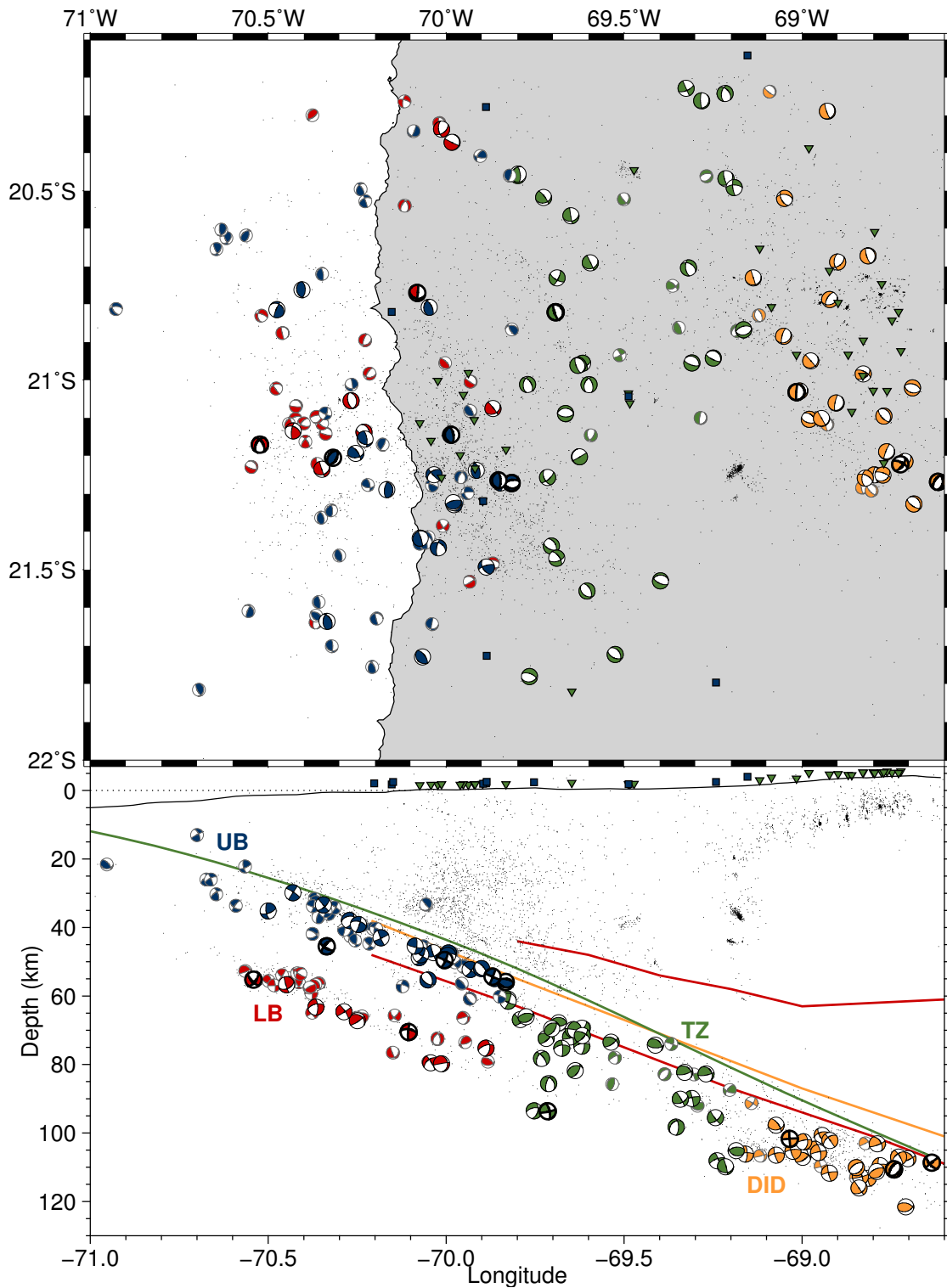


**Figure 3.4:** Overview of the calculated fault plane solutions in the study area. Colors indicate regions of interest. Quality C events are small, quality B events large, and quality A events bold. Red lines are the continental and the oceanic Moho, the yellow line is the top of the oceanic crust, as constrained by receiver functions (Yuan et al., 2000). The green line is the regional envelope of the Wadati-Benioff-Zone (Hayes et al., 2012).

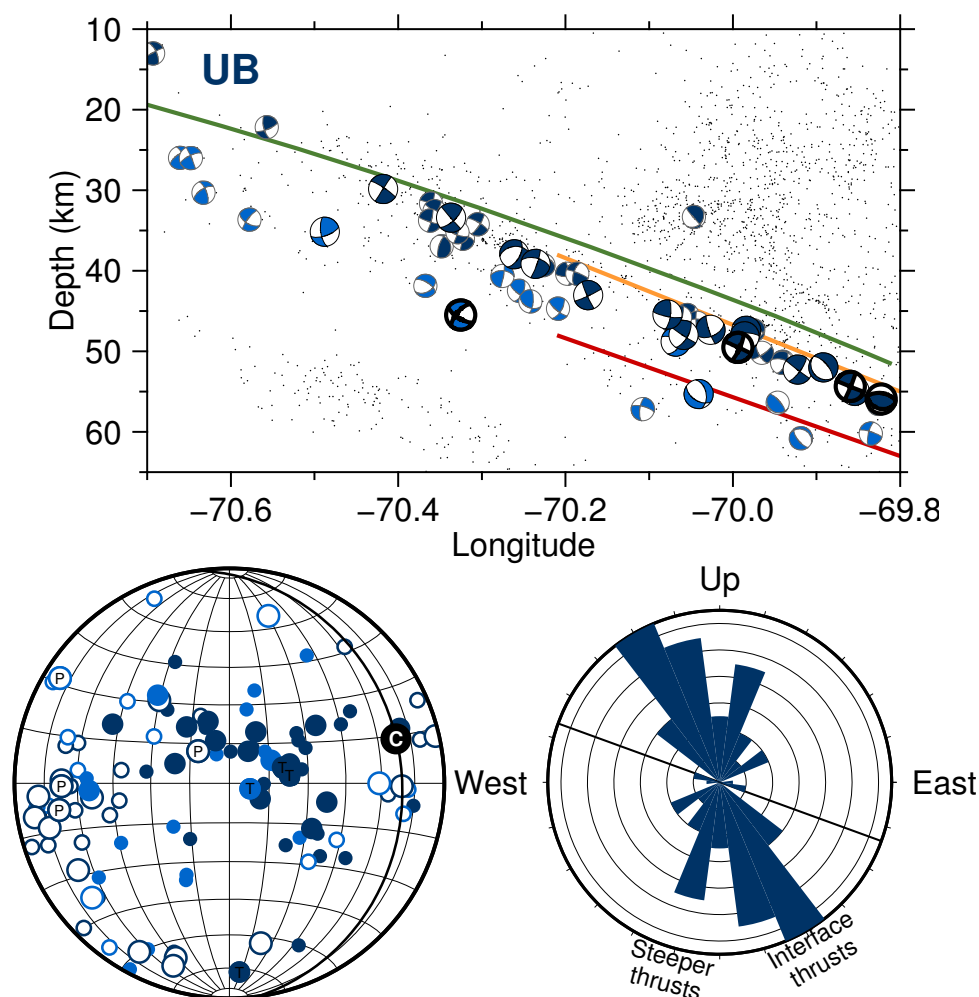


**Figure 3.5:** Focal mechanisms in the upper two bands of seismicity within the oceanic crust and near the oceanic Moho. Top: depth profile, close-up of Figure 3.4, bottom. Left-hand side: Lower hemisphere stereographic projection of P- and T-axes (open and closed circles) with orientation of the slab surface (black line) and convergence direction (C). Light colors indicate events closer to the plate interface, dark colors events further away. Quality C events are printed small, quality B events large, quality A events are bold (profile) or marked 'P' or 'T' (stereographic projection). Right-hand side: Polar histogram of T-axes in the profile plane, bin width 15°. Concentric grid interval marks two events, dip of the plate interface is marked by a black line. Groups of events that are mentioned in the text are labeled outside the histogram.



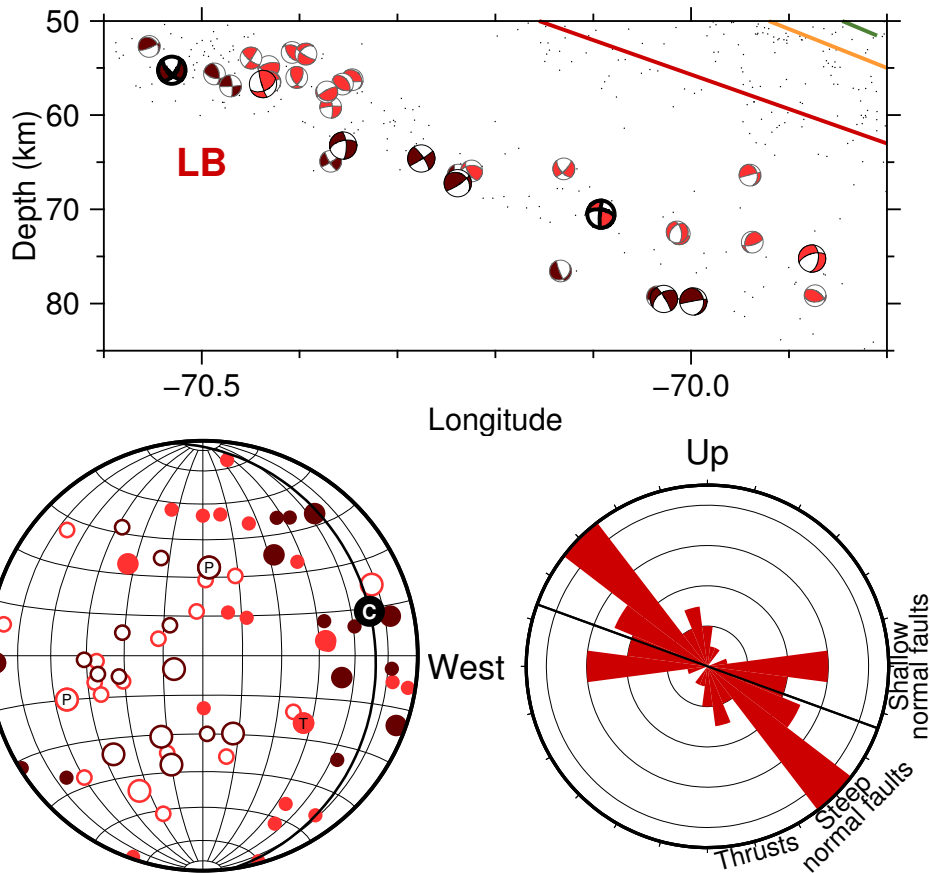


**Figure 3.6:** Focal mechanisms in the lower band of seismicity within the oceanic mantle. Subfigures and symbols as in Figure 3.5.

and have an azimuth that loosely follows the convergence direction. This trend is more vaguely defined trench-ward and becomes more pronounced arc-ward, near the lower end of the transitional zone. A number of events show the unique feature of T-axes dip that are 'tipping backward'. This means that they have T-axes that plunge significantly westward. Most of these events are located in the upper, trench-ward part of this zone, within 30 km of the downdip end of interface seismicity.

### 3.3.4 Deeper intermediate depth (DID)

At deeper intermediate depth, focal mechanisms are generally of rather high quality because here events have a comparatively high magnitude and ray paths to the WF-subnet are subvertical, and therefore little affected by unmodeled velocity heterogeneities. All focal mechanisms show a normal faulting focal mechanism that again can be split into two well separated subsets (Fig. 3.8).

A much higher number of events have one near-vertical and one near-horizontal nodal plane that form a '+' in profile view. Accordingly, the T-axes plunge between 30 and 45° eastward. Instead of the dip obtained from receiver functions (Yuan et al., 2000), the T-axes seem to follow the dip of the regional envelope of intermediate depth seismicity,

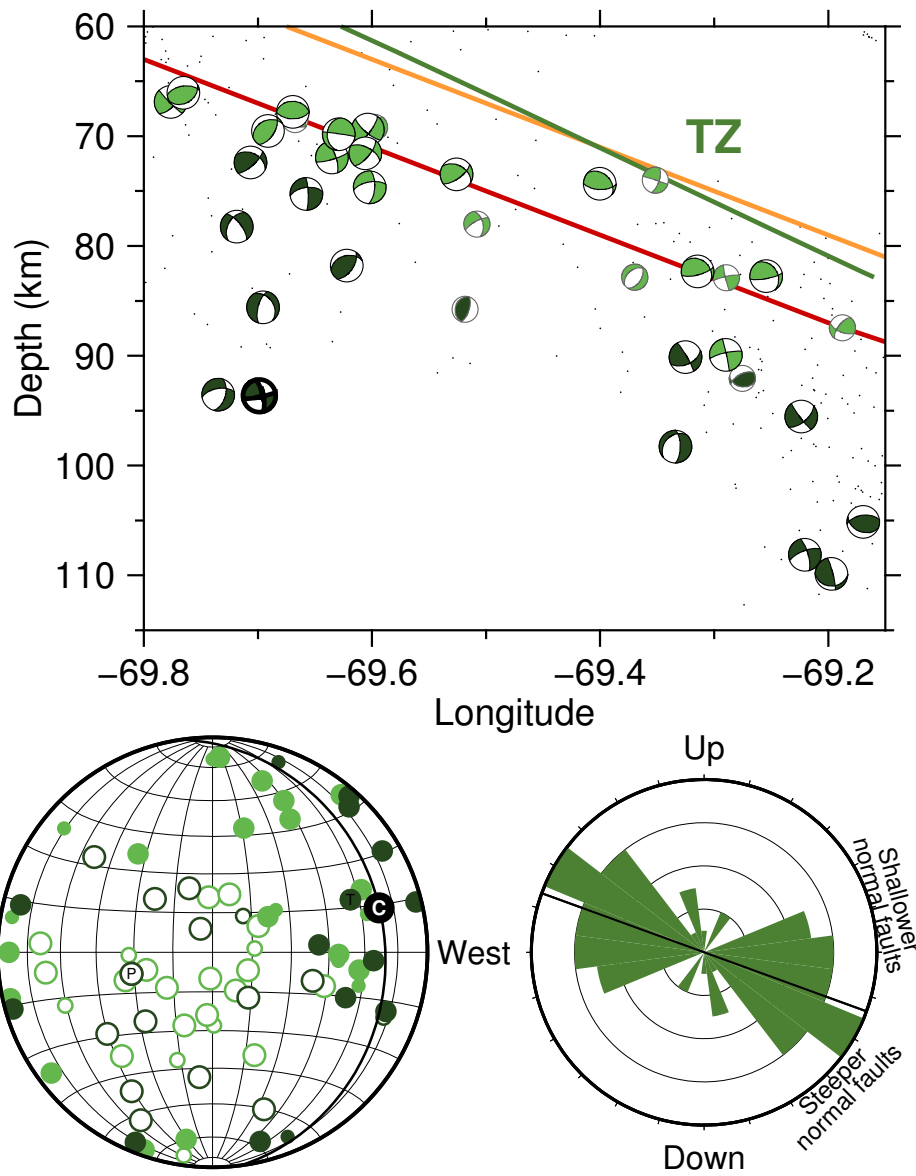


**Figure 3.7:** Focal mechanisms for the transitional zone below the downdip end of interface seismicity. Subfigures and symbols as in Figure 3.5.

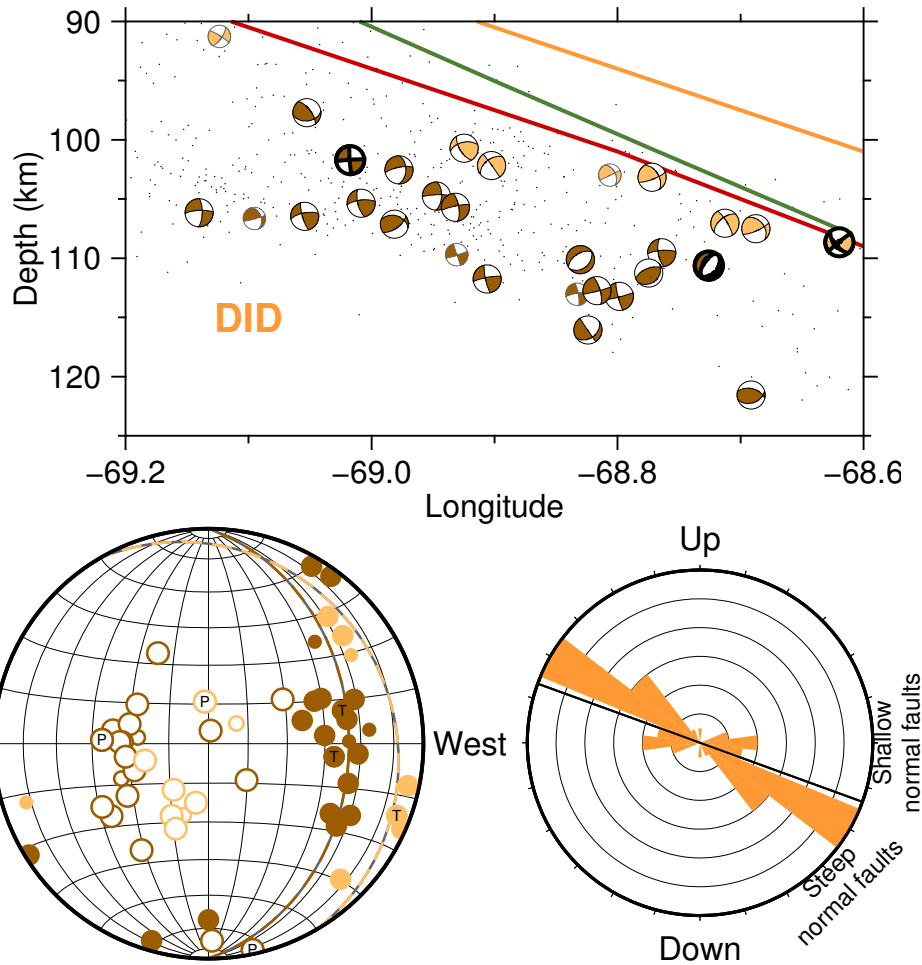


**Figure 3.8:** Focal mechanisms for the earthquakes at deeper intermediate depth. Sub-figures and symbols as in Figure 3.5.

as modeled by the Slab 1.0 model (Hayes et al., 2012). These events are more common in the lower part of the earthquake cluster (darker colored events in Fig. 3.8). They are constrained by two quality A events.

The other subset consists of only six events, which feature significantly shallower dipping nodal planes that form an 'x' in profile view and that accordingly have subhorizontal T-axes. It is supported by one quality A event and comprises the uppermost events within the zone of deeper intermediate depth earthquakes (lighter colored events in Fig. 3.8).

The difference between the '+'- and the 'x'-events can qualitatively easily be seen in the polarity data, as the nodal plane of the '+'-events cross cuts the WF-subnet, causing a polarity flip within the network, whereas the nodal plane of the 'x'-events runs in between the WF- and the AF-network (Fig. 3.9). Rietbrock and Waldhauser (2004) have made a similar observation.

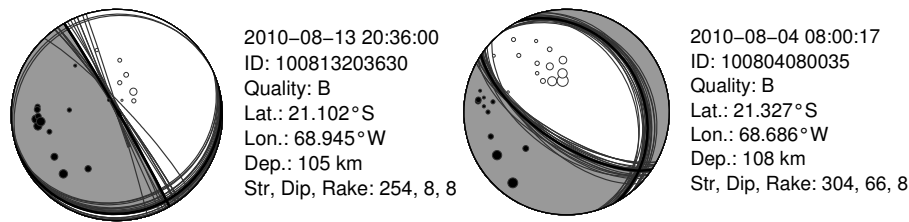


**Figure 3.9:** Examples of focal mechanism with one steep and one subhorizontal nodal plane ('+', left) and with two dipping nodal planes ('x', right). Symbols as in Figure 3.3.

### 3.4 Discussion

The evolution of faulting styles along the subduction pathway is summarized in Figure 3.10. It exhibits a clear twofold zoning. Shallow earthquakes are predominantly thrust faulting events, while intermediate depth earthquakes are predominantly normal faulting events. The sharp separation between these two regimes occurs at the downdip end of interface seismicity. This is a strong indication that this point is the downdip end of inter-plate coupling. Above, the slab is in compression, collisional forces act on the subducting plate and affect the entire oceanic crust. The plate interface is inter-seismically coupled. The continent acts as a backstop. Stress becomes transferred to the overriding plate. Below the downdip end of seismic coupling, the slab is under tension. This is a strong indication for the stress-field being dominated by mantle-side slab-pull beyond and below this point. The change in stress regime occurs at the point, where the reflectivity response of the plate interface broadens to form the so-called 'E'-layer that has earlier been interpreted as representing a zone of aseismic creep (Nedimovic et al., 2003).

The upper bands of shallow seismicity contain, besides the interface-thrust events, a family of steeply dipping thrust faulting events (Fig. 3.5). These may be reactivated bend-faults (Fig. 1.1), as it has been suggested by Ranero et al. (2005). However, spontaneous faulting of the relatively undisturbed medium within the compressive stress-field, possibly assisted by metamorphic mineral reactions, cannot be excluded as an earthquake nucleation mechanism.

At intermediate depth, T-axes have a tendency to align with the slab with increasing depth, both downdip and normal to the slab. If the heterogeneity of internal structures within the slab does not increase along the subduction pathway, this can be an indication for a progressive increase of differential stresses. Differential stresses can be relatively low trench-ward and increase arc-ward, in case the lowest principal stress decreases as a result of a stronger downwards directed tensional force component. The origin of such a component of the force vector is likely to be a net negative buoyancy, which can be due to the progressive densification of the rock matrix, because of ongoing metamorphic mineral reactions. A net positive buoyancy of the slab towards the trench may also enhance the coupling at the plate interface. In Chapter 4, I discuss whether densifying mineral reactions can be expected within the subducting slab and which minerals they would involve. Furthermore, an incipient viscous coupling to mantle convection could increase differential stresses on the slab.

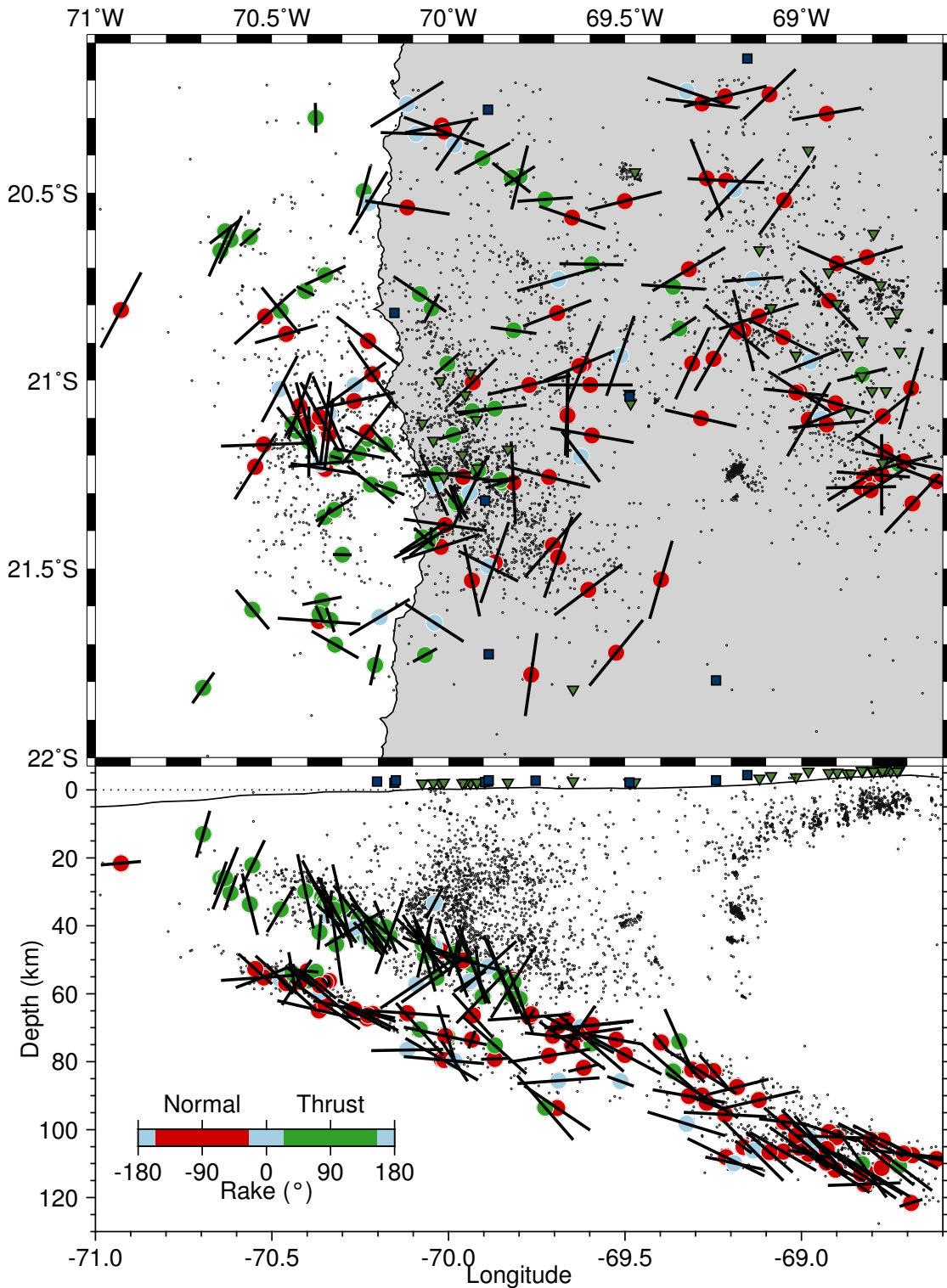


**Figure 3.10:** Rakes (color) and orientations of the T-axes (black lines) in the study area. Top: Map view. Bottom: Profile. Length of the T-axes represents the projection in the respective plane.

The end-member of the possible evolution of the tensional component of the stress-field is to be observed in the double seismic zone at deeper intermediate depth (Fig. 3.8). Here, the T-axes are well aligned with the slab. Furthermore, they tend to be more strictly directed downdip in the lower band than in the upper band. Rietbrock and Waldhauser (2004) observe the same behavior, but locate the upper band in the oceanic crust, not as I in the oceanic mantle. In the framework of the possible progressive slab densification, this could mean that the mantle that hosts the upper band of seismicity is indeed more buoyant than the mantle in the lower band. A reactivation of bend-faults as suggested by Rietbrock and Waldhauser (2004) and Ranero et al. (2005) is plausible only for the events that have shallowly dipping nodal planes ('x'-events, Fig. 3.9) that are more concentrated in the upper band of seismicity. The steeper faults at depth ('+'-events) are less likely to belong to the same family of faults, because the outer-rise normal faults have been imaged to have the form of listric faults at depth, that means that they *flatten* out at depth (Ranero et al., 2003) and do not steepen. The steeper set of events may here indeed represent spontaneous faulting of the relatively undisturbed medium in the prevailing stress-field, possibly assisted by metamorphic mineral reactions.

At shallow intermediate depth, which means in the lower band at shallow intermediate depth and in the transitional zone (Figs. 3.6 and 3.7), the downward tensional trend is present but not as pronounced as at deeper intermediate depth. Presumably, the principal stresses at each earthquake source result here from the superposition of multiple similarly strong forces. The dominant force is certainly the mantle-side slab-pull force, which is plausible because the T-axes scatter broadly within the slab plane. Possible other forces are weaker ocean-side ridge-push forces and unbending forces.

Ridge-push forces act as compressing forces in convergence direction. In the transitional zone, beyond the end of seismic coupling, they are probably responsible for the shallowing and 'backward tipping' T-axes.

Internal fluid over-pressure may possibly trigger the seismic events in the lower band of seismicity at shallow intermediate depth that show rather randomly oriented focal mechanisms (Fig. 3.6, light color). The presence of fluids implies the presence of a fluid source, here a dehydrating mineral. Generally, seismic rupture will occur along a preferably oriented weakness-zone that can be generated by fine-grained reaction products and fluid inclusions that result from the progress of the dehydration reaction. Their orientation is controlled by a number of internal factors such as a gradient in chemical potential or the texture of the medium (Plümper et al., 2017). If the differential stresses are low and seismic rupture occurs because of reduction of the normal stress due to fluid over-pressure, the orientation of the fault-plane is dominated by these internal factors. If the observed, rather random orientation of focal mechanism in the upper part of the lower band of seismicity is real, I suspect it to be caused by fluid over-pressure within a regime of not very large differential stresses (Fig. 3.6, lighter colored events).

### 3.5 Conclusion

In this chapter I presented the first undisturbed top-to-bottom analysis of focal mechanisms in the Central Andean subduction zone. The analysis includes shallow seismicity, intermediate depth seismicity, as well as the previously not observed seismicity in the oceanic mantle at shallow intermediate depth.

A change in stress regime is supported by the data from collision-dominated stresses at shallow depth to mantle-side slab-pull at intermediate depth. This change occurs at the line where interface seismicity comes to an end and the reflectivity response of the plate interface broadens characteristically.

Seismicity in the oceanic crust exhibits not only earthquakes that rupture the plate interface, but also such that probably reactivate outer-rise bend-faults.

At intermediate depth, the T-axes of the focal mechanisms successively align with the slab plane. This is an indication that mantle-side slab-pull forces probably increase along the subduction path-way, suggesting a progressive densification of the slab. Reactivation of outer-rise bend-faults can only explain a small number of focal mechanisms at intermediate depth. The faulting style of other intermediate depth earthquakes is most probably dominated by the stress-field, and/or internal structures.

Finally, there are indications for a local perturbation of the stress-field in the oceanic mantle at shallow intermediate depth, which is possibly related to fluid over-pressure.





# Chapter 4

## Petrophysical modeling

In the previous two chapters, I attributed a number of observations to phenomena that are associated with metamorphic mineral reactions. In this chapter, I elaborate on the major metamorphic mineral phase changes that occur within the subducting oceanic crust and mantle. I address the petrophysical implications of such reactions with a special focus on densification and fluid release.

As a preparation for Chapter 5, I will formulate expectations on the P- to S-wave velocity ratio ( $V_P/V_S$ -ratio) of the rocks in isotropic and non-porous state, as well as in the presence of fluid-filled pore-space and considering anisotropic conditions. To predict the  $V_P/V_S$ -ratio in the different geodynamic situations that can be met in the Central Andean forearc system, I consult, where possible, laboratory measurements published in previous studies. For the challenging prediction of the  $V_P/V_S$ -ratio of subducting metamorphosing rocks, that possibly undergo fluid release, I perform petrophysical modeling and anisotropy calculations to get a complete and coherent understanding of the elastic rock properties.

### 4.1 Properties of isotropic non-porous subducting lithosphere

When the oceanic lithosphere enters the subduction system it has a fixed chemical composition. The mineral assemblage then changes solely in dependence on temperature and pressure. Temperature and pressure conditions during subduction can be estimated from general rules of thumb.

I therefore constrained the chemical composition of the rock and computed the mineral assemblage by using the Gibb's free energy minimization toolbox *Perple\_X* (Connolly, 2005, 2009). I calculated isotropic dry-rock elastic rock properties from a comprehensive table of equations of state.

I modeled the petrophysical effects of the emergence of fluid-filled pore-space which is due to metamorphic fluid release by employing a poroelastic model. As governing factors the poroelastic model considers elasticity of both the grain matrix and the fluid, as well as the absolute amount of pore-space and the pore-space geometry.

### 4.1.1 Thermodynamic considerations

I used the Gibb's free energy minimization code *Perple\_X* to compute thermodynamic phase equilibria. *Perple\_X* finds the amount  $x_j$  of a number of  $p$  mineral phases of a specific composition ("pseudo compounds") that minimizes the Gibb's energy of the system at constant pressure and temperature:

$$G^{\text{sys}} = \sum_{j=1}^p x_j G_j. \quad (4.1)$$

The amount of the  $i = 1, \dots, n$  chemical constituents  $\psi$  (given as oxides of the chemical elements) that make up the mineral phases must sum up to the chemical composition of the system:

$$\Psi_i^{\text{sys}} = \sum_{j=1}^p x_j \psi_i^j. \quad (4.2)$$

Individual chemical constituents can be regarded as saturated, which means that an arbitrary amount can be used to build pseudo compounds, but that it will not be built as a pure phase.

Pseudo compounds were combined to solid solutions that represent mineral phases. The solid solution mineral phases I used are listed in Table C.1, additional pure end-member mineral phases are listed in Table C.2 (see Appendix).

Gibb's energies of the mineral phase end-members were expressed as polynomial equations of state whose coefficients have been explored in extensive research efforts. I used the database *hpha02ver.dat*, which is a compilation of thermodynamic coefficients which are relevant to compute mineral phase relations published in Holland and Powell (1998), augmented by such which are relevant for the computation of seismic wave speeds by Hacker and Abers (2004).

### 4.1.2 Elastic properties

*Perple\_X* facilitates the computation of elastic rock properties. In Chapter 5, I will estimate the  $V_P/V_S$ -ratio in the subducting slab and will come back to the theoretical values computed here for interpretation.

Dry rock bulk- and shear modulus ( $K$  and  $\mu$ ) of a mineral phase at temperature ( $T$ ) and pressure ( $P$ ) were computed as follows (Connolly, 2017):

$$K(T, P) = K_0 + k_1(P - P_r) + k_2(T - T_r) \quad (4.3)$$

$$\mu(T, P) = \mu_0 + \mu_1(P - P_r) + \mu_2(T - T_r), \quad (4.4)$$

where the coefficients  $K_0$  and  $\mu_0$  are in the order of  $10^{10}$  Pa,  $k_1$  and  $\mu_1$  are in the order of  $10^5$  Pa/Pa and  $k_2$  and  $\mu_2$  are in the order of  $-10^7$  Pa/K.  $P_r$  and  $T_r$  are the reference pressure and temperature. The moduli are adiabatic, which means that entropy is conserved. Temperature and pressure are not treated as independent variables. I compute whole rock ('grain') elastic properties ( $K_{gr}$  and  $\mu_{gr}$ ) as the Hashin–Shtrikman-averages of the

**Table 4.1:** *Composition of rocks used for thermodynamic modeling.*

Element	Amount (wt%)		
Rock	Altered oceanic crust	Dry peridoite	Hydrated peridotite
SiO <sub>2</sub>	48.9	44.7	39.3
Al <sub>2</sub> O <sub>3</sub>	16.6	1.8	1.6
FeO	9.6	9.9	8.7
MgO	7.1	42.1	37.1
CaO	13.7	1.6	1.5
NaO	2.2	—	—
K <sub>2</sub> O	0.6	—	—
H <sub>2</sub> O	saturated	—	saturated
Reference	Staudigel et al. (1996)	John et al. (2010)	

constituent's elastic moduli. The difference between the upper and the lower bound has been tested to be <1 GPa and is therefore negligible.

The  $V_P/V_S$ -ratio can be computed from the bulk- and shear modulus as:

$$V_P/V_S = \sqrt{\frac{K}{\mu} + \frac{4}{3}}. \quad (4.5)$$

It also results from measurements of Poisson's ratio ( $\nu$ ) using:

$$V_P/V_S = \sqrt{\frac{1}{1 - 2\nu} + 1}. \quad (4.6)$$

For isotropic materials, an intuitive lower bound on  $V_P/V_S$  is the one of a ( $\nu = 0$ )-material, that does not extend horizontally upon vertical compression. This bound transforms to a lower bound of  $V_P/V_S = \sqrt{2} \approx 1.4$ . A typical value of  $\nu = 0.25$ , that results from approximately equal Lamé parameters ( $\lambda \approx \mu$ ), yields a typical  $V_P/V_S = \sqrt{3} \approx 1.73$ . The upper bound is given by  $\nu = 0.5$ , where  $\lim_{\nu \rightarrow 0.5} (V_P/V_S) = \infty$ .

I performed petrophysical modeling for rocks of the oceanic crust and mantle that experience metamorphism, reviewed the elastic properties of rocks that form a typical continental crust, and assessed the possible effects of anisotropy.

### 4.1.3 Dynamic creation of pore-space

When the rock matrix densifies during a metamorphic mineral reaction, a void volume fraction is created. The void volume fraction can be interpreted as an initial porosity  $\Phi_0$ . It equals the relative change in density of the reaction:

$$\Phi_0 = \frac{\Delta\rho}{\rho}, \quad (4.7)$$

where  $\rho$  is the density of the metamorphosed rock and  $\Delta\rho$  is the difference in density after and before the reaction.

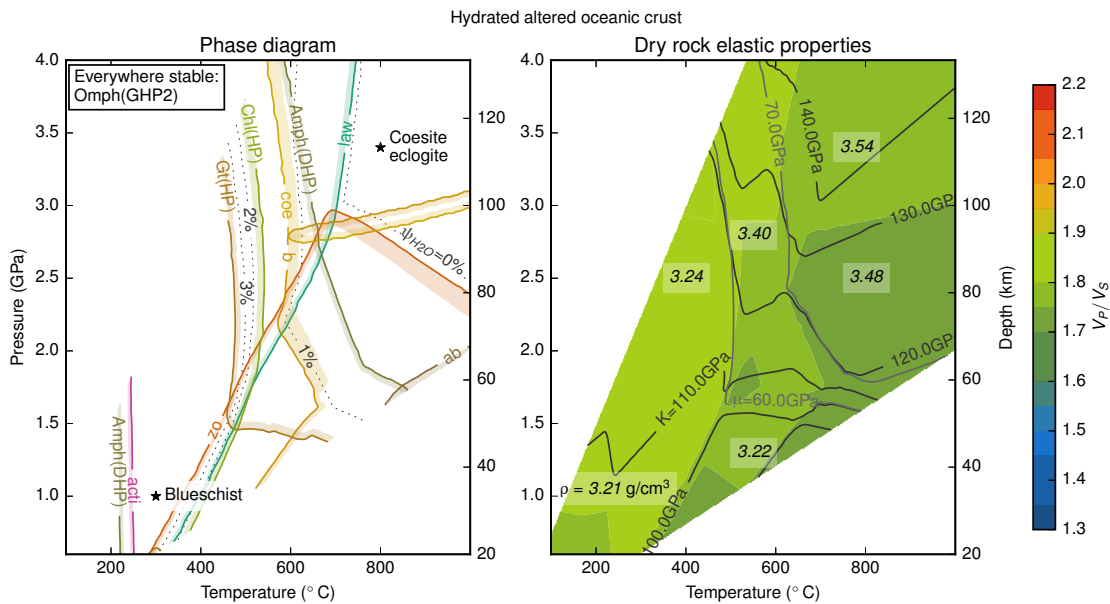


**Figure 4.1:** Phase diagram and elastic properties of hydrated altered oceanic crust subject to metamorphism during subduction. Mineral bound water ( $\psi_{H_2O}$ ) in wt%. Composition see Tab. 4.1. Phase name abbreviations see Tabs. C.1 and C.2.

#### 4.1.4 Petrology of subducting oceanic crust

For the oceanic crust, I used the chemical model proposed by Staudigel et al. (1996) and later used by Hacker et al. (2003b). I assumed that the oceanic crust was fully hydrated and therefore added  $H_2O$  as a saturated constituent to the composition (Tab. 4.1).

The petrophysical model is shown in Figure 4.1. The metamorphic rocks that develop from this composition are:

- Two blueschists which are defined by the stability field between the breakdown of actinolite to sodium bearing amphiboles near 200° C and the creation of garnet near 450° C. They are:
  - A lawsonite and chlorite bearing blueschist at higher pressures
  - A zoisite bearing blueschist at lower pressures
- A number of eclogites, which are defined by the creation of garnet, which contain either lawsonite or zoisite, and which further subdivide into:
  - Amphibole and potentially chlorite bearing eclogites
  - A quartz eclogite
  - A coesite eclogite

The index mineral glaucophane for the blueschist facies is contained within the solid solution model Amph(DHP) and cannot be distinguished from other amphiboles in

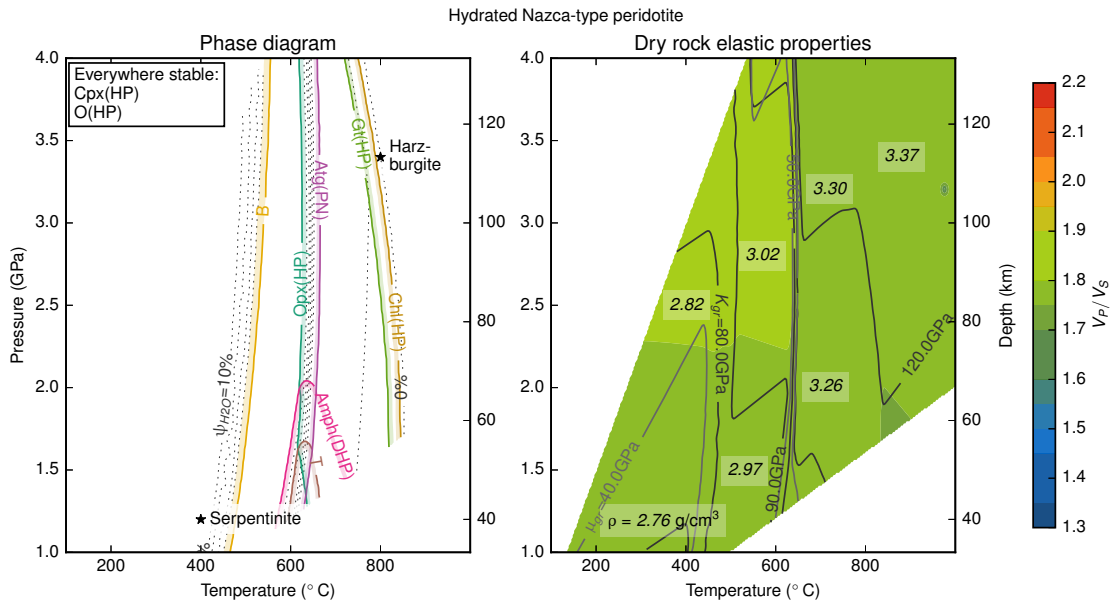
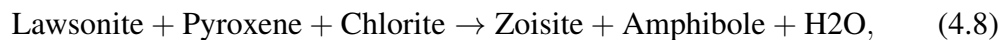


**Figure 4.2:** Phase diagram and elastic properties of a hydrated Nazca-type peridotite subject to metamorphism during subduction. Composition see Tab. 4.1. Phase name abbreviations see Tab. C.1

terms of nomenclature. Omphacite, which is indicative of greenschist, cannot be distinguished from other clinopyroxenes, because the solid solution model Omph(GHP2) also includes both augit end-members: hedenbergite and diopside (Tab. C.1).

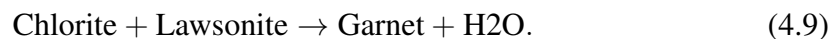
The rocks show  $V_P/V_S$ -ratios between 1.72 and 1.85. Chlorite, lawsonite, zoisite, and the amphiboles, all carry mineral bound water, but altogether not more than 3 wt%. In terms of the  $V_P/V_S$ -ratio, the breakdown of chlorite, the creation of zoisite, as well as the quartz–coesite-transition have potentially detectable effects.

The most prominent dehydration reaction at lower pressures (below 1.5 GPa) is the breakdown of lawsonite and chlorite altogether with pyroxene to zoisite, amphibole, and fluid:

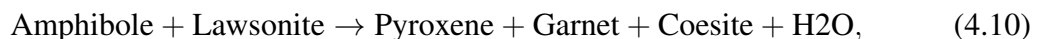


occurring in the temperature interval between 380° and 410° C. The solid rock matrix densifies by 0.01 g/cm<sup>3</sup>, which equals a generation of a void volume fraction of 0.3 vol%.

At high pressures the reactions involve other mineral phases. Above 1.5 GPa and at temperatures between 450° and 500° C, the dehydration of chlorite with lawsonite happens under the creation of garnet:



This reaction releases 2 wt% of fluid and generates a void volume fraction of 5 vol% by the densification of the rock matrix by 0.16 g/cm<sup>3</sup>. The breakdown of amphibole and lawsonite to garnet, pyroxene and coesite above ~2.5 GPa and 600° C:



releases 1.4 wt% of fluid and generates a void volume fraction of 4 vol% by the densification of the rock matrix by  $0.14\text{ g cm}^3$ .

### 4.1.5 Petrology of subducting oceanic mantle

I computed elastic rock properties of a *dry* peridotite using the composition given in Tab. 4.1. Under the range of P-T-conditions that prevail in a subduction system, a harzburgite forms. It has harzburgitic composition and a  $V_P/V_S$ -ratio of 1.74.

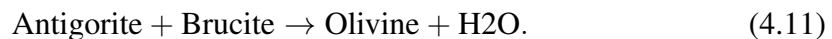
A number of metamorphic rocks result from the composition of a *hydrated* peridotite (Tab. 4.1) in the P-T-range of a subduction system (Fig. 4.2). They are:

- Two serpentinites, namely:
  - A brucite bearing serpentinite
  - A brucite-free serpentinite
- Two harzburgites which form from serpentinite:
  - A chlorite harzburgite
  - A chlorite-free harzburgite which is stable at higher temperatures

The rocks show  $V_P/V_S$ -ratios between 1.73 and 1.83. The very low  $V_P/V_S$ -ratios predicted for 105 km depth near  $1000^\circ\text{ C}$  is a numerical artifact. The transition from serpentinite to chlorite harzburgite is marked by an increase in bulk- and shear modulus of  $\sim 20\text{ GPa}$ , but only by a slight drop in  $V_P/V_S \leq 0.05$ .

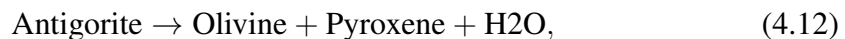
Three main metamorphic dehydration reactions occur.

Antigorite partly breaks down in a sliding reaction in the presence of brucite to form olivine and water at a temperature of  $\sim 500^\circ\text{ C}$ :



During this reaction, the density of the solid matrix increases by  $0.2\text{ g/cm}^3$ , which corresponds to a generation of 7 vol%, 4 wt% of water are released.

Antigorite finally breaks down to form olivine, pyroxene, and fluid at a temperature of  $\sim 640^\circ\text{ C}$ :



a reaction that is accompanied by 8 vol% volume generation and the release of 5 wt% water.

Chlorite breaks down at temperatures of  $\sim 840^\circ\text{ C}$ , where chlorite reacts to olivine, garnet, and fluid:



by which 2 vol% of void volume are generated and 1 wt% water is released.

**Table 4.2:** *Poisson's ratios and derived  $V_P/V_S$  as measured by Kern and Schenk (1988).*

Rock	$\nu$	$V_P/V_S$
Granite	0.21	1.65
Orthogneiss	0.23	1.69
Granodiorite	0.24	1.71
Felsic Granulite	0.24	1.71
Metabasite	0.27	1.78
Dioritic Gneiss	0.28	1.81

### 4.1.6 Petrology of the continental crust

Kern and Schenk (1988) performed comprehensive investigations of the in-situ elastic properties of the upper and middle continental crust on a representative and nearly complete cross section in Calabria, southern Italy. They measured the seismic P- and S-wave velocity as well as pressure and temperature derivatives on a range of thoroughly classified upper and mid-crustal rocks, namely acidic, mafic, and pelitic rocks, metamorphosed to granulite- and amphibolite facies, as well as post tectonic granitoid intrusions. They explicitly recognize the sensitiveness of the Poisson's ratio to the lithology of upper and mid-crustal rocks.

I summarize the values which they measured in Tab. 4.2. They find Poisson's ratios in the range of 0.21 and 0.28 that transform to  $V_P/V_S$ -ratios between 1.65 and 1.81. Remarkably,  $V_P/V_S$ -ratios qualitatively correlate with the quartz content of the rock, with felsic compositions typically having lower  $V_P/V_S$ -ratios than mafic compositions.

## 4.2 The influence of fluid-filled pore-space on elasticity

The generation of pore-space and the release of fluid that accompanies the mineral dehydration reactions (4.8) to (4.13) which occur during subduction can have a strong effect on the  $V_P/V_S$ -ratio.

### 4.2.1 Poroelastic modeling

I modeled the effect of fluid-filled pores on the elastic properties of the rock by assuming small variations of the elastic moduli of the medium with empty pores,  $K_{dry}$  and  $\mu_{dry}$ , to be a linear function of porosity ( $\Phi$ ) and elastic piezosensitivity of the respective modulus ( $\theta_K$  and  $\theta_\mu$ ):

$$K_{dry} = K_{gr}(1 - \theta_K \Phi) \quad (4.14)$$

$$\mu_{dry} = \mu_{gr}(1 - \theta_\mu \Phi). \quad (4.15)$$

Pores were parameterized as having the shape of oblate spheroids with the aspect ratio  $\alpha$  (Takei, 2002; Shapiro, 2003). Round ('swiss cheese'-like) pores have an aspect ratio of 1, while elongated ('crack'-like) pores have a low aspect ratio smaller than  $\sim 10^{-2}$ .

Other pore-space models that have been calculated for other geometries map into an elastically equivalent  $\alpha$  (Fig. 4.3, Takei (2002)). A tube or an equilibrium geometry (pores that occupy the triple junction at grain boundaries, minimizing the surface energy) are elastically equivalent to pores having the form of oblate spheroids with high aspect ratios, while cracks are elastically equivalent to pores having the form of oblate spheroids with low aspect ratios.

Following this approach, I approximated elastic piezosensitivities for  $K$  and  $\mu$  ( $\theta_K$  and  $\theta_\mu$ ) as (Shapiro, 2003):

$$\theta_K \approx \frac{K_{gr}(3K_{gr} + 4\mu_{gr})}{\pi\alpha\mu_{gr}(3K_{gr} + \mu_{gr})} \quad (4.16)$$

$$\theta_\mu \approx \frac{1}{5} \left( 1 + \frac{4(3K_{gr} + 4\mu_{gr})(9K_{gr} + 4\mu_{gr})}{3\pi\alpha(3K_{gr} + \mu_{gr})(3K_{gr} + 2\mu_{gr})} \right). \quad (4.17)$$

Note that  $\theta_K$  and  $\theta_\mu$  are linear functions of the inverse pore aspect ratio ( $\alpha^{-1}$ ). Here, I neglect the explicit additional terms for stiff porosity from Shapiro (2003), because tests showed that round pores behave like stiff pores in terms of elastic parameters. Further, I was not interested in effects that involve the presence of both kinds of pores. This finding reduced the number of parameters. Accordingly, I treated elongated pores as compliant and round pores as stiff.

From equations (4.14) and (4.15) I computed the elastic properties  $K_{wet}$  and  $\mu_{wet}$  of the rock containing fluid-filled pores using the Gassmann-Equation:

$$K_{wet} = \frac{K_{gr}}{1 + \left( \frac{K_{dry}}{K_{gr} - K_{dry}} + \frac{K_f}{\Phi(K_{gr} - K_f)} \right)^{-1}} \quad (4.18)$$

$$\mu_{wet} = \mu_{dry}, \quad (4.19)$$

where  $K_f$  is the fluid bulk modulus, as predicted by the CORK-equation (Holland and Powell, 1991, 1998).

I could then compute the  $V_P/V_S$ -ratio of a porous or fractured, fluid-filled rock as a function of the microstructural parameters  $\alpha$  and  $\Phi$  as:

$$(V_P/V_S)_{wet}(\alpha, \Phi) = \sqrt{\frac{K_{wet}(\alpha, \Phi)}{\mu_{wet}(\alpha, \Phi)} + \frac{4}{3}}. \quad (4.20)$$

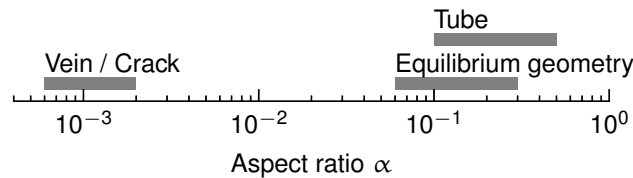


**Figure 4.3:** Equivalent aspect ratio following Takei (2002). The pore-space geometries of a 'crack', a 'tube', or the 'equilibrium geometry' are elastically equivalent to the oblate spheroid model geometry with a certain  $\alpha$  that I use.



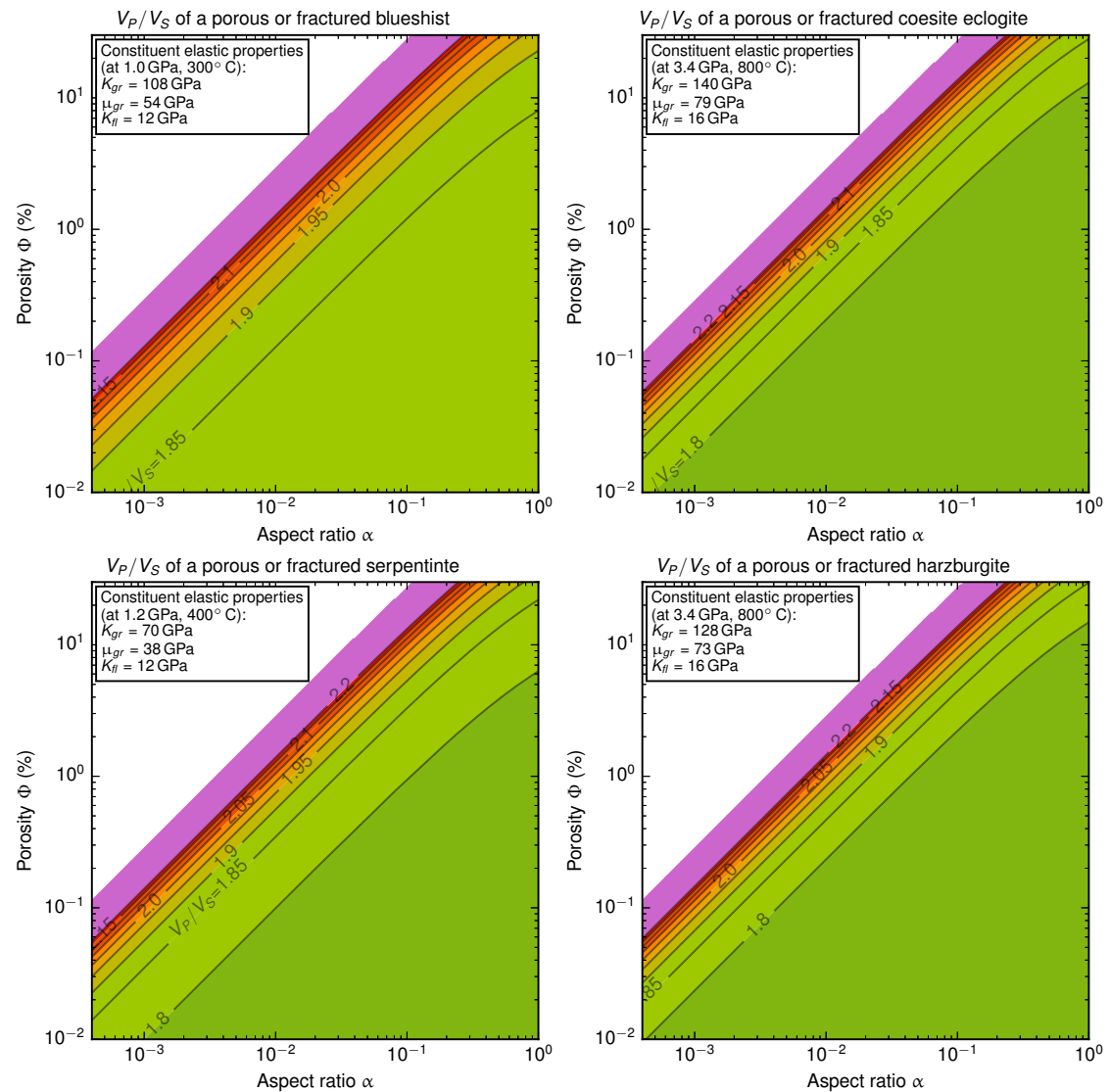


**Figure 4.4:** Results of poroelastic modeling for dehydrating subducting altered oceanic crust at  $\sim 30$  km and  $\sim 110$  km depth (top) and subducting oceanic mantle at  $\sim 40$  km and  $\sim 110$  km depth (bottom).

## 4.2.2 Results

For the elastic properties of the grains that represent a blueschist, a coesite eclogite, a serpentinite, and a harzburgite, I computed elastic properties for the case that they were porous or fractured, and filled with an aqueous fluid. The results as a function of pore aspect ratio  $\alpha$  and porosity  $\Phi$  are shown in Figure 4.4.

For all host rock lithologies and  $P$ - $T$ -conditions, the  $V_P/V_S$ -ratio increases exponentially as a function of increasing porosity and/or decreasing aspect ratio. The corresponding P- and S-wave velocity reductions are for serpentinite within the range found in laboratory measurements (Ito, 1990; Kono et al., 2007).

The  $\alpha$ - $\Phi$  (in %) space is diagonally approximately divided into three fields:

- $\Phi/\alpha \lesssim 40$  This is the bottom right-hand side region of the diagrams in Figure 4.4.  $V_P/V_S$  is consistently near the value of the non-porous lithology. Most notably, for almost spherical pores ( $\alpha \gtrsim 0.5$ ), even for porosities as high as several percent,  $V_P/V_S$  does not significantly exceed the non-porous values. Fluids stored in such pores are not detectable via their influence on elastic properties.
- $\Phi/\alpha \approx 100$  This is the central diagonal region of the diagrams in Figure 4.4, stretching from bottom left to top right. The term  $\theta_\mu \Phi$  in Eq. (4.15) here converges to 0.3, the effect of  $\alpha$  and  $\Phi$  on  $V_P/V_S$  is strong, with values between 1.9 and 2.2. The assumption of linear change in elastic moduli through small changes in porosity holds true, but is strained beyond this limit. Fluids stored in such pores strongly influence the  $V_P/V_S$ -ratio, and it can be used to constrain the pore-space geometry.
- $\Phi/\alpha \gtrsim 300$  This is the top left-hand side region of the diagrams in Figure 4.4. The term  $\theta_\mu \Phi$  reaches unity and Eq. (4.15) becomes unphysical,  $V_P/V_S$  cannot be computed anymore by this relationship, because  $\mu$  becomes negative (white area in Fig. 4.4).

I conclude that the  $V_P/V_S$ -ratio only increases strongly due to the emergence of fluid-filled pore-space during mineral dehydration reactions if pores are elongated. Round pores need to make up a very large volume fraction in order to elevate the  $V_P/V_S$ -ratio notably. Considerable pore volumes have no detectable effect on the  $V_P/V_S$ -ratio, if the pores are round. I can interpret a significantly increased, but not too large  $V_P/V_S$ -value poroelastically as a rock which contains pore-space that fulfills the relationship  $\Phi \approx 100\alpha$ .

### 4.2.3 Sensitivity on pore pressure

The porosity has another important relationship to the pore aspect ratio and the relative fluid pressure ( $\lambda = P_f/P$ ). The porosity ( $\Phi$ ) that remains elastically open at lithostatic pressure  $P$  as a function of  $\lambda$  is given as (Shapiro, 2003):

$$\Phi(\alpha, \lambda) = \Phi_0 \exp\left(-K_{gr}^{-1} \theta_K(\alpha) P(1 - \lambda)\right), \quad (4.21)$$

where  $\theta_K$  is proportional to the inverse aspect ratio  $\alpha^{-1}$  (Eq. (4.16)) and  $\Phi_0$  is the initial pore-space that I interpreted in the framework of metamorphic densification of the rock matrix as the volume reduction of the dehydration reaction (Eq. (4.7)). The existence of compliant pore-space under high confining pressures implies that pore fluid pressure is equilibrated at a near lithostatic level ( $\lambda \approx 1$ ), because only then it remains open (Fig. 4.5). Under only partially drained conditions ( $\lambda < 0.9$ ) compliant porosity closes. In contrast to this, stiff porosity remains open, even if pores are void, at least for the short time span before viscous processes begin to dominate deformation processes. In that sense, the statement that a high  $V_P/V_S$ -ratio relates to a high fluid pressure (e.g. Audet et al. (2009); Moreno et al. (2014)) is based on the implicit assumption that porosity is compliant.

## 4.3 Effects of anisotropic elastic properties

Among the bulk minerals that occur in a subduction zone, antigorite and olivine show widely recognized seismic anisotropy. I now introduce the effects which anisotropic elastic rock properties have on the travel time of seismic waves. I quantified these effects for the major anisotropic lithologies that can be expected in a subduction environment.

### 4.3.1 Nomenclature

In an anisotropic medium, seismic velocities depend on the propagation direction. The polarization directions of longitudinal- and shear-waves may become tilted compared to the propagation direction. If this is the case, the resulting waves are termed quasi longitudinal- and quasi shear-waves. Furthermore, the S-wave field becomes separated into two. With respect to the symmetry planes of the medium, these are called (quasi) horizontally polarized (q)SH-waves, and (quasi) vertically polarized (q)SV-waves, each having a separate propagation velocity. I measured the first arrival time of any wave-train and do not expect a strong tilt of the polarization direction, so that the velocities I determined are phase velocities.

In the observational practice, the S-waves are distinguished by the order in which they arrive, namely as a fast S-wave (S1-wave) and a slow one (S2-wave). The S2-wave occurs in the coda of the S1-wave, both of which occur in the coda of the P-wave. The amplitude, and therefore observability, of the respective wave train depends on its amplitude which in turn is governed by the radiation pattern of the seismic source with respect to the orientation of the anisotropic medium. If a fast S-wave is excited, it is this wave of which the arrival time is typically observed. The P- to S-wave velocity ratio inferred from such an observation will be the  $V_P/V_{S1}$ -ratio.

### 4.3.2 Parameterization

Anisotropy may be caused by two phenomena. First, crystal anisotropy occurs if the crystal of a mineral itself is microscopically anisotropic. This anisotropy has a macro-

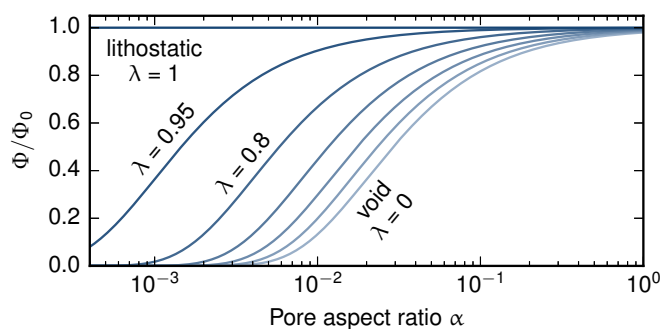


**Figure 4.5:** Open porosity fraction as function of relative fluid pressure ( $\lambda$ ) and pore aspect ratio (Eq. (4.21)) for a coesite eclogite at 3.4 GPa confining pressure (110 km depth).

**Table 4.3:** *Elastic tensors used for computation of anisotropic wave speeds.*

Elastic Modulus (GPa)	Olivine <sup>1</sup>	Antigorite <sup>2</sup>	Peridotite <sup>3</sup>	Serpentinite <sup>2</sup>	Porous layers	Fluid layers
$C_{11}$	320.5	208.1	236.9	172.0	111.8	120.5
$C_{22}$	233.5	201.6	205.9	163.0	111.8	120.5
$C_{33}$	196.5	96.9	195.4	89.5	111.3	119.6
$C_{44}$	64.0	16.9	63.0	31.6	30.2	0.0
$C_{55}$	78.7	18.4	69.8	27.0	30.2	0.0
$C_{66}$	77.0	65.5	71.4	56.5	31.5	38.0
$C_{12}$	71.6	66.4	72.4	54.2	48.8	44.5
$C_{13}$	68.1	16.0	71.1	27.3	49.3	44.3
$C_{23}$	76.8	4.9	72.1	30.7	49.3	44.3
Density (g/cm <sup>3</sup> )	3.36	2.62	3.36	2.62	—	—

<sup>1</sup> Abramson et al. (1997)    <sup>2</sup> Bezacier et al. (2010)    <sup>3</sup> Ismail and Mainprice (1998)

scopic expression if all the crystals show a lattice preferred orientation (LPO). Second, structural anisotropy occurs if a rock has preferably oriented inhomogeneities, such as layers or faults with considerably different elastic properties. For the case of a layered medium, a long wavelength equivalent, effectively anisotropic medium of hexagonal symmetry can be computed using Backus averages (Backus, 1962). The anisotropy parameters are then determined as the values of the *isotropic* elastic properties of the constituents, averaged in an appropriate way.

I described seismic velocities in an anisotropic medium using the formulations for orthorhombic symmetry as given by Auld (1973). Such a medium has three orthogonal symmetry planes. The orthorhombic symmetry is sufficient to describe the types of anisotropy that can be expected in a subduction environment.

The seismic velocities are parameterized relative to the normals of the symmetry planes along the three orthogonal axes  $x$ ,  $y$ , and  $z$ . I used stiffness tensors from literature for the most prominent subduction related minerals and rocks. I rotated them to a common coordinate system so that  $C_{11} \geq C_{22} \geq C_{33}$  (Tab. 4.3). In terms of elasticity, the hexagonal symmetry of a layered (backus-averaged) medium is a special case of the orthogonal symmetry. The seismic velocities are isotropic in the plane of the layering or foliation. They are lowest along the normal of that plane, the symmetry axis, which I therefore defined as the  $z$ -axis. Seismic velocities then vary solely in dependence on the propagation angle  $\Xi$ , which I measured relative to the layering down from the  $z$ -axis. In orthorhombic media, I observe the highest and the lowest  $V_P/V_S$ -values in the  $x$ - $z$  symmetry-plane, so that I measure  $\Xi_{xz}$  in that plane. The seismic velocities in this plane

compute as (Auld, 1973):

$$V_{qP} = \sqrt{\frac{A+B}{2\rho}} \quad (4.22)$$

$$V_{qSV} = \sqrt{\frac{A-B}{2\rho}} \quad (4.23)$$

$$V_{SH} = \sqrt{\frac{C_{66} \sin^2 \Xi_{xz} + C_{44} \cos^2 \Xi_{xz}}{\rho}}, \quad (4.24)$$

where:

$$A = C_{11} \sin^2 \Xi_{xz} + C_{33} \cos^2 \Xi_{xz} + C_{55} \quad (4.25)$$

$$B = \sqrt{(C_{55} + C_{11} \sin^2 \Xi_{xz} + C_{33} \cos^2 \Xi_{xz})^2 - 4C} \quad (4.26)$$

and:

$$C = (C_{11} \sin^2 \Xi_{xz} + C_{55} \cos^2 \Xi_{xz})(C_{55} \sin^2 \Xi_{xz} + C_{33} \cos^2 \Xi_{xz}) - (C_{13} + C_{55})^2 \sin^2 \Xi_{xz} \cos^2 \Xi_{xz}. \quad (4.27)$$

$C_{ij}$  are the components of the stiffness tensor. In the symmetry plane, the SH-wave is a pure shear-wave, the qSV-wave a quasi shear-wave, and the qP-wave a quasi P-wave.

### 4.3.3 Crystallographic anisotropy

The olivine crystal has an orthorhombic symmetry. The antigorite crystal has a monoclinic symmetry. However, in the antigorite crystal, the crystallographic  $c$ -axis is tilted with respect to the  $a$ - $b$ -plane by only  $\sim 1^\circ$  (Bezacier et al., 2010). I therefore also treated it as orthorhombic (in fact it could even be treated as hexagonal, because the elastic properties in the  $x$ - $y$ -plane are almost isotropic, Tab. 4.3). The rock that contains predominantly olivine is a peridotite. The rock that contains predominantly antigorite is a serpentinite.

Elastic stiffness tensors (Tab. 4.3) have been measured for olivine, antigorite, and serpentinite using optical methods that make use of the frequency shift of a laser pulse that is scattered in an acoustically excited crystal lattice (Abramson et al., 1997; Bezacier et al., 2010). The stiffness tensors of peridotites have been computed from LPO measurements of a broad range of natural peridotites (Ismail and Mainprice, 1998). I used these values to compute seismic wave speeds as a function of  $\Xi_{xz}$ . The results are shown in Figure 4.6.

Monocrystalline olivine shows qP-wave velocities at ambient conditions that vary from 7.7 km/s normal to the lineation to 9.9 km/s parallel to it. SH-wave velocities range from 4.2 to 4.9 km/s and qSV-wave velocities from 4.9 to 5.2 km/s, where the highest S-wave velocity is the one of an qSV-wave that travels diagonally ( $\Xi_{xz} \sim 40^\circ$ ) to the lineation. For peridotites it has been recognized that the intensity of the LPO does not correlate with the geodynamic setting from which they originate (Ismail and Mainprice, 1998).

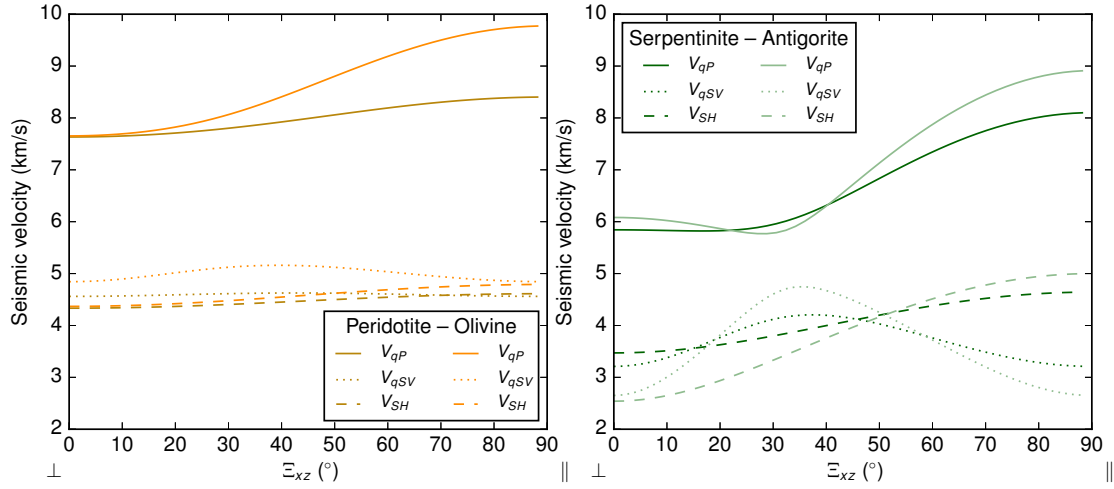


**Figure 4.6:** Anisotropic seismic velocities for serpentinite and its main constituent mineral antigorite (left) as well as for peridotite and its main constituent mineral olivine (right), in  $x$ - $z$ -plane. Velocities are computed from values in Abramson et al. (1997), Bezacier et al. (2010), and Ismail and Mainprice (1998).

This results in rather similar stiffness tensors for a broad range of foliated peridotites. I chose the averaged elastic constants as tabled for 1000° C and 0.3 GPa by Ismail and Mainprice (1998) to compute the anisotropic seismic velocities of peridotites. Their seismic anisotropy is much weaker compared to the monocrystalline olivine crystal. qP-wave velocities vary only between 7.7 and 8.4 km/s, S-wave velocities between 4.3 and 4.6 km/s normal and parallel to the lineation (Fig. 4.6).

Antigorite shows a much stronger variation of seismic wave speeds as a function of propagation direction (Bezacier et al., 2010). The qP-wave velocity is about 6 km/s normal to the foliation, has a minimum of 5.9 km/s at a  $\Xi_{xz} \sim 30^\circ$ , and is as high as 9 km/s parallel to the foliation. SH- and qSV-wave velocities are similar and low normal to the foliation (2.5 km/s). Both waves travel at a maximum speed of 5 km/s: the qSV-wave at an angle of  $30^\circ$  to the foliation, and the SH-wave parallel to the foliation. The serpentinite rock I used for comparison has a very strongly foliated fabric and should be considered as an end-member rock with respect to anisotropy (Bezacier et al., 2010). Its anisotropy pattern is similar to that of pure antigorite but overall weaker. qP-wave velocities vary between 5.9 and 8.0 km/s and S-wave velocities between 3.1 and 4.5 km/s (Fig. 4.6).

I computed the  $V_P/V_S$ -ratio of the two natural mineral aggregates peridotite and serpentinite as a function of  $\Xi_{xz}$ . The results are shown in Figure 4.7. The peridotite shows no large anisotropy in terms of  $V_P/V_S$ . The fast S-wave is the qSV-wave and the  $V_{qP}/V_{qSV}$ -ratio varies between 1.7 and 1.8. In contrast to that, the serpentinite shows a very strong direction dependence of the  $V_P/V_S$ -ratio. The  $V_{qP}/V_{qSV}$ -ratio varies from 1.8 normal to the foliation, over 1.4 in a direction diagonal to the foliation ( $\Xi_{xz} \sim 30^\circ$ ), to a value as high as 2.5 parallel to the foliation. In most directions the SH-wave is the fast S-wave, so that the  $V_{qP}/V_{SH}$ -ratio is generally lower, near 1.7. Only in the range  $20^\circ < \Xi_{xz} < 40^\circ$  the qSV-wave is the fast S-wave.

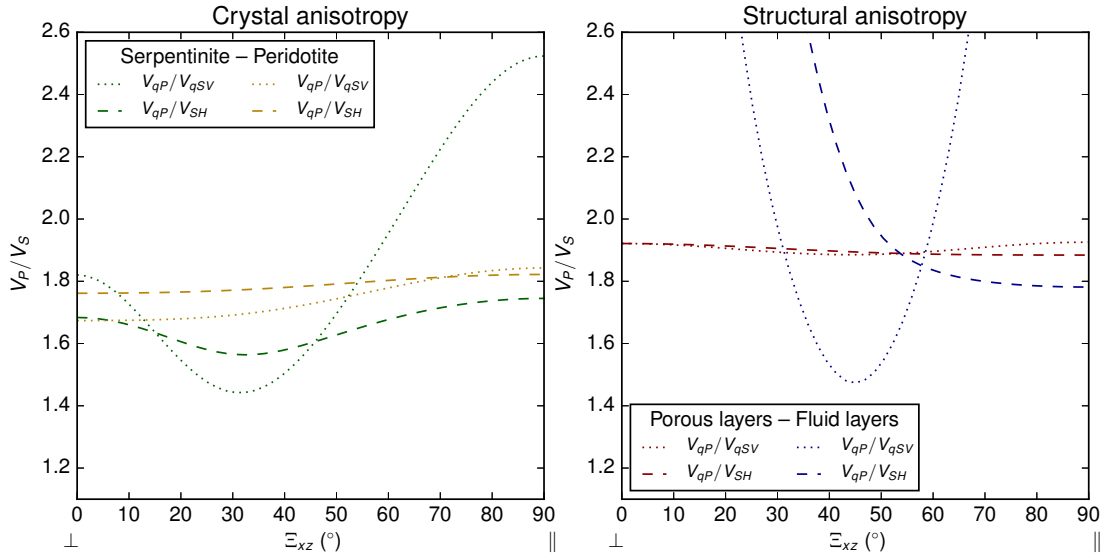


**Figure 4.7:** Anisotropic  $V_P/V_S$  ratios for strongly foliated serpentinite and peridotite rocks (in  $x$ - $z$ -plane, s.f. Fig. 4.6) and an isotropic serpentinite with intercalated layers of a fractured, fluid-filled serpentinite ( $\alpha/\phi = 100$ ) and pure fluid.

#### 4.3.4 Structural anisotropy

In order to investigate the possible influence of structural anisotropy on the  $V_P/V_S$ -ratio, I used Backus averaging (Backus, 1962) to compute the stiffness tensor of two layered composite rocks that can be regarded as end-members with respect to structural anisotropy (Tab. 4.3). They have elastic properties that are averages of the constituent's elastic properties:

- A serpentinite ( $K = 70$  GPa,  $\mu = 38$  GPa) containing 50 vol% layers of a porous, fluid-filled serpentinite ( $\Phi/\alpha = 100$ ,  $K = 70$  GPa,  $\mu = 25$  GPa) and
- A serpentinite containing 0.1 vol% layers that are a pure fluid phase ( $K = 12$  GPa,  $\mu = 0$  GPa).

The serpentinite with porous layers shows only weak anisotropy and a  $V_P/V_S$ -value of 1.9 that is intermediate between the one of the serpentinite (1.8) and the porous layers (2.0).

The serpentinite with the pure fluid-filled layers has an infinite  $V_P/V_S$ -ratio normal to the layering and an infinite  $V_{qP}/V_{qSV}$ -ratio parallel to the layering. The lowest  $V_P/V_S$ -ratio of 1.4 occurs at  $\Xi_{xz} = 45^\circ$ , and the  $V_P/V_S$ -ratio of the rock matrix can be seen parallel to the layering (Fig. 4.7).

#### 4.3.5 The $V_P/V_S$ -ratio of anisotropic mantle rocks

Anisotropy can cause both very high and very low  $V_P/V_S$ -values. Very high values above 2.0 may be expected for the  $V_{qP}/V_{qSV}$ -ratio of strongly foliated serpentinite rocks parallel to the foliation direction. It can also be expected normal or parallel to the

layering of rocks that contain fluid layers. Very low values near 1.4 can be expected in diagonal directions to the foliation  $30^\circ < \Xi_{xz} < 45^\circ$  for strongly foliated serpentinite rocks or for rocks containing fluid layers.

Under the prerequisite that a natural seismic source excites at least some energy in any direction, the typically observed S-wave is the S1-wave. The S2-wave vanishes in the S1-wave coda. The typical signature of anisotropic rocks in terms of  $V_P/V_S$ -ratios is then a low to very low value. Low  $V_P/V_S$ -values translate to also low  $\nu$ -values. This means that upon axial compression an anisotropic medium would react with little or no lateral extension, a circumstance that is intuitively plausible for layered media.

## 4.4 Conclusion

A number of mineral dehydration reactions may occur within the subducting slab in the crust as well as in the mantle. These reactions are associated with a densification of the rock matrix and the release of fluid. Fluid-filled pore-space is created.

The pore-space can only be detected by means of a measurement of the  $V_P/V_S$ -ratio of the rock, if the pore-space satisfies the geometric condition  $\Phi/\alpha \gtrsim 100$ , where  $\Phi$  is porosity (in %) and  $\alpha$  is the pore aspect ratio. This means that crack-like pores influence the  $V_P/V_S$ -ratio much stronger than round pores. Simultaneously, crack-like pores only remain open as long as a near-lithostatic fluid pressure is maintained. This means that a high  $V_P/V_S$ -ratio can be interpreted as proxy for elevated pore pressure, if pores are crack-like.

The presence of anisotropy typically lowers the measured  $V_P/V_S$ -ratio. This is the case because anisotropy causes two S-waves to emerge, a fast and a slow one. As the slow S-wave often vanishes in the coda of the fast S-wave, the anisotropic  $V_P/V_S$ -ratio is the  $V_P/V_{S1}$ -ratio, which is low.



## Chapter 5

# Estimation of the $V_P/V_S$ -ratio using arrival time differences of closely spaced seismic events

The  $V_P/V_S$ -ratio is a sensitive indicator for the presence of fluids or strongly anisotropic media (Chapter 4). The identification of  $V_P/V_S$ -anomalies is therefore a useful tool to test whether mineral dehydration reactions occur along the subduction pathway.

In this chapter I apply a method to estimate the  $V_P/V_S$ -ratio directly from the arrival times of closely spaced seismic events. I relate different regions within the subducting slab to the mineral phase diagrams. This allows me to discuss, where regions of abnormally high or low  $V_P/V_S$ -ratio are likely to indicate the presence of fluid-filled pore space or anisotropy.

### 5.1 Seismic tomography studies of other subduction zones

To estimate the  $V_P/V_S$ -ratio for a rock volume within the earth, methods of seismic tomography are popular. Such methods compute the travel times of seismic waves through a rock volume that is located in between a set of seismic sources and a set of seismic receivers, and invert for the velocity structure. The resolution and accuracy of such methods is typically best, where the rock volume is well surrounded by seismic sources and receivers. The inversion process may be ill-posed at the rims of the volume such that the solution may become biased by the starting model or damping parameters (e.g. Thurber (1993)).

The seismic velocity structure in terms of P- and S-wave velocities have been determined for various segments of the Japan trench, beneath the islands of Honshu (Zhang et al., 2004; Shelly et al., 2006; Tsuji et al., 2008) and Hokkaido (Nakajima et al., 2009), for the Central Andean subduction zone (Dorbath et al., 2008; Comte et al., 2016), all using the *tomoDD* algorithm (Zhang and Thurber, 2003, 2006), and for the North Island (Reyners et al., 2006) and northern South Island (Eberhart-Phillips and Bannister, 2010) of New Zealand using the *SimulPS* algorithm (Evans et al., 1994).

Beneath New Zealand, the subducting slab did not reveal any internal structure, but

could only be imaged as a whole at depth between 25 and 250 km. It exhibits intermediate  $V_P/V_S$ -ratios between 1.70 and 1.75, which the authors interpret as indicative for a forsterite–enstatite– $H_2O$ -system being present there (Reyners et al., 2006; Eberhart-Phillips and Bannister, 2010). The shallow portion of the lower band of seismicity between 30 and 60 km depth seems to exhibit slightly elevated  $V_P/V_S$ -ratios of  $\sim 1.85$  (Eberhart-Phillips and Bannister, 2010), but the authors do not comment on this.

Beneath Japan, the tomographic images reveal some internal structure of the slab. The oceanic crust shows  $V_P/V_S$ -ratios ranging from 1.80 updip to 1.65 downdip, which is consistent with the prevalence of blueschist at shallower depth and eclogite at greater depth ( $> 80$  km). The oceanic mantle subdivides into two distinct bands. The uppermost mantle between the oceanic Moho and the lower band of seismicity shows a  $V_P/V_S$ -ratio as high as 1.85, which the authors explain as a result of the presence of a serpentinized chlorite dunite there. Below that, around the lower band of seismicity, the  $V_P/V_S$ -ratio is as low as 1.6, which the authors explain to originate from the presence of a peridotite that contains fluid in spheroidal pores (Zhang et al., 2004; Shelly et al., 2006; Tsuji et al., 2008; Nakajima et al., 2009). This, according to the theoretical considerations of Takei (2002), implies that the fluid would have a bulk modulus  $\sim 25$  times lower than the rock matrix.

Beneath Northern Chile, the subducting slab is divided in a similar manner. In the upper plane, Dorbath et al. (2008) find rather low  $V_P/V_S$ -values near 1.67, which they attribute to the presence of a fluid-filled blueschist at shallower depth and a fluid-filled eclogite at greater depth. In between both seismic planes they find high  $V_P/V_S$ -ratios near 1.8, which they attribute to a slightly hydrated harzburgite. In the LSZ they find very low  $V_P/V_S$ -values of 1.57, which they cannot explain.

In the Central Andes Comte et al. (2016) measure an intermediate  $V_P/V_S$ -ratio of 1.76 in the subducting slab at intermediate depth and a slightly increased value of  $\sim 1.8$  in the overlying mantle wedge. They interpret this structure as the dehydrating slab mantle and crust in the bottom and a pathway of ascending melt above.

In the southern Andes, Moreno et al. (2014) find a large spread in  $V_P/V_S$ -ratios in the shallow part of the plate interface between 1.7 and 2.0. They interpret the high values as representing zones of fluid over-pressure.

Local tomography studies of the continental forearc crust report intermediate  $V_P/V_S$ -values of 1.73 (Schurr et al., 2006), between 1.69 and 1.79 (Heit, 2006), and of 1.76 (Koulakov et al., 2006).

Considering the results from all subduction zones, quite a good agreement between travel time calculations and petrological models seems to exist for the upper plane of seismicity. For the lower band of seismicity, in contrast, the results are not in a very good accordance. This disagreement might partly be attributed to the low resolution of tomographic methods at the boundary of the model, where the lower band of seismicity is located.

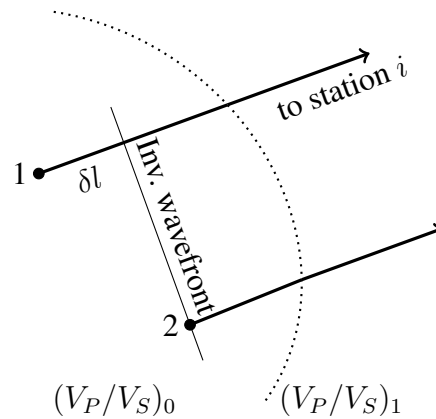


**Figure 5.1:** Drawing that illustrates the idealized near source ray geometry assumed by Lin and Shearer (2007).

## 5.2 Method

The  $V_P/V_S$ -ratio has been estimated using differential P- and S- wave arrival times following Lin and Shearer (2007) in continental fault gauges (Lin and Shearer, 2009) and volcanic edifices (Dawson et al., 2015; Lin et al., 2015). The advantage of this method is that it has its greatest sensitivity in the volume near the source, while tomographic methods have their greatest sensitivity along the ray path between the source and the receiver. It is therefore especially suited to estimate the  $V_P/V_S$ -ratio in the direct vicinity of a set of seismic events.

### 5.2.1 Assumptions and theory

The original idea was published by Lin and Shearer (2007) and later critically evaluated by Palo et al. (2016).

#### 5.2.1.1 Original problem statement

Lin and Shearer (2007) consider a pair of closely spaced seismic events 1 and 2 (Fig. 5.1). They state that under the assumptions that:

- (i) the ray paths of event 1 and 2 are similar, differing only by  $\delta l$ ,
- (ii) the seismic velocities are locally constant, and
- (iii) the P- and S-ray paths coincide,

a local seismic body wave velocity  $V$  can be calculated from the difference of travel times  $T^i$  to station  $i$ , using the origin time  $t_0$  and the arrival time  $t$  of both events, as:

$$\frac{\delta l^{(i)}}{V_{\text{local}}} = T_2^{(i)} - T_1^{(i)} \quad (5.1)$$

$$= (t_{0_2} + t_2^{(i)}) - (t_{0_1} + t_1^{(i)}) \quad (5.2)$$

$$= (t_{0_2} - t_{0_1}) + (t_2^{(i)} - t_1^{(i)}) \quad (5.3)$$

$$= \delta t_0 + \delta t^{(i)}. \quad (5.4)$$

From assumption (iii) follows that:

$$\frac{V_P}{V_S} = \frac{\delta t_0 + \delta t_s^{(i)}}{\delta t_0 + \delta t_p^{(i)}} \quad (5.5)$$

which can be rewritten in slope–intercept-form as:

$$\delta t_s^{(i)} = \left( \frac{V_P}{V_S} \right) \delta t_p^{(i)} + \delta t_0 \left( 1 - \frac{V_P}{V_S} \right). \quad (5.6)$$

This equation is also valid for the mean of the differential arrival times at more than one station:

$$\langle \delta t_s \rangle = \left( \frac{V_P}{V_S} \right) \langle \delta t_p \rangle + \delta t_0 \left( 1 - \frac{V_P}{V_S} \right). \quad (5.7)$$

The braces  $\langle \rangle$  denote the average over all stations. Subtraction of Eq. 5.6 from Eq. 5.7 gives:

$$\delta t_s^{(i)} - \langle \delta t_s \rangle = \left( \frac{V_P}{V_S} \right) (\delta t_p^{(i)} - \langle \delta t_p \rangle). \quad (5.8)$$

This equation states that the in-situ P- to S-wave velocity ratio can be computed as the slope of the de-meant differential P- against S- wave arrival times of a pair of closely spaced seismic events. For a brief notation I write generally for two arbitrary events  $k$  and  $l$ :

$$\hat{\delta} t_p^{(ikl)} = \delta t_p^{(ikl)} - \langle \delta t_p^{(kl)} \rangle = \delta t_p^{(ikl)} - \frac{1}{J} \sum_{j=1}^J \delta t_p^{(jkl)} \quad (5.9)$$

$$\hat{\delta} t_s^{(ikl)} = \delta t_s^{(ikl)} - \langle \delta t_s^{(kl)} \rangle = \delta t_s^{(ikl)} - \frac{1}{J} \sum_{j=1}^J \delta t_s^{(jkl)}, \quad (5.10)$$

where the station in question is  $i$  and the other stations that contribute to the mean of the arrival time differences are  $j$ .

The advantage of Equation (5.8) is that it states that the near-source  $V_P/V_S$ -ratio can be computed only from arrival times of seismic events: It is independent of any localization procedure.

### 5.2.1.2 Revision of assumptions

The disadvantage of Eq. (5.8) is that it is based on assumptions that are impossible to be completely fulfilled, or that trade-off against each other.

The conditions are not independent of each other, but some are preconditions of others and some are even mutually exclusive. For assumption (i) to be fulfilled, Lin and Shearer (2007) state that the inter-event distance  $d$  should be small 'compared to the source-receiver distance'. This is not generally true, as even at very small distances  $d$ , (i) can easily be violated in the case where both events occur on two sides of a strong velocity contrast, that is where assumption (ii) is violated. On the contrary, in the case of a constant  $V_P/V_S$ -ratio,  $d$  can be arbitrary. The source-receiver distance is indeed of no importance. Instead,  $d$  should be smaller than the minimal lateral velocity anomaly, so that it is assured that both rays pass through the same anomalies on their ray path to the station. Assumption (i) can then be argued to be true, if there is evidence for a rather homogeneous overburden. Consequently, assumption (ii) becomes of greater importance. Still it would be favorable to use the smallest possible inter-event distance. However, the smaller the inter-event distance, the smaller the arrival time difference (because  $\lim_{d \rightarrow 0} \delta T = 0$ ), and the more accurate the arrival time measurement needs to be. In this manner, a small  $d$  can only be realized, if the accuracy of the measurement is sufficient.

Assumption (ii) is therefore the necessary condition that needs to be fulfilled for the method to deliver any useful result at all, because the linear relationship of Equation (5.8) would not withstand significantly different ray paths for both events. In this manner, the linearity of the  $\hat{\delta t}_p$  vs.  $\hat{\delta t}_s$  distribution is an indicator of whether (ii) is the case within the accuracy of the measurement. I introduced an independent test, where I estimated the linearity of the  $\hat{\delta t}_p$  vs.  $\hat{\delta t}_s$  observations as the ratio of the eigenvalues of the covariance matrix  $C$  of the distribution:

$$\epsilon = \frac{\max(\text{eig } C)}{\min(\text{eig } C)}, \quad (5.11)$$

where

$$C = \begin{pmatrix} \sum (\hat{\delta t}_p)^2 & \sum \hat{\delta t}_p \hat{\delta t}_s \\ \sum \hat{\delta t}_p \hat{\delta t}_s & \sum (\hat{\delta t}_s)^2 \end{pmatrix}. \quad (5.12)$$

A high  $\epsilon$  represents an elongated distribution, whereas a low  $\epsilon$  represents a more isometric one.

If (ii) holds true for a volume that is occupied by more than two events, all of them can be combined to achieve a more robust fit and the problem of assuring (ii) turns into the problem of combining events so that they deliver a robust fit. Therefore, for the case of a microseismic event cloud, the events 1 and 2 have not to be assumed to be within a volume of constant seismic velocities, but more generally the combination of events  $k$  and  $l$  needs to be found, for which Equation (5.8) results in a robust fit.

Assumption (iii) is generally not fulfilled in the case of a non-constant  $V_P/V_S$ -ratio in the subsurface, which means that the factor of proportionality in Equation (5.8) is not necessarily the near-source  $V_P/V_S$ -ratio. I therefore relabeled it more generally to  $\gamma$  and

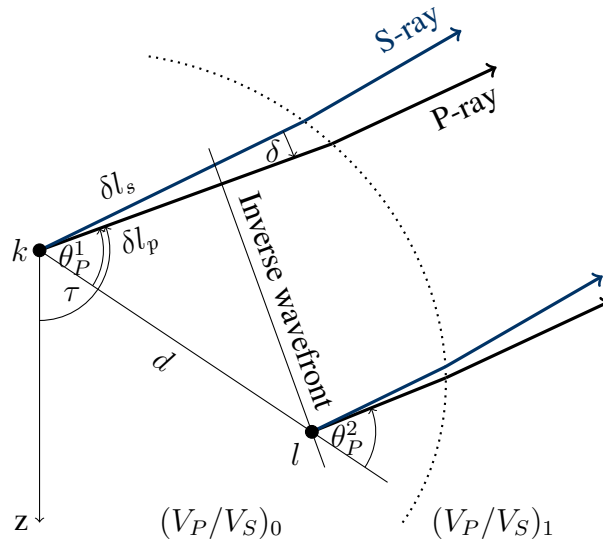


**Figure 5.2:** Illustration of a more realistic near source ray geometry than depicted in Figure 5.1.

reformulated Equation (5.8) to:

$$\hat{\delta}t_s^{(ikl)} = \gamma \cdot \hat{\delta}t_p^{(ikl)}, \quad (5.13)$$

where  $\gamma$  is a biased estimator of the near-source  $V_P/V_S$ -ratio. In the next section, I show how the  $\gamma$ -slope and the  $V_P/V_S$ -ratio are related in dependence of the true subsurface  $V_P/V_S$ -structure.

### 5.2.1.3 Relation between the $\gamma$ -slope and the $V_P/V_S$ -ratio

In the case of a constant  $V_P/V_S$ -ratio in the subsurface,  $\gamma = V_P/V_S$ . Else, the path of the first arriving P- or S-wave is strongly dependent on the velocity structure in the subsurface. Palo et al. (2016) found that when a  $V_P/V_S$ -gradient is present, the  $\gamma$ -value will be a biased estimator of the  $V_P/V_S$ -ratio, because either the P- or the S-ray will take a 'shortcut' and arrive earlier than it would be expected in the case of a constant subsurface  $V_P/V_S$ -ratio. A near-source ray geometry that takes this *shortcut effect* into account is depicted in Figure 5.2. With the vertical take-off angle of the P-ray  $\tau$  and the differential take-off angle between the P- and the S-ray  $\delta$  (Fig. 5.2) Palo et al. (2016) derive for a constant  $V_P/V_S$ -gradient:

$$\gamma = \frac{V_P}{V_S} \underbrace{\left( \frac{\cos \delta \sin \tau - \sin \delta \cos \tau}{\sin \tau} \right)}_{\beta}, \quad (5.14)$$

where  $\delta > 0^\circ$  for a decreasing  $V_P/V_S$ -ratio with depth,  $\delta < 0^\circ$  for an increasing  $V_P/V_S$ -ratio with depth,  $0^\circ \leq \tau < 90^\circ$  for downgoing rays, and  $90^\circ < \tau \leq 180^\circ$  for upward going rays.  $\beta$  is the bias (s.f. Fig. 5.3). For upward going rays, as it is the typical case for local seismic networks, and increasing  $V_P/V_S$  with depth, the ray-path for the

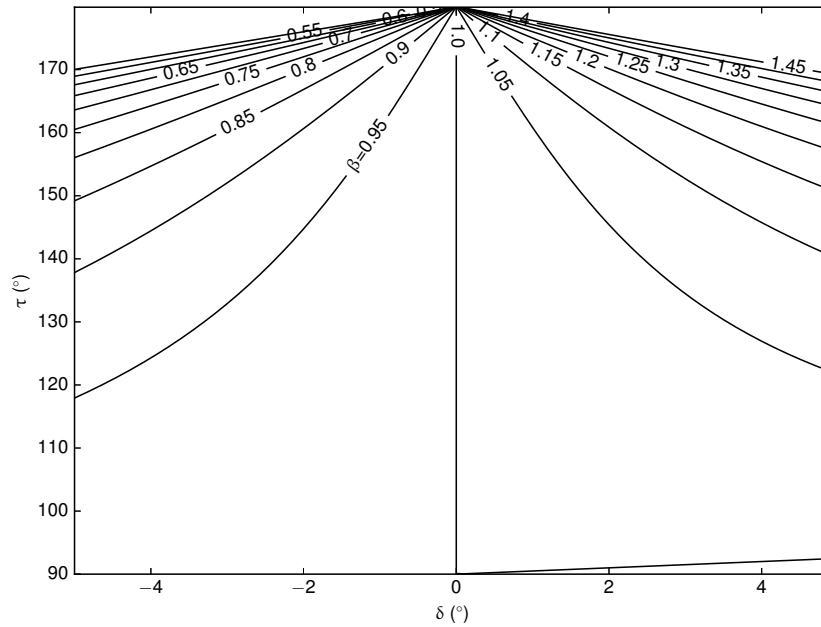


**Figure 5.3:** Visualization of the right-hand side of Eq. (5.14).

S wave is shorter ( $\delta < 0$ ) and  $\gamma$  will underestimate the local  $V_P/V_S$ -ratio ( $\beta < 1$ ). For decreasing  $V_P/V_S$  with depth, the P-ray will take the shortcut and  $\gamma$  will overestimate the local  $V_P/V_S$ -ratio ( $\beta > 1$ ).

Even though the magnitude of  $\beta$  has been derived analytically only for linear velocity gradients, Snell's law suggests that the sign of  $\delta$  can be determined from only the absolute difference between the local velocities at the source and at the receiver. Velocity variations along the ray path cannot influence the sign of  $\delta$ . In order for the *shortcut effect* to flip the sign of an anomaly at depth, ray path differences would have to be unrealistically large. For example, for a low anomaly of a  $V_P/V_S = 1.5$  structure at depth, to produce an erroneous high anomaly of  $\gamma = 2.0$ , an unrealistically high  $\beta = 2.0/1.5 = 1.3$  would be necessary (s.f. Fig. 5.3). Therefore, in practice, a high (low) anomaly in  $\gamma$  always represents an even higher (lower) anomaly in near-source  $V_P/V_S$ -ratio. The shortcut effect becomes less pronounced in the case of a favorably shaped anomaly (e.g. spherical), for low frequencies, as well as for weak anomalies.

To investigate the shortcut effect for complex anomaly geometries, I compute synthetic arrival times for a given source-receiver geometry in arbitrary  $V_P$  and  $V_S$  models using the *NonLinLoc* subroutines *Grid2Time* and *Time2EQ* (Lomax et al., 2000), which make use of the finite difference ray tracing algorithm of Podvin and Lecomte (1991).

I constructed a number of  $V_P$ - and  $V_S$ -anomalies around the source volume of a set of seismic events that are plausible to exist in the lower band of seismicity.  $V_P$  and  $V_S$  in the models were inferred from results of petrophysical modeling as to represent realistic lithologies of the subsurface (Appendix D). The results are summarized in Table 5.1. It turns out that the  $\gamma$ -values always underestimate the magnitude of a high- $V_P/V_S$ -anomaly in the subsurface. The shortcut effect is strongest for more planar anomalies.

**Table 5.1:** Summary of synthetic recovery tests.

Geometry	$V_P$ (km/s)	$V_S$ (km/s)	$V_P/V_S$ given	$\gamma$ recovered	$\gamma - V_P/V_S$	Fig.
Homogenous subsurface	7.80	4.53	1.72	1.72	0	D.1
Serpentinized mantle	7.00	3.90	1.79	1.73	-0.06	D.2
Fluid-filled layer	6.65	3.10	2.15	1.74	-0.41	D.3
Very high $V_P/V_S$ layer	7.49	3.08	2.43	1.75	-0.68	D.4
Serpentinized mantle beneath a very high $V_P/V_S$ layer	7.00	3.90	1.79	1.78	-0.01	D.5
Fluid-filled bend-faults	6.65	3.10	2.15	—	—	D.6
Fluid-filled sphere around seismicity cluster	6.65	3.10	2.15	2.17	0.02	D.7
Fluid-filled cylinders at tip of serpentinized bend faults	6.65	3.10	2.15	1.92	-0.23	D.8

For spherical anomalies the biasing effect may not be very large. Near-source heterogeneities in the  $V_P/V_S$ -ratio tend to disturb the linearity of the  $\hat{\delta}t_p$  vs.  $\hat{\delta}t_s$  distribution.

#### 5.2.1.4 Inversion scheme

In the case of noisy data, errors and outliers in arrival time measurements need to be considered when inverting for  $\gamma$ . If the error of the arrival time measurement  $\sigma_t$  is known, I compute the error in de-meaned differential arrival time (Eqs. (5.9) and (5.10)) using error propagation as:

$$\sigma_{\hat{\delta}t}^{(ikl)} = \sigma_t^{(ik)} + \sigma_t^{(il)} + \frac{1}{J} \sum_{j=1}^J \left( \sigma_t^{(jk)} + \sigma_t^{(jl)} \right). \quad (5.15)$$

I compute the slope of the linear regression  $\gamma$  in Eq. (5.13) by minimizing the weighted least square  $\chi^2$  misfit function, accounting for errors in both coordinates (Press et al., 2007):

$$\chi^2 = \sum_{m=1}^M \frac{(\hat{\delta}t_s^{(m)} - \gamma \cdot \hat{\delta}t_p^{(m)})^2}{\sigma_{\hat{\delta}t_s^{(m)}}^2 + \gamma^2 \sigma_{\hat{\delta}t_p^{(m)}}^2}. \quad (5.16)$$

The index ( $m$ ) denotes is the unique index to any observation.

The standard deviation of  $\gamma$  is found by sampling the  $\chi^2$  misfit function and finding the difference in  $\gamma$  for which  $\Delta\chi^2 = 1$  (Press et al., 2007). This difference is the standard deviation and will be reported in the form  $\gamma \pm \sigma_\gamma$ . The goodness-of-fit can be evaluated using the corresponding  $p$ -value, which is the value of the cumulative distribution function at the minimum  $\chi^2$  from Eq. (5.16).



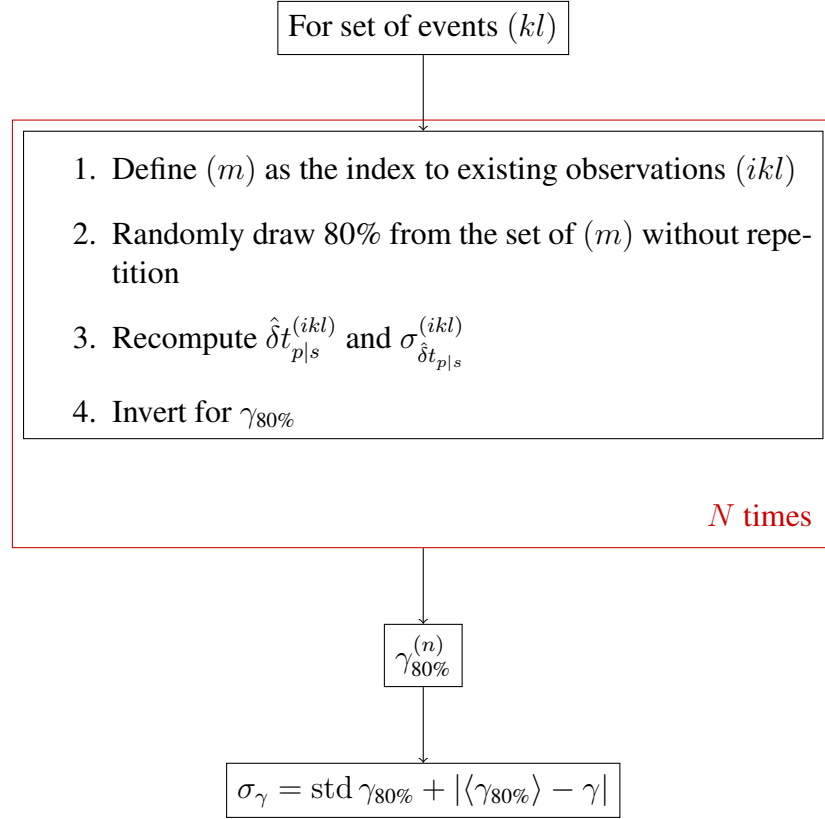


**Figure 5.4:** Flowchart that illustrates how the confidence interval  $\sigma_\gamma$  has been determined.

In the case where  $\sigma_t$  cannot be estimated correctly, I approximate it as the absolute arrival time residual  $r$  after the localization procedure and the application of source specific station terms (see Sec. 2.3):

$$\sigma_{t_p}^{(ik)} \approx r_p^{(ik)} \quad (5.17)$$

$$\sigma_{t_s}^{(ik)} \approx r_s^{(ik)}. \quad (5.18)$$

The  $\sigma_{\hat{\delta}t}$ -terms then provide only a relative weight of the data points. The absolute value of  $\chi^2$  becomes meaningless and instead of a standard deviation only a confidence interval can be computed.

I computed the confidence interval of  $\gamma$  as the result from a jackknife test where randomly 80% of the  $\delta t^{(m)}$  observations are drawn,  $\hat{\delta}t^{(m)}$  is recomputed and the fit is re-performed  $N$  times (see Fig. 5.4). I chose to sample 80% of the observations in order to be able to compute a confidence interval also for a scientifically interesting cluster in the lower band of seismicity. The cluster has too few observations to use the bootstrapping technique, which would require to sample 67% of the observations. The confidence interval  $\sigma_\gamma$  is computed as:

$$\sigma_\gamma = \text{std } \gamma_{80\%} + |\langle \gamma_{80\%} \rangle - \gamma|. \quad (5.19)$$

The braces  $\langle \rangle$  denote here the average over all test results and the term *std* the standard deviation of the distribution.

## 5.2.2 Application to the microseismic event cloud in the Central Andes

Lin and Shearer (2009) and Dawson et al. (2015) implicitly assume that within the small earthquake clusters which they investigate, the  $V_P/V_S$ -ratio is constant and may be computed according to Equation (5.8). Their clusters occupy volumes of a few kilometers in diameter.

Within a microseismic event cloud, no such especially dense clusters exist that would be a 'natural' way of grouping events. Instead, the spatial distribution of seismicity is dense everywhere and occupies a large volume. The constancy of the  $V_P/V_S$ -value in the vicinity of an arbitrary set of events needed to be tested. The strategy that I followed to identify volumes of a constant  $V_P/V_S$ -ratio (or rather a constant  $\gamma$ -value as a proxy for a constant  $V_P/V_S$ -ratio) is described in Section 5.2.2.1 and shown in Figure 5.5.

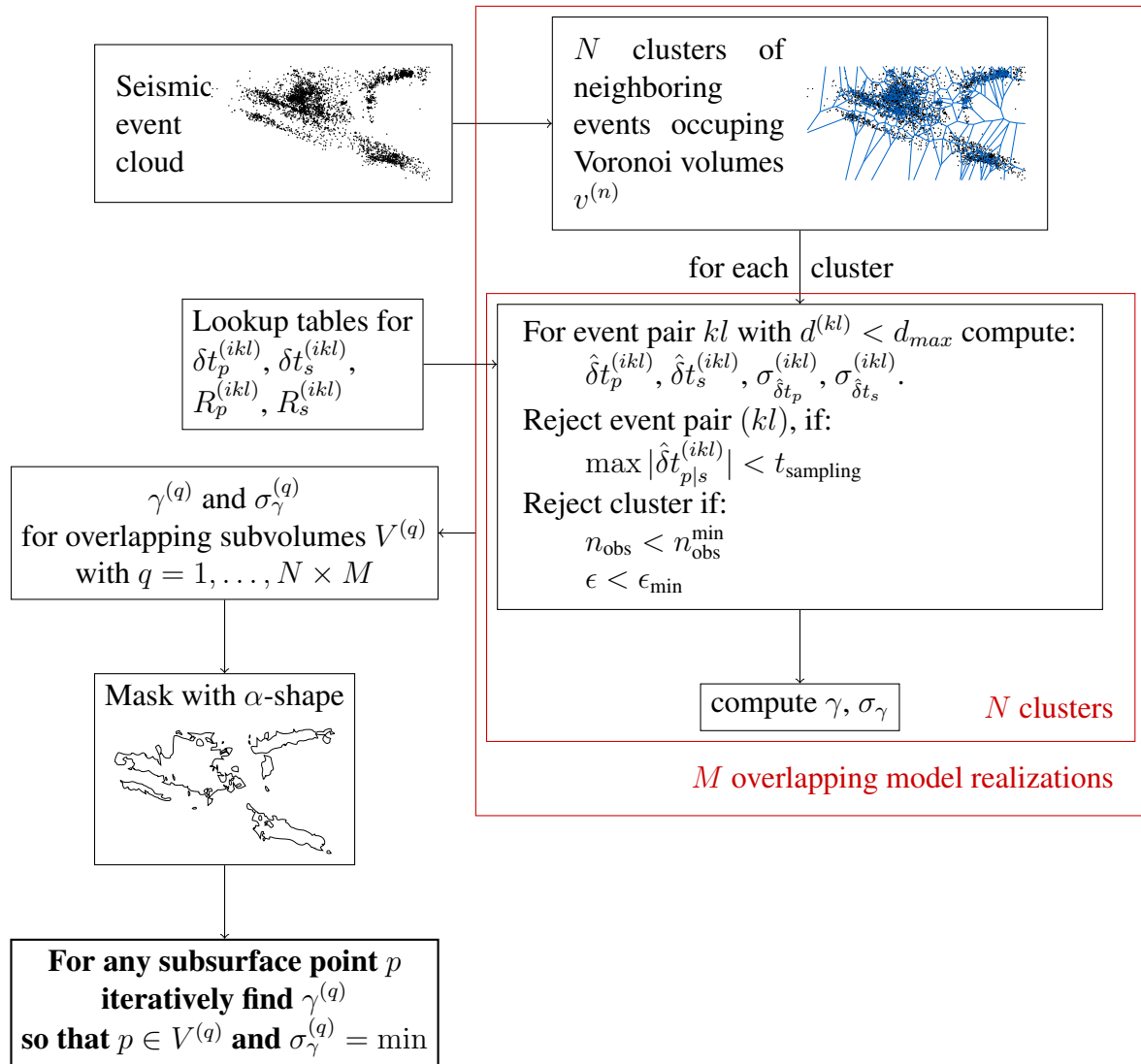
To remove outliers before any further processing, an arrival time observation of event  $k$  on station  $i$  was only considered, if the arrival time residual  $r^{(ik)}$  was smaller than the threshold value  $r_{\max}$  (Tab. 5.2).

### 5.2.2.1 Search for constant $\gamma$

I randomly selected  $N$  earthquake locations as seeds. I chose  $N = 100$ , so that on average  $\sim 50$  events made up one cluster. All nearest neighbors of a seed were grouped within a cluster, which occupied the Voronoi volume  $v$  (the volume that is closest to the seed location). For each cluster, an event pair  $(kl)$  was only considered, if  $d^{(kl)}$  was smaller than the threshold value  $d_{\max}$ . This is the size of the smallest lateral  $V_P/V_S$ -anomaly I expected on the ray path (Sec. 5.2.1.2). The event pair has also only been considered, if the largest absolute  $\hat{\delta}t$  was larger than the sampling interval. This is the upper limit of accuracy of the arrival time measurement I expected. The entire cluster was rejected if after these exclusions the  $\hat{\delta}t_p$  vs.  $\hat{\delta}t_s$  distribution consisted of too few observations ( $n_{\text{obs}} < n_{\text{obs}}^{\min}$ ) or did not exhibit a linear shape ( $\epsilon < \epsilon_{\min}$ ). If all quality control tests were passed, I assumed that the  $V_P/V_S$ -ratio is constant within the Voronoi volume and computed  $\gamma$  and  $\sigma_\gamma$  for this cluster. All threshold values are listed in Table 5.2. They have been chosen so that the inversion delivers physically reasonable results for the entire seismic event cloud.

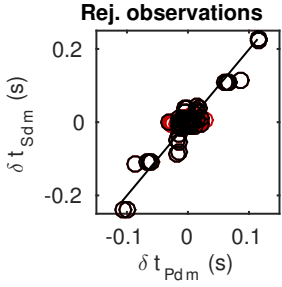
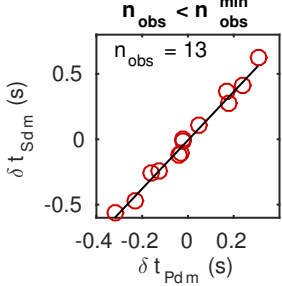
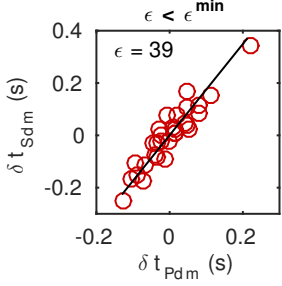
This procedure was applied to all  $N$  clusters in  $M$  model realizations. The results were stored as sets of  $q = 1, \dots, N \times M$  seed locations with associated  $\gamma^{(q)}$  and  $\sigma_\gamma^{(q)}$ . Note, that the Voronoi volume associated with each seed is uniquely defined by the location of all seeds within one model realization.

To represent the most confident distribution of  $\gamma$ , I found for each subsurface point the one  $\gamma$ -value among all  $M$  models that had the lowest  $\sigma_\gamma$ . To do so, I initialized grids with  $\gamma = \text{'not-a-number'}$  and  $\sigma_\gamma = \infty$  at every node. I successively projected the  $\gamma$ - and  $\sigma_\gamma$ -values to the grid nodes that were inside their associated Voronoi volume. The



**Figure 5.5:** Flowchart that illustrates how the best fitting distribution of  $\gamma$  has been determined. The precomputed values  $\delta t$  and  $R$  are defined in Equations (5.20) and (5.21).

**Table 5.2:** Parameters used for quality control for determining the spatial distribution of  $\gamma$ .

Parameter	Value	Description	Example of rejected data
$r_{\max}$	0.05 s	Maximum absolute arrival time residual. Outliers should not be considered.	
$d_{\max}$	5 km	Maximum inter-event-distance. Events must be close.	
$t_{\text{sampling}}$	0.01 s	Sampling interval. Scattering of $\hat{\delta}t_p^{(i)}$ and $\hat{\delta}t_s^{(i)}$ values must be significant.	
$n_{\text{obs}}^{\min}$	25	Minimum number of observations. There must be sufficient data.	
$\epsilon_{\min}$	50	Minimum eigenvalue ratio of $\hat{\delta}t_p^{(i)}$ vs. $\hat{\delta}t_s^{(i)}$ pairs. Pointcloud must be elongated.	

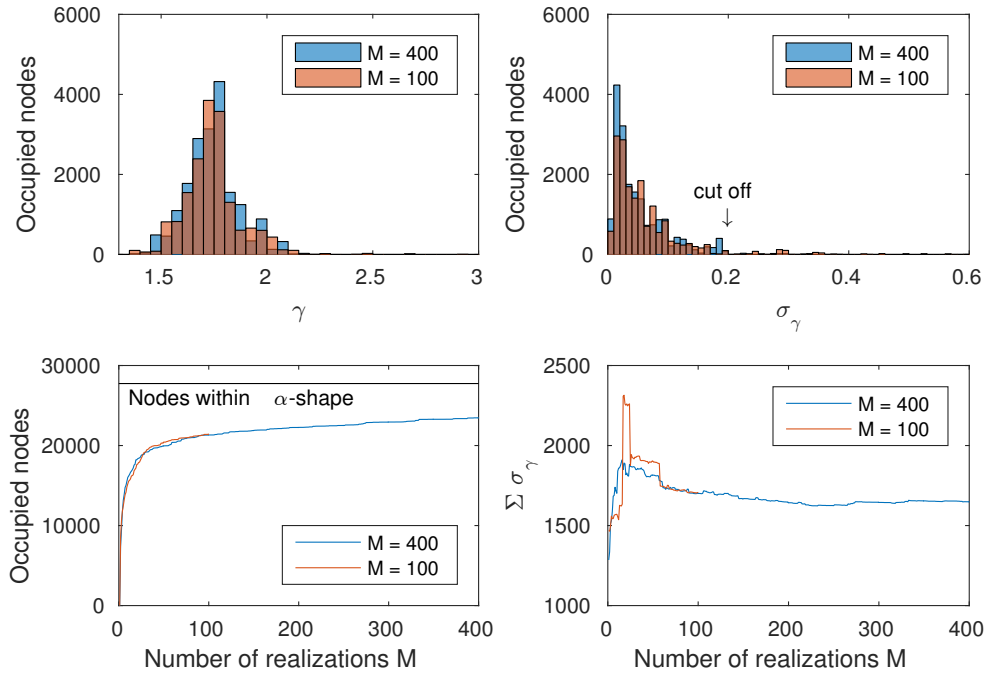


**Figure 5.6:** Convergence of the 3D-distribution of  $\gamma$  towards physically sensible values on a regular grid after comparison of 100 and 400 model realizations (s.f. Fig. 5.5). Top left: Number of grid nodes occupied with different values of  $\gamma$ . The distribution is in a physically sensible range for  $V_P/V_S$ -ratios. Top right: Number of grid nodes occupied with different confidence-interval-values. Low confidence intervals become overrepresented after more iterations. No significant number of confidence-interval-values above 0.2 occur. Bottom left: The number of occupied nodes increased monotonously. Bottom right: The cumulative confidence interval converged towards an intermediate value. Both sets of model realizations were initialized with a different random number seed.

nodes of both grids (the  $\gamma$ -grid and the  $\sigma_\gamma$ -grid) were updated, if the newly projected  $\sigma_\gamma$  was lower than the  $\sigma_\gamma$  that has been previously stored to the grid.

I limited the  $\gamma$ -grid and the  $\sigma_\gamma$ -grid to the volume that was defined by the  $\alpha$ -shape of the microseismic event cloud with  $\alpha = d_{\max}$ . The  $\alpha$ -shape is the hull around a point cloud that cannot be accessed by a sphere with a diameter larger than  $\alpha$ . It qualitatively limits the resolution of the method to the vicinity of the seismic event cloud.

Figure 5.6 shows how this iterative procedure converges towards low  $\sigma_\gamma$ -values and physically plausible  $\gamma$ -values. After  $\sim 80$  iterations, the cumulative confidence interval ( $\sum \sigma_\gamma$ ) did not fluctuate strongly anymore. The number of nodes with assigned a values slowly approached a constant value. Not all nodes inside the  $\alpha$ -shape got a value assigned, because for some volumes seismicity was too sparse or phase readings were too bad to pass all the quality control criteria (s.f. Fig. 5.5 and Tab. 5.2).

### 5.2.2.2 Lookup tables

The repeated inversion for  $\gamma$  required the repeated combination of event pairs. To facilitate this computation, I precomputed  $\delta t_{p|s}^{(ikl)}$  observations, from which  $(ikl)$  tuples could be selected and  $\hat{\delta t}_{p|s}^{(ikl)}$  could be recomputed in order to invert for  $\gamma$  following:

$$\underbrace{\delta t_s^{(ikl)}}_{t_s^{(ik)} - t_s^{(il)}} - \langle \underbrace{\delta t_s^{(kl)}}_{t_s^{(k)} - t_s^{(l)}} \rangle = \gamma \left( \underbrace{\delta t_p^{(ikl)}}_{t_p^{(ik)} - t_p^{(il)}} - \langle \underbrace{\delta t_p^{(kl)}}_{t_p^{(k)} - t_p^{(l)}} \rangle \right). \quad (5.20)$$

The storage of the arrival time differences  $t^{(ik)} - t^{(il)}$  in lookup tables facilitated the search for constant  $\gamma$ .

In the arrival time catalog, only nominal errors have been assigned to the arrival time picks. Therefore,  $\sigma_t$  was not known and only confidence intervals could be computed. I also stored combinations of arrival time residuals  $r$  (Eqs. (5.17) and (5.18)) as pairwise  $R^{(ikl)}$  for each station  $i$  in lookup tables. The measurement error was computed as:

$$\sigma_{\hat{\delta t}}^{(ikl)} = \underbrace{R^{(ikl)}}_{r^{(ik)} + r^{(il)}} + \langle \underbrace{R^{(kl)}}_{r^{(k)} + r^{(l)}} \rangle. \quad (5.21)$$

### 5.2.3 Verification of results using event repicking

For a small subset of events in the lower band of seismicity I manually re-picked P- and S-wave arrival times and estimated absolute timing errors individually. In this case, I applied only the  $d_{\max}$ -criterion before the inversion, but none of the others (s.f. Tab. 5.2). I computed  $\sigma_\gamma^{\chi^2}$  and the  $p$ -value from  $\chi^2$  from Eq. (5.16).

## 5.3 Regional distribution of $\gamma$

The distribution of  $\gamma$ -values in the Central Andean forearc around 21° S that yielded the best  $\sigma_\gamma$ -values is shown in Figure 5.7, the corresponding distribution of  $\sigma_\gamma$ -values in Figure 5.9. The  $\gamma$ -value could be determined in five geodynamic units:

1. In the entire upper, middle, and lower crust of the continental forearc beneath the Coastal Cordillera between 70.2 and 69.7° W.
2. In the upper continental crust and in two mid-crustal seismicity clusters, beneath the Precordillera between 69.2 and 68.7° W.
3. In the subducting oceanic crust, between 70.5 and 69.7° W
4. In the subducting oceanic mantle at a shallow level, trench-ward, between 70.5 and 70.3° W.
5. In the subducting oceanic mantle at a deeper level, arc-ward, between 69.2 and 68.8° W.

I present the results for the different seismicity domains and discuss them in detail in the following.

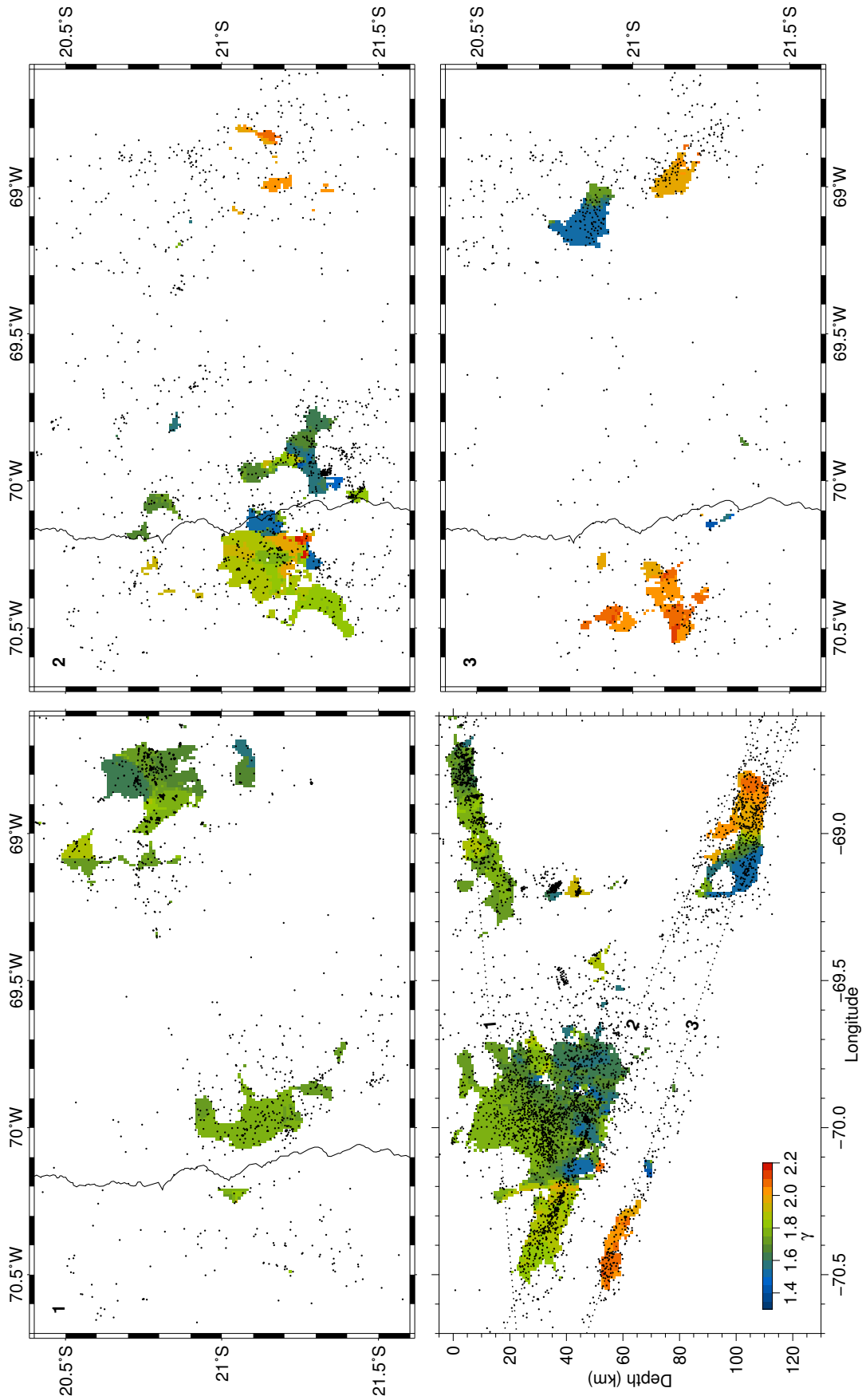


**Figure 5.7:** Three dimensional distribution of  $\gamma$  in the volume under consideration. Bottom left: profile of averaged values. Top left, top right and bottom right: Slices along lines 1, 2, and 3 marked in the profile, respectively. Seismicity is shown in a band 5 km above and below the slice.

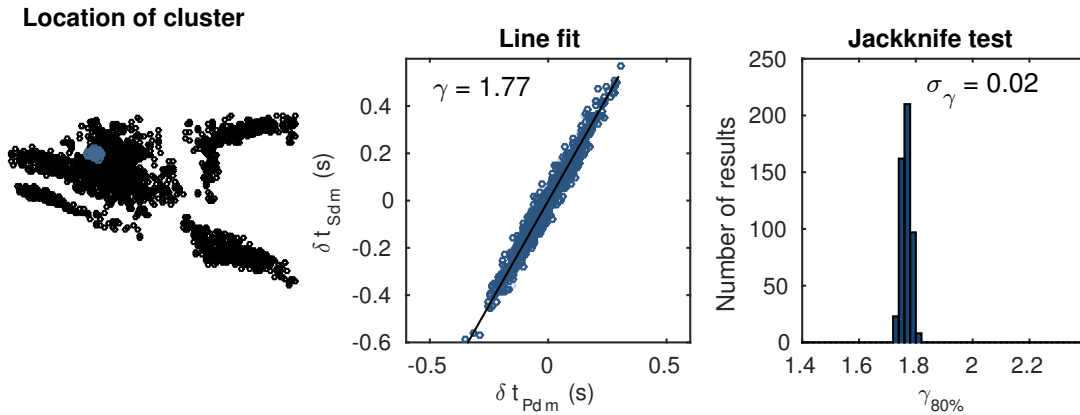


**Figure 5.8:** Estimates for  $\gamma$  and  $\sigma_\gamma$  in the continental crust at 26 km depth. Left: Location of the cluster. Center: The  $\hat{\delta}t_p$  vs.  $\hat{\delta}t_s$  distribution for that cluster and line fit. Right: Distribution of  $\gamma_{80\%}$  from the jackknife test.

### 5.3.1 Coastal Cordilleran crust

In the continental crust below the Coastal Cordillera (Figs. 5.7 and 5.9, profile and slice 1) confidence intervals are typically better than 0.02.  $\gamma$  takes values ranging between 1.7 and 1.8 in the western and shallower part (Fig. 5.8). I interpret the  $\gamma$ -values in accordance with Kern and Schenk (1988) as accurately representing the  $V_P/V_S$ -ratio of volcanic, rather mafic, upper and middle crustal rocks (Tab. 4.2). In the more eastern and deeper part,  $\gamma$ -values are low between 1.6 and 1.7. More felsic compositions, as suggested by the data of Kern and Schenk (1988), seem unrealistic in this deeper crustal level, because felsic rocks occur as a consequence of magmatic differentiation in upper crustal levels. In contrast, the influence of a weakly anisotropic, horizontally layered fabric can exhibit  $V_P/V_S$ -values that are below intermediate ( $\sim 1.7$ ) and that manifest themselves in such rather low  $\gamma$ -measurements.

In the most eastern part, between 30 and 45 km depth, confidence intervals are typically poor (0.15 to 0.20) and  $\gamma$ -values low. It is possible that this part does not represent the lowermost continental crust, but the tip of the continental mantle wedge. It has been argued that continental mantle wedges in subduction zones are serpentinized and show an anisotropic fabric (e.g. Bezacier et al. (2010)). In accordance with this scenario, the low  $\gamma$ -values would represent the  $V_P/V_{S1}$ -ratio of an anisotropic fabric of a sub-horizontally layered serpentinized peridotite, sampled by mostly upward traveling seismic rays.

### 5.3.2 Precordilleran crust

In the continental crust below the Precordillera (Fig. 5.7 and 5.9, profile and slice 1), in the upper crustal level,  $\gamma$  takes intermediate to above-intermediate values between 1.70 and 1.85. Confidence intervals vary widely from below 0.05 to above 0.2. The lower values agree with  $V_P/V_S$ -ratios of rather felsic, igneous or metamorphic upper crustal rocks as found by Kern and Schenk (1988) (Tab. 4.2). The higher values are consistently



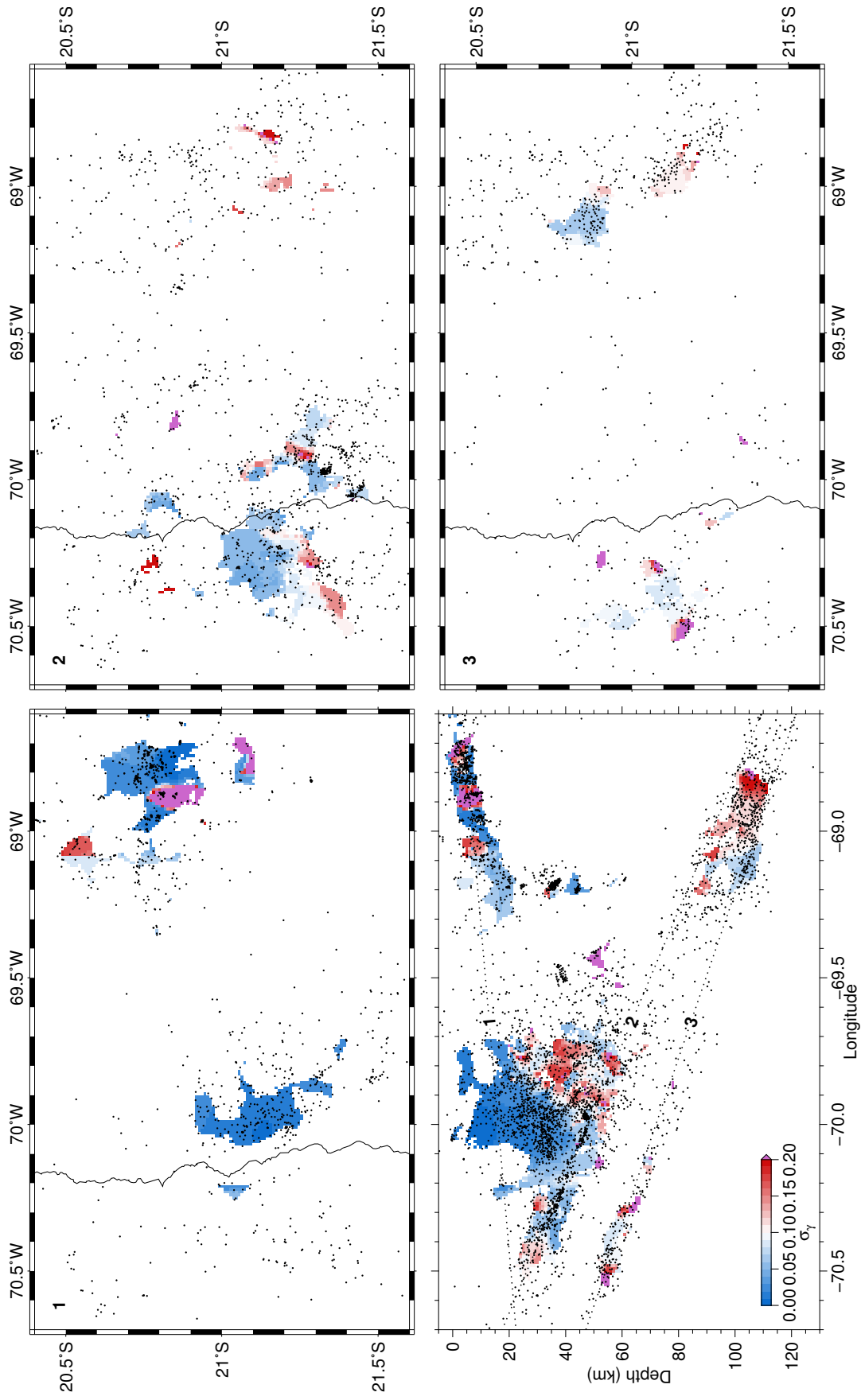


**Figure 5.9:** Three dimensional distribution of  $\sigma_\gamma$  in the volume under consideration. Panels as in Figure 5.7.

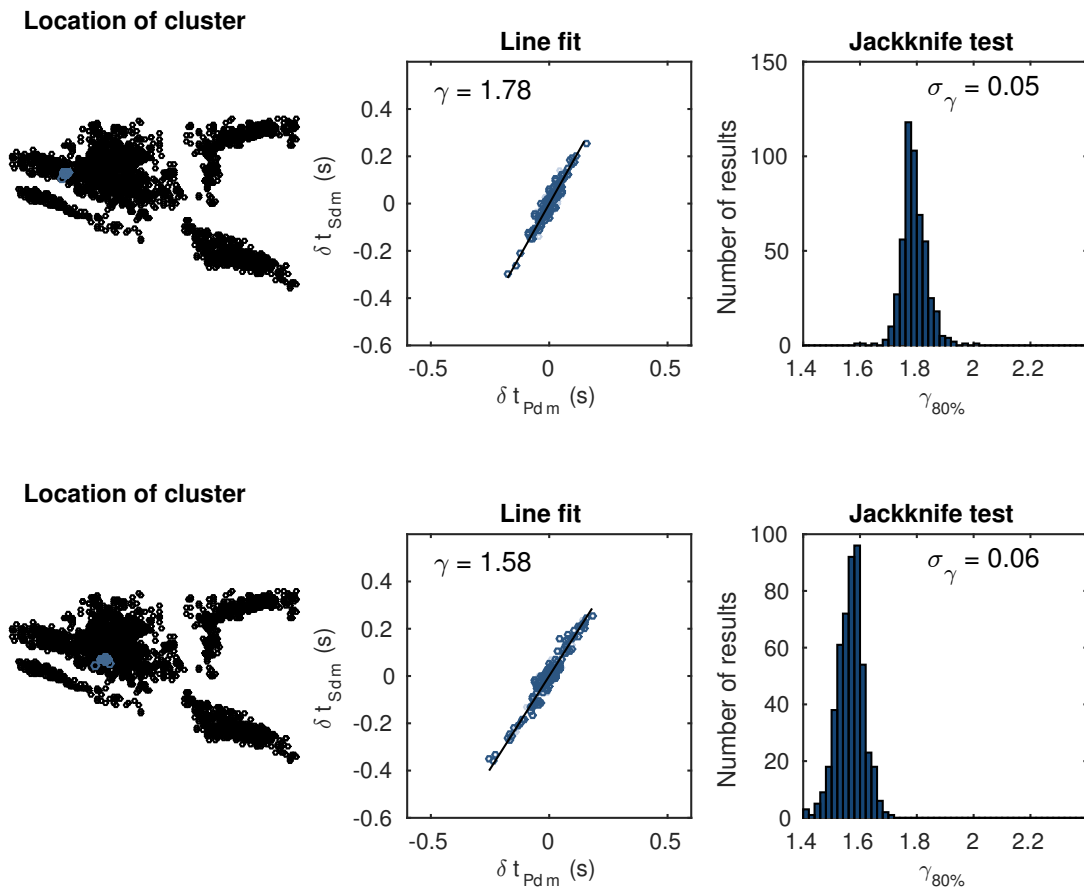


**Figure 5.10:** Two estimates for  $\gamma$  in the oceanic crust. Top: at 38 km depth. Bottom: at 48 km depth. Subfigures as in Figure 5.8.

associated with larger confidence intervals so that I interpret them as overestimates, representing the same lithology. Else, if they accurately represent rather high  $V_P/V_S$ -values of  $\sim 1.85$ , they would have to be interpreted as igneous or metamorphic rocks of mafic composition.

In a lower crustal level, two seismicity clusters, one above the other, show  $\gamma$ -values of 1.5 (the upper one) and 1.9 (the lower one), both within good confidence intervals. From an earlier interpretation that these clusters occur due to migrating fluids which meet a strong lateral stress contrast at the brittle-ductile boundary (Bloch et al., 2014), it becomes clear that both migrating fluids and structural anisotropy may influence the  $V_P/V_S$ -ratio in the direct vicinity of the clusters and that the  $V_P/V_S$ -ratio does not have to be constant over time. Both, the high and low  $\gamma$ -values are in accordance with this scenario and I do not interpret them further.

### 5.3.3 Upper band of seismicity

In the oceanic crust of the subducting slab (Fig. 5.7 and 5.9, profile and slice 2)  $\gamma$  is typically high offshore (1.75 to 2.10 west of 70.2° W, Fig. 5.10, top) and low onshore (1.40 to 1.65 east of 70.2° W, Fig. 5.10, bottom). Confidence intervals are good, except for extreme  $\gamma$ -values of 1.4 and 2.2 offshore, which I therefore do not interpret.

$\gamma$ -values just above 1.75 are in agreement with results from thermodynamic modeling, which predict a lawsonite blueschist at the pressure-temperature conditions in this area, having the same  $V_P/V_S$ -value (Fig. 4.1). Locally higher  $\gamma$ -values are plausible to be the consequence of fluid-filled pore-space (Fig. 4.4, top left) that may be present at this part of the subduction system. Fluids may be expelled at this depth in small amounts (<1 wt%) from the commencing breakdown of chlorite and lawsonite (Eq. (4.8)) or they may originate from a deeper fluid source and migrate upward. The upper limit of pore volume generation during metamorphic mineral breakdown is given by the densification of the rock matrix due to the complete breakdown of chlorite as 0.6 vol%.

The low  $\gamma$ -values a little deeper and further east (Fig. 5.10, bottom) are too low to be explained by the solid metamorphic lithologies that may be expected at this depth. Anisotropy is a tempting explanation for low  $\gamma$ -values, but, except for chlorite, which does not exist in major amounts in the oceanic crust, none of the minerals shows a pronounced seismic anisotropy. The only phase that could contribute to a relatively slow P-wave velocity in certain directions is a free and isolated fluid phase that would have to be present in a layered fabric and have low  $K$ - and vanishing  $\mu$ -values. Such a structure would be one that is laminated at  $\Xi \sim 40 - 50^\circ$  to the predominant ray path direction (Fig. 4.7, right-hand side).

### 5.3.4 Lower band of seismicity

In the oceanic mantle of the subducting slab within the lower band of seismicity at a relatively shallow depth of  $\sim 55$  km (Figs. 5.7 and 5.9, profile and slice 3, Fig. 5.11),  $\gamma$ -values are elevated, in the range of 2.0 to 2.1. The confidence intervals are good in the central part of the cluster ( $\sim 0.05$ ), where seismic event density is relatively high, and worse in the other parts ( $> 0.1$ ).

The entire suite of dry, isotropic rocks that may occur in an oceanic mantle has  $V_P/V_S$ -values that are significantly lower than this  $\gamma$ -value (Fig. 4.2). Even anisotropic, strongly foliated peridotites do not exhibit  $V_P/V_S$ -values as large as the observed one in any direction (Fig. 4.7). I therefore rule out the existence of an either isotropic or anhydrous lithology there.

A strongly foliated serpentinite, on the contrary, does show  $V_P/V_{S2}$ -values higher than the observed  $\gamma$  in the direction parallel to the foliation of the mineral, where the S2-wave is polarized normal to it ( $V_P/V_{SH}$  in Fig. 4.7, left-hand side).  $\gamma$  would then underestimate the near-source  $V_P/V_S$ -ratio. However, this velocity ratio can only be detected, if no shear energy is radiated parallel to the cleavage. This is little plausible, given that the focal mechanisms of these earthquakes scatter broadly, i.e. radiate seismic energy polarized in any direction (see Sec. 3.3.2).

Finally, a fractured or porous, fluid-filled serpentinite can have a  $V_P/V_S$ -ratio equal to

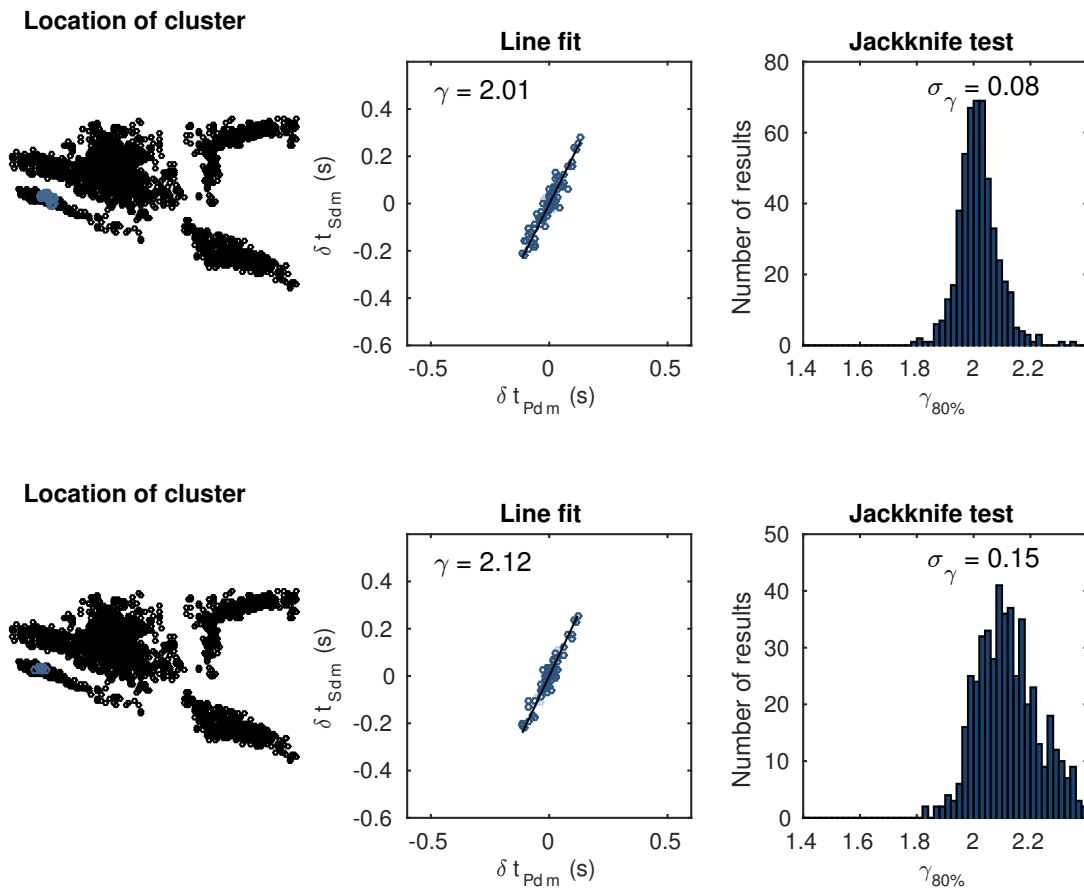


**Figure 5.11:** Two good estimates for  $\gamma$  in the LSZ at 57 km depth. The clusters are partly overlapping. Subfigures as in Figure 5.8.

or higher than the observed  $\gamma$  (Fig. 4.4). At this depth, temperatures are in the order of 300° to 500° C, so that the most plausible dehydration reaction is the breakdown of antigorite in the presence of brucite (Fig.4.2, Eq. (4.11)). It generates a maximum of 7% of porosity.

In order to discuss the possible relative contributions of anisotropy and fluids, I examine the data of this cluster in more detail in Section 5.4.

### 5.3.5 Deeper intermediate depth

In the oceanic mantle of the subducting slab at greater depth between 100 and 110 km,  $\gamma$  could be determined for two clusters (Figs. 5.7 and 5.9, profile and slice 3, Fig. 5.12). The southern cluster shows a high  $\gamma$ -value of 2.0 with a fair confidence interval of 0.1. The northern cluster shows a very low  $\gamma$ -value of 1.52 and a good confidence interval of 0.08.

The high  $\gamma$ -value can be explained by a fractured and fluid-filled medium, as in the shallow oceanic mantle. The most probable dehydration reaction would be the final

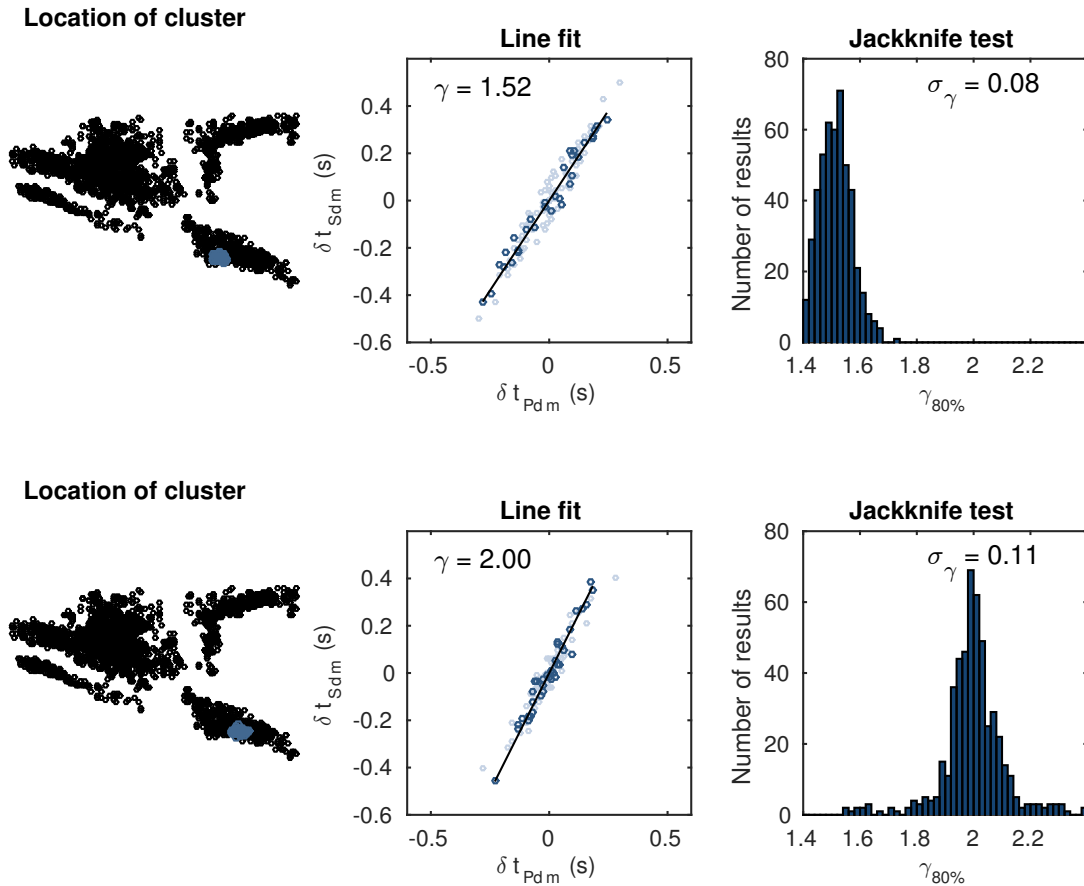


**Figure 5.12:** The two estimates for  $\gamma$  in the oceanic mantle at 105 km depth. Light dots indicate observations that were rejected because arrival times were recorded on no more than two stations. Subfigures as in Figure 5.8.

breakdown of antigorite near 640° C (Eq. (4.12)). If the events did instead occur in the oceanic crust, the dehydration reaction would be the breakdown of amphibole and lawsonite (Eq. (4.10)).

The low  $\gamma$ -value can represent a strongly foliated anisotropic serpentinite that is sampled by seismic rays at an angle of  $\Xi = 20 \dots 40^\circ$  to the foliation (Fig. 4.7, left-hand side). This is plausible, because the foliation may be slab parallel and the subduction geometry implies this angle between the slab and the predominantly upward traveling seismic rays. A free fluid phase that is present in strongly anisotropic layers would yield a comparable-value for the  $V_P/V_S$ -ratio (Fig. 4.7, right-hand side).

## 5.4 Validation of $V_P/V_S$ in the shallow oceanic mantle

I determined a rather high value of  $\gamma = 2.0 \dots 2.1$  in the shallow oceanic mantle by the application of the estimation of  $V_P/V_S$  using arrival time differences of closely spaced seismic events. To verify this observation, I identified all events that contributed to any

$\gamma$  observation with confidence intervals better than 0.1 in this geodynamic unit and carefully re-pick the arrival times of the seismic phases. I manually assigned an arrival time error to each pick. I used not only the AF-network, but also on the neighboring stations of the IPOC-network. To test the robustness of the result, I recomputed  $\gamma$ -values, as well as the statistical parameters  $\sigma_\gamma^2$ , the  $p$ -value,  $\epsilon$  and  $n$  (number of events). I did so for different subsets of events and different subsets of seismic stations. I investigated the effect of the take-off angle distribution and quantified the shortcut effect for different anomaly geometries.

### 5.4.1 Result for the whole cluster

In total, 34 seismic events contributed to good fits in the shallow oceanic mantle (Fig. 5.13). They were recorded on the AF-network, the core network, and at some proximate stations of the IPOC-network, the backbone network. The arrival times of seismic phases were picked on common receiver gathers for all events in order to exploit similarities between waveforms of different events at one receiver.

The stations AF08 of the AF network and PB02 of the IPOC network had to be excluded from the processing, even though they belong to the core network with respect to their location. For some events they showed a weaker precursor phase 'R' before an obvious S-wave arrival (Fig. 5.14). As  $\gamma$ -estimates seemed to be biased by this phase, I excluded these station from the core network (s.f. Sec. 5.4.3).

The inversions for  $\gamma$  for different subsets of events by consideration of records on the core network yielded  $p = 0$  for the manually assigned data errors. This indicated that these errors were probably overestimates. In such a case, the corresponding model errors  $\sigma_\gamma^2$  would be overestimates as well. I therefore multiplied all data errors by a factor of  $1/1.65$ . I found this factor by trial and error in order to obtain plausible  $p$ -values in the range ( $0.001 < p < 0.05$ ) for  $\hat{\delta}t_p$  vs.  $\hat{\delta}t_s$  distributions that had an  $\epsilon > 30$ . By doing so, I obtained a statistically meaningful model error, but I lost the possibility to quantify the goodness of the fit using the  $p$ -value.

In this second independent measurement, the whole cluster has a  $\gamma$ -value of  $1.97 \pm 0.07$ , which is in fair agreement with the values between 2.0 and 2.1, which resulted from the bulk processing of the data from the entire seismic event cloud.

### 5.4.2 Results for subsets of events

I divided the cluster into five subsets with respect to the center of the cluster, respectively one subset north, east, west, and south of it, and one close to it. Northern and southern, as well as eastern and western subsets were mutually exclusive. The results are shown in Figure 5.15.

Linearities of the  $\hat{\delta}t_p$  vs.  $\hat{\delta}t_s$  distributions in terms of  $\epsilon$  are poorest for the northern and the eastern subset. They also have the fewest observations ( $n$ ), and the  $\gamma$ -values that are farthest away from, and lower than the one of the whole cluster. Compared to these observations, the  $\hat{\delta}t_p$  vs.  $\hat{\delta}t_s$  distributions of the southern and western subsets consist of more observations, have higher linearities, show smaller model errors, and exhibit a  $\gamma$ -value closer to the one of the whole cluster. The  $\hat{\delta}t_p$  vs.  $\hat{\delta}t_s$  distribution of the central

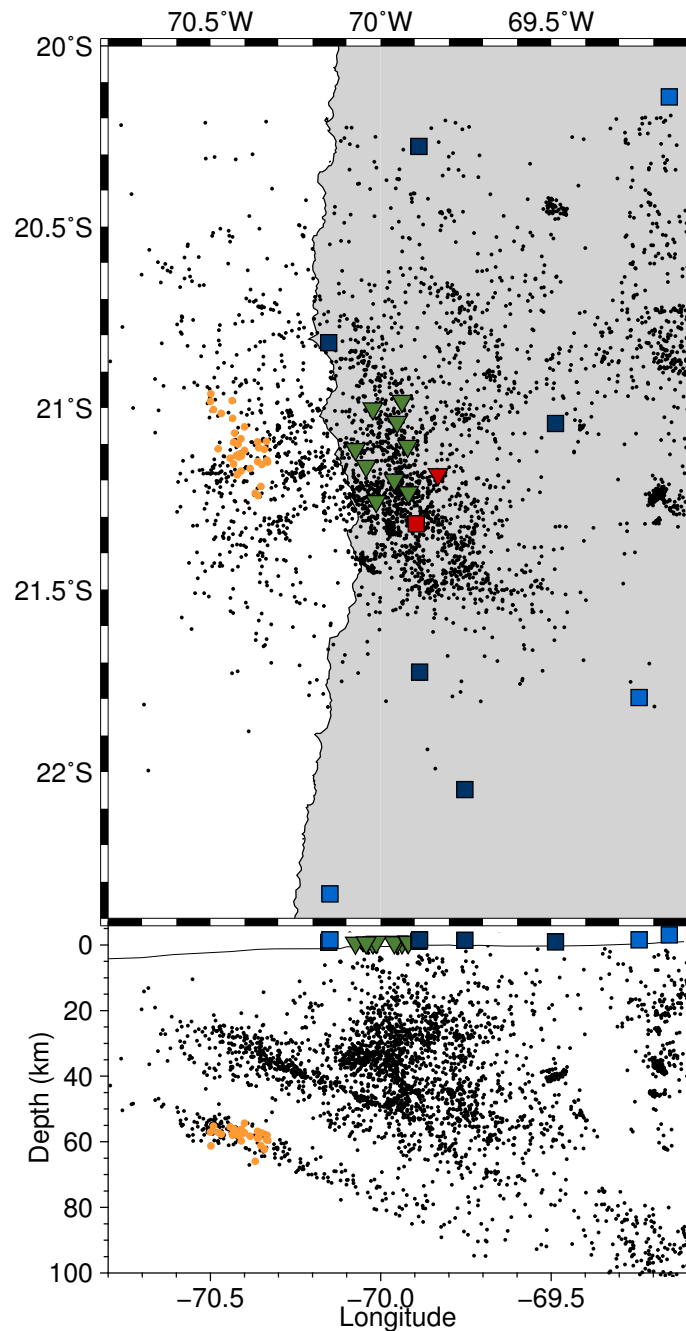


**Figure 5.13:** Distribution of seismic events and stations for detailed analysis of the  $V_P/V_S$ -ratio. Orange points: seismic events that contribute to the detailed analysis. Squares: IPOC-network. Triangles: AF-network. Green stations: core network that produced good results. Red stations: Stations close to the core network that impaired good results. Dark blue stations: Stations of the backbone network that registered almost all of the orange events. Light blue stations: Stations of the IPOC network that registered only few of the events.

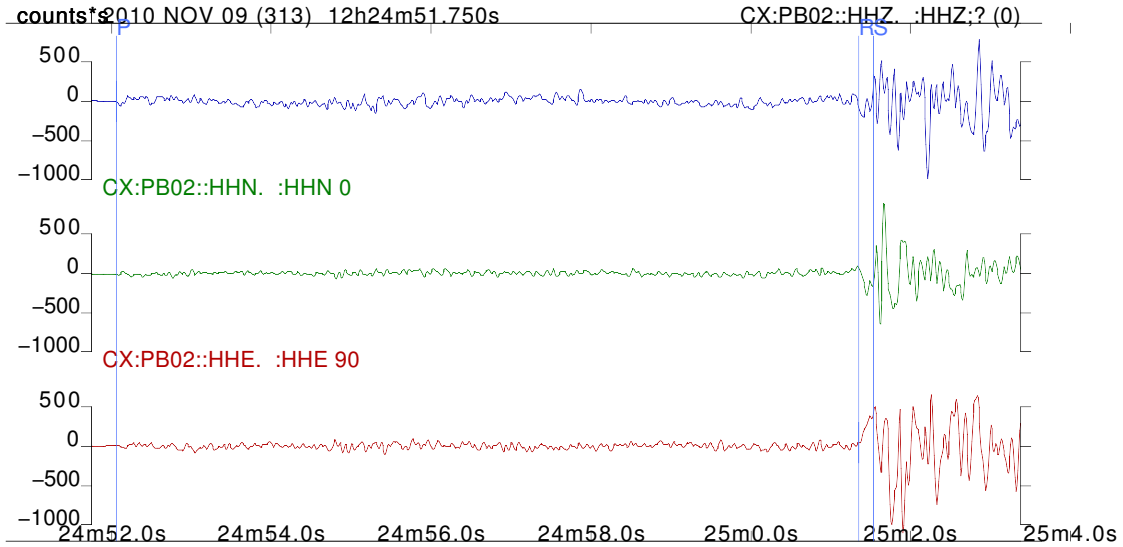


**Figure 5.14:** Seismogram of a seismic event from the shallow oceanic mantle recorded at station PB02. A precursor phase ('R') that arrives 0.15 s before the S-wave is visible.

subset of events has the best linearity, the best  $p$ -value among the subsets, and a model error as well as  $\gamma$ -value that is comparable to the whole cluster and to the western and southern subsets.

I suspect that the  $V_P/V_S$ -ratio is indeed significantly lower within the northeastern part of the cluster compared to the rest of it. However, as the northern and eastern subsets have poor statistical qualities and their  $\gamma$ -values differ substantially from each other, I do not interpret them. The measurement of the whole cluster most probably records an average of a broader spatial distribution of  $V_P/V_S$ -values. For my interpretation I therefore decide to focus on the central subset of events. It has a maximal diameter of  $\sim 9$  km and a maximal depth extend of  $\sim 5$  km. The convex hull of the events bounds a volume of  $\sim 90$  km<sup>3</sup>.

### 5.4.3 Station selection

To test the effect of the station distribution on the results, I performed the inversion for  $\gamma$  for three different station configurations using the whole cluster and the central subset of events. The results are shown in Figure 5.16.

I obtained the best results in terms of the  $\epsilon$ - and  $p$ -value when I considered only the core network. When I included either of the station PB02 or AF08, the  $p$ - and  $\epsilon$ -values worsen significantly, which is probably because of an S-wave precursor phase (Fig. 5.14) that occurred only for some events and was mistaken for an S-wave during picking.

Regarding the arrival time, it is possible that this phase is a near-source P- to S-converted phase, a near-receiver S- to P-converted phase, or a fast S-wave in an anisotropic medium. The phase has seemingly a lower frequency content than the later arriving S-wave train and could therefore also be a dispersive early low frequency arrival. A detailed polarization and frequency analysis can probably give hints on how to treat this phase correctly within the processing. Here, I decided to exclude the stations. The mistakenly picked



precursor 'R'-phases were automatically excluded during the bulk processing of the whole microseismic event cloud (Sec. 5.2.2), because they also produce a large arrival time residual during localization, so that  $r > r_{\max}$ .

For the core network with the additional 'ill' stations (see Fig. 5.16, middle), the  $p$ - and  $\epsilon$ -values become worse, indicating that the  $\hat{\delta}t_p$  vs.  $\hat{\delta}t_s$  distribution is not linear anymore. The  $\gamma$ -value is lower than the one for the core network only, indicating an absence of the 'R'-phase there.

When I included the entire IPOC-network in the processing (see Fig. 5.16, bottom),  $p$  remained high,  $\epsilon$  increased a little and the  $\gamma$ -value decreased further.

I conclude that the  $\hat{\delta}t_p$  vs.  $\hat{\delta}t_s$  distribution behaves well linearly for the core network, but scatters rather strongly for the spatially distributed backbone network. I suspect a physical reason for this behavior, because I could confirm the well behaved linear relationship on the core network with two independent measurements and trust the arrival time readings on the backbone network.

#### 5.4.4 Distribution of take-off angles

To pinpoint the near source characteristics of the observations with different source–receiver-configurations, I examined the P-wave take-off angles of the two configurations (see Fig. 5.17). On all stations, the result using all events compares well to the one using only the central subset but has a much larger number of observations ( $n$ ). I therefore used all events on all stations and compared the result to the one obtained for the central subset of the core network. The take-off angles cannot be measured directly, but are a result of the localization procedure and depend on the velocity model. I used the original P-wave velocity model which I have also used for the localization procedure.

The angular distribution of rays of all events recorded at all stations shows a rather broad range of azimuths of N30° . . . 150°S and dips between 30° . . . 70° from vertical. The azimuthal distribution of rays of the central event subset recorded at the core network is much narrower, with azimuths of N60° . . . 120°S. Dips are similar, 30° . . . 60°. The distribution of differential take-off angles ( $\Delta\theta = |\theta_1 - \theta_2|$ ) and the mean relative take-off angles ( $\theta = (\theta_1 + \theta_2)/2$ , s.f. Fig. 5.2) are also comparable. I expect the biasing effect to be mainly attributed to the ray azimuth.

The reason for the breakdown of the linearity of the  $\hat{\delta}t_p$  vs.  $\hat{\delta}t_s$  distribution when using data from a spatially extended network is not intuitively clear. Possible explanations are the presence of the ambiguous seismic 'R'-phase that occurs and vanishes in dependence of the ray azimuth. Furthermore, a complex distribution of seismic velocities in the subsurface can produce different shortcut effects (Sec. 5.2.1.3) for different ray paths.

Purely crystallographic anisotropy effects are little plausible to give rise to the azimuthal variation of  $\gamma$ , because the observed  $\gamma$ -value is highest and too high in the dip direction of the slab. The highest  $V_P/V_S$ -values in an anisotropic serpentinite fabric occur for propagation directions  $\pm 30^\circ$  parallel to the fabric and become lower perpendicular to it (Fig.4.7). This means that, for the observed effect to occur, a foliation (i.e. the petrographic  $x$ - $y$ -plane) would have to be oriented dip-parallel. This is little plausible, because serpentinite fabrics are observed to easily orient themselves parallel to any slip

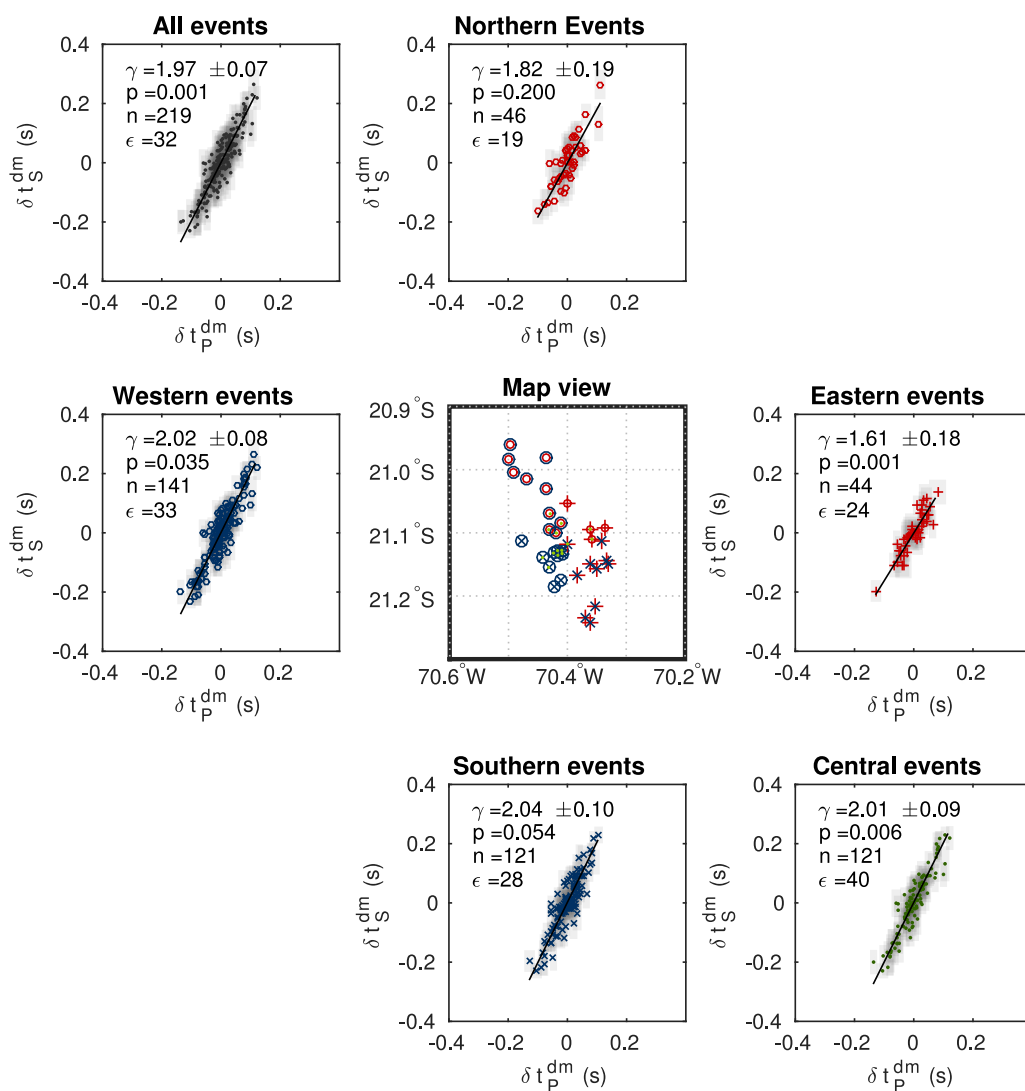


**Figure 5.15:** Internal distribution of  $\gamma$ -values of the events that make up the clusters shown in Figure 5.11. Symbols indicating the event location in the map view (center) correspond to symbols in the regression plots (others). Grey shade indicates the data error. Only stations of the core network have been used, see Figure 5.16.

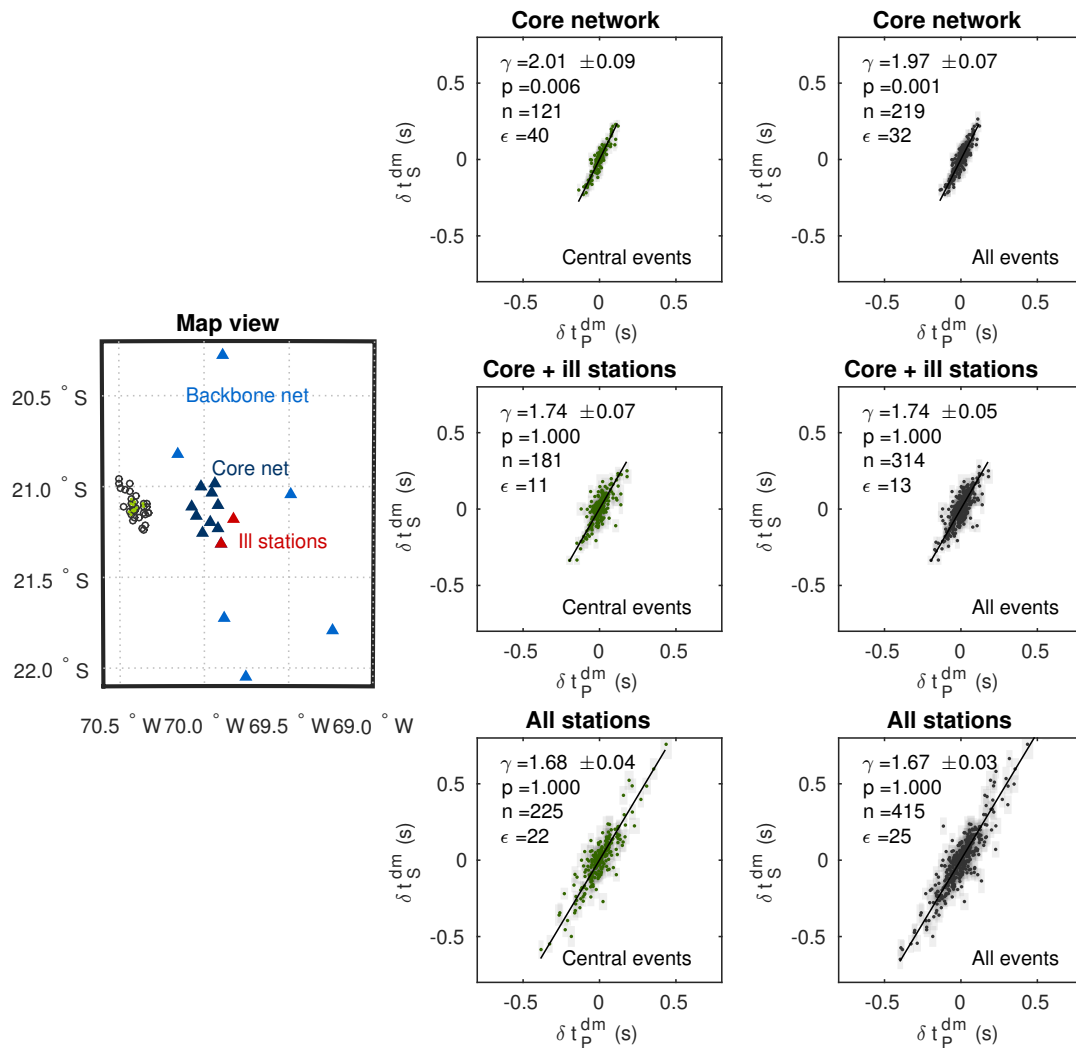


**Figure 5.16:** Dependence of the measurement of the  $\gamma$ -value on the seismic stations used. Left: Map view of station and event distribution. Mid column: Regression plots using central subset of events for different station distributions. Right column: Regression plots using the whole cluster. The top two regression plots correspond to those on the bottom right-hand side and top left-hand side in Figure 5.15.

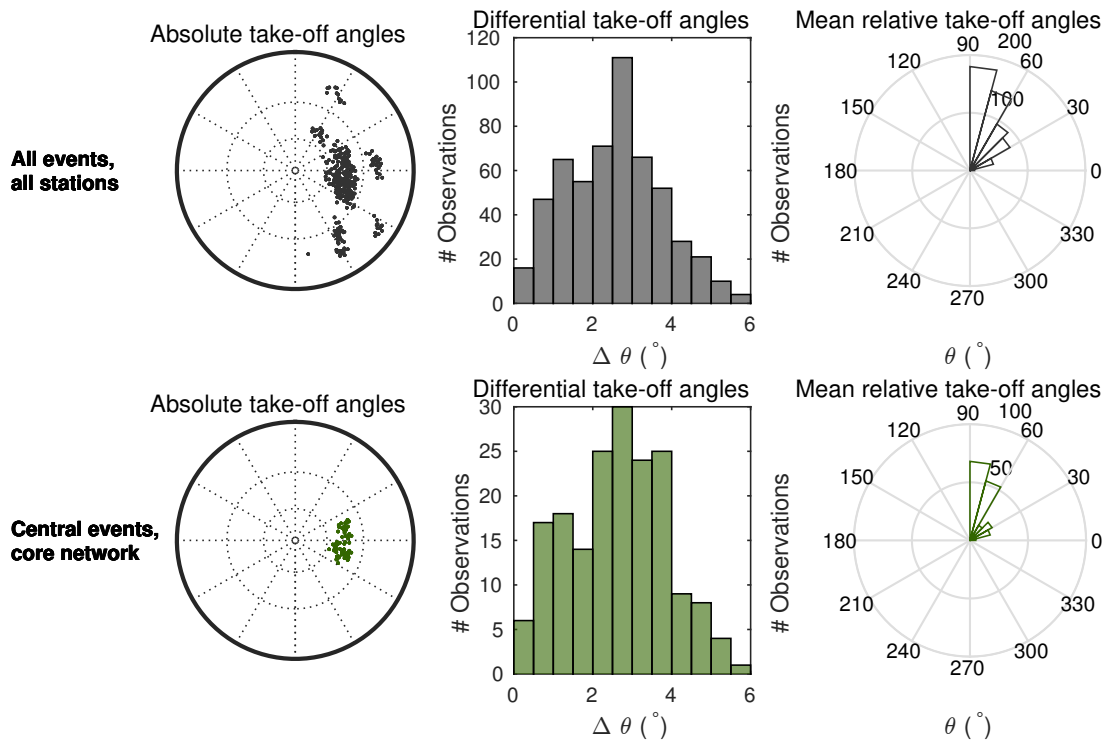


**Figure 5.17:** Ray take-off angles at the source. Left: Absolute take-off angles in stereographic projection (upper hemisphere). Middle: Differences in take-off-angles between respectively both events of each event pair. Right: Take-off angle relative to the inter-event vector ( $0^\circ$ =parallel,  $90^\circ$ =perpendicular).

direction. In contrast to that, relative movement within the subducting slab has been suggested to be either bending, which produces slab–surface-parallel layering, or faulting of bend-faults, which produces bend–fault-parallel layering.

Furthermore, as  $\gamma \gtrsim 2.0$ , the observed S-wave would have to be the slow SV-wave. This wave would vanish in the SH-coda, because focal mechanisms of the seismic sources do radiate seismic energy polarized in all directions (Sec. 3.3).

A geometry that has a cylindrical shape of high  $V_P/V_S$  around the seismicity cluster and a slab-normal, overly wide bend–fault-like shape towards the slab surface (Fig. D.8) is capable of producing the observed linear  $\hat{\delta}t_p$  vs.  $\hat{\delta}t_s$  distribution on the core network and a scattered  $\hat{\delta}t_p$  vs.  $\hat{\delta}t_s$  distribution on the backbone network. I conclude that such a geometry is therefore plausible to exist in the volume under consideration.

## 5.5 Discussion

The estimation of the near-source  $V_P/V_S$ -ratio provides evidence that the crust and the mantle of the subducting slab are hydrated, and that a free fluid phase attributed to metamorphic dehydration reactions is present within certain regions. I identified three regions in the slab, where I associate high  $V_P/V_S$ -values with dehydration reactions. At

shallow depth within the oceanic crust ( $\sim 30$  km), lawsonite + chlorite dehydration may take place (Eq. (4.8)). At shallow intermediate depth within the oceanic mantle (60 km), the dehydration of antigorite may occur (Eq. (4.11)). At 110 km depth the reaction is most probably the final dehydration of antigorite (Eq. (4.12)), under the prerequisite that seismicity occurs in the oceanic mantle. If seismicity at deeper intermediate depth occurs within the oceanic crust, high  $V_P/V_S$ -ratios are probably caused by eclogitization (garnet + coesite formation, Eq. (4.10)). The regions in between should accordingly consist of the lithologies that are met along the subduction trajectory on the phase diagrams (Figs. 4.1 and 4.2).

### 5.5.1 Lithology at deeper intermediate depth

Seismicity at deeper intermediate depth in the region has the form of a continuous, globally detectable nest of seismic activity. In contrast to that, in terms of  $\gamma$ , it here appears to be separated into a northern region of very low  $\gamma$ -values and a southern region of very high  $\gamma$ -values. I suspect that the geodynamic situation in both subregions is still comparable. Within both regions, a fluid-filled and highly anisotropic medium that hosts the final dehydration of a strongly foliated antigorite can be present. A change in the direction of the foliation north and south of  $21^\circ$  S might be sufficient to exhibit the different  $\gamma$ -values as a function of the angle between the seismic ray and the foliation. A change in direction of the foliation can for example be caused by a change in slab dip.

### 5.5.2 Pore geometry in regions of high $\gamma$

From poroelastic considerations (Sec. 4.2.2) it follows that in a porous medium, for a given  $V_P/V_S$ -ratio, pore volume  $\Phi$  and pore aspect ratio  $\alpha$  are related to each other. Furthermore, the maximum pore volume that is generated through a metamorphic mineral reaction is given by the void volume fraction generated through the densification of the rock matrix.

I combined the results of the measurements of high  $\gamma$  ( $>2.0$ ), the results of the thermodynamic modeling, and the results of the poroelastic modeling in Figure 5.18. I treated the two dehydration reactions of antigorite equally, because both reactions (Eqs. (4.11) and (4.12)) are similar with respect to their associated densification and fluid release.

I find that the observed  $\gamma$ -values are consistent with  $\Phi$  (in percent) and  $\alpha$  that obey the relation:

$$\Phi \approx 100\alpha; \quad (5.22)$$

this means, the higher the pore volume, the more globular it must be. In regions of high  $\gamma$ , pore space is therefore most probably vein- or crack-like and minor in volume. The geometry–volume-relationship Eq. (5.22) coincides for all lithologies with the geometrical percolation threshold (Garboczi et al., 1995), which is the critical volume fraction of randomly oriented overlapping pores for which long ranged interconnectivity emerges. Percolation theory suggests that such features have good draining capabilities.

The existence of compliant pore space under high confining pressures implies further that pore fluid pressure is equilibrated at a near lithostatic level, because it only remains

open as long as a near lithostatic fluid pressure is maintained. Under only partially drained conditions it closes (Fig. 5.18).

Previous studies that have investigated the dehydration of serpentinite arrive at conclusions that are in accordance with these findings. Combined thermodynamic and hydraulic modeling indicates that reactive fluid release during de-serpentinization forms interconnected vein-networks in a self-organized manner (Plümper et al., 2017). In laboratory experiments it has independently been shown that the breakdown of antigorite yields vein- or crack-like structures that are filled with nanocrystalline reaction products (Chollet et al., 2011; Proctor and Hirth, 2015). These structures are interpreted as porous fluid conduits sustaining near lithostatic fluid pressures because of their distinct microstructure and mineral content. They exhibit very little porosity. Dehydration structures observed in serpentinitized peridotites from paleo-subduction-zones are comparable in texture and do not show large amounts of open porosity either (Plümper et al., 2017; Healy et al., 2009). Such structures fulfill the relationship Eq. (5.22) and, when active, would cause elastic rock properties comparable to those that I observe.

## 5.6 Conclusion

The method proposed by Lin and Shearer (2007) to estimate the  $V_P/V_S$ -ratio in the vicinity of dense earthquake clusters directly from arrival time measurements of P- and S-waves yields biased results. The method tends to smear the real value of a subsurface  $V_P/V_S$ -anomaly towards the background value. Anomalies observed with this method therefore still exist, but their magnitude is in reality probably higher than estimated. Existing anomalies are probable to remain undetected by the method. I termed the biased estimator  $\gamma$ .

I extended the method and applied it to the entire cloud of local seismicity in the Central Andean forearc region. The results are physically reasonable and repeatable.

The model of subsurface  $\gamma$  is remarkably fine-grained and consistent with numerous of earlier observations of  $V_P/V_S$ -ratios from subduction zones. In the continental crust I find values that comply with values measured for mafic magmatic rocks below the Coastal Cordillera and with values measured for intermediary magmatic rocks below the Precordillera. Also in the subducting slab, the  $\gamma$ -values are consistent with the metamorphic lithologies that I predicted in Chapter 4 using petrophysical models. Regions with high  $\gamma$ -values provide evidence for ongoing mineral dehydration reactions in the lower band of seismicity and at deeper intermediate depth. This implies the hydration of the subducting slab to 30 km depth below the plate interface.

The good coherence of petrophysical models and  $\gamma$ -values indicates that the biasing shortcut effect is probably not very pronounced at seismic frequencies of a few Hertz.

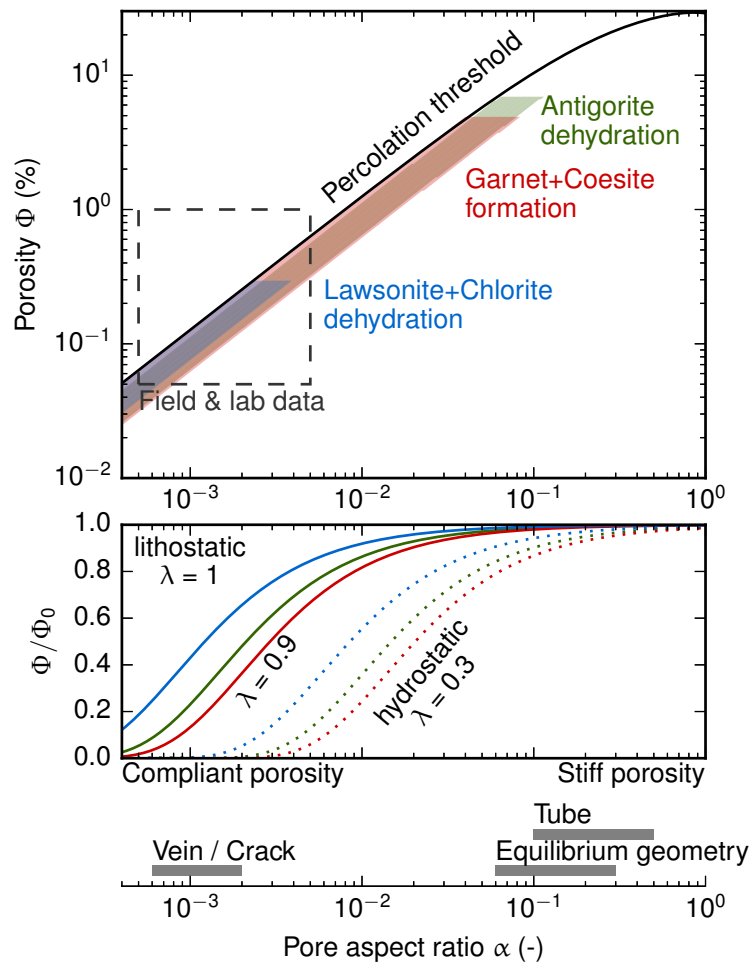


**Figure 5.18:** Results of measurements of high  $V_P/V_S$ -ratios, projected to the  $\Phi$ - $\alpha$  space of the predicted lithology. Top: Shaded areas indicate the pore-space properties that are in accordance with the seismological measurements. The upper bound of  $\Phi$  is the void volume fraction of the dehydration reaction ( $\Phi_0$ ). Also shown is the approximate pore-space geometry observed in laboratory and field studies and the computationally determined geometrical percolation threshold (Garboczi et al., 1995). Middle: Reduction of pore volume due to confining pressure as a function of relative pore pressure (Shapiro, 2003). Bottom: Equivalent aspect ratio (Takei, 2002).





# Chapter 6

## Conclusion

In this thesis, I used ground velocity recordings of small earthquakes that occurred in the Central Andean subduction zone at 21° S, in order to gain understanding of the deep water cycle and the driving forces of subduction. The results of this analysis are summarized in Figure 6.1.

I localized the seismic events with high precision. My results show seismicity in the continental crust and the subducting slab. Slab-related seismicity occurs along one band of seismicity at the partially coupled part of the plate-interface and along two more bands within the oceanic crust and mantle. I computed focal mechanisms for the slab-related seismicity and  $\gamma$ -values as an estimator for the near-source  $V_P/V_S$ -ratio for the entire seismic event cloud. I constructed a petrophysical model that allows for the interpretation of the results in terms of mineral composition, fluid over-pressure, and elastic anisotropy.

### 6.1 Joint interpretation

Seismicity of the continental lithosphere reaches down to the lower crust in the cold trench-ward forearc region onshore. It is confined to the shallow crust towards the magmatic arc. The boundary between these two regions is likely to be the brittle-ductile boundary. It is sharp and coincides with a reflective structure that has been imaged earlier and has been interpreted as a fluid or magma ascent path.  $\gamma$ -values indicate that the forearc crust is of rather mafic composition towards the trench and becomes of more intermediary composition towards the magmatic arc. The deepest earthquakes of the continental lithosphere may even occur within the mantle wedge. Here,  $\gamma$ -values indicate a horizontally layered, anisotropic fabric that is probably attributed to a serpentinization of the mantle material.

In the subducting slab, seismicity occurs at shallow and intermediate depth. Shallow seismicity results from the high differential stresses within the coupling zone between the Nazca and the South American plate. The thrust faulting events occur at the plate interface and probably along reactivated outer-rise bend-faults.  $\gamma$ -estimates are consistent with the presence of a blueschist there, as suggested by the petrophysical model. I find no evidence for widespread fluid over-pressure. The downdip end of coupling between

the oceanic and the continental plate is located at 55 km depth. At this point, interface seismicity comes to an end, the stress-field changes from compressional to extensional, and the reflectivity signature of the plate interface broadens characteristically. This is also the classical lower limit of shallow seismicity, where seismicity may occur unassisted by the simple brittle failure mechanism due to high differential stresses. However, earthquake nucleation may also be assisted by transformational faulting or shear-heating thermal runaway.

Intermediate depth seismicity occurs in the oceanic crust and mantle. The slab is under tension, so that beyond the down-dip end of interplate coupling the stress-field is dominated by slab-pull and interface coupling has come to an end. Seismicity of the oceanic crust at intermediate depth is sparse and weak. I therefore was unable to perform a comprehensive analysis of focal mechanisms and  $\gamma$ -values there. As deformation in principle should be ductile, I propose that seismic rupture is assisted by any of the mechanisms suggested earlier for intermediate depth seismicity: dehydration embrittlement, transformational faulting, or shear-heating thermal runaway.

There are strong indications that the subducting oceanic mantle is hydrated to a depth of  $\sim 25$  km below the oceanic Moho and that intermediate depth seismicity there is assisted by the two-step dehydration reaction of antigorite. At shallow intermediate depth the  $\gamma$ -value indicates the presence of fluid-filled, over-pressured fractures in the source volume of intermediate depth earthquakes. The variability of focal mechanisms may indicate the presence of fluid over-pressure in an environment of not very large differential stresses. The petrophysical model indicates that at this depth antigorite may break down in the presence of brucite. This reaction would be a plausible source of a free fluid phase within the subducting lithosphere at 50 km depth.

The progressive alignment of focal mechanisms indicates that differential stresses become stronger along the subduction pathway, possibly because of the ongoing densification of the rock matrix due to metamorphic mineral densification or a viscous force transfer of mantle convection to the slab.

In the interval between 100 and 120 km depth, intermediate depth seismicity intensifies and constitutes a narrow double seismic zone within the oceanic mantle. The  $\gamma$ -values are again indicative for the presence of a free fluid phase at this depth that is likely to originate from the final dehydration of antigorite. These observations again favor a mechanism that is related to a mineral dehydration reaction for earthquake nucleation. A very low  $\gamma$ -value in the north may indicate strong elastic anisotropy of the fluid-filled medium.

Beyond this nest of intermediate depth seismicity, the mantle is likely to be mostly dehydrated, apart from some hydrogen contained in chlorite and/or nominally anhydrous minerals. The lower temperature relative to its surrounding in combination with the now comparable composition should result in a higher total density compared to the surrounding mantle. This in turn would lead to a net negative buoyancy of the slab.

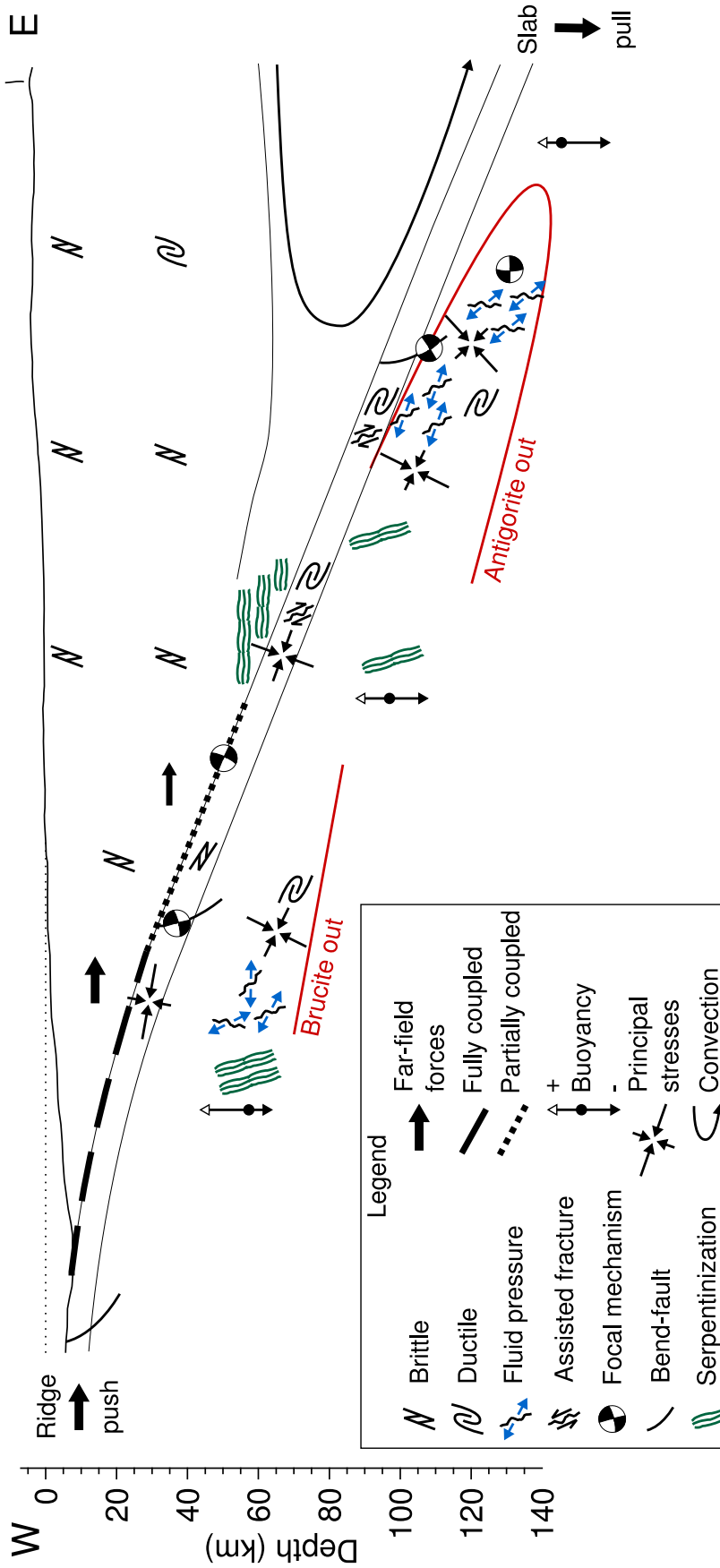


**Figure 6.1:** Joint interpretation of the properties of the subducting slab near the earthquake sources that are in agreement with the petrophysical model. Beach ball plots are drawn in the profile plane (southern hemisphere projection)

## 6.2 Outlook

The overall results demonstrate that sea-water is stored within the subducting lithosphere and is released below the continent. The next part of the deep water cycle, fluid ascend and melt generation, has been imaged in a number of studies using the methods of seismic tomography and active source seismic reflection experiments in the Central Andes and elsewhere.

The results of this thesis can be deepened, for example by determining absolute velocities of the subsurface medium. With the petrophysical constraints on the petrology of the mantle presented here, this would allow to assess the degree of hydration of the subducting lithosphere, which would be a step towards the quantification of the deep water cycle.

An inversion of the focal mechanisms for the stress-field within the slab can shed further light on the process of ocean–continent-collision, slab-buoyancy, and slab-densification. From petrophysical considerations, the density of the incoming lithosphere can be estimated. This would be another indication for the amount of hydration of the slab.

Finally, the data presented here can be compared to complex numerical models that have a wide range of physical processes implemented. By tuning these models in a way that they match the new observations, a more complete understanding of the subduction process can be gained.

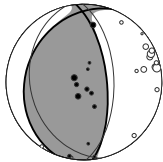
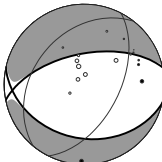
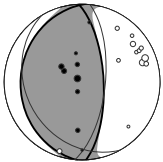
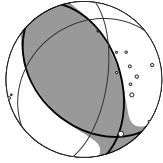
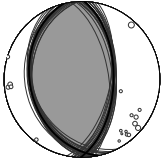
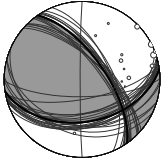
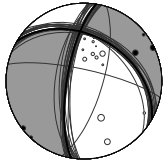
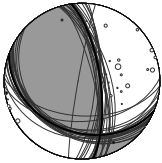
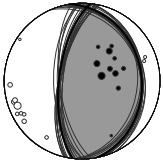
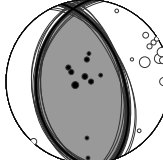
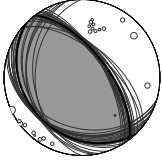
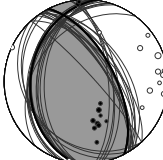
# Appendices

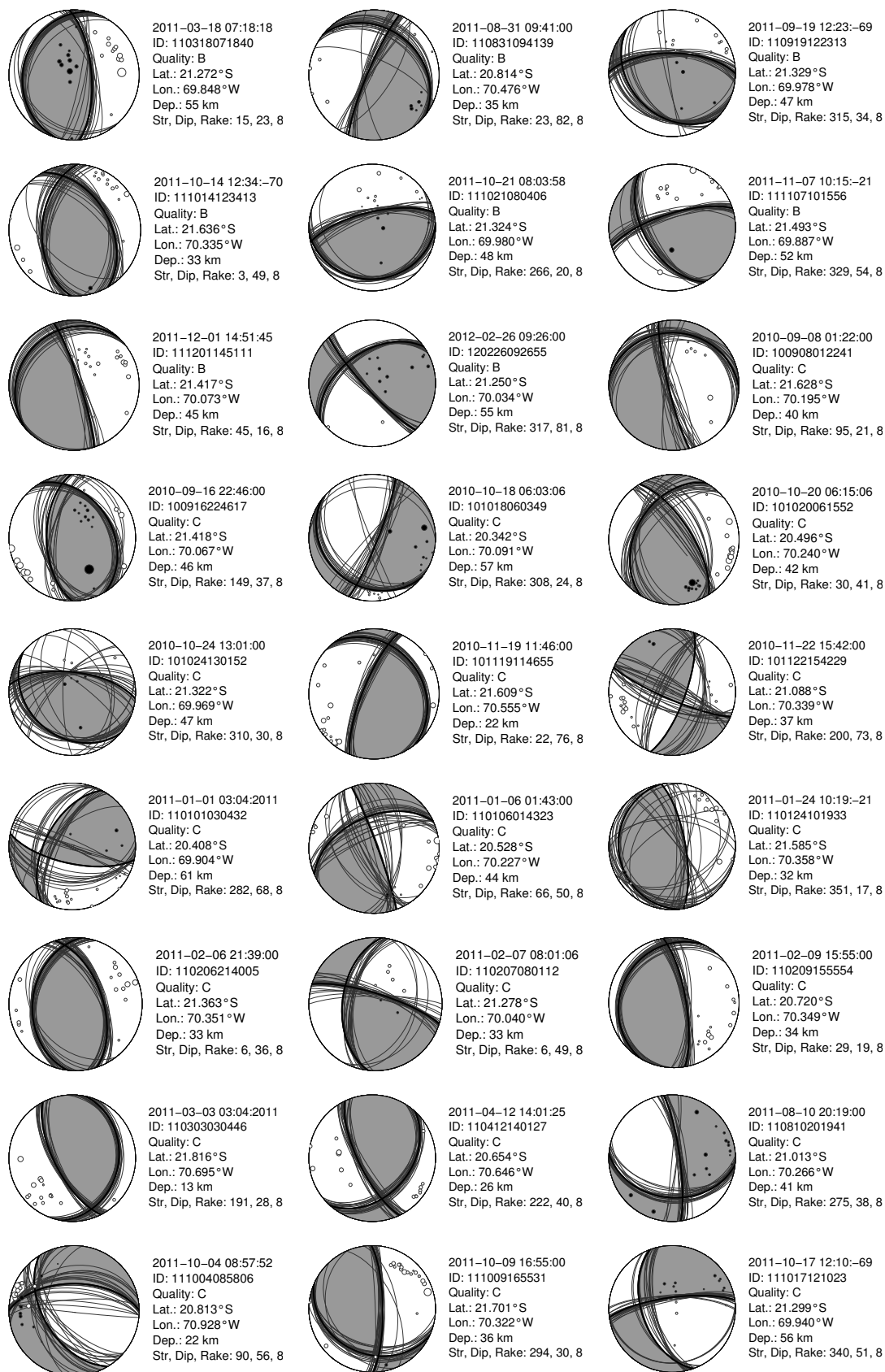


# Appendix A

## Fault plane solutions

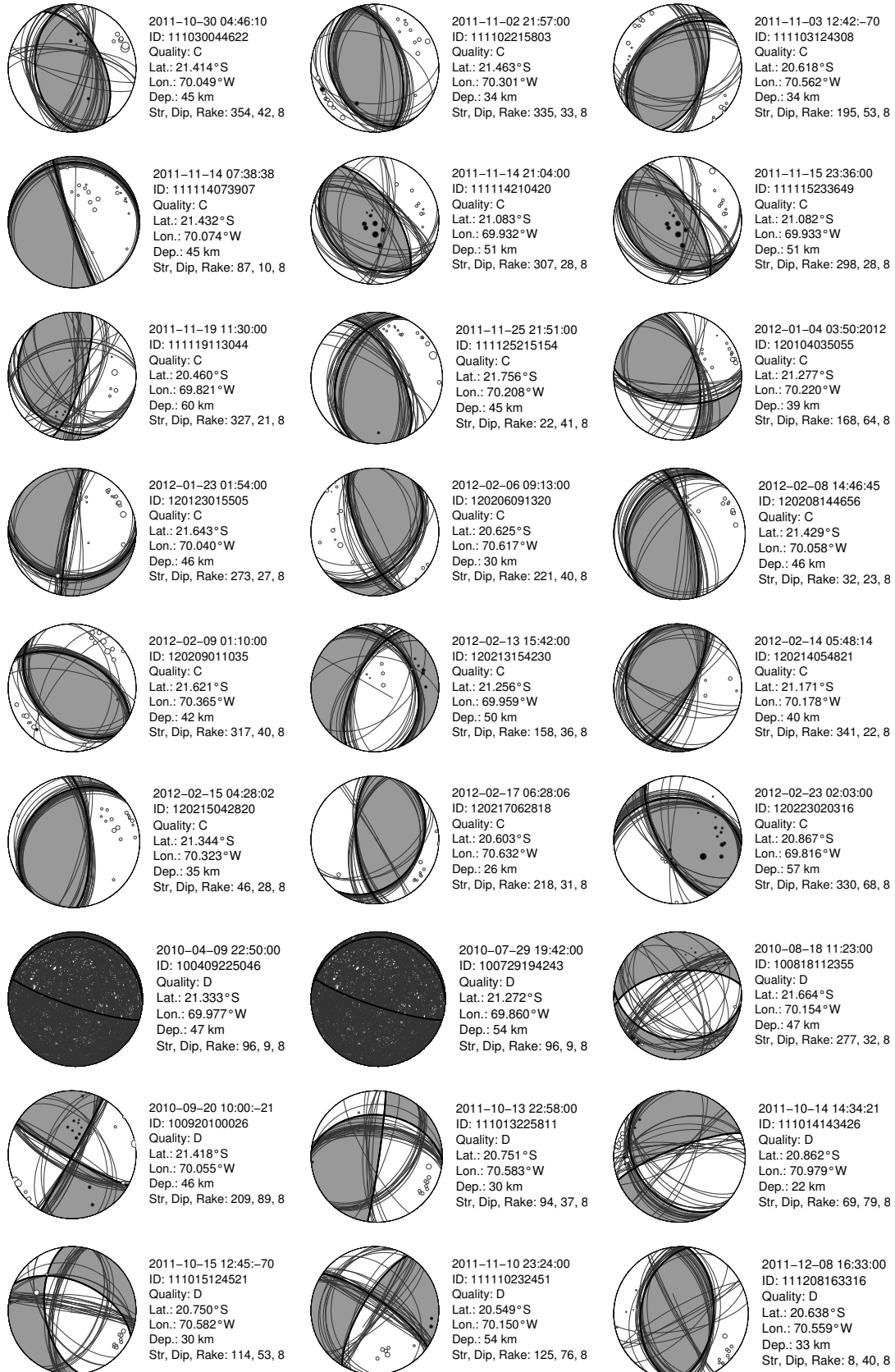
**Table A.1:** Inversion results obtained with RMT (Quality A), with starting model and HASH (Quality B-D) with results obtained with small perturbations of the take-off angle. Dots indicate P-wave polarity measurement (black positive, white negative) and P/S-amplitude ratio (proportional to the square root of the diameter of the circle). All upper hemisphere projections.

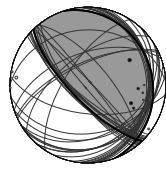
Upper band		
 <p>2010-12-11 04:43:12 ID: 101211044348 Mw: 3.9 Quality: A Lat.: 21.145°S Lon.: 69.986°W Dep.: 50 km DC/CLVD: 87% / 13% Str, Dip, Rake: 169, 66, 3</p>	 <p>2011-03-24 22:19:00 ID: 110324221932 Mw: 3.64 Quality: A Lat.: 21.272°S Lon.: 69.816°W Dep.: 56 km DC/CLVD: 96% / 4% Str, Dip, Rake: 78, 59, 3</p>	 <p>2011-08-13 23:21:00 ID: 110813232140 Mw: 3.88 Quality: A Lat.: 21.265°S Lon.: 69.853°W Dep.: 54 km DC/CLVD: 90% / 10% Str, Dip, Rake: 177, 68, 3</p>
 <p>2012-02-15 13:58:00 ID: 120215135904 Mw: 3.48 Quality: A Lat.: 21.205°S Lon.: 70.318°W Dep.: 45 km DC/CLVD: 70% / 30% Str, Dip, Rake: 210, 53, 3</p>	 <p>2010-04-17 02:05:00 ID: 100417020512 Quality: B Lat.: 20.762°S Lon.: 70.405°W Dep.: 30 km Str, Dip, Rake: 347, 34, 8</p>	 <p>2010-04-27 13:07:00 ID: 100427130737 Quality: B Lat.: 21.194°S Lon.: 70.254°W Dep.: 38 km Str, Dip, Rake: 145, 66, 8</p>
 <p>2010-09-06 04:21:09 ID: 100906042201 Quality: B Lat.: 21.442°S Lon.: 70.022°W Dep.: 47 km Str, Dip, Rake: 120, 42, 8</p>	 <p>2010-09-06 08:05:20 ID: 100906080527 Quality: B Lat.: 21.156°S Lon.: 70.228°W Dep.: 39 km Str, Dip, Rake: 172, 71, 8</p>	 <p>2010-09-22 13:34:00 ID: 100922133418 Quality: B Lat.: 21.289°S Lon.: 70.167°W Dep.: 43 km Str, Dip, Rake: 170, 25, 8</p>
 <p>2010-11-13 06:35:06 ID: 101113063515 Quality: B Lat.: 21.239°S Lon.: 69.916°W Dep.: 52 km Str, Dip, Rake: 3, 37, 8</p>	 <p>2010-11-29 14:17:48 ID: 101129141736 Quality: B Lat.: 21.729°S Lon.: 70.067°W Dep.: 49 km Str, Dip, Rake: 315, 27, 8</p>	 <p>2010-12-10 15:41:00 ID: 101210154138 Quality: B Lat.: 20.808°S Lon.: 70.048°W Dep.: 48 km Str, Dip, Rake: 7, 33, 8</p>



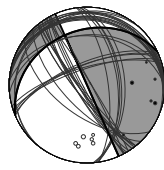


## Fault plane solutions

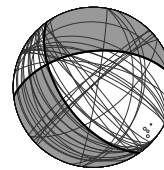




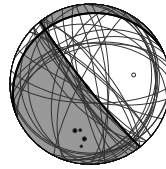
2011-12-13 21:11:00  
ID: 111213211129  
Quality: D  
Lat.: 20.984°S  
Lon.: 70.435°W  
Dep.: 36 km  
Str, Dip, Rake: 161, 19, 8



2011-12-26 03:55:2011  
ID: 111226035531  
Quality: D  
Lat.: 20.471°S  
Lon.: 70.018°W  
Dep.: 59 km  
Str, Dip, Rake: 336, 90, 8

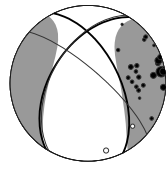


2012-01-15 00:07:00  
ID: 120115000751  
Quality: D  
Lat.: 20.662°S  
Lon.: 70.519°W  
Dep.: 38 km  
Str, Dip, Rake: 83, 53, 8

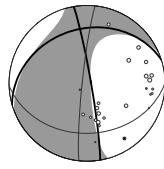


2012-01-30 05:24:30  
ID: 120130052417  
Quality: D  
Lat.: 20.531°S  
Lon.: 69.918°W  
Dep.: 62 km  
Str, Dip, Rake: 67, 14, 8

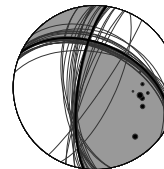
## Lower band



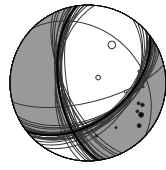
2011-09-21 17:48:00  
ID: 110921174900  
Mw: 3.46  
Quality: A  
Lat.: 21.171°S  
Lon.: 70.523°W  
Dep.: 55 km  
DC/CLVD: 48% / 52%  
Str, Dip, Rake: 150, 58, 3



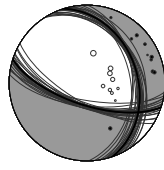
2011-12-06 13:02:00  
ID: 111206130232  
Mw: 3.56  
Quality: A  
Lat.: 20.770°S  
Lon.: 70.081°W  
Dep.: 71 km  
DC/CLVD: 49% / 51%  
Str, Dip, Rake: 186, 85, 3



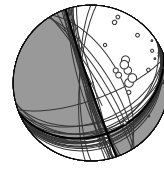
2010-07-16 02:39:00  
ID: 100716023949  
Quality: B  
Lat.: 21.135°S  
Lon.: 70.430°W  
Dep.: 57 km  
Str, Dip, Rake: 8, 73, 8



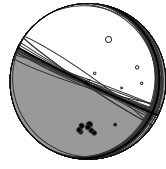
2010-10-14 04:02:10  
ID: 101014040227  
Quality: B  
Lat.: 20.337°S  
Lon.: 70.013°W  
Dep.: 80 km  
Str, Dip, Rake: 352, 59, 8



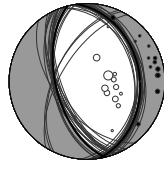
2011-03-10 17:45:00  
ID: 110310174556  
Quality: B  
Lat.: 21.138°S  
Lon.: 70.231°W  
Dep.: 67 km  
Str, Dip, Rake: 288, 67, 8



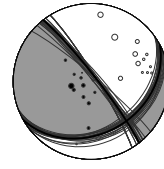
2011-03-27 11:54:00  
ID: 110327115438  
Quality: B  
Lat.: 21.235°S  
Lon.: 70.349°W  
Dep.: 63 km  
Str, Dip, Rake: 341, 88, 8



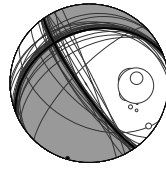
2011-10-05 07:15:15  
ID: 111005071549  
Quality: B  
Lat.: 20.372°S  
Lon.: 69.983°W  
Dep.: 80 km  
Str, Dip, Rake: 193, 10, 8



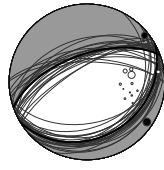
2011-10-09 00:50:00  
ID: 111009005055  
Quality: B  
Lat.: 21.055°S  
Lon.: 70.267°W  
Dep.: 65 km  
Str, Dip, Rake: 172, 33, 8



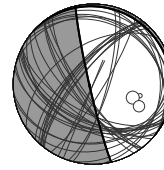
2011-11-30 19:12:00  
ID: 111130191310  
Quality: B  
Lat.: 21.075°S  
Lon.: 69.869°W  
Dep.: 75 km  
Str, Dip, Rake: 142, 84, 8



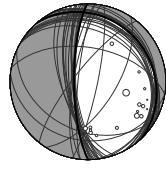
2010-04-06 03:56:2010  
ID: 100406035654  
Quality: C  
Lat.: 21.023°S  
Lon.: 70.478°W  
Dep.: 56 km  
Str, Dip, Rake: 68, 35, 8



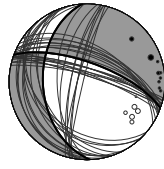
2010-04-12 03:55:2010  
ID: 100412035553  
Quality: C  
Lat.: 21.104°S  
Lon.: 70.424°W  
Dep.: 55 km  
Str, Dip, Rake: 240, 29, 8



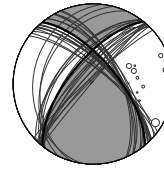
2010-04-12 15:49:00  
ID: 100412154958  
Quality: C  
Lat.: 20.876°S  
Lon.: 70.460°W  
Dep.: 57 km  
Str, Dip, Rake: 130, 5, 8



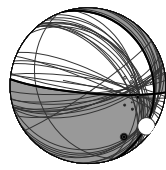
2010-04-20 22:54:00  
ID: 100420225426  
Quality: C  
Lat.: 20.321°S  
Lon.: 70.019°W  
Dep.: 79 km  
Str, Dip, Rake: 138, 19, 8



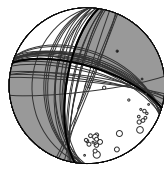
2010-08-21 04:26:08  
ID: 100821042656  
Quality: C  
Lat.: 20.830°S  
Lon.: 70.519°W  
Dep.: 55 km  
Str, Dip, Rake: 110, 70, 8



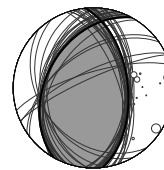
2010-08-27 13:48:00  
ID: 100827134843  
Quality: C  
Lat.: 21.163°S  
Lon.: 70.396°W  
Dep.: 56 km  
Str, Dip, Rake: 39, 66, 8



2010-09-10 16:38:00  
ID: 100910163846  
Quality: C  
Lat.: 21.069°S  
Lon.: 70.422°W  
Dep.: 56 km  
Str, Dip, Rake: 160, 18, 8

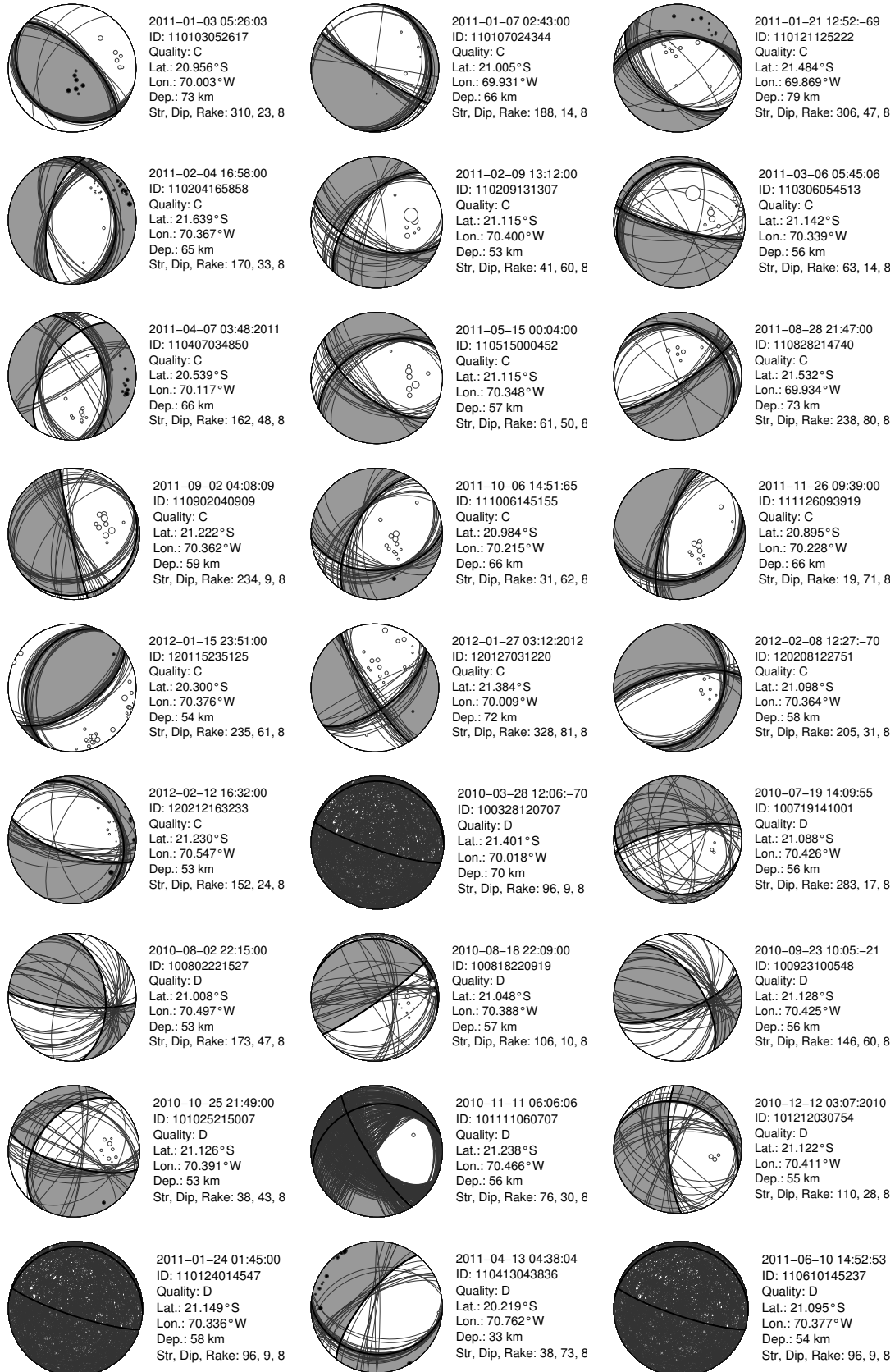


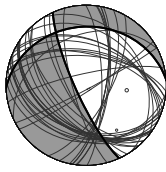
2010-09-28 09:31:00  
ID: 100928093130  
Quality: C  
Lat.: 20.263°S  
Lon.: 70.117°W  
Dep.: 77 km  
Str, Dip, Rake: 107, 70, 8



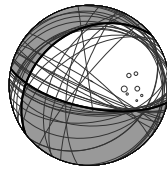
2010-10-05 08:42:47  
ID: 101005084257  
Quality: C  
Lat.: 21.116°S  
Lon.: 70.442°W  
Dep.: 54 km  
Str, Dip, Rake: 29, 41, 8

## Fault plane solutions



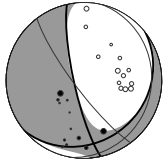


2012-01-01 05:35:01  
ID: 120101053609  
Quality: D  
Lat.: 20.396°S  
Lon.: 70.031°W  
Dep.: 76 km  
Str, Dip, Rake: 87, 28, 8

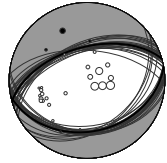


2012-02-22 11:08:00  
ID: 120222110811  
Quality: D  
Lat.: 21.089°S  
Lon.: 70.431°W  
Dep.: 54 km  
Str, Dip, Rake: 52, 33, 8

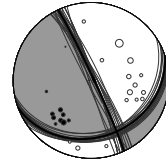
## Transition zone



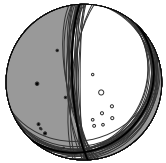
2010-04-17 03:50:2010  
ID: 100417035040  
Mw: 4.42  
Quality: A  
Lat.: 20.821°S  
Lon.: 69.692°W  
Dep.: 94 km  
DC/CLVD: 71% / 29%  
Str, Dip, Rake: 341, 77, 3



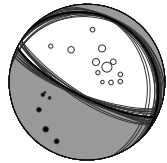
2010-04-14 13:06:00  
ID: 100414130632  
Quality: B  
Lat.: 20.868°S  
Lon.: 69.164°W  
Dep.: 105 km  
Str, Dip, Rake: 259, 35, 8



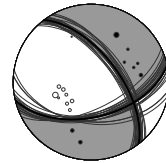
2010-04-26 13:04:00  
ID: 100426130438  
Quality: B  
Lat.: 20.691°S  
Lon.: 69.595°W  
Dep.: 75 km  
Str, Dip, Rake: 155, 87, 8



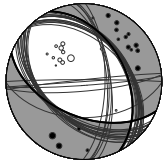
2010-08-16 13:39:00  
ID: 100816134005  
Quality: B  
Lat.: 20.262°S  
Lon.: 69.282°W  
Dep.: 90 km  
Str, Dip, Rake: 357, 78, 8



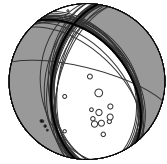
2010-08-21 22:20:00  
ID: 100821222056  
Quality: B  
Lat.: 20.942°S  
Lon.: 69.250°W  
Dep.: 83 km  
Str, Dip, Rake: 131, 16, 8



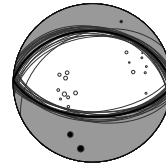
2010-08-27 00:18:00  
ID: 100827001838  
Quality: B  
Lat.: 20.956°S  
Lon.: 69.617°W  
Dep.: 82 km  
Str, Dip, Rake: 257, 53, 8



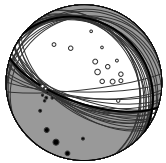
2010-08-31 01:03:00  
ID: 100831010409  
Quality: B  
Lat.: 21.438°S  
Lon.: 69.704°W  
Dep.: 72 km  
Str, Dip, Rake: 292, 53, 8



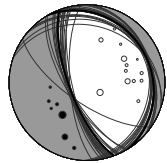
2010-09-08 05:36:08  
ID: 100908053655  
Quality: B  
Lat.: 20.242°S  
Lon.: 69.250°W  
Dep.: 96 km  
Str, Dip, Rake: 141, 48, 8



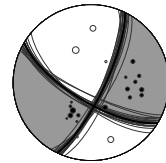
2010-09-11 03:32:2010  
ID: 100911033209  
Quality: B  
Lat.: 21.089°S  
Lon.: 69.665°W  
Dep.: 68 km  
Str, Dip, Rake: 91, 35, 8



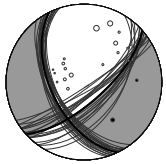
2010-09-12 18:16:00  
ID: 100912181659  
Quality: B  
Lat.: 20.955°S  
Lon.: 69.310°W  
Dep.: 82 km  
Str, Dip, Rake: 129, 23, 8



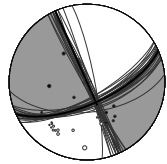
2010-09-23 16:13:00  
ID: 100923161329  
Quality: B  
Lat.: 20.962°S  
Lon.: 69.630°W  
Dep.: 72 km  
Str, Dip, Rake: 149, 19, 8



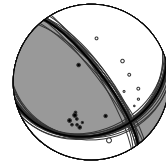
2011-01-24 17:28:00  
ID: 110124172832  
Quality: B  
Lat.: 20.730°S  
Lon.: 69.688°W  
Dep.: 86 km  
Str, Dip, Rake: 301, 70, 8



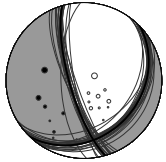
2011-01-30 08:26:50  
ID: 110130082703  
Quality: B  
Lat.: 21.257°S  
Lon.: 69.715°W  
Dep.: 78 km  
Str, Dip, Rake: 334, 55, 8



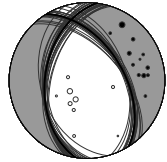
2011-02-06 03:11:2011  
ID: 110206031149  
Quality: B  
Lat.: 20.228°S  
Lon.: 69.326°W  
Dep.: 98 km  
Str, Dip, Rake: 156, 90, 8



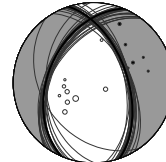
2011-02-06 17:46:00  
ID: 110206174651  
Quality: B  
Lat.: 20.518°S  
Lon.: 69.726°W  
Dep.: 94 km  
Str, Dip, Rake: 143, 77, 8



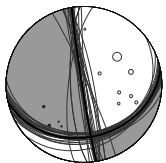
2011-02-28 20:45:00  
ID: 110228204557  
Quality: B  
Lat.: 20.468°S  
Lon.: 69.214°W  
Dep.: 108 km  
Str, Dip, Rake: 344, 75, 8



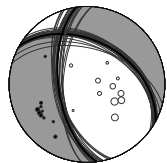
2011-03-02 19:49:00  
ID: 110302194919  
Quality: B  
Lat.: 21.012°S  
Lon.: 69.771°W  
Dep.: 67 km  
Str, Dip, Rake: 148, 52, 8



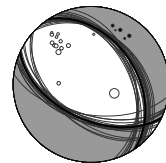
2011-04-10 00:19:00  
ID: 110410001929  
Quality: B  
Lat.: 21.012°S  
Lon.: 69.599°W  
Dep.: 69 km  
Str, Dip, Rake: 23, 43, 8



2011-09-12 19:07:00  
ID: 110912190733  
Quality: B  
Lat.: 20.566°S  
Lon.: 69.650°W  
Dep.: 75 km  
Str, Dip, Rake: 351, 88, 8

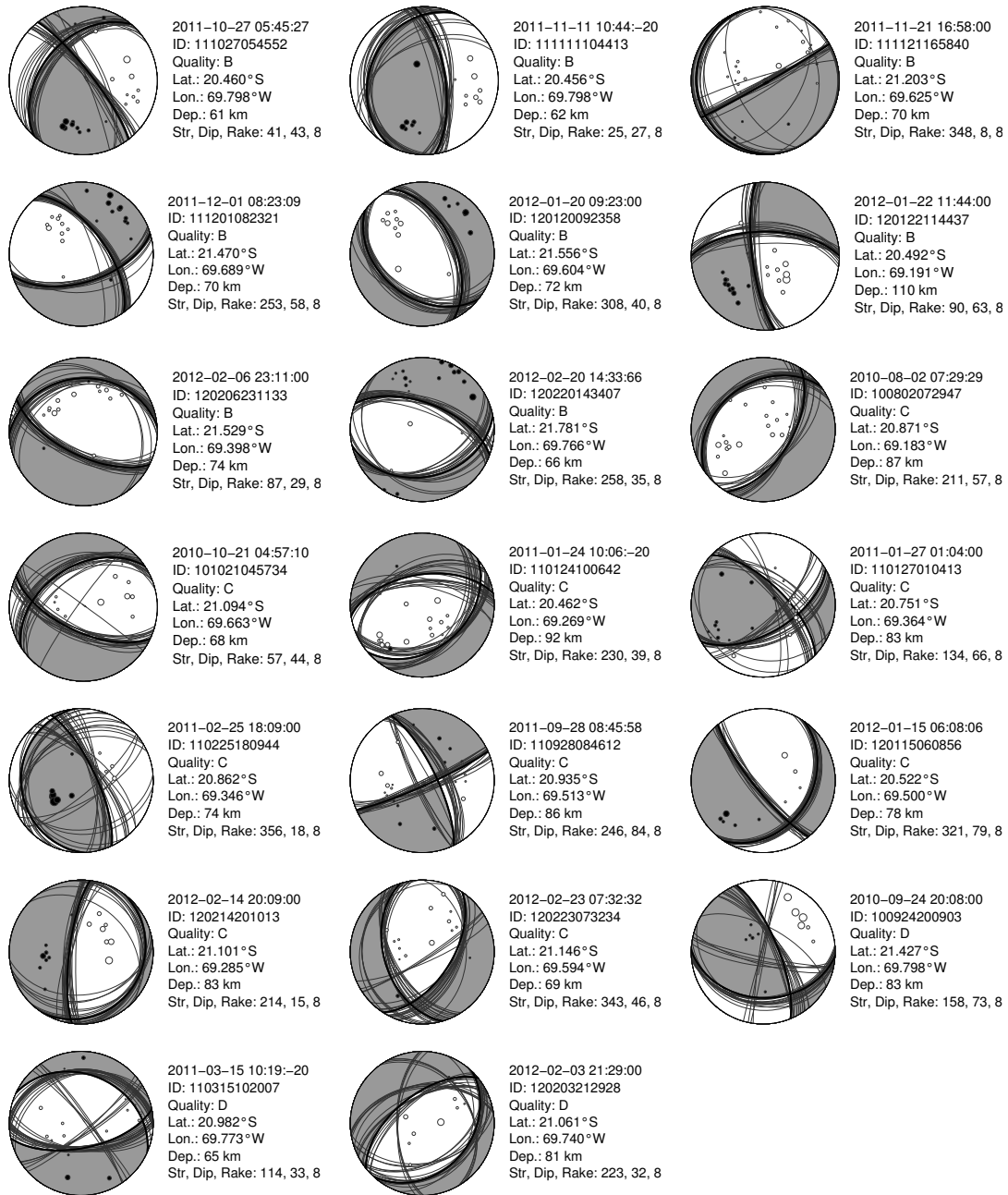


2011-09-19 13:34:00  
ID: 110919133508  
Quality: B  
Lat.: 20.704°S  
Lon.: 69.319°W  
Dep.: 90 km  
Str, Dip, Rake: 119, 44, 8

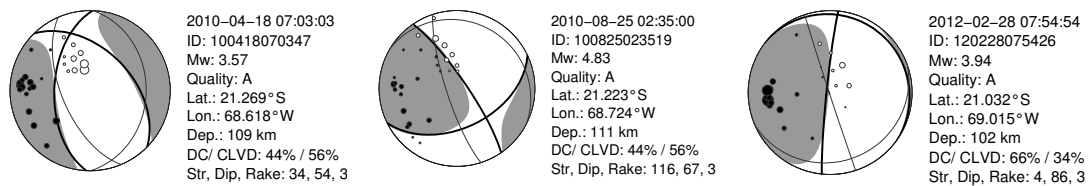


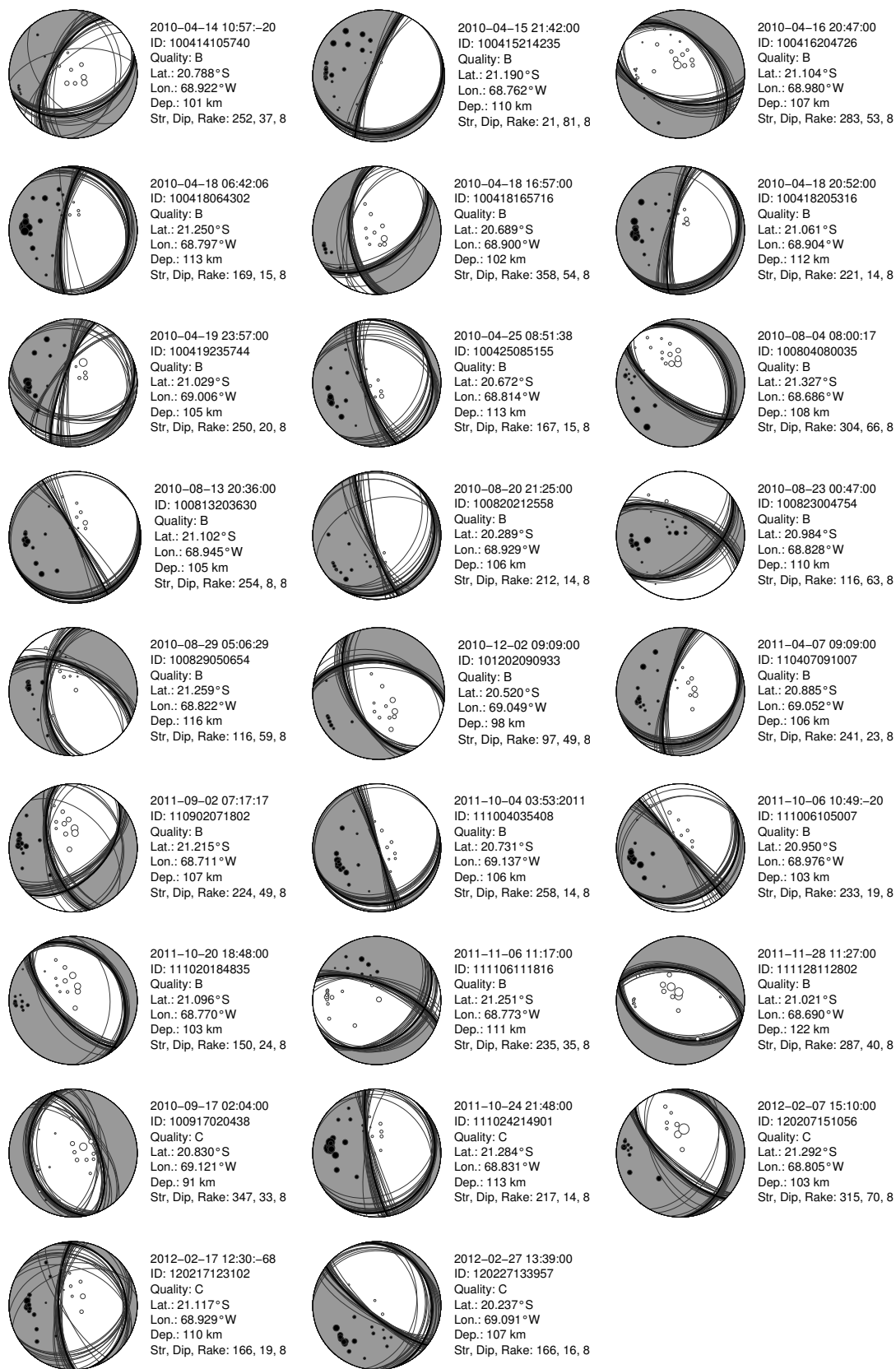
2011-09-25 17:07:00  
ID: 110925170809  
Quality: B  
Lat.: 21.723°S  
Lon.: 69.525°W  
Dep.: 73 km  
Str, Dip, Rake: 295, 53, 8

## Fault plane solutions



## Deeper intermediate depth

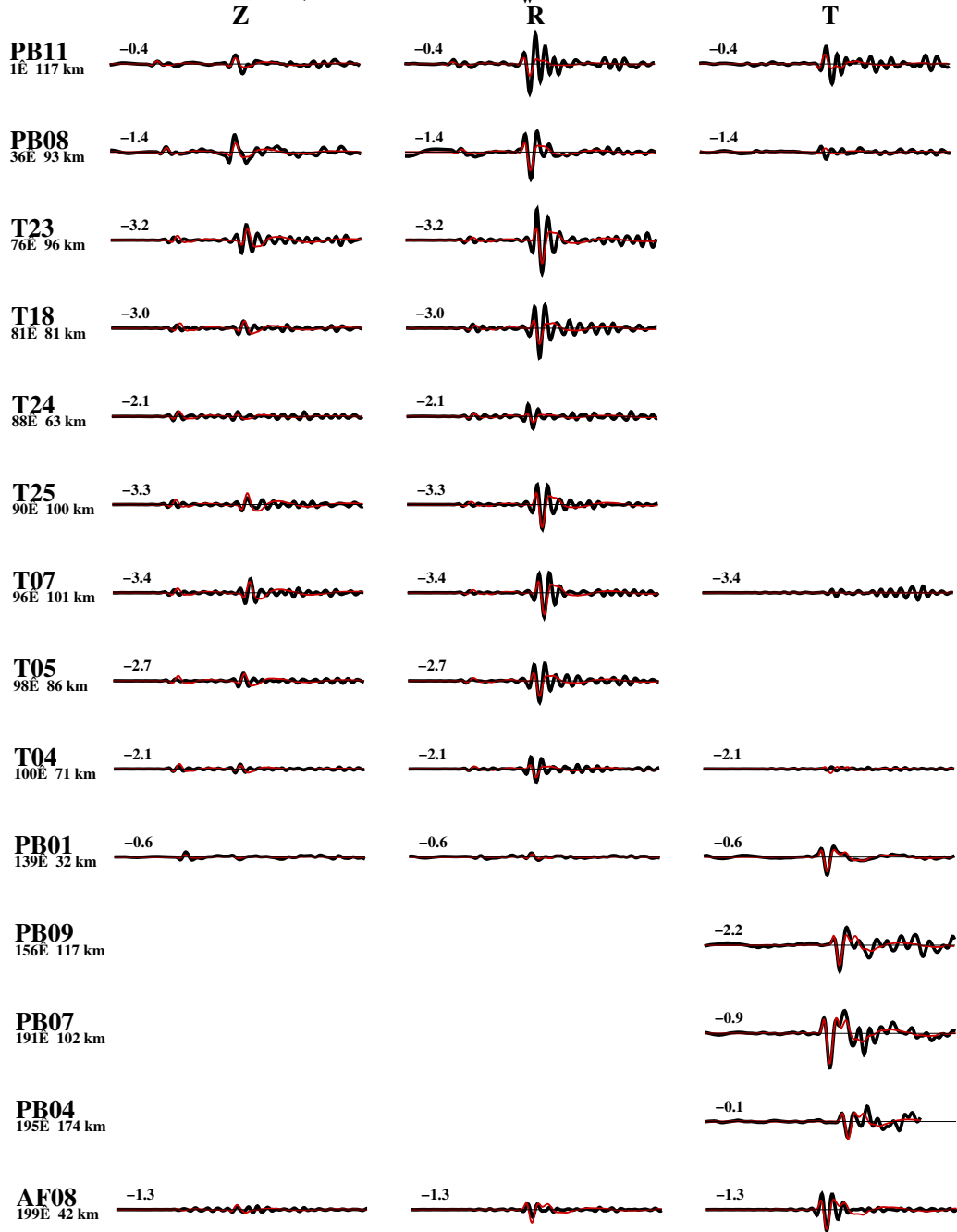




## **Appendix B**

### **Results of full-waveform moment tensor inversions**

100417\_0350, 10/ 4/17 3:50:26  $M_w=4.4$  2-20s 96km DC:71%





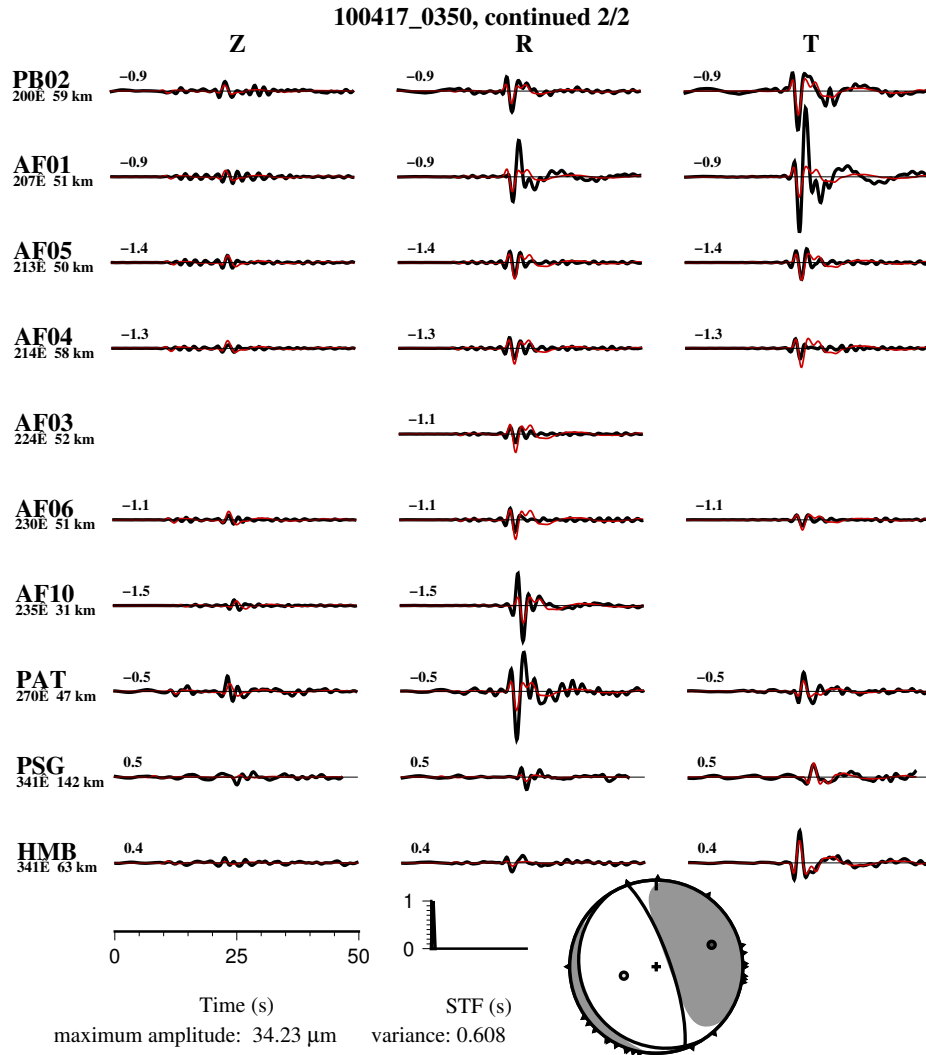
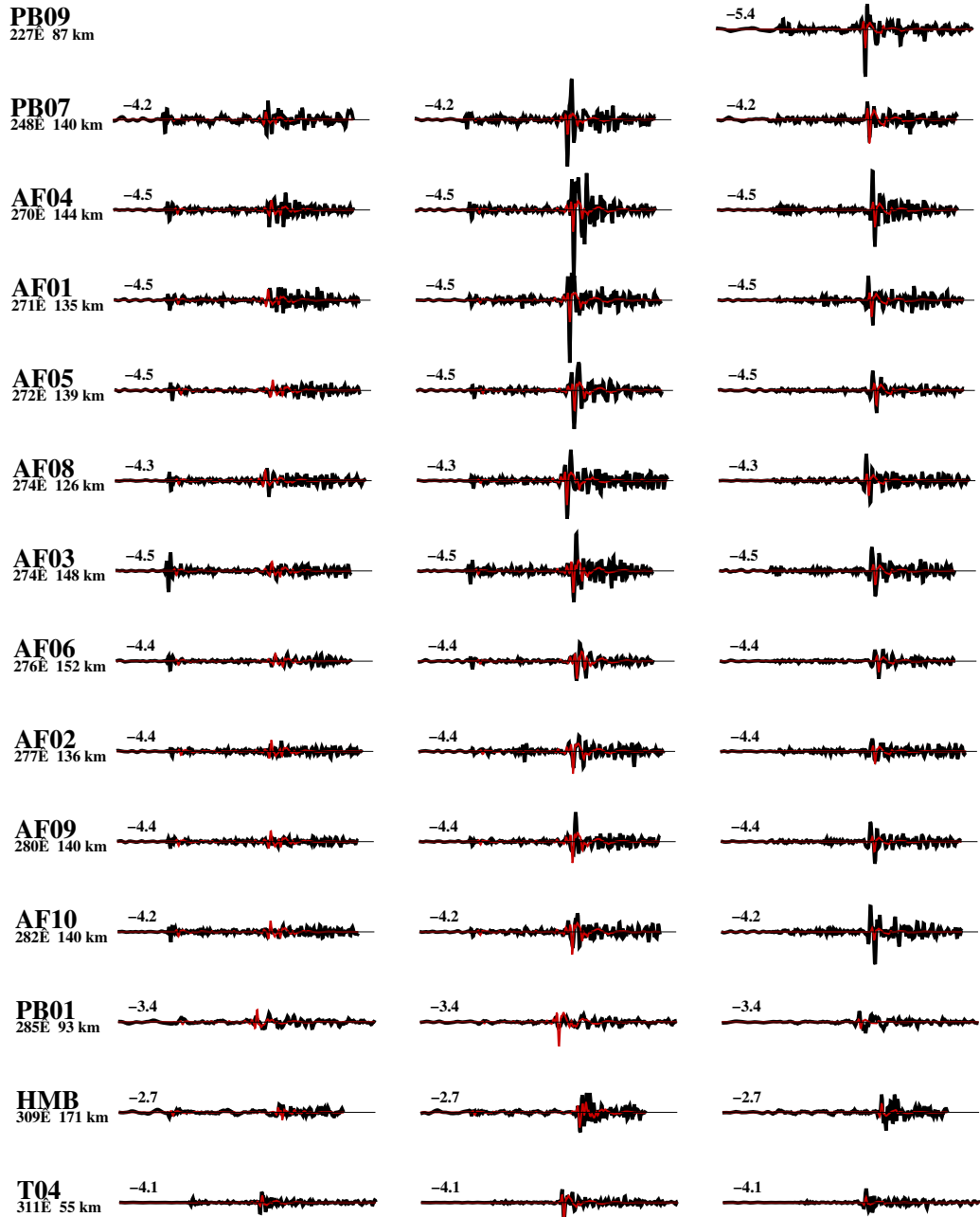


Figure B.1: Full waveform inversion results for Event 2010-04-17 03:50. Black lines: observed seismograms. Red lines: modeled seismograms. Numbers: Time shift of the modeled seismogram (seconds). Labels on the left-hand side are station names, backazimuth, and epicentral distance. Z: vertical component. R: radial component. T: transverse component. Band pass filter: 2-20 s.

100418\_0703, 10/ 4/18 7: 3:29  $M_w=3.6$  0-5s 108km DC:44%



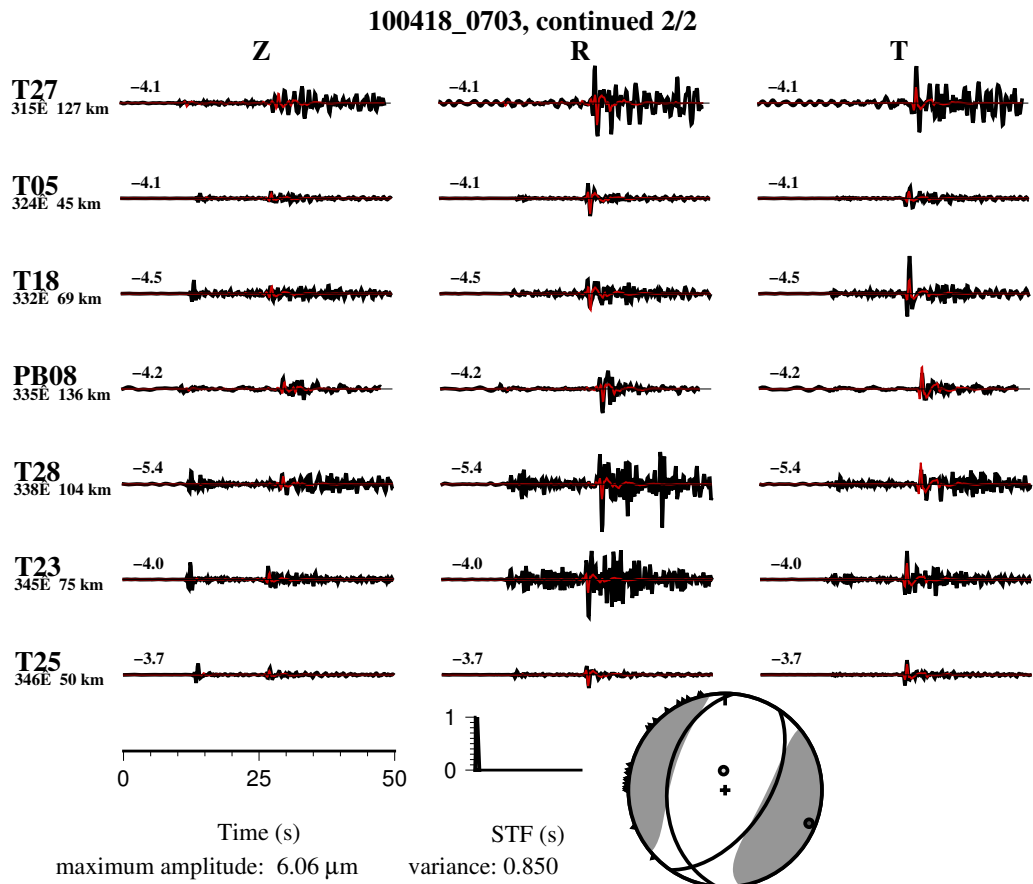
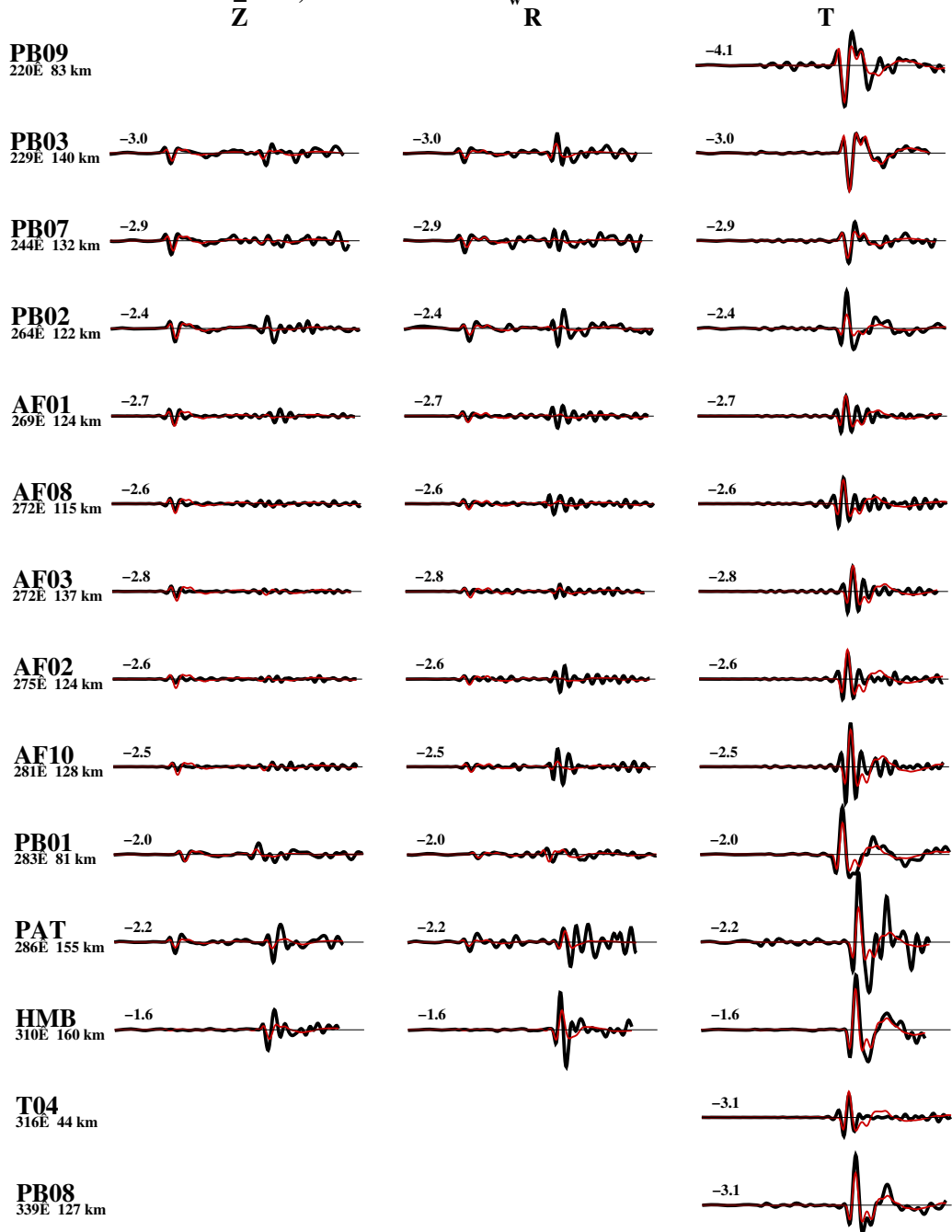


Figure B.2: Full waveform inversion results for Event 2010-04-18 07:03. Band pass filter: 0.5-5 s. Lines and labels as in Figure B.1.

100825\_0235, 10/ 8/25 2:35: 1  $M_w=4.8$  2-20s 114km DC:44%



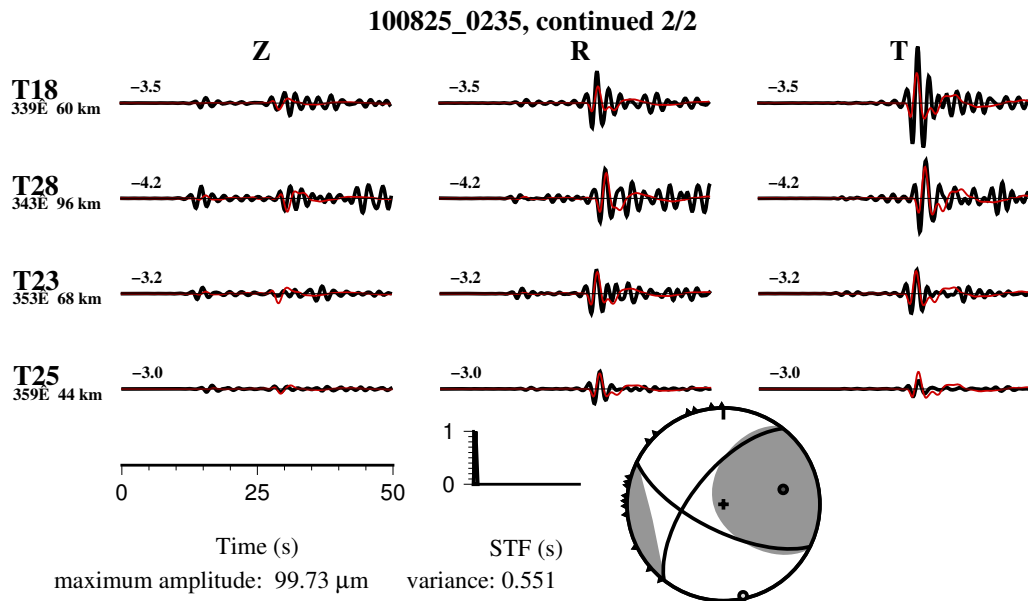
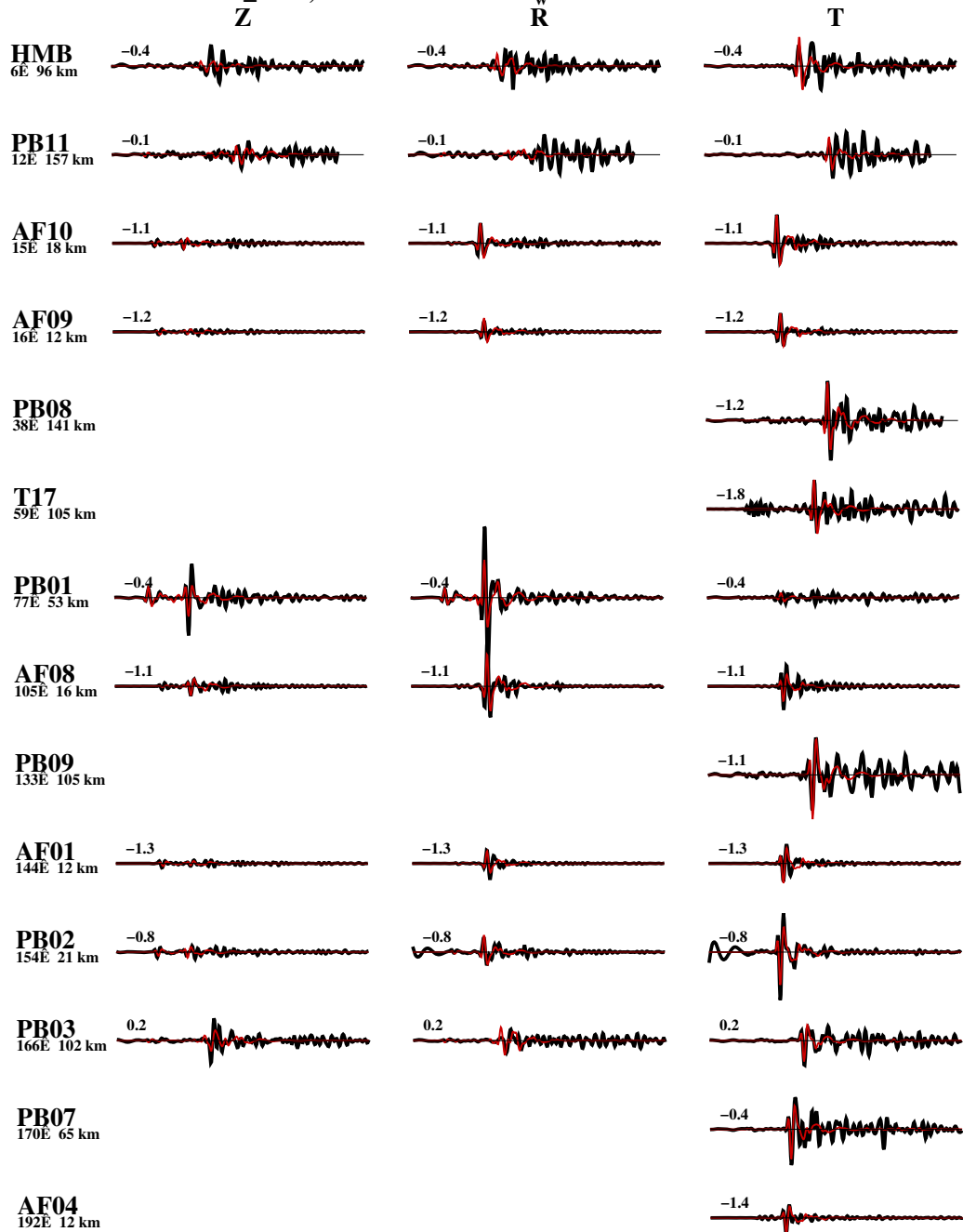


Figure B.3: Full waveform inversion results for Event 2010-08-25 02:35. Band pass filter: 2-20 s. Lines and labels as in Figure B.1.

101211\_0443, 10/12/11 4:43:40  $M_w=3.9$  1-5s 48km DC:87%



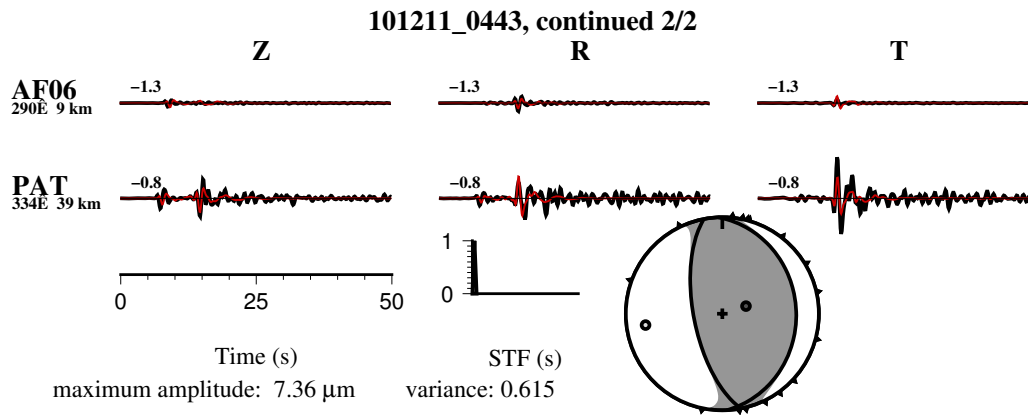
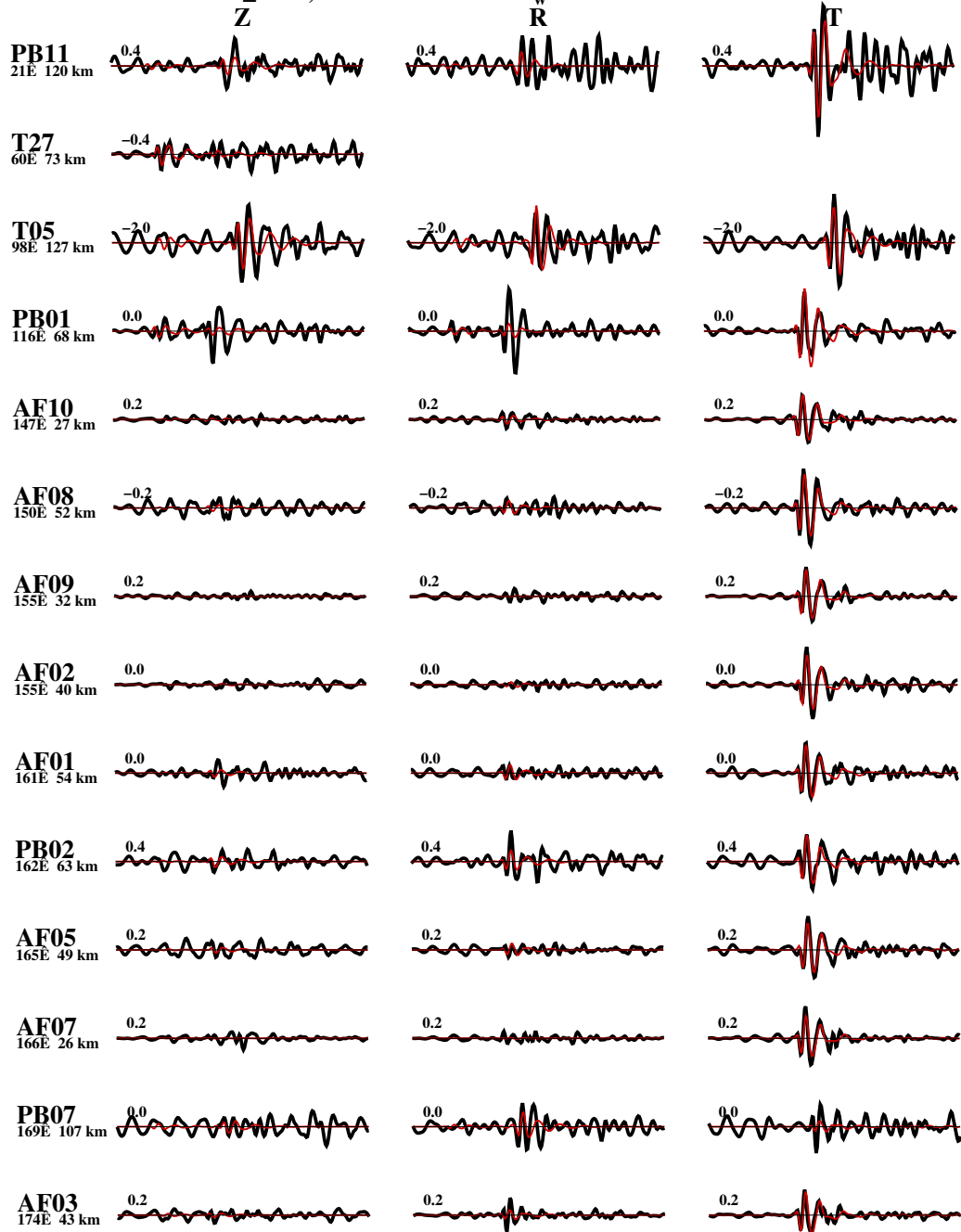


Figure B.4: Full waveform inversion results for Event 2010-12-11 04:43. Band pass filter: 1-5 s. Lines and labels as in Figure B.1.

111206\_1302, 11/12/ 6 13: 2:21  $M_w=3.6$  2-5s 75km DC:49%





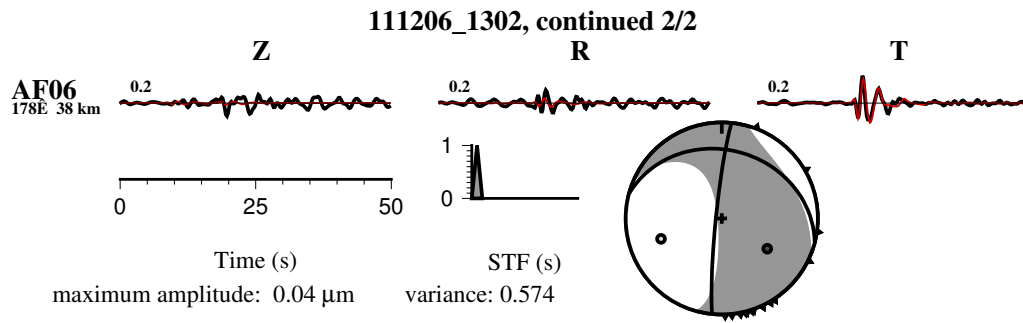
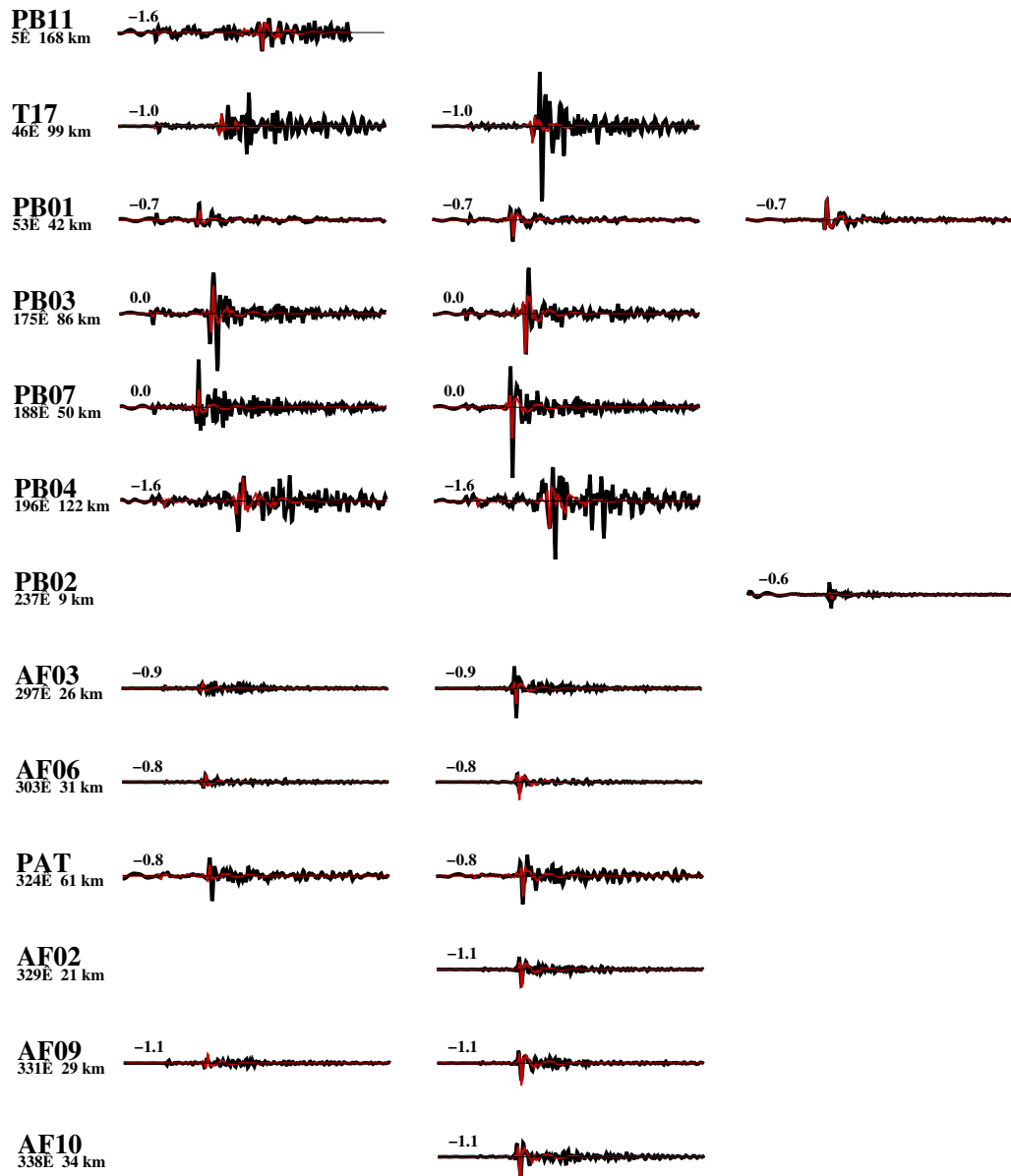


Figure B.5: Full waveform inversion results for Event 2011-02-06 13:02. Band pass filter: 2-5 s. Lines and labels as in Figure B.1.

110324\_2219, 11/ 3/24 22:19:23  $M_w=3.6$  0-5s 57km DC:96%



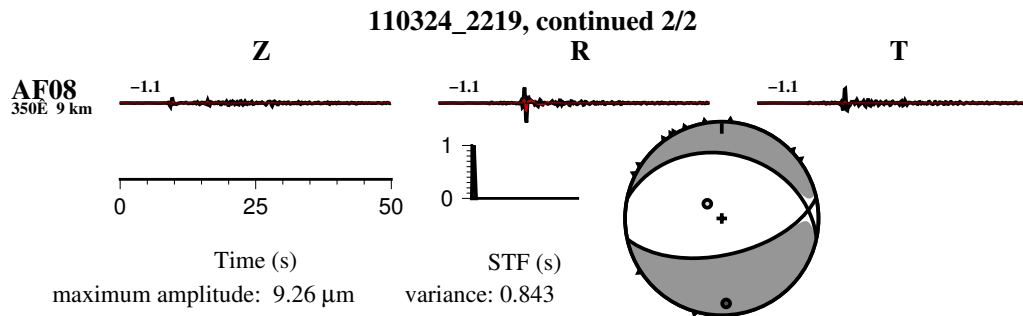
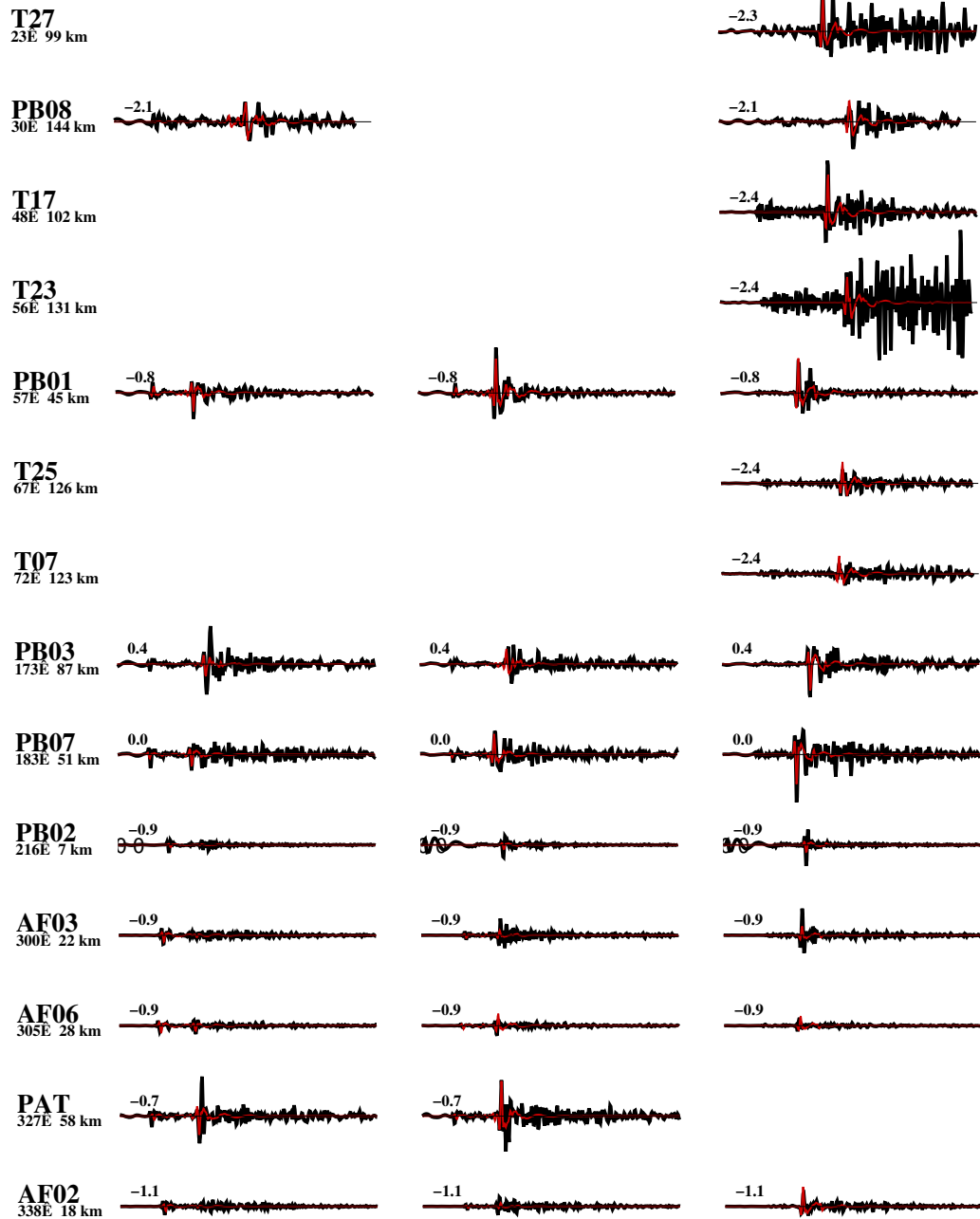


Figure B.6: Full waveform inversion results for Event 2011-03-24 22:19. Band pass filter: 0.5-5 s. Lines as and labels in Figure B.1.

110813\_2321, 11/ 8/13 23:21:31  $M_w=3.9$  0-5s 54km DC:90%



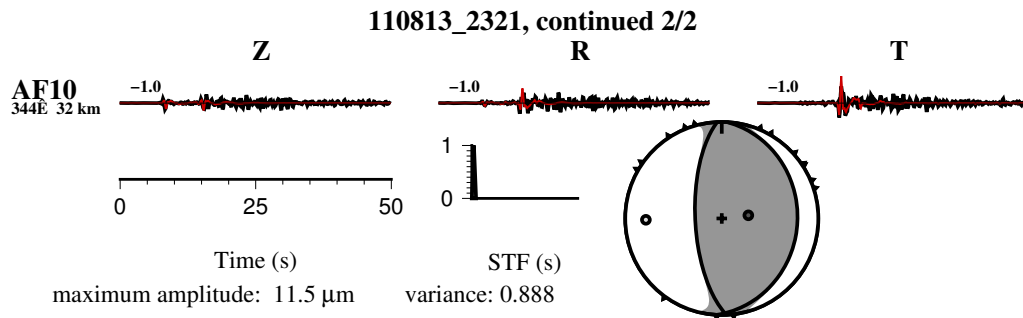


Figure B.7: Full waveform inversion results for Event 2011-08-13 23:21. Band pass filter: 0.5-5 s. Lines as and labels in Figure B.1.

110921\_1748, 11/ 9/21 17:48:49  $M_w=3.5$  0-5s 54km DC:48%

Z

R

T

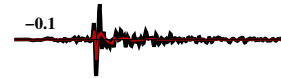
**PSG**  
13E 179 km



**HMB**  
33E 118 km



**PAT**  
44E 54 km



**PB08**  
51E 182 km



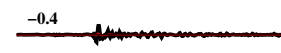
**AF07**  
70E 55 km



**AF10**  
71E 64 km



**AF06**  
82E 47 km



**AF02**  
83E 62 km



**AF03**  
88E 49 km



**AF08**  
91E 71 km



**AF05**  
93E 58 km



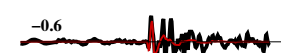
**AF01**  
96E 63 km



**PB02**  
104E 67 km



**PB09**  
117E 149 km



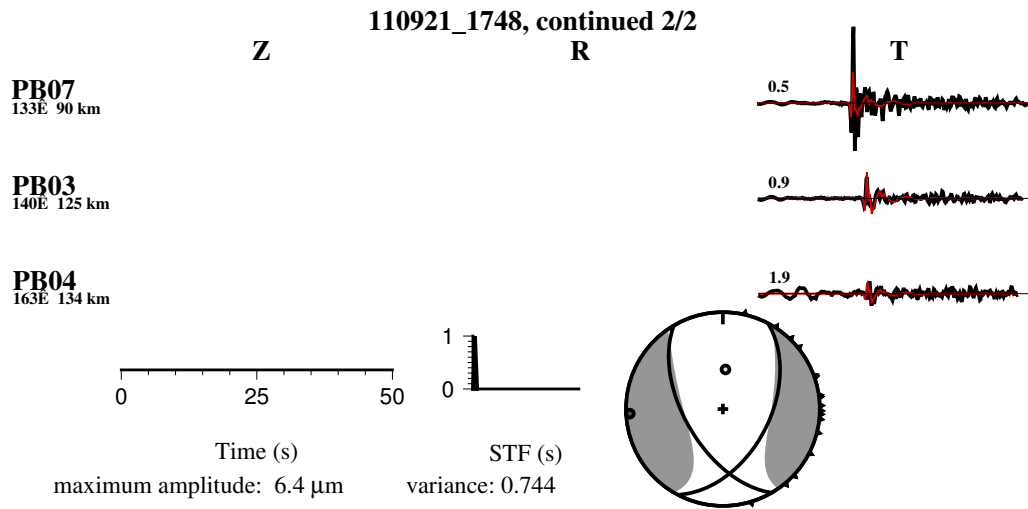
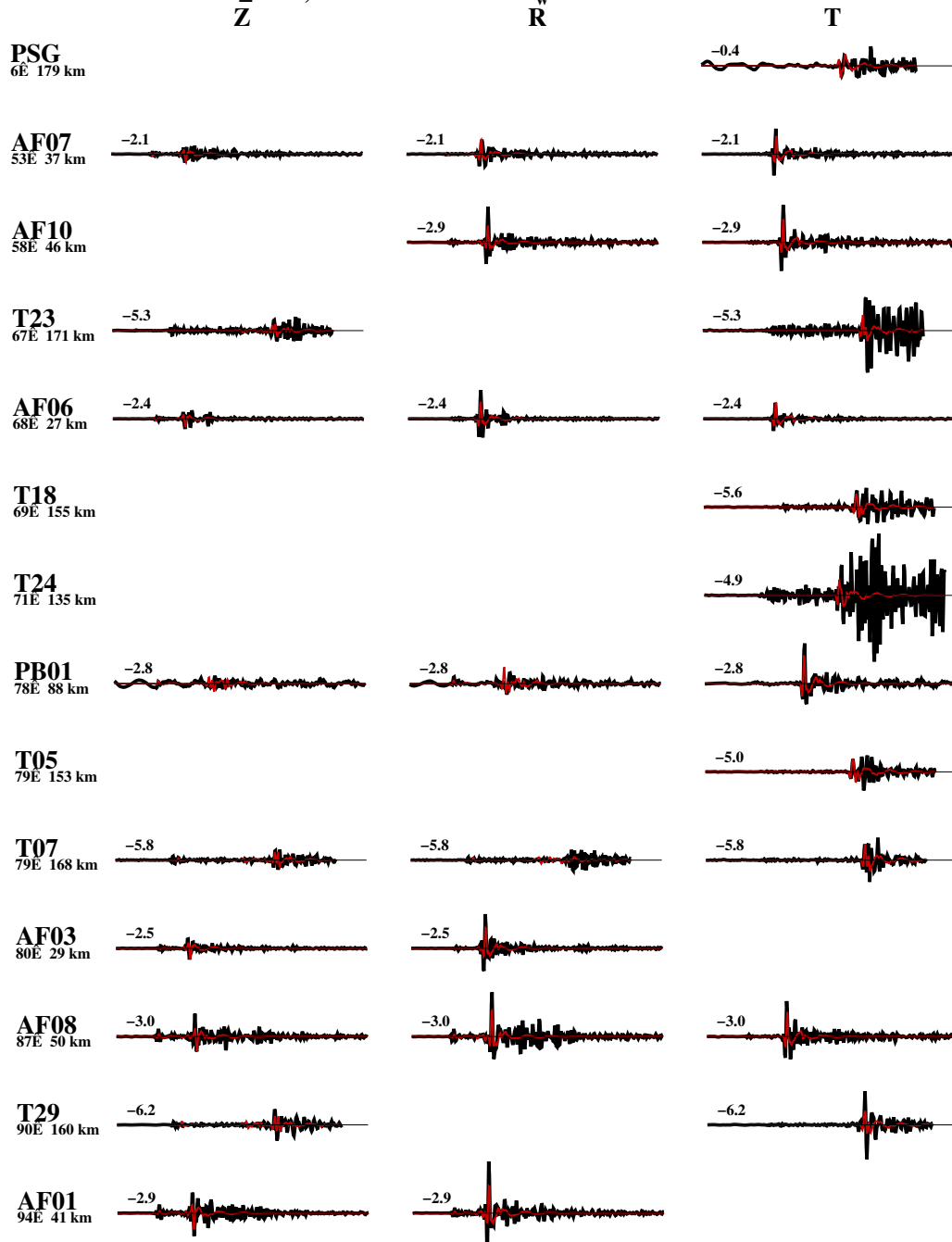


Figure B.8: Full waveform inversion results for Event 2011-09-21 17:48. Band pass filter: 0.5-5 s. Lines as and labels in Figure B.1.

120215\_1358, 12/ 2/15 13:58:56  $M_w=3.5$  0-5s 45km DC:70%





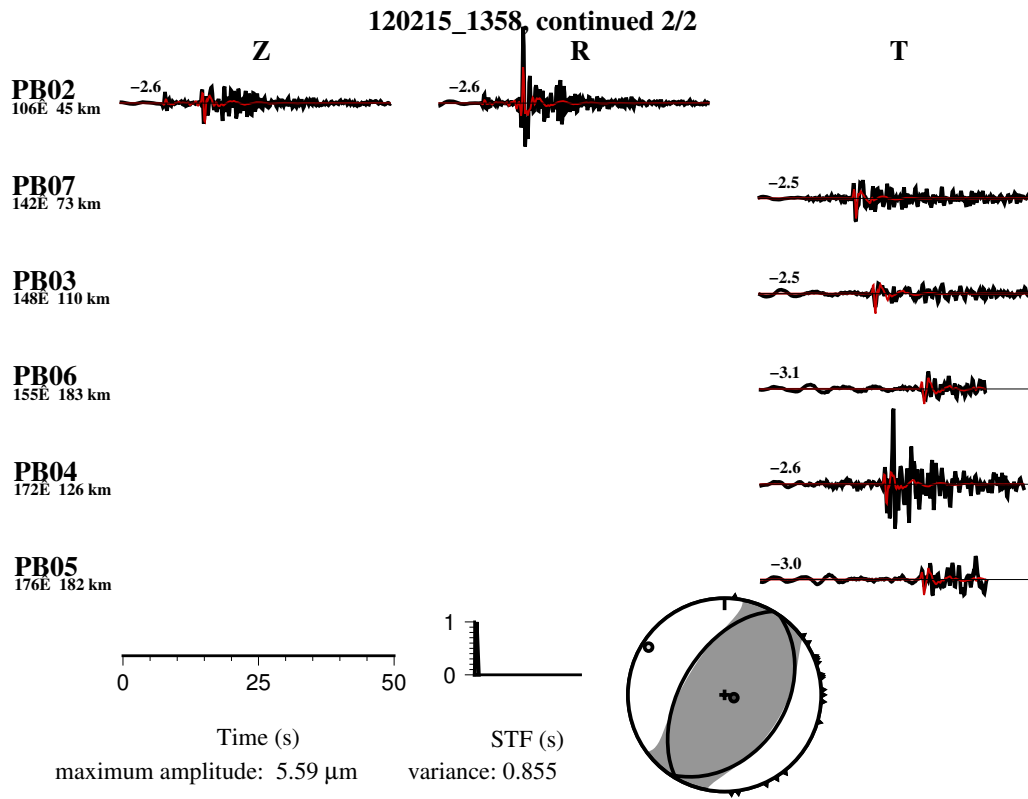
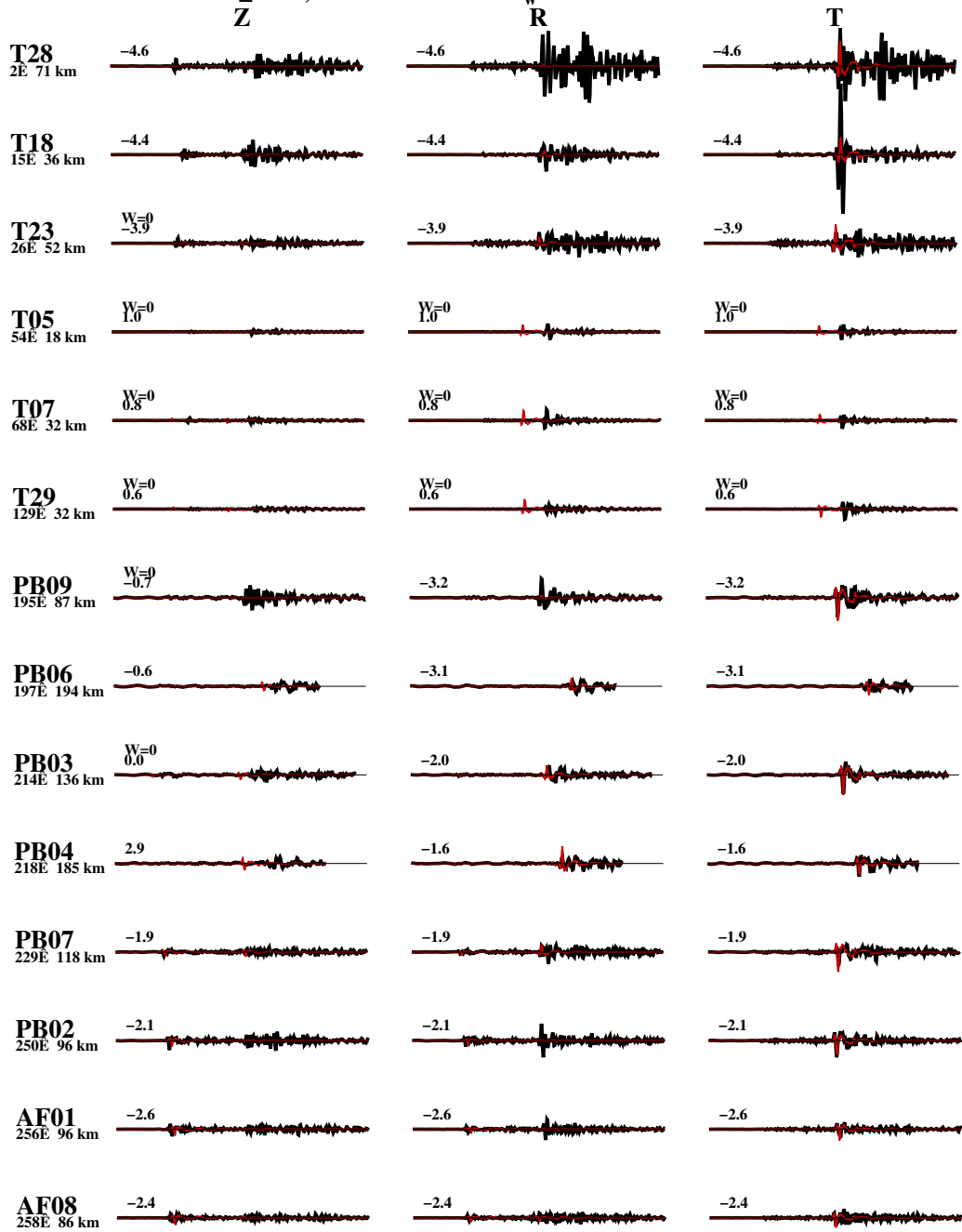


Figure B.9: Full waveform inversion results for Event 2012-02-15 13:58. Band pass filter: 0.5-5 s. Lines as and labels in Figure B.1.

120228\_0754, 12/ 2/28 7:54:10  $M_w=3.9$  0-5s 102km DC:66%



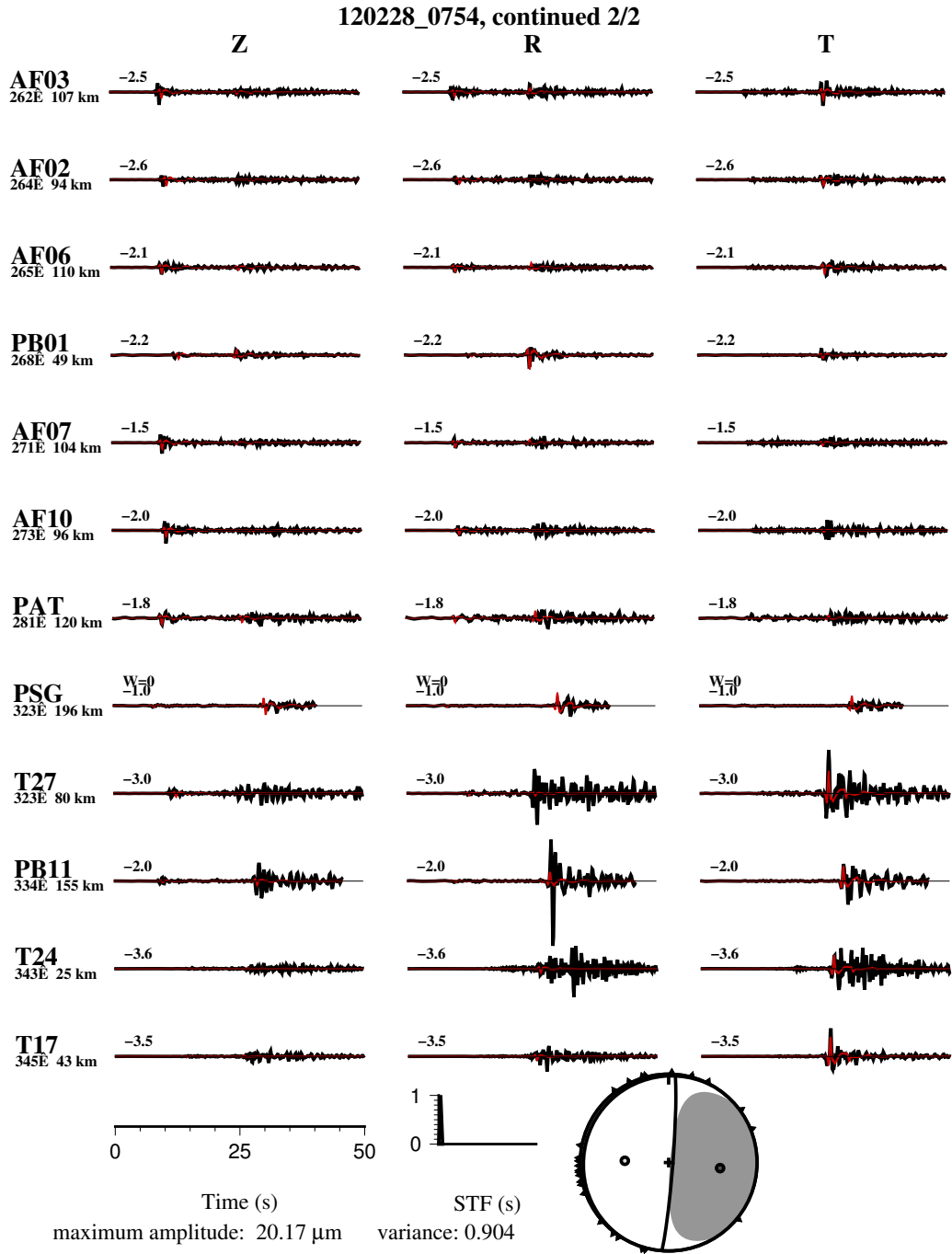


Figure B.10: Full waveform inversion results for Event 2012-02-28 07:54. Band pass filter: 0.5-5 s. Lines as and labels in Figure B.1.



# **Appendix C**

## **Mineral phase models**

**Table C.1:** Abbreviations of solid solution phases used for thermodynamic modeling

Abbreviation	Name	Endmembers	Composition
O(HP)	Olivine	Forsterite Fayalite	Mg <sub>2</sub> SiO <sub>4</sub> Fe <sub>2</sub> SiO <sub>4</sub>
Opx(HP)	Orthopyroxene	Enstatite Ferrosilite Ferric Opx endmember + Tschermak's substitutes	Mg <sub>2</sub> Si <sub>2</sub> O <sub>6</sub> Fe <sub>2</sub> Si <sub>2</sub> O <sub>6</sub> MgFe <sub>3+Al</sub> SiO <sub>6</sub> (Mg, Fe)Si → Al <sub>2</sub>
Cpx(HP)	Clinopyroxene	Hedenbergite Diopside Essenite Jadeite Acmite Ca-tschermaks pyroxene	CaFeSi <sub>2</sub> O <sub>6</sub> CaMgSi <sub>2</sub> O <sub>6</sub> CaAl <sub>2</sub> SiO <sub>6</sub> NaAlSi <sub>2</sub> O <sub>6</sub> NaFeSi <sub>2</sub> O <sub>6</sub> CaFe <sub>3+Al</sub> SiO <sub>6</sub>
Omph(GHP2)	Omphacite	Hedenbergite Diopside Jadeite Acmite	CaFeSi <sub>2</sub> O <sub>6</sub> CaMgSi <sub>2</sub> O <sub>6</sub> NaAlSi <sub>2</sub> O <sub>6</sub> NaFeSi <sub>2</sub> O <sub>6</sub>
Gt(HP)	Garnet	Spessartine Almandine Pyrope Grossular	Mn <sub>3</sub> Al <sub>2</sub> Si <sub>3</sub> O <sub>12</sub> Fe <sub>3</sub> Al <sub>2</sub> Si <sub>3</sub> O <sub>12</sub> Mg <sub>3</sub> Al <sub>2</sub> Si <sub>3</sub> O <sub>12</sub> Ca <sub>3</sub> Al <sub>2</sub> Si <sub>3</sub> O <sub>12</sub>
B	Brucite	Brucite Fe-Brucite	Mg(OH) <sub>2</sub> Fe(OH) <sub>2</sub>
Atg(PN)	Antigorite	Antigorite Fe-Antigorite + Tschermak's substitutes	Mg <sub>48</sub> Si <sub>34</sub> O <sub>85</sub> (OH) <sub>62</sub> Fe <sub>48</sub> Si <sub>34</sub> O <sub>85</sub> (OH) <sub>62</sub> (Mg, Fe)Si → Al <sub>2</sub>
Chl(HP)	Chlorite	Daphnite Amesite Clinochlore Al-free chlorite Mn-chlorite	Fe <sub>5</sub> Al <sub>2</sub> Si <sub>3</sub> O <sub>10</sub> (OH) <sub>8</sub> Mg <sub>4</sub> Al <sub>4</sub> Si <sub>2</sub> O <sub>10</sub> (OH) <sub>8</sub> Mg <sub>5</sub> Al <sub>2</sub> Si <sub>3</sub> O <sub>10</sub> (OH) <sub>8</sub> Mg <sub>6</sub> Si <sub>4</sub> O <sub>10</sub> (OH) <sub>8</sub> Mn <sub>5</sub> Al <sub>2</sub> Si <sub>3</sub> O <sub>10</sub> (OH) <sub>8</sub>
T	Talc	Talc Fe-Talc + Tschermak's substitutes	Mg <sub>3</sub> Si <sub>4</sub> O <sub>10</sub> (OH) <sub>2</sub> Fe <sub>3</sub> Si <sub>4</sub> O <sub>10</sub> (OH) <sub>2</sub> (Mg, Fe)Si → Al <sub>2</sub>
Amph(DPW)	Amphibole	Tremolite Ferroactinolite Pargasite Tschermakite Glaucophane	Ca <sub>2</sub> Mg <sub>5</sub> Si <sub>8</sub> O <sub>22</sub> (OH) <sub>2</sub> Ca <sub>2</sub> Fe <sub>5</sub> Si <sub>8</sub> O <sub>22</sub> (OH) <sub>2</sub> NaCa <sub>2</sub> Mg <sub>4</sub> Al <sub>3</sub> Si <sub>6</sub> O <sub>22</sub> (OH) <sub>2</sub> Ca <sub>2</sub> Mg <sub>3</sub> Al <sub>4</sub> Si <sub>6</sub> O <sub>22</sub> (OH) <sub>2</sub> Na <sub>2</sub> Mg <sub>3</sub> Al <sub>2</sub> Si <sub>8</sub> O <sub>22</sub> (OH) <sub>2</sub>

**Table C.2:** *Abbreviations of pure mineral phases used for thermodynamic modeling*

Abbreviation	Name	Composition
acti	Actinolite	$\text{Mg}_3\text{Ca}_2\text{Fe}_2\text{Si}_8\text{O}_{22}(\text{OH})_2$
coe	Coesite	$\text{SiO}_2$
qz	Quartz	$\text{SiO}_2$
law	Lawsonite	$\text{CaAl}_2\text{Si}_2\text{O}_7(\text{OH})_2 \cdot \text{H}_2\text{O}$
zo	Zoisite	$\text{Ca}_2\text{Al}_3\text{Si}_3\text{O}_{12}(\text{OH})$
ab	Albite	$\text{NaAlSi}_3\text{O}_8$





## Appendix D

# Quantification of a complex shortcut effect

- A homogeneous subsurface has no shortcut effect:  $\gamma = V_P/V_S$  (Fig. D.1).
- Slab-parallel layered anomalies have a shortcut effect that tends to smear  $\gamma$ -value to a value in between the the background  $V_P/V_S$ -value and the anomalous  $V_P/V_S$ -value. For a high- $V_P/V_S$ -anomaly I find:  $(V_P/V_S)_{\text{background}} < \gamma < (V_P/V_S)_{\text{anomaly}}$ . There is no azimuthal dependence on  $\gamma$  (Figs. D.2, D.3, D.4, D.5).
- I next model a geometry that resembles slab-normal, 15 km thick (i.e. overly wide), fluid-filled bend-faults (Fig. D.6), which are just as wide as the seismicity cluster. It has a shortcut effect that is different for different ray paths, even within the core network. This becomes immediately evident in low  $\epsilon$ -values, irrespective of the station geometry. Such a structure is capable of producing dispersive guided waves that might explain the early arriving phase, possibly of low frequency, observed at station PB02 (Fig. 5.14).
- A purely spherical anomaly around the seismicity cluster (Fig. D.7) has only a weak shortcut effect that is almost equal in all directions, so that for this geometry:  $\gamma \approx V_P/V_S$ , irrespective of the station configuration.
- A geometry that has a cylindrical shape of high  $V_P/V_S$  around the seismicity cluster and a slab-normal, overly wide bend-fault-like shape towards the the slab surface (Fig. D.8) produces linear  $\hat{\delta}t_p$  vs.  $\hat{\delta}t_s$  distribution on the core network and a scattered  $\hat{\delta}t_p$  vs.  $\hat{\delta}t_s$  distribution on the backbone network.

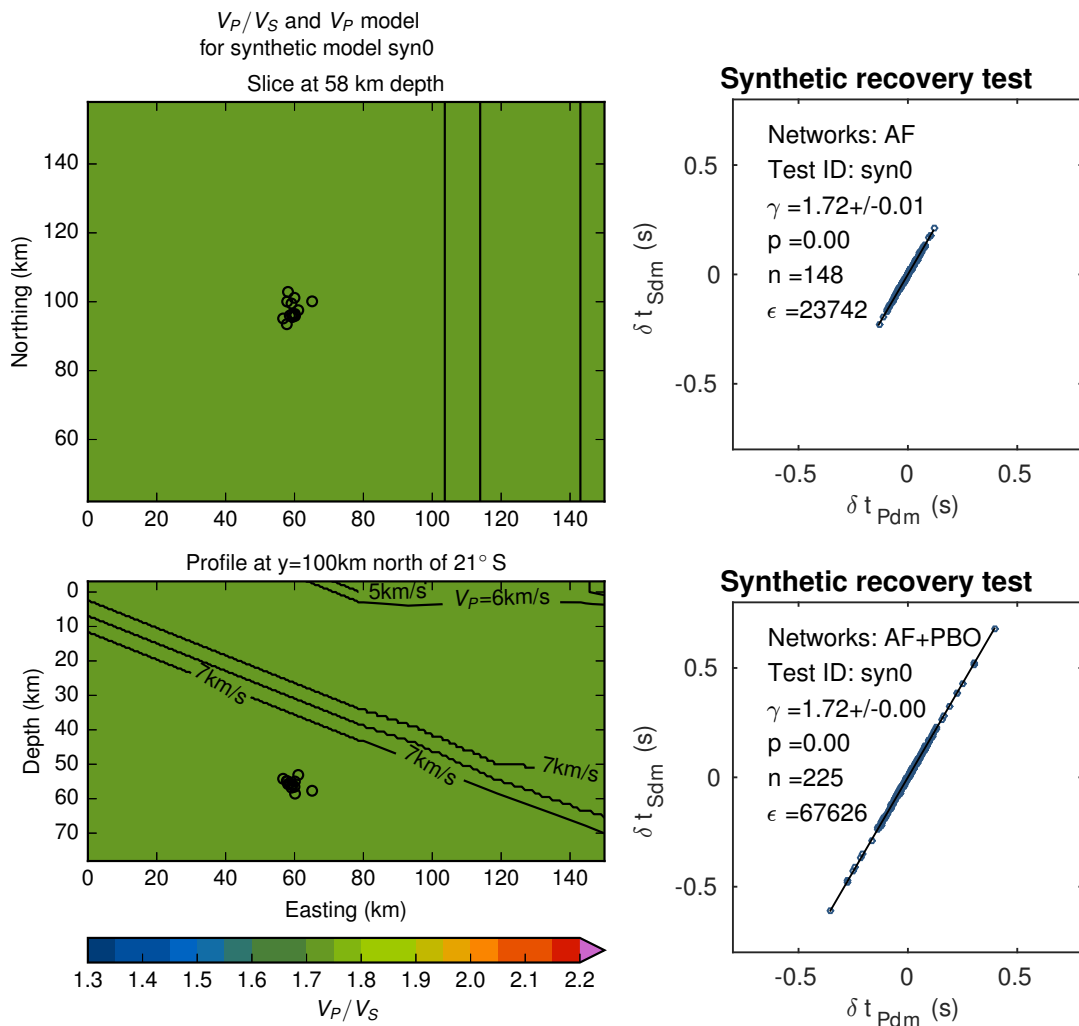


**Figure D.1:** Synthetic  $V_P/V_S$ - and  $V_P$ -model (left) and recovery tests with noise-free data (right), for the AF-network (top) and additional nearby stations from the PBO-network (bottom) for a velocity model with constant  $V_P/V_S$ .

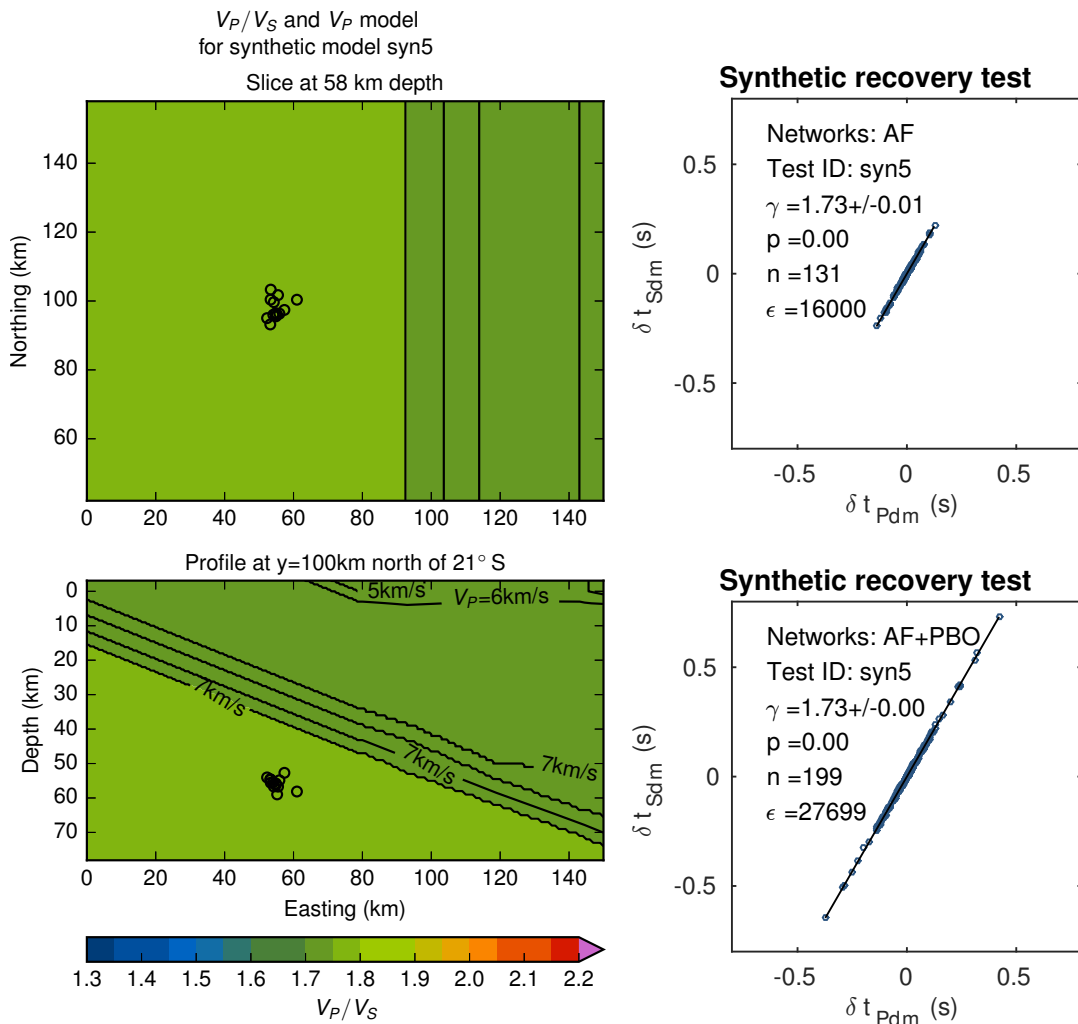


**Figure D.2:** As Fig. D.1, but for a  $V_P/V_S$  structure that represents a serpentinized mantle.

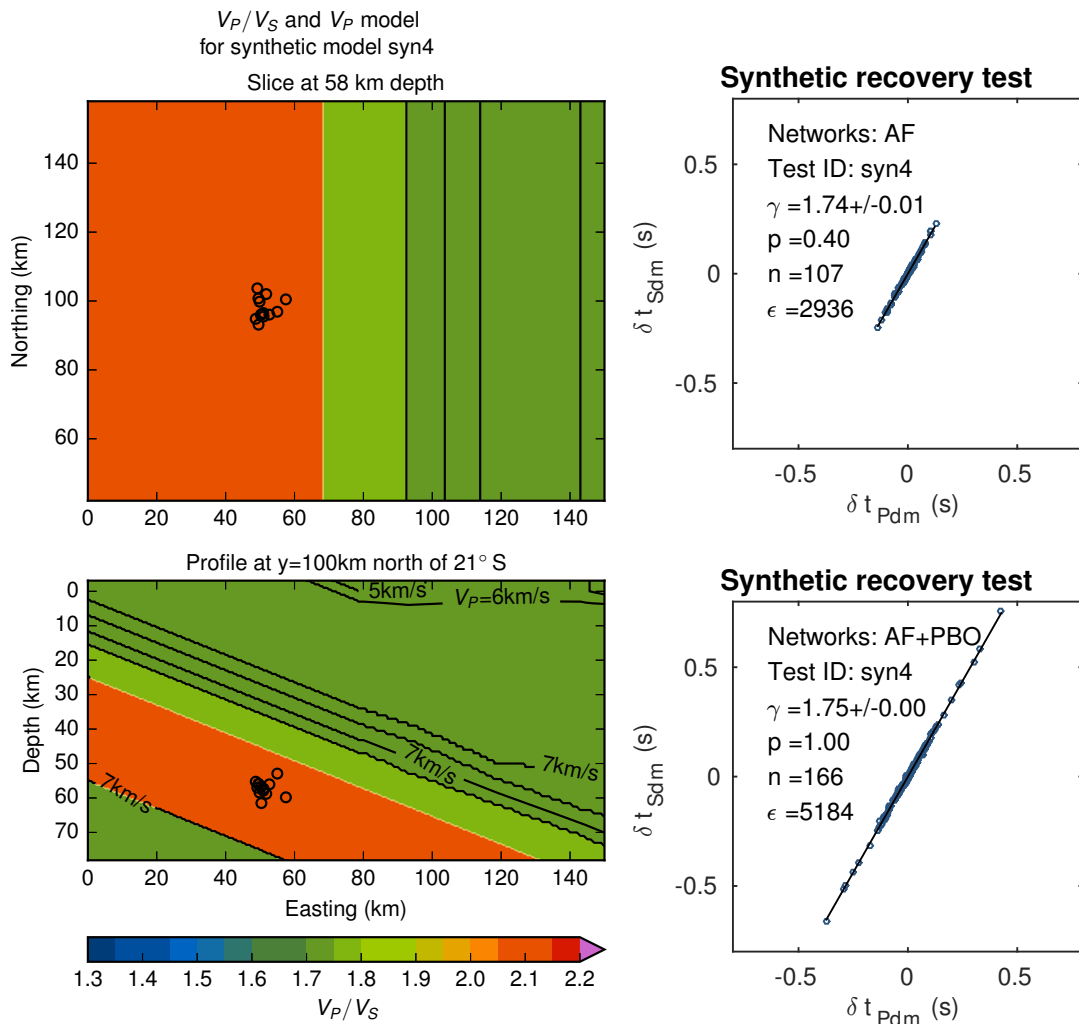


**Figure D.3:** As Fig. D.1, but for a  $V_P/V_S$  structure that represents a layer with a fractured, fluid-filled serpentinite in the oceanic mantle.

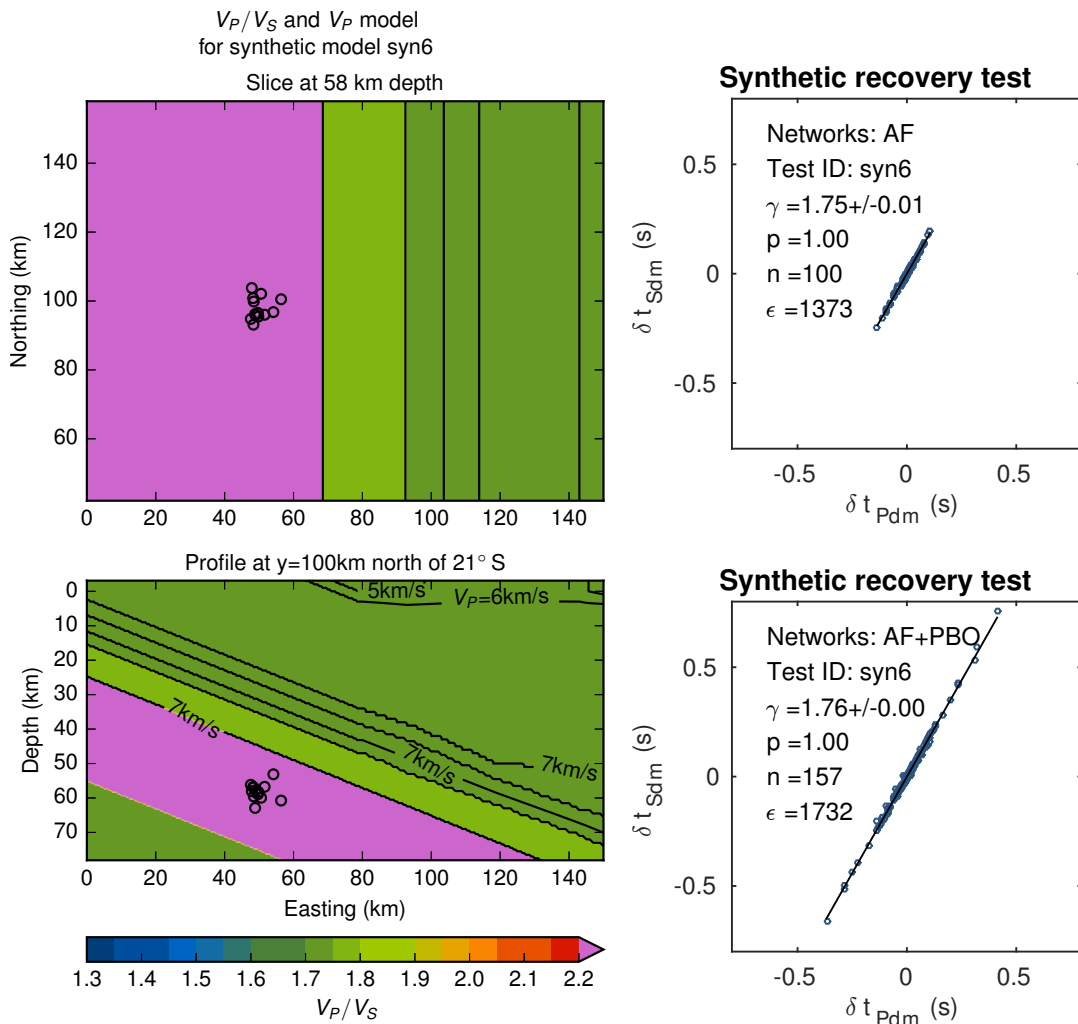


**Figure D.4:** As Fig. D.1, but for a  $V_P/V_S$  structure that represents a layer with an extremely high  $V_P/V_S$ -value.

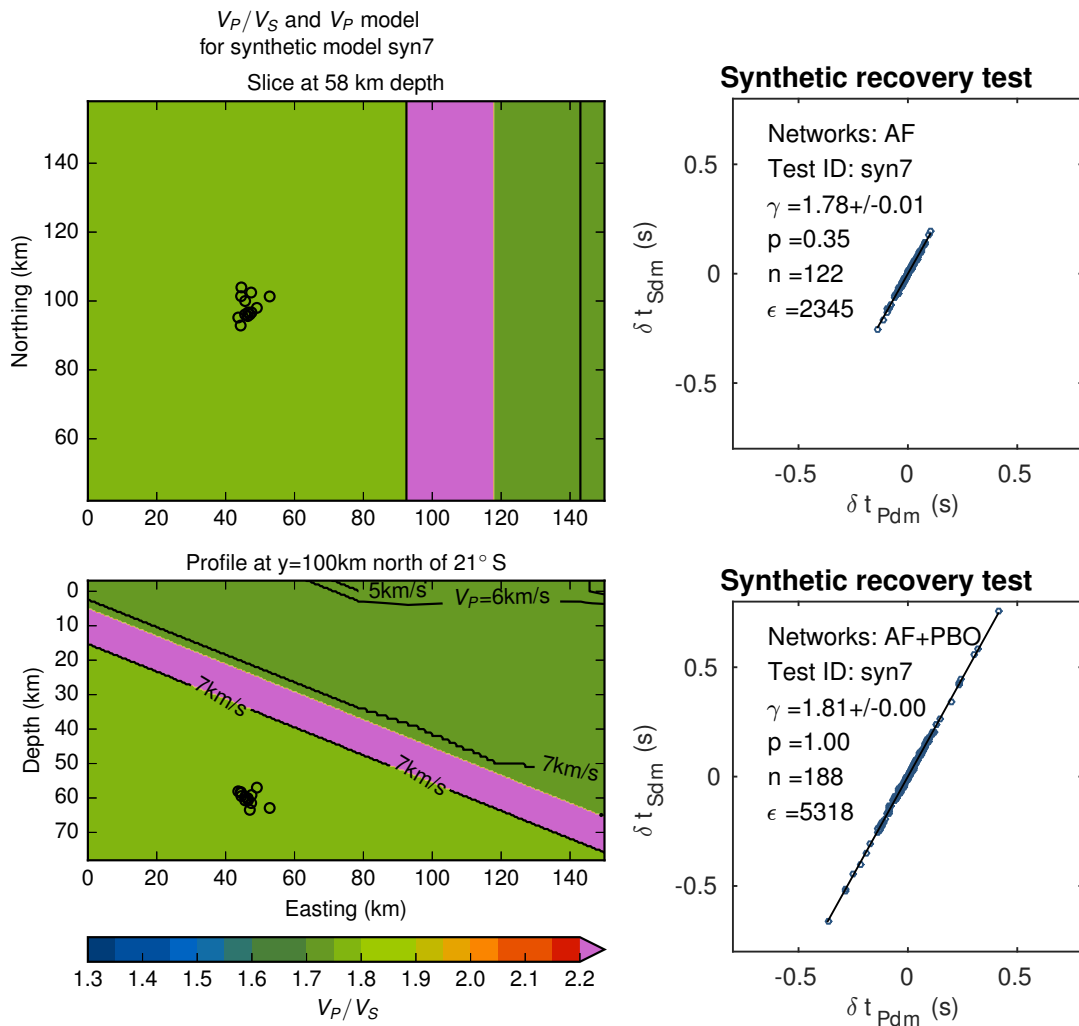


**Figure D.5:** As Fig. D.1, but for a  $V_P/V_S$  structure that represents a completely serpentinized mantle an overlying extremely high  $V_P/V_S$ -value in the oceanic crust.

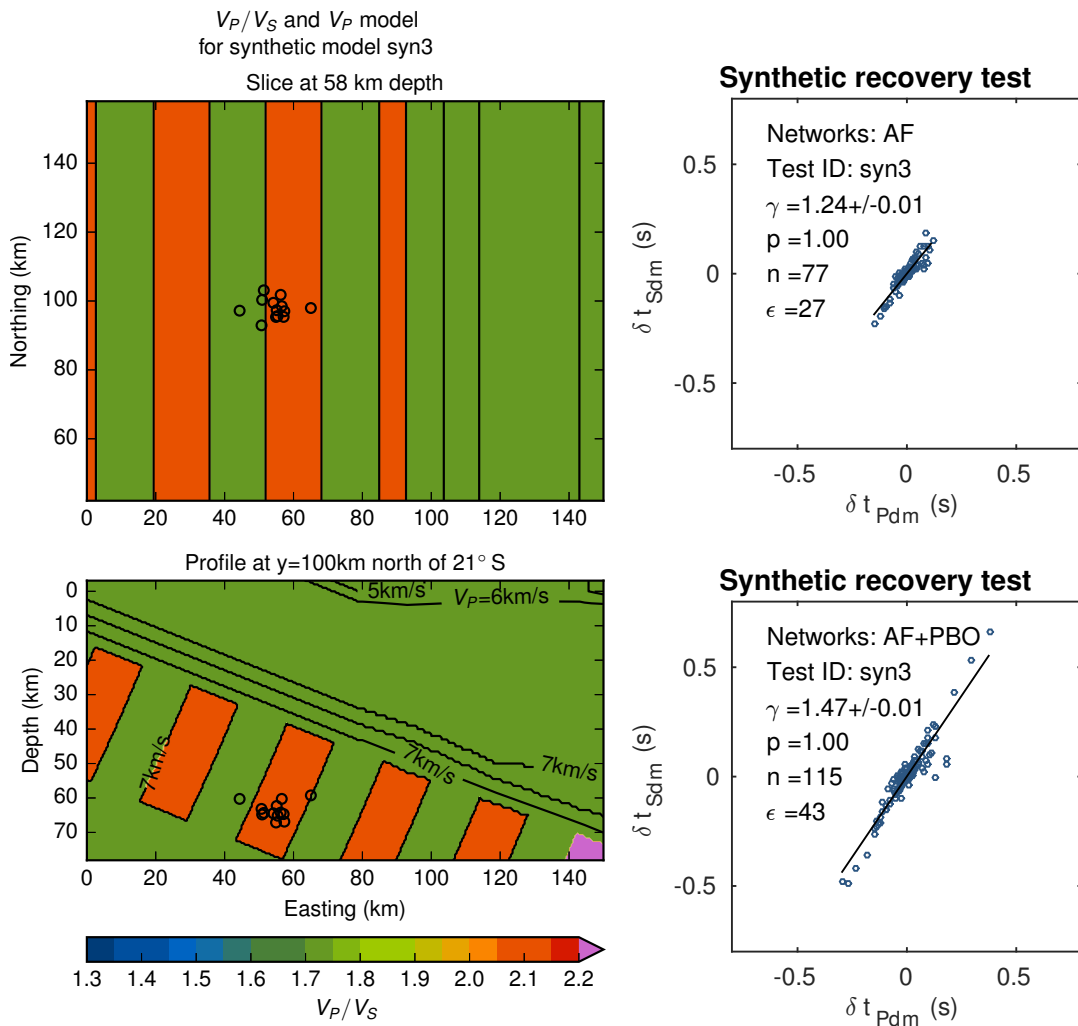


**Figure D.6:** As Fig. D.1, but for a  $V_P/V_S$  structure that represents a set of fractured and fluid-filled bend-faults in the oceanic mantle.

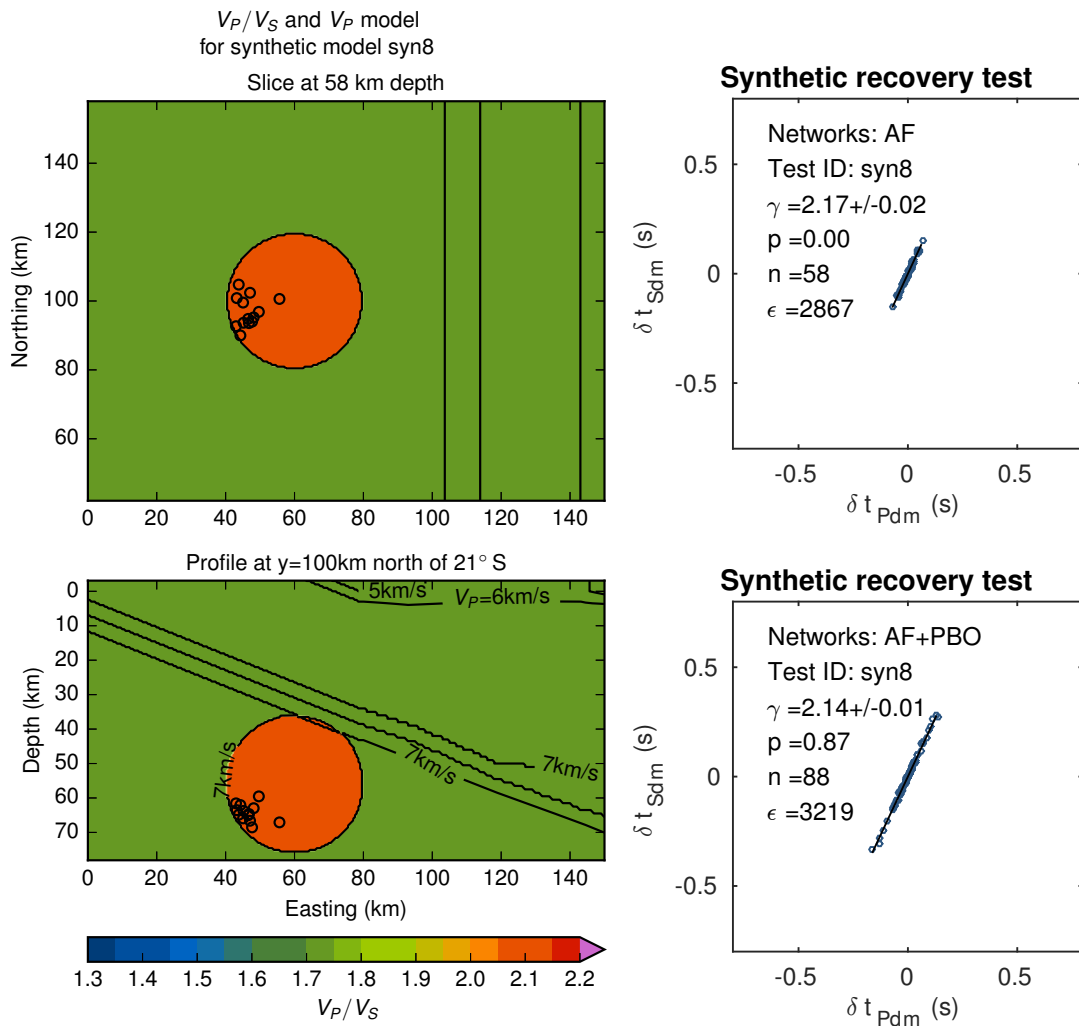


**Figure D.7:** As Fig. D.1, but for a  $V_P/V_S$  structure that represents a sphere of fractured and fluid-filled serpentinite around the seismicity cluster.



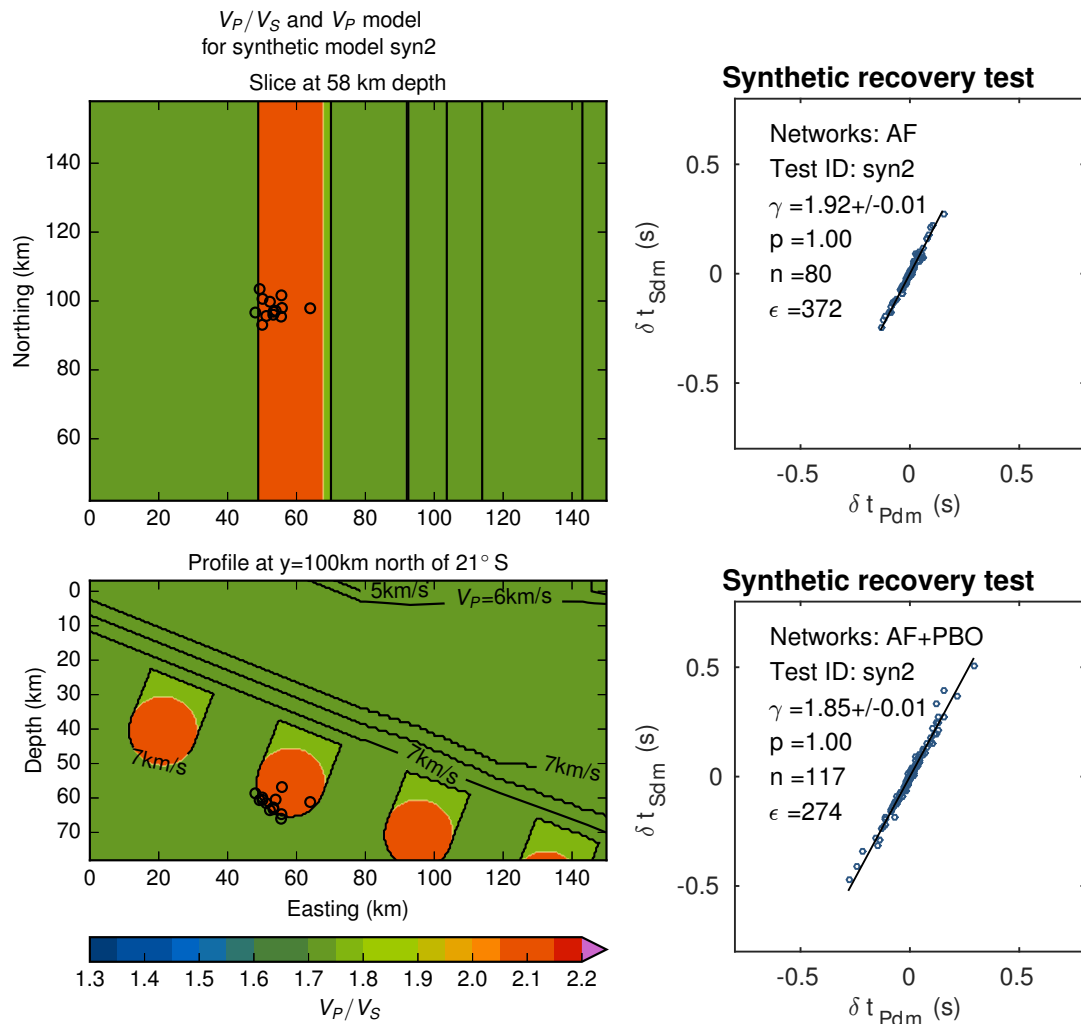


**Figure D.8:** As Fig. D.1, but for a  $V_P/V_S$  structure that represents a set of serpentinized bend-faults in the oceanic mantle with cylindrical fractured and fluid-filled tips.



# Bibliography

- Abramson, E., Brown, J., Slutsky, L., and Zaug, J. (1997). The elastic constants of San Carlos olivine to 17 GPa. *Journal of Geophysical Research: Solid Earth*, 102(B6):12253–12263.
- Angermann, D., Klotz, J., and Reigber, C. (1999). Space-geodetic estimation of the Nazca-South America Euler vector. *Earth and Planetary Science Letters*, 171(3):329–334.
- Audet, P., Bostock, M. G., Christensen, N. I., and Peacock, S. M. (2009). Seismic evidence for overpressured subducted oceanic crust and megathrust fault sealing. *Nature*, 457(7225):76–78.
- Auld, B. A. (1973). *Acoustic fields and waves in solids*.
- Backus, G. E. (1962). Long-wave elastic anisotropy produced by horizontal layering. *Journal of Geophysical Research*, 67(11):4427–4440.
- Bezacier, L., Reynard, B., Bass, J. D., Sanchez-Valle, C., and Van de Moortèle, B. (2010). Elasticity of antigorite, seismic detection of serpentinites, and anisotropy in subduction zones. *Earth and Planetary Science Letters*, 289(1):198–208.
- Bloch, W., Kummerow, J., Salazar, P., Wigger, P., and Shapiro, S. A. (2014). High-resolution image of the North Chilean subduction zone: seismicity, reflectivity and fluids. *Geophysical Journal International*, 197(3):1744–1749.
- Bouchon, M. (1981). A simple method to calculate Green's functions for elastic layered media. *Bulletin of the Seismological Society of America*, 71(4):959–971.
- Braeck, S. and Podladchikov, Y. (2007). Spontaneous thermal runaway as an ultimate failure mechanism of materials. *Physical Review Letters*, 98(9):095504.
- Brudzinski, M., Thurber, C., Hacker, B., and Engdahl, E. (2007). Global Prevalence of Double Benioff Zones. *Science*, 316:1472–1474.
- Chlieh, M., de Chabalier, J., Ruegg, J., Armijo, R., Dmowska, R., Campos, J., and Feigl, K. (2004). Crustal deformation and fault slip during the seismic cycle in the North Chile subduction zone, from GPS and InSAR observations. *Geophys. J. Int.*, 158:695–711.

- Chlieh, M., Perfettini, H., Tavera, H., Avouac, J.-P., Remy, D., Nocquet, J.-M., Rolandone, F., Bondoux, F., Gabalda, G., and Bonvalot, S. (2011). Interseismic coupling and seismic potential along the Central Andes subduction zone. *Journal of Geophysical Research: Solid Earth*, 116(B12).
- Chollet, M., Daniel, I., Koga, K. T., Morard, G., and Van De Moortèle, B. (2011). Kinetics and mechanism of antigorite dehydration: implications for subduction zone seismicity. *Journal of Geophysical Research: Solid Earth (1978–2012)*, 116(B4).
- Comte, D., Carrizo, D., Roecker, S., Ortega-Culaciati, F., and Peyrat, S. (2016). Three-dimensional elastic wave speeds in the northern Chile subduction zone: variations in hydration in the supraslab mantle. *Geophysical Journal International*, 207(2):1080–1105.
- Comte, D., Dorbath, L., Pardo, M., Monfret, T., Haessler, H., Rivera, L., Frogneux, M., Glass, B., and Meneses, C. (1999). A double-layered seismic zone in Arica, northern Chile. *Geophysical Research Letters*, 26(13):1965–1968.
- Comte, D. and Suarez, G. (1994). An inverted double seismic zone in Chile: Evidence of phase transformation in the subducted slab. *Science*, 263:212–215.
- Connolly, J. (2005). Computation of phase equilibria by linear programming: a tool for geodynamic modeling and its application to subduction zone decarbonation. *Earth and Planetary Science Letters*, 236(1):524–541.
- Connolly, J. (2009). The geodynamic equation of state: what and how. *Geochemistry, Geophysics, Geosystems*, 10(10).
- Connolly, J. (2017). Perple\_X Thermodynamic Data Files, [http://www.perplex.ethz.ch/perplex\\_thermodynamic\\_data\\_file.html](http://www.perplex.ethz.ch/perplex_thermodynamic_data_file.html). online.
- Dawson, P., Chouet, B., and Pitt, M. (2015). Tomographic image of a seismically active volcano: Mammoth Mountain, California. *Journal of Geophysical Research: Solid Earth*.
- Delouis, B., Pardo, M., Legrand, D., and Monfret, T. (2009). The Mw 7.7 Tocopilla earthquake of 14 November 2007 at the southern edge of the northern Chile seismic gap: Rupture in the deep part of the coupled plate interface. *Bulletin of the Seismological Society of America*, 99(1):87–94.
- Dobson, D. P., Meredith, P. G., and Boon, S. A. (2002). Simulation of subduction zone seismicity by dehydration of serpentine. *Science*, 298(5597):1407–1410.
- Dorbath, C., Gerbault, M., Carlier, G., and Guiraud, M. (2008). Double seismic zone of the Nazca plate in northern Chile: High-resolution velocity structure, petrological implications, and thermomechanical modeling. *Geochemistry, Geophysics, Geosystems*, 9(7).

## BIBLIOGRAPHY

---

- Dziewonski, A., Chou, T.-A., and Woodhouse, J. (1981). Determination of earthquake source parameters from waveform data for studies of global and regional seismicity. *Journal of Geophysical Research: Solid Earth*, 86(B4):2825–2852.
- Eberhart-Phillips, D. and Bannister, S. (2010). 3-D imaging of Marlborough, New Zealand, subducted plate and strike-slip fault systems. *Geophysical Journal International*, 182(1):73–96.
- Ekström, G., Nettles, M., and Dziewoński, A. (2012). The global CMT project 2004–2010: Centroid-moment tensors for 13,017 earthquakes. *Physics of the Earth and Planetary Interiors*, 200:1–9.
- Evans, J. R., Eberhart-Phillips, D., and Thurber, C. (1994). User's manual for SIMULPS12 for imaging Vp and Vp/Vs; a derivative of the "Thurber" tomographic inversion SIMUL3 for local earthquakes and explosions. Technical report, US Geological Survey,.
- Faccenda, M., Gerya, T., Mancktelow, N., and Moresi, L. (2012). Fluid flow during the slab unbending and dehydration: Implications for intermediate-depth seismicity, slab weakening and deep water recycling. *Geochem. Geophys. Geosyst.*, 13(1):Q01010.
- Frohlich, C. (2006). *Deep earthquakes*. Cambridge university press.
- Garboczi, E., Snyder, K., Douglas, J., and Thorpe, M. (1995). Geometrical percolation threshold of overlapping ellipsoids. *Physical review E*, 52(1):819–828.
- GFZ and IGP (2006). IPOC Seismic Network, Integrated Plate Boundary Observatory Chile. Other/Seismic Network.
- Gonzalez, G., Cembrano, J., Carrizo, D., Macci, A., and Schneider, H. (2003). The link between forearc tectonics and Pliocene–Quaternary deformation of the Coastal Cordillera, northern Chile. *J. South Am. Earth Sci.*, 16(5):321–342.
- Gräber, F. M. and Asch, G. (1999). Three-dimensional models of P wave velocity and P-to-S velocity ratio in the southern central Andes by simultaneous inversion of local earthquake data. *Journal of Geophysical Research: Solid Earth*, 104(B9):20237–20256.
- Green, H. W. and Houston, H. (1995). The mechanics of deep earthquakes. *Annual Review of Earth and Planetary Sciences*, 23(1):169–213.
- Hacker, B., Peacock, S., Abers, G., and Holloway, S. (2003a). Are intermediate-depth earthquakes in subducting slabs linked to metamorphic dehydration reactions? *J. Geophys. Res.*, 108:2030.
- Hacker, B. R. and Abers, G. A. (2004). Subduction Factory 3: An Excel worksheet and macro for calculating the densities, seismic wave speeds, and H<sub>2</sub>O contents of minerals and rocks at pressure and temperature. *Geochemistry, Geophysics, Geosystems*, 5(1).

- Hacker, B. R., Abers, G. A., and Peacock, S. M. (2003b). Subduction factory 1. Theoretical mineralogy, densities, seismic wave speeds, and H<sub>2</sub>O contents. *Journal of Geophysical Research: Solid Earth*, 108(B1).
- Hardebeck, J. L. and Shearer, P. M. (2002). A new method for determining first-motion focal mechanisms. *Bull. Seismol. Soc. Am.*, 92:2264–2276.
- Hardebeck, J. L. and Shearer, P. M. (2003). Using S/P Amplitude Ratios to Constrain the Focal Mechanisms of Small Earthquakes. *Bull. Seismol. Soc. Am.*, 93:2434–2444.
- Hayes, G. P., Herman, M. W., Barnhart, W. D., Furlong, K. P., Riquelme, S., Benz, H. M., Bergman, E., Barrientos, S., Earle, P. S., and Samsonov, S. (2014). Continuing megathrust earthquake potential in Chile after the 2014 Iquique earthquake. *Nature*, 512(7514):295–298.
- Hayes, G. P., Wald, D. J., and Johnson, R. L. (2012). Slab1. 0: A three-dimensional model of global subduction zone geometries. *Journal of Geophysical Research: Solid Earth*, 117(B1).
- Healy, D., Reddy, S. M., Timms, N. E., Gray, E. M., and Brovarone, A. V. (2009). Trench-parallel fast axes of seismic anisotropy due to fluid-filled cracks in subducting slabs. *Earth and Planetary Science Letters*, 283(1):75–86.
- Heit, B. S. (2006). *Teleseismic tomographic images of the Central Andes at 21 S and 25.5 S: an inside look at the Altiplano and Puna plateaus*. Geoforschungszentrum.
- Holland, T. and Powell, R. (1991). A Compensated-Redlich-Kwong (CORK) equation for volumes and fugacities of CO<sub>2</sub> and H<sub>2</sub>O in the range 1 bar to 50 kbar and 100–1600 C. *Contributions to Mineralogy and Petrology*, 109(2):265–273.
- Holland, T. and Powell, R. (1998). An internally consistent thermodynamic data set for phases of petrological interest. *Journal of metamorphic Geology*, 16(3):309–343.
- Husen, S., Kissling, E., Flueh, E., and Asch, G. (1999). Accurate hypocentre determination in the seismogenic zone of the subducting Nazca Plate in northern Chile using a combined on-/offshore network. *Geophysical Journal International*, 138(3):687–701.
- Igarashi, T., Matsuzawa, T., Umino, N., and Hasegawa, A. (2001). Spatial distribution of focal mechanisms for interplate and intraplate earthquakes associated with the subducting Pacific plate beneath the northeastern Japan arc: A triple-planed deep seismic zone. *Journal of Geophysical Research: Solid Earth*, 106(B2):2177–2191.
- Incel, S., Hilaiet, N., Labrousse, L., John, T., Deldicque, D., Ferrand, T., Wang, Y., Renner, J., Morales, L., and Schubnel, A. (2017). Laboratory earthquakes triggered during eclogitization of lawsonite-bearing blueschist. *Earth and Planetary Science Letters*, 459:320–331.

## BIBLIOGRAPHY

---

- Ismail, W. B. and Mainprice, D. (1998). An olivine fabric database: an overview of upper mantle fabrics and seismic anisotropy. *Tectonophysics*, 296(1):145–157.
- Ito, K. (1990). Effects of H<sub>2</sub>O on elastic wave velocities in ultrabasic rocks at 900 C under 1 GPa. *Physics of the earth and planetary interiors*, 61(3-4):260–268.
- Ito, K. (1999). Seismogenic layer, reflective lower crust, surface heat flow and large inland earthquakes. *Tectonophysics*, 306:423–433.
- John, T., Medvedev, S., Rüpke, L. H., Andersen, T. B., Podladchikov, Y. Y., and Austrheim, H. (2009). Generation of intermediate-depth earthquakes by self-localizing thermal runaway. *Nature Geoscience*, 2(2):137–140.
- John, T., Scherer, E. E., Schenk, V., Herms, P., Halama, R., and Garbe-Schönberg, D. (2010). Subducted seamounts in an eclogite-facies ophiolite sequence: the Andean Raspas Complex, SW Ecuador. *Contributions to Mineralogy and Petrology*, 159(2):265–284.
- Jung, H., Fei, Y., Silver, P. G., and Green, H. W. (2009). Frictional sliding in serpentine at very high pressure. *Earth and Planetary Science Letters*, 277(1):273–279.
- Jung, H., Green, H. W., and Dobrzhinetskaya, L. F. (2004). Intermediate-depth earthquake faulting by dehydration embrittlement with negative volume change. *Nature*, 428(6982):545–549.
- Kelemen, P. B. and Hirth, G. (2007). A periodic shear-heating mechanism for intermediate-depth earthquakes in the mantle. *Nature*, 446(7137):787–790.
- Kern, H. and Schenk, V. (1988). A model of velocity structure beneath Calabria, southern Italy, based on laboratory data. *Earth and planetary science letters*, 87(3):325–337.
- Kirby, S. H. (1987). Localized polymorphic phase transformations in high-pressure faults and applications to the physical mechanism of deep earthquakes. *Journal of Geophysical Research: Solid Earth*, 92(B13):13789–13800.
- Klotz, J., Abolghasem, A., Khazaradze, G., Heinze, B., Vietor, T., Hackney, R., Bataille, K., Maturna, R., Viramonte, J., and Perdomo, R. (2006). Long-Term Signals in the Present-Day Deformation Field of the Central and Southern Andes and Constraints on the Viscosity of the Earth's Upper Mantle. In Oncken, O., Chong, G., Franz, G., Giese, P., Götze, H.-J., Ramos, V. A., Strecker, M. R., and Wigger, P., editors, *The Andes*, pages 65–89. Springer Verlag, Berlin, Heidelberg.
- Kono, Y., Ishikawa, M., and Arima, M. (2007). Effect of H<sub>2</sub>O released by dehydration of serpentine and chlorite on compressional wave velocities of peridotites at 1GPa and up to 1000 C. *Physics of the Earth and Planetary Interiors*, 161(3):215–223.
- Koulakov, I., Sobolev, S., and Asch, G. (2006). P- and S- velocity images of the lithosphere-asthenosphere system in the Central Andes from local-source tomographic inversion. *Geophys. J. Int.*, 167:106–126.

- Kummerow, J., Shapiro, S. A., Häring, M., and Asanuma, H. (2010). Application of a Waveform Similarity- Based Location Algorithm to the Basel 1 Microseismic Data. *PHASE Annual Report*, pages 15–21.
- Lamb, S. (2006). Shear stresses on megathrusts: Implications for mountain building behind subduction zones. *J. Geophys. Res.*, 111(B7):B07401.
- Lin, G., Amelung, F., Shearer, P. M., and Okubo, P. G. (2015). Location and size of the shallow magma reservoir beneath Kīlauea caldera, constraints from near-source Vp/Vs ratios. *Geophysical Research Letters*, 42(20):8349–8357.
- Lin, G. and Shearer, P. (2007). Estimating local Vp/Vs ratios within similar earthquake clusters. *Bulletin of the Seismological Society of America*, 97(2):379–388.
- Lin, G. and Shearer, P. M. (2009). Evidence for water-filled cracks in earthquake source regions. *Geophysical Research Letters*, 36(17):L17315.
- Lomax, A., Virieux, J., Volant, P., and Berge, C. (2000). Probabilistic earthquake location in 3D and layered models: Introduction of a Metropolis-Gibbs method and comparison with linear locations. In Thurber, C. H. and Rabinowitz, N., editors, *Advances in Seismic Event Location*, pages 101–134. Springer, Amsterdam, The Netherlands.
- Lüth, S. (2000). Ergebnisse weitwinkelseismischer Untersuchungen und die Struktur der Kruste auf einer Traverse über die zentralen Anden bei 21° S. *Berliner geowiss. Abh.*, 37.
- Métois, M., Socquet, A., Vigny, C., Carrizo, D., Peyrat, S., Delorme, A., Maureira, E., Valderas-Bermejo, M.-C., and Ortega, I. (2013). Revisiting the North Chile seismic gap segmentation using GPS-derived interseismic coupling. *Geophysical Journal International*, 194(3):1283–1294.
- Moreno, M., Haberland, C., Oncken, O., Rietbrock, A., Angiboust, S., and Heidbach, O. (2014). Locking of the Chile subduction zone controlled by fluid pressure before the 2010 earthquake. *Nature Geoscience*, 7(4):292–296.
- Nábělek, J. and Xia, G. (1995). Moment-tensor analysis using regional data: Application to the 25 March, 1993, Scotts Mills, Oregon, Earthquake. *Geophysical Research Letters*, 22(1):13–16.
- Nábělek, J. L. (1984). *Determination of earthquake source parameters from inversion of body waves*. PhD thesis, M. I. T., Dept. of Earth, Atmospheric and Planetary Sciences.
- Nakajima, J., Tsuji, Y., Hasegawa, A., Kita, S., Okada, T., and Matsuzawa, T. (2009). Tomographic imaging of hydrated crust and mantle in the subducting Pacific slab beneath Hokkaido, Japan: Evidence for dehydration embrittlement as a cause of intraslab earthquakes. *Gondwana Research*, 16(3):470–481.



## BIBLIOGRAPHY

---

- Nedimovic, M. R., Hyndman, R. D., Ramachandran, K., and Spence, G. D. (2003). Reflection signature of seismic and aseismic slip on the northern Cascadia subduction interface. *Nature*, 424:416–420.
- NEIC (2017). Search Earthquake Catalog, <https://earthquake.usgs.gov/earthquakes/search/>.
- Oncken, O., Asch, G., Haberland, C., Metchie, J., Sobolev, S., Stiller, M., Yuan, X., Brasse, H., Buske, S., Giese, P., Görze, H.-J., Lueth, S., Scheuber, E., Shapiro, S., Wigger, P., Yoon, M.-K., Bravo, P., Vieytes, H., Chong, G., Gonzales, G., Wilke, H.-G., Lüschen, E., Martinez, E., Rössling, R., Ricaldi, E., and Rietbrock, A. (2003). Seismic imaging of a convergent continental margin and plateau in the central Andes (Andean continental research project 1996 (ANCORP'96)). *J. Geophys. Res.*, 108(B7):2328.
- Palo, M., Tilmann, F., and Schurr, B. (2016). Applicability and Bias of VP/VS Estimates by P and S Differential Arrival Times of Spatially Clustered Earthquakes. *Bulletin of the Seismological Society of America*, 106(3):1055–1063.
- Plümper, O., John, T., Podladchikov, Y. Y., Vrijmoed, J. C., and Scambelluri, M. (2017). Fluid escape from subduction zones controlled by channel-forming reactive porosity. *Nature Geoscience*.
- Podvin, P. and Lecomte, I. (1991). Finite difference computation of traveltimes in very contrasted velocity models: a massively parallel approach and its associated tools. *Geophysical Journal International*, 105(1):271–284.
- Press, W. H., Teukolsky, S. A., Vetterling, W. T., and Flannery, B. P. (2007). *Numerical recipes 3rd edition: The art of scientific computing*. Cambridge University Press.
- Pritchard, M., Norabuena, E., Ji, C., Boroscsek, R., Comte, D., Simons, M., Dixon, T. H., and Rosen, P. (2007). Geodetic, teleseismic, and strong motion constraints on slip from recent southern Peru subduction zone earthquakes. *Journal of Geophysical Research: Solid Earth*, 112(B3).
- Proctor, B. and Hirth, G. (2015). Role of pore fluid pressure on transient strength changes and fabric development during serpentine dehydration at mantle conditions: Implications for subduction-zone seismicity. *Earth and Planetary Science Letters*, 421:1–12.
- Ranero, C. R., Morgan, J. P., McIntosh, K., and Reichert, C. (2003). Bending-related faulting and mantle serpentinization at the Middle America trench. *Nature*, 425(6956):367–373.
- Ranero, C. R., Villaseñor, A., Phipps Morgan, J., and Weinrebe, W. (2005). Relationship between bend-faulting at trenches and intermediate-depth seismicity. *Geochemistry, Geophysics, Geosystems*, 6(12).

- Reutter, K., Döbel, R., Bogdanic, T., and Kley, J. (1994). Geological map of the central Andes. In Reutter, K., Scheuber, E., and Wigger, P., editors, *Tectonics of the Southern Central Andes, Structure and Evolution of an Active Continental Margin*. Springer, Berlin.
- Reyners, M., Eberhart-Phillips, D., Stuart, G., and Nishimura, Y. (2006). Imaging subduction from the trench to 300 km depth beneath the central North Island, New Zealand, with Vp and Vp/Vs. *Geophysical Journal International*, 165(2):565–583.
- Richards-Dinger, K. B. and Shearer, P. M. (2000). Earthquake locations in southern California obtained using source-specific station terms. *J. Geophys. Res.*, 105:10,939–10,960.
- Rietbrock, A. and Haberland, C. (2001). A tear in the subducting Nazca slab: Evidence from local earthquake tomography and high precision hypocenters. *Eos Trans. AGU*, 82:T31A–0822.
- Rietbrock, A. and Waldhauser, F. (2004). A narrowly spaced double-seismic zone in the subducting Nazca plate. *Geophys. Res. Lett.*, 31:L10608.
- Ruegg, J., Campos, J., Armijo, R., Barrientos, S., Briole, P., Thiele, R., Arancibia, M., Canuta, J., Duquesnoy, T., Chang, M., et al. (1996). The Mw= 8.1 Antofagasta (North Chile) earthquake of July 30, 1995: first results from teleseismic and geodetic data. *Geophysical Research Letters*, 23(9):917–920.
- Ruiz, S., Metois, M., Fuenzalida, A., Ruiz, J., Leyton, F., Grandin, R., Vigny, C., Madariaga, R., and Campos, J. (2014). Intense foreshocks and a slow slip event preceded the 2014 Iquique Mw 8.1 earthquake. *Science*, 345(6201):1165–1169.
- Rüpke, L. H., Morgan, J. P., Hort, M., and Connolly, J. A. (2004). Serpentine and the subduction zone water cycle. *Earth and Planetary Science Letters*, 223(1):17–34.
- Salazar, P. (2011). *The upper crustal microseismicity image from the North Chilean subduction zone: implications for tectonics and fluid migration*. PhD thesis, Freie Universität Berlin, Berlin, Germany.
- Salazar, P., Kummerow, J., Wigger, P., Shapiro, S., and Asch, G. (2016). State of stress and crustal fluid migration related to west-dipping structures in the slab-forearc system in the northern Chilean subduction zone. *Geophysical Journal International*, page ggw463.
- Schurr, B., Asch, G., Hainzl, S., Bedford, J., Hoechner, A., Palo, M., Wang, R., Moreno, M., Bartsch, M., Zhang, Y., et al. (2014). Gradual unlocking of plate boundary controlled initiation of the 2014 Iquique earthquake. *Nature*, 512(7514):299–302.
- Schurr, B., Asch, G., Rietbrock, A., Trumbull, R., and Haberland, C. (2003). Complex patterns of fluid and melt transport in the central Andean subduction zone revealed by attenuation tomography. *Earth Planet. Sci. Lett.*, 215:105–119.

## BIBLIOGRAPHY

---

- Schurr, B., Asch, G., Rosenau, M., Oncken, O., Barrientos, S., Salazar, P., and Vilotte, J.-P. (2012). The 2007 M7.7 Tocopilla northern Chile earthquake sequence- along and across strike rupture segmentation and the role of Mejillones Peninsula. *J. Geophys. Res.*, 117(B5):B05305.
- Schurr, B. and Nábělek, J. (1999). New techniques for the analysis of earthquake sources from local array data with an application to the 1993 Scotts Mills, Oregon, aftershock sequence. *Geophysical journal international*, 137(3):585–600.
- Schurr, B., Rietbrock, A., Asch, G., Kind, R., and Oncken, O. (2006). Evidence for lithospheric detachment in the central Andes from local earthquake tomography. *Tectonophysics*, 415(1–4):203–223.
- Shapiro, S. A. (2003). Elastic piezosensitivity of porous and fractured rocks. *Geophysics*, 68(2):482–486.
- Shearer, P. M. (1997). Improving local earthquake locations using the L1 norm and waveform cross correlation: Application to the Whittier Narrows, California, aftershock sequence. *J. Geophys. Res.*, 102:8,269–8,283.
- Shelly, D. R., Beroza, G. C., Zhang, H., Thurber, C. H., and Ide, S. (2006). High-resolution subduction zone seismicity and velocity structure beneath Ibaraki Prefecture, Japan. *Journal of Geophysical Research: Solid Earth*, 111(B6).
- Spence, W. (1987). Slab pull and the seismotectonics of subducting lithosphere. *Reviews of Geophysics*, 25(1):55–69.
- Springer, M. (1999). Interpretation of heat-flow density in the Central Andes. *Tectonophysics*, 306(3–4):377–395.
- Staudigel, H., Plank, T., White, B., and Schmincke, H.-U. (1996). Geochemical fluxes during seafloor alteration of the basaltic upper oceanic crust: DSDP Sites 417 and 418. *Subduction top to bottom*, pages 19–38.
- Takei, Y. (2002). Effect of pore geometry on Vp/Vs: From equilibrium geometry to crack. *Journal of Geophysical Research: Solid Earth (1978–2012)*, 107(B2):ECV–6.
- Thurber, C. (1993). Local earthquake tomography: velocities and Vp/Vs-theory. *Seismic tomography: theory and practice*, pages 563–583.
- Tsuji, Y., Nakajima, J., and Hasegawa, A. (2008). Tomographic evidence for hydrated oceanic crust of the Pacific slab beneath northeastern Japan: implications for water transportation in subduction zones. *Geophysical Research Letters*, 35(14).
- Turcotte, D. L. and Schubert, G. (2014). *Geodynamics*. Cambridge University Press.
- Ulmer, P. and Trommsdorff, V. (1995). Serpentine stability to mantle depths and subduction-related magmatism. *Science*, 268(5212):858–861.

- Wang, K. (2002). Unbending combined with dehydration embrittlement as a cause for double and triple seismic zones. *Geophys. Res. Lett.*, 29(18):1889.
- Wigger, P., Salazar, P., Kummerow, J., Bloch, W., Asch, G., and Shapiro, S. (2016). West–Fissure- and Atacama-Fault Seismic Network (2005/2012). Other/Seismic Network.
- Yamasaki, T. and Seno, T. (2003). Double seismic zone and dehydration embrittlement of the subducting slab. *J. Geophys. Res.*, 108(B4):2212.
- Yoon, M., Buske, S., Shapiro, S., and Wigger, P. (2008). Reflection Image Spectroscopy across the Andean subduction zone. *Tectonophysics*, 472:51–61.
- Yuan, X., Sobolev, S. V., Kind, R., Oncken, O., Bock, G., Asch, G., Schurr, B., Graeber, F., Rudloff, A., Hanka, W., Wylegalla, K., Tibi, R., Haberland, C., Rietbrock, A., Giese, P., Wigger, P., Röwer, P., Zandt, G., Beck, S., Wallace, T., Pardo, M., and Comte, D. (2000). Subduction and collision processes in the Central Andes constrained by converted seismic phases. *Nature*, 408:958–961.
- Zhang, H. and Thurber, C. (2006). Development and applications of double-difference seismic tomography. *Pure and Applied Geophysics*, 163(2-3):373–403.
- Zhang, H. and Thurber, C. H. (2003). Double-difference tomography: The method and its application to the Hayward fault, California. *Bulletin of the Seismological Society of America*, 93(5):1875–1889.
- Zhang, H., Thurber, C. H., Shelly, D., Ide, S., Beroza, G. C., and Hasegawa, A. (2004). High-resolution subducting-slab structure beneath northern Honshu, Japan, revealed by double-difference tomography. *Geology*, 32(4):361–364.



# Curriculum Vitae

Mein Lebenslauf wird aus Gründen des Datenschutzes in der elektronischen Fassung meiner Arbeit nicht veröffentlicht.

For privacy reasons my CV is not published in the electronic version of my thesis.

## Publications and Conference Abstracts

Bloch, W., Schurr, B., Kummerow, J., Salazar, P., and Shapiro, S. (2017). Herdmechanismen kleiner Erdbeben in der Subduktionszone der Zentralen Anden. *Jahrestagung der Deutschen Geophysikalischen Gesellschaft*.

Bloch, W., John, T., Kummerow, J., Wigger, P., Salazar, P., Krüger, O. S., and Shapiro, S. A. (2016a). Seismologische Messung und petrophysikalische Modellierung des P-zu-S-Wellen-Geschwindigkeitsverhältnisses im Mantel einer subduzierenden Platte. *Mitteilungen*, 3:5–8.

Bloch, W., John, T., Kummerow, J., Wigger, P., Salazar, P., and Shapiro, S. (2016b). Watching dehydration: transient vein-shaped porosity in the oceanic mantle of the subducting Nazca slab. *Geophysical Research Abstracts*.

Wigger, P., Salazar, P., Kummerow, J., Bloch, W., Asch, G., and Shapiro, S. (2016). West-Fissure- and Atacama-Fault Seismic Network (2005/2012). Other/Seismic Network.

Bloch, W., Kummerow, J., John, T., Wigger, P., and Shapiro, S. (2015a). Evidence for Metamorphic Slab Dehydration in the Central Andean Subduction Zone, Derived from Volumetric Vp/Vs Measurements And Thermodynamical Modeling. In Wagner, J. and Elger, K., editors, *GeoBerlin2015 - Dynamic Earth from Alfred Wegener to today and beyond - Abstracts*, pages 90–91.

Bloch, W., Kummerow, J., John, T., Wigger, P., and Shapiro, S. (2015b). Hinweise auf metamorphe Entwässerungsreaktionen in der Subduktionszone der zentralen Anden, abgeleitet aus volumetrischen Vp/Vs-Beobachtungen. *Jahrestagung der Deutschen Geophysikalischen Gesellschaft*.

Bloch, W., Kummerow, J., Salazar, P., Wigger, P., and Shapiro, S. A. (2014a). High-resolution image of the North Chilean subduction zone: seismicity, reflectivity and fluids. *Geophysical Journal International*, 197(3):1744–1749.

Bloch, W., Kummerow, J., Wigger, P., and Shapiro, S. (2014b). Abbild von P- zu S-Wellengeschwindigkeitsverhältnissen in der Nord-Chilenischen Subduktionszone. *Jahrestagung der Deutschen Geophysikalischen Gesellschaft*, pages 225–226.

- Bloch, W., Kummerow, J., Wigger, P., and Shapiro, S. (2014c). An image of P- to S-wave velocity ratios in the forearc of the Central Andean subduction zone. *Geophysical Research Abstracts*.
- Bloch, W., Kummerow, J., Wigger, P., and Shapiro, S. (2014d). Local seismicity and Vp/Vs at shallow to intermediate depth during the late interseismic phase of the Central Andean seismic gap. In *presented at 2014 Fall Meeting, AGU, San Francisco*.
- Bloch, W., Kummerow, J., and Wigger, P. (2013a). High-resolution image of seismicity at the fore-arc of the northern Chilean Iquique segment. *Geophysical Research Abstracts*, 15.
- Bloch, W., Kummerow, J., and Wigger, P. (2013b). Hoch-auflösende Abbildung von hoher Seismizität im fore-arc des Nordchilenischen Iquique-Segments. *Jahrestagung der Deutschen Geophysikalischen Gesellschaft*, pages 338–338.
- Bloch, W., Kummerow, J., Wigger, P., Shapiro, S., and Salazar, P. (2012). Crustal and Slab Related Seismicity in the Northern Chilean Coastal Cordillera. *Geophysical Research Abstracts*, 14.
- Bloch, W., Tanner, D. C., and Paul, J. (2011). Störungskörper in einem Seitenverschiebungssystem bei Hardeggen. In *Neue Untersuchungen zur Geologie der Leinetalgrabenstruktur*, pages 79–82. Universitätsdrucke Göttingen, Göttingen.





